

DTIC
FINAL REPORT
R&D 9142-EN-01
N68171-01-M-5806
THE UNIVERSITY OF READING, UK

**THE ANALYSIS OF HYPERSPECTRAL IMAGERY AND TESTING THE
WAVELET VARIOGRAM**

Final Report (RSSUSA - 6/2)

Dr Margaret A. Oliver

September 2001 to April 2001

United States Army

ENVIRONMENTAL RESEARCH OFFICE OF THE U.S. ARMY

London, England

CONTRACT NUMBER - N68171-01-M-5808

Contractor - Approved for Public Release; distribution unlimited

20020429 040

**THE ANALYSIS OF HYPERSPECTRAL IMAGERY AND TESTING THE
WAVELET VARIOGRAM**

Final Report (RSSUSA - 6/2)

Dr Margaret A. Oliver

September 2001 to April 2001

United States Army

ENVIRONMENTAL RESEARCH OFFICE OF THE U.S. ARMY

London, England

CONTRACT NUMBER - N68171-01-M-5808

Contractor - Approved for Public Release; distribution unlimited

REPORT DOCUMENTATION PAGEForm Approved
OMB No. 0704-0188

Public reporting burden for this collection of information is estimated to average 1 hour per response, including the time for reviewing instructions, searching existing data sources, gathering and maintaining the data needed, and completing and reviewing this collection of information. Send comments regarding this burden estimate or any other aspect of this collection of information, including suggestions for reducing this burden to Washington Headquarters Services, Directorate for Information Operations and Reports, 1215 Jefferson Davis Highway, Suite 1204, Arlington, VA 22202-4302, and to the Office of Management and Budget, Paperwork Reduction Project (0704-0188), Washington, DC 20503

1. AGENCY USE ONLY (Leave blank)		2. REPORT DATE 28. 02. 02	3. REPORT TYPE AND DATES COVERED Interim report September 2001 to April 2002	
4. TITLE AND SUBTITLE The Analysis of Hyperspectral Imagery and Testing the Wavelet Variogram			5. FUNDING NUMBERS N68171-01-M-5808	
6. AUTHOR(S) Dr Margaret A. Oliver			8. PERFORMING ORGANIZATION REPORT NUMBER RSSUSA - 6/2	
7. PERFORMING ORGANIZATION NAME(S) AND ADDRESS(ES) University of Reading, Whiteknights, Reading RG6 6DW, United Kingdom.				
9. SPONSORING / MONITORING AGENCY NAME(S) AND ADDRESS(ES) USARDSG-UK, Environmental Sciences Branch, Edison House, 233 Old Marylebone Road,			10. SPONSORING / MONITORING AGENCY REPORT NUMBER	
11. SUPPLEMENTARY NOTES Final report.				
12a. DISTRIBUTION / AVAILABILITY STATEMENT No limitation on distribution/availability.			12b. DISTRIBUTION CODE	
13. ABSTRACT (Maximum 200 Words) This report contains one interim report, together with the most recent results. Part I describes the work done during a visit by Mr Bosch of the Topographic Engineering Center, Alexandria. Part II describes the analysis of selected pixels from part of a SPOT image of Fort A. P. Hill chosen to represent several different types of ground cover. The classes have distinct characteristics evident in the variograms. Part III describes the analysis of hyperspectral data: the hydice imagery for Fort Hood and hymap imagery for Fort A. P. Hill for six different ground cover classes at each site. For Fort Hood the spectra vary considerable for the different ground cover classes and the variograms have certain distinctive features. The spectra for Fort A. P. Hill are less distinctive apart from one class, but the amplitudes of the periodic functions fitted to the variograms provide one means of discrimination. For both sites three principal components accounted for most of the variation. When the pixels were plotted in a projection of the first two components four clear groups were evident for Fort Hood and three for A. P. Hill. A non-hierarchical multivariate method of classification was also applied. Appendix I contains the GenStat program to fit periodic functions, Appendix II a paper submitted to the International Journal of Remote Sensing, and Appendix III a paper submitted to Mathematical Geology.				
14. SUBJECT TERMS wavelet variogram, ground cover classes, SPOT image, hyperspectral imagery, Fort Hood, Fort A. P. Hill			15. NUMBER OF PAGES 12	
17. SECURITY CLASSIFICATION OF REPORT			16. PRICE CODE	
18. SECURITY CLASSIFICATION OF THIS PAGE			20. LIMITATION OF ABSTRACT	
19. SECURITY CLASSIFICATION OF ABSTRACT				

NSN 7540-01-280-5500

Standard Form 298 (Rev. 2-89)
Prescribed by ANSI Std. Z39-18
298-102

--

TABLE OF CONTENTS

Contents	Page Number
Preface	ix
Executive Summary	x
PART I: Report on visit by Edward Bosch	1
PART II: Analysis of selected classes of ground cover at Fort A. D. Hill	1
Class 10	4
Class 20	5
Class 30	6
Class 40	7
Class 50	8
Class 60	9
Class 70	10
Summary of analysis of classes	11
PART III: Analysis of hyperspectral imagery from Fort Hood and Fort A. P. HILL	12
Fort Hood spectra	12
Spectra	13
Variography	14
Visual appraisal of ground cover class spectra and variograms	16
Multivariate analysis of Fort Hood spectra	16
Principal component analysis	16
Non-hierarchical <i>k</i> -means dynamic clustering	17
Class 1 pixels	20
Class 2 pixels	20
Class 3 pixels	21
Class 4 pixels	21
Class 5 pixels	21
Class 6 pixels	22
Summary of results	23
Fort A. P. Hill spectra	73
Spectra	74
Variography	74
Multivariate analysis of Fort A. P. Hill spectra	75
Principal component analysis	75
Non-hierarchical <i>k</i> -means dynamic clustering	76
Class 1 pixels	77
Class 2 pixels	77
Class 3 pixels	77
Class 4 pixels	77
Class 5 pixels	78
Class 6 pixels	78
Summary of results	78
Conclusions	79
Acknowledgement	79
Appendix I	104
Appendix II	110
Appendix III	123

LIST OF TABLES

Table	Page
Table 1. Summary statistics for the six spectral classes for Fort A. P. Hill.	2
Table 2. Model parameters for the functions fitted to the experimental variograms of the six spectral classes for Fort A. P. Hill.	11
Table 3. Classes of different ground cover type and number of pixels in each for Fort Hood.	13
Table 4. Summary of trend analysis and model parameters of variograms for selected pixels for Fort Hood.	65-67
Table 5. Eigenvalues and eigenvectors for Fort Hood using all spectra.	68-69
Table 6. Classes from the non-hierarchical classification of Fort Hood spectra using 66 wavebands and the first three principal components.	70-72
Table 7. Classes of different ground cover type and number of pixels in each for Fort A. P. Hill.	73
Table 8. Summary of trend analysis and model parameters of variograms for selected pixels for Fort A. P. Hill.	98-99
Table 9. Eigenvalues and eigenvectors for Fort A. P. Hill using all spectra.	100-101
Table 10. Classes from the non-hierarchical classification of Fort A. P. Hill spectra using 63 wavebands and the first three principal components.	102-103

LIST OF FIGURES

Figure	Page Number
Figure 1. a) Part of SPOT image for Fort A. P. Hill, b) locations of six of the seven classes from the SPOT image of A. P. Hill.	3
Figure 2. Class 10: a) pixel values of NIR, b) histogram, c) experimental variogram (symbols) circular variogram model, (line), d) experimental variogram (symbols) stable exponential variogram model.	4
Figure 3. Class 20: a) pixel values of NIR, b) histogram, c) experimental variogram (symbols), d) experimental variogram (symbols) circular variogram model (line).	5
Figure 4. Class 30: a) pixel values of NIR, b) histogram, c) experimental variogram (symbols), d) experimental variogram (symbols) circular variogram model (line).	6
Figure 5. Class 40: a) pixel values of NIR, b) histogram, c) experimental variogram (symbols), d) experimental variogram (symbols) pentaspherical variogram model (line).	7
Figure 6. Class 50: a) pixel values of NIR, b) histogram, c) experimental variogram (symbols), d) experimental variogram (symbols) circular variogram model (line).	8
Figure 7. Class 60: a) pixel values of NIR, b) histogram, c) experimental variogram (symbols), d) experimental variogram (symbols) circular variogram model (line).	9
Figure 8. Class 70: a) pixel values of NIR, b) histogram, c) experimental variogram (symbols), d) experimental variogram (symbols) pentaspherical variogram model (line).	10
Figure 9. a) Colour image of part of Fort Hood and b) the locations and sizes of the classes of pixels.	12
Figure 10. Plot of individual pixels in the projection of principal components 1 and 2 using the PC scores. The ground cover classes are shown near to the relevant group of pixels, and the line shows the approximate separation between classes 2 and 5.	17
Figure 11. Sum of squares criterion plotted against g (number of groups) for: a) 33 wavebands, b) 66 wavebands, and c) the scores of the first five principal components.	19
Figure 12. Ft Hood: pixel 1: a) spectrum, b) experimental variogram of raw values, and c) experimental variogram and fitted model (PPF) of quadratic residuals.	24
Figure 13. Ft Hood: pixel 25: a) spectrum, b) experimental variogram of raw values, and c) experimental variogram and fitted model (PES) of quadratic residuals.	24
Figure 14. Ft Hood: pixel 50: a) spectrum, b) experimental variogram of raw values, and c) experimental variogram of quadratic residuals.	25
Figure 15. Ft Hood: pixel 71: a) spectrum, b) experimental variogram of raw values, and c) experimental variogram and fitted model (PPF) of quadratic residuals.	26
Figure 16. Ft Hood: pixel 76: a) spectrum, b) experimental variogram of raw values, and c) experimental variogram of quadratic residuals.	26
Figure 17. Ft Hood: pixel 77: a) spectrum, b) experimental variogram and fitted model (PPF) of quadratic residuals.	27
Figure 18. Ft Hood: pixel 78: a) spectrum, b) experimental variogram of quadratic residuals.	27
Figure 19. Ft Hood: pixel 79: a) spectrum, b) experimental variogram of quadratic residuals.	28
Figure 20. Ft Hood: pixel 80: a) spectrum, b) experimental variogram of quadratic residuals.	28
Figure 21. Ft Hood: pixel 82: a) spectrum, b) experimental variogram of raw values, and c) experimental variogram and fitted model (PPF) of quadratic residuals.	29
Figure 22. Ft Hood: pixel 85: a) spectrum, b) experimental variogram and fitted model (PPF) of quadratic residuals.	29

LIST OF FIGURES (cont.)

Figure	Page Number
Figure 23. Ft Hood: pixel 90: a) spectrum, b) experimental variogram of raw values, and c) experimental variogram and fitted model (PPF) of quadratic residuals.	30
Figure 24. Ft Hood: pixel 91: a) spectrum, b) experimental variogram and fitted model (PPF) of quadratic residuals.	30
Figure 25. Ft Hood: pixel 95: a) spectrum, b) experimental variogram of raw values, and c) experimental variogram and fitted model (PPF) of quadratic residuals.	31
Figure 26. Ft Hood: pixel 96: a) spectrum, b) experimental variogram and fitted model (PPF) of quadratic residuals	31
Figure 27. Ft Hood: pixel 100: a) spectrum, b) experimental variogram of raw values, and c) experimental variogram and fitted model (PPF) of quadratic residuals.	32
Figure 28. Ft Hood: pixel 104: a) spectrum, b) experimental variogram of raw values, and c) experimental variogram and fitted model (PPF) of quadratic residuals.	32
Figure 29. Ft Hood: pixel 107: a) spectrum, b) variogram and fitted model (PEF) of raw values clipped, c) variogram and fitted model (PPF) of quadratic residuals.	33
Figure 30. Ft Hood: pixel 108: a) spectrum, b) experimental variogram and fitted model (PPF) of quadratic residuals.	33
Figure 31. Ft Hood: pixel 111: a) spectrum, b) experimental variogram and fitted model (PPF) of quadratic residuals.	34
Figure 32. Ft Hood: pixel 114: a) spectrum, b) experimental variogram and fitted model (PPF) of quadratic residuals.	34
Figure 33. Ft Hood: pixel 120: a) spectrum, b) experimental variogram of raw values, and c) experimental variogram and fitted model (PPF) of quadratic residuals.	35
Figure 34. Ft Hood: pixel 121: a) spectrum, b) experimental variogram and fitted model (PPF) of quadratic residuals.	35
Figure 35. Ft Hood: pixel 124: a) spectrum, b) experimental variogram of raw values and c) experimental variogram and fitted model (PPF) of quadratic residuals.	36
Figure 36. Ft Hood: pixel 128 a) spectrum, b) experimental variogram of raw values, and c) experimental variogram and fitted model (PPF) of quadratic residuals.	37
Figure 37. Ft Hood: pixel 131 a) spectrum, b) experimental variogram and fitted model (PPF) of quadratic residuals.	37
Figure 38. Ft Hood: pixel 134: a) spectrum, b) experimental variogram of raw values, and c) experimental variogram and fitted model (PPF) of quadratic residuals.	38
Figure 39. Ft Hood: pixel 139: a) spectrum, b) experimental variogram of raw values, and b) experimental variogram and fitted model (PPF) of quadratic residuals.	38
Figure 40. Ft Hood: pixel 140: a) spectrum, b) experimental variogram and fitted model (PPF) of quadratic residuals.	39
Figure 41. Ft Hood: pixel 141 a) spectrum, b) experimental variogram and fitted model (PPF) of quadratic residuals.	39
Figure 42. Ft Hood: pixel 142: a) spectrum, b) experimental variogram and fitted model (PPF) of quadratic residuals.	40
Figure 43. Ft Hood: pixel 143: a) spectrum, b) experimental variogram and fitted model (PPF) of quadratic residuals.	40
Figure 44. Ft Hood: pixel 140: a) spectrum, b) experimental variogram and fitted model (PPF)	

LIST OF FIGURES (cont.)

Figure	Page Number
Figure 45. Ft Hood: pixel 159: a) spectrum, b) experimental variogram of raw values, and c) experimental variogram and fitted model (PPF) of quadratic residuals.	41
Figure 46. Ft Hood: pixel 160: a) spectrum, b) experimental variogram and fitted model (PPF) of quadratic residuals.	42
Figure 47. Ft Hood: pixel 161: a) spectrum, b) experimental variogram and fitted model (PPF) of quadratic residuals.	42
Figure 48. Ft Hood: pixel 162: a) spectrum, b) experimental variogram of raw values, and c) experimental variogram and fitted model (PPF) of quadratic residuals.	43
Figure 49. Ft Hood: pixel 163: a) spectrum, b) experimental variogram and fitted model (PPF) of raw values, and c) as b) but clipped at 500 nm lag distance.	44
Figure 50. Ft Hood: pixel 163 a) spectrum, b) variogram and fitted model (PPF) of raw values, c) variogram and model (periodic) of linear residuals, clipped.	44
Figure 51. Ft Hood: pixel 167: a) spectrum, b) experimental variogram and fitted model (PPF) of raw values.	45
Figure 52. Ft Hood: pixel 168: a) spectrum, b) experimental variogram and fitted model (PPF) of raw values.	45
Figure 53. Ft Hood: pixel 169: a) spectrum, b) experimental variogram and fitted model (PPF) of raw values.	46
Figure 54. Ft Hood: pixel 171: a) spectrum, b) experimental variogram and fitted model (PPF) of raw values.	46
Figure 55. Ft Hood: pixel 188: a) spectrum, b) experimental variogram and fitted model (PPF) of raw values.	47
Figure 56. Ft Hood: pixel 190: a) spectrum, b) experimental variogram and fitted model (PPF) of raw values.	47
Figure 57. Ft Hood: pixel 193: a) spectrum, b) experimental variogram and fitted model (PPF) of raw values.	48
Figure 58. Ft Hood: pixel 195: a) spectrum, b) experimental variogram and fitted model (PPF) of raw values, and c) variogram of linear residuals.	48
Figure 59. Ft Hood: pixel 198: a) spectrum, b) experimental variogram and fitted model (PPF) of raw values.	49
Figure 60. Ft Hood: pixel 204: a) spectrum, b) experimental variogram and fitted model (PPF) of raw values.	49
Figure 61. Ft Hood: pixel 206: a) spectrum, b) experimental variogram and fitted model (PPF) of raw values.	50
Figure 62. Ft Hood: pixel 207: a) spectrum, b) experimental variogram and fitted model (PPF) of raw values, c) as b) but clipped at 500 nm lag distance.	50
Figure 63. Ft Hood: pixel 213: a) spectrum, b) experimental variogram and fitted model (PPF) of raw values, and c) variogram of linear residuals.	51
Figure 64. Ft Hood: pixel 214: a) spectrum, b) experimental variogram and fitted model (PPF) of raw values.	51
Figure 65. Ft Hood: pixel 230: a) spectrum, b) experimental variogram and fitted model (PEF) of quadratic residuals.	52
Figure 66. Ft Hood: pixel 234: a) spectrum, b) variogram and fitted model (PEF) of raw values,	

- c) variogram and fitted model (PEF) of quadratic residuals.

52

LIST OF FIGURES (cont.)

Figure	Page Number
Figure 67. Ft Hood: pixel 242: a) spectrum, b) experimental variogram and fitted model (PES) of raw values, c) experimental variogram and fitted model (PEF) of raw values, clipped at 500nm lag distance, d) experimental variogram and fitted model (PEF) of quadratic residuals and e) experimental variogram and fitted model (PPF) of quadratic residuals, clipped at 300 nm lag distance.	53
Figure 68. Ft Hood: pixel 250: a) spectrum, b) experimental variogram of raw values, and c) experimental variogram and fitted model (PPF) of quadratic residuals.	54
Figure 69. Ft Hood: pixel 255: a) spectrum, b) experimental variogram of raw values, and c) experimental variogram and fitted model (PPF) of quadratic residuals.	54
Figure 70. Ft Hood: pixel 257: a) spectrum, b) experimental variogram of raw values, and c) experimental variogram and fitted model (PPF) of quadratic residuals.	55
Figure 71. Ft Hood: pixel 260: a) spectrum, b) experimental variogram and fitted model (PPF) of quadratic residuals.	55
Figure 72. Ft Hood: pixel 261: a) spectrum, b) experimental variogram and fitted model (PPF) of quadratic residuals.	56
Figure 73. Ft Hood: pixel 266: a) spectrum, b) experimental variogram of raw values, and c) experimental variogram and fitted model (PPF) of quadratic residuals.	56
Figure 74. Ft Hood: pixel 268: a) spectrum, b) experimental variogram of quadratic residuals.	57
Figure 75. Ft Hood: pixel 269: a) spectrum, b) experimental variogram of quadratic residuals.	57
Figure 76. Ft Hood: pixel 272: a) spectrum, b) experimental variogram of raw values and d) experimental variogram and fitted model (PPF) of quadratic residuals.	58
Figure 77. Ft Hood: pixel 273: a) spectrum, b) experimental variogram of quadratic residuals.	58
Figure 78. Ft Hood: pixel 278: a) spectrum, b) experimental variogram of raw values and c) experimental variogram of quadratic residuals.	59
Figure 79. Ft Hood: pixel 282: a) spectrum, b) experimental variogram of raw values and c) experimental variogram of quadratic residuals.	59
Figure 80. Ft Hood: pixel 284: a) spectrum, b) experimental variogram and fitted model (PPF) of quadratic residuals	60
Figure 81. Ft Hood: pixel 288: a) spectrum, b) experimental variogram of raw values, c) experimental variogram and fitted model (PEF) of quadratic residuals, d) variogram and fitted model (PEF) of quadratic residuals clipped at 500 nm.	61
Figure 82. Ft Hood: pixel 300: a) spectrum, b) experimental variogram of raw values, c) experimental variogram and fitted model (PEF) of quadratic residuals, d) variogram and fitted model (PES) of quadratic residuals clipped at 500 nm, e) variogram and fitted <i>long wavelength</i> model (PPF) of quadratic residuals.	62
Figure 83. Ft Hood: pixel 317: a) spectrum, b) experimental variogram of raw values, c) experimental variogram and fitted model (PPF) of quadratic residuals, d) variogram and fitted model (PEF) of quadratic residuals clipped at 500 nm.	63
Figure 84. Ft Hood: pixel 323: a) spectrum, b) experimental variogram and fitted <i>long wavelength</i> model (PPF) of quadratic residuals.	64

Figure 85. Ft Hood: pixel 327: a) spectrum, b) experimental variogram and fitted model (PEF) of quadratic residuals, c) as b) fitted to *long wavelength* model (PEF). 64

LIST OF FIGURES (cont.)

Figure	Page Number
Figure 86. a) Colour image of part of Fort A. P. Hill, and b) the locations and sizes of the classes of pixels.	73
Figure 87. Plot of individual pixels in the projection of principal components 1 and 2 using the PC scores. The ground cover classes are shown near to the relevant group of pixels, and the lines shows the approximate separation between classes 2, 3 and 4.	75
Figure 88. Sum of squares criterion plotted against g (number of groups) for: a) 63 wavebands, and b) the scores of the first five principal components.	76
Figure 89. A.P. Hill: pixel 1: a) spectrum, b) experimental variogram of raw values, c) and d) experimental variogram and fitted models of quadratic residuals – short wavelength PES and long wavelength PPF, respectively.	90
Figure 90. A.P. Hill: pixel 4: a) spectrum, b) experimental variogram of raw values and c) experimental variogram of quadratic residuals.	81
Figure 91. A.P. Hill: pixel 40: a) spectrum, b) and c) experimental variogram and fitted models of quadratic residuals - short and long wavelength PPF model.	81
Figure 92. A.P. Hill: pixel 44: a) spectrum, b) experimental variogram of raw values, c) experimental variogram of linear residuals, d) and e) experimental variogram and fitted models of quadratic residuals - short wavelength PEF and long wavelength PPF, respectively.	82
Figure 93. A.P. Hill: pixel 50: a) spectrum, b) and c) experimental variogram and fitted models of quadratic residuals - short PES and long wavelength PPF model.	83
Figure 94. A.P. Hill: pixel 54: a) spectrum, b) and c) experimental variogram and fitted models of quadratic residuals - short (PES) and long wavelength (PPF model).	83
Figure 95. A.P. Hill: pixel 65: a) spectrum, b) and c) experimental variogram and fitted models of quadratic residuals – short PES and long wavelength PPF model.	84
Figure 96. A.P. Hill: pixel 70: a) spectrum, b) experimental variogram of raw values, c) variogram of linear residuals and d) variogram of quadratic residuals.	84
Figure 97. A.P. Hill: pixel 75: a) spectrum, b) experimental variogram and fitted model of quadratic residuals (short wavelength PES model).	85
Figure 98. A.P. Hill: pixel 76: a) spectrum, b) experimental variogram of raw values, c) and d) variograms and fitted models of quadratic residuals - short wavelength PES model and long wavelength PPF model.	85
Figure 99. A.P. Hill: pixel 79: a) spectrum, b) experimental variogram of raw values, c) and d) variograms and fitted models of quadratic residuals - short wavelength PES model and long wavelength PPF model.	86
Figure 100. A.P. Hill: pixel 87 a) spectrum, b) experimental variogram of raw values, c) experimental variogram of linear residuals, d) and e) experimental variogram and fitted models of quadratic residuals - short wavelength PES and long wavelength PPF, respectively.	87

Figure 101. A.P. Hill: pixel 90: a) spectrum, b) and c) experimental variogram and fitted models of quadratic residuals - short PES and long wavelength PPF model.	88
Figure 102. A.P. Hill: pixel 104: a) spectrum, b) and c) experimental variogram and fitted models of quadratic residuals - short PES and long wavelength PPF model.	89

LIST OF FIGURES (cont.)

Figure	Page Number
Figure 103. A.P. Hill: pixel 107: a) spectrum, b) variogram of raw values, c) and d) variogram and fitted models of quadratic residuals - short PES and long wave PPF.	89
Figure 104. A.P. Hill: pixel 108: a) spectrum, b) experimental variogram of quadratic residuals.	90
Figure 105. A.P. Hill: pixel 115: a) spectrum, b) experimental variogram of raw values, c) and d) experimental variogram and fitted models of quadratic residuals - short wavelength PEF and long wavelength PPF model.	90
Figure 106. A.P. Hill: pixel 119: a) spectrum, b) and c) experimental variogram and fitted models of quadratic residuals - short PES and long wavelength PPF model.	91
Figure 107. A.P. Hill: pixel 120: a) spectrum, b) and c) experimental variogram and fitted models of quadratic residuals - short PES and long wavelength PPF model.	91
Figure 108. A.P. Hill: pixel 133: a) spectrum, b) experimental variogram of raw values, c) experimental variogram of linear residuals, d) and e) experimental variogram and fitted models of quadratic residuals - short wavelength PEF and long wavelength PPF, respectively.	92
Figure 109. A.P. Hill: pixel 139: a) spectrum, b) and c) experimental variogram and fitted models of quadratic residuals - short PEF and long wavelength PPF model.	93
Figure 110. A.P. Hill: pixel 141: a) spectrum, b) and c) variogram and fitted models of raw data, short PES and long PPF, d) variogram of quadratic residuals (PPF).	93
Figure 111. A.P. Hill: pixel 160: a) spectrum, b) experimental variogram and fitted model (PPF) of raw values c) experimental variogram and fitted model of linear residuals, long wavelength PPF, and d) and e) experimental variogram and fitted models of quadratic residuals - short wavelength PEF and long wavelength PPF, respectively.	94
Figure 112. A.P. Hill: pixel 165: a) spectrum, b) and c) experimental variogram and fitted models of raw values, short and long wavelength d) and e) experimental variogram and fitted models of linear residuals - short wavelength PEF and long wavelength PPF, respectively.	95
Figure 113. A.P. Hill: pixel 166: a) spectrum, b) experimental variogram and fitted models of raw data, short wavelength PPF model and c) experimental variogram and fitted models of linear residuals, short wavelength PEF.	96
Figure 114. A.P. Hill: pixel 167: a) spectrum, b) experimental variogram of raw data, c) experimental variogram of linear residuals.	96
Figure 115. A.P. Hill: pixel 168: a) spectrum, b) and c) experimental variogram and fitted models (PPF) of raw values, short and long wavelength d) and e) experimental variogram and fitted models of linear residuals - short wavelength PES and long wavelength PPF, respectively.	97

PREFACE

This report was sponsored by the United States Army Research, Development and standardization Group-UK (USARDGSG-UK), London, NW1 5TH, United Kingdom, under contract PR-N68171-00-M-5508, entitled, "Application of geostatistical methods and wavelets to the analysis of hyperspectral imagery and the testing of a moving variogram". It is monitored by the U. S. Army Topographic Engineering Center (TEC), Alexandria, Virginia 22315-3863. The work was done by the University of Reading, Whiteknights, Reading, RG6 6DW, United Kingdom. The USARDGSG-UK Program Manager is Mr. Jerry Comati, and the TEC Contracting Officer's Representative is Mr. James Shine

EXECUTIVE SUMMARY

This report contains one interim report, together with the most recent results. Part I describes the work done during a visit by Mr Bosch of the Topographic Engineering Center, Alexandria. Part II describes the analysis of selected pixels from part of a SPOT image of Fort A. P. Hill. They were chosen to represent several different types of ground cover. The NIR part of the spectrum was analysed for these pixels. There were seven classes of pixels and the values in each were subject to an exploratory data analysis. The results show that several classes have distinct characteristics that were distinguished by the variograms of the class data and their model parameters.

Part III describes the analysis of hyperspectral data: the hydice imagery for Fort Hood and hymap imagery for Fort A. P. Hill. Pixels were selected for six different ground cover classes at each site. The spectrum for each pixel was plotted and examined visually. All of the experimental variograms computed for each spectrum showed evidence of trend and this was usually removed satisfactorily by linear and quadratic functions. The variograms were recomputed on the residuals and modelled with several periodic functions for which a program was written in GenStat. For Fort Hood the spectra vary considerably for the different ground cover classes and the variograms have certain distinctive features. The spectra for Fort A. P. Hill are less distinctive apart from one class, but the amplitudes of the periodic functions fitted to the variograms provide one means of discrimination. To explore these data further principal component analyses were done. For both sites three components accounted for most of the variation. Certain sections of the spectrum accounted for the variation on these axes. When the pixels were plotted in a projection of the first two components four clear groups were evident for Fort Hood and three for A. P. Hill. A non-hierarchical multivariate method of classification was applied to 50% of the waveband data and to the scores of the leading principal components. The results using the latter provided the best discrimination and the best relation with the ground cover classes. There are features in the spectra and the variograms that enable discrimination between ground cover classes, which is supported by the multivariate analyses.

Appendix I is a GenStat program to fit periodic functions to the experimental variogram. In addition Appendix II is the text of another paper resulting from work with Mr Shine and Mr Slocum. This has been submitted to the International Journal of Remote Sensing. The comparison between the usual variogram estimator (Matheron's method of moments) and the wavelet based variograms is given in Appendix II. The results suggest that the wavelet variograms can remove long-range trend features whether they arise from stepped functions, such as those related to the boundaries between different types of soil or rock, or from smooth variation that can be represented by a trend surface. This would avoid the need to examine the data for trend first. The effects of local trend or drift, which are less common in most earth science data, appear to be amplified by the wavelet-based variograms, however. An oral presentation of this work will be made at the GeostatsUK meeting in Reading, England, in March 2002. Professor Webster has devoted most of his time on this contract to preparing the theoretical part of the text with Mr Bosch for publication and writing Fortran code for the simulations.

PART I REPORT ON VISIT BY E. BOSCH

The purpose of the visit by Mr Bosch was to continue with our work to publish a paper on the wavelet variogram. This was started as part of the previous project and is now nearing completion. Professor Webster has made considerable input into this in making the mathematics more comprehensible to non-mathematicians. The paper shows the relation between the conventional variogram of geostatistics and a variogram based on the wavelet transform. The discovery of the relation by Mr Bosch is novel as far as we know.

Professor Webster spent three days working with us on this and during this time many analyses were done to try to gain insight into what the two approaches do. The analyses were done on two sets of real data and one set of simulated data. It seems that if there is long-range trend present in the data the wavelet variogram can deal with it whereas it must be removed before the analysis of the conventional variogram. Also where there are distinct boundaries (different classes of soil along a transect) it seems that the Daubechies wavelet variogram disregards the effect of the boundaries and the variogram relates to the variation between the class boundaries.

The other two days that Mr Bosch was in Reading were spent in preparing data for analysis during the second part of this project. In addition, we examined different levels of thresholding in a wavelet analysis of the Fort A. P. Hill SPOT data. The aim of this is to compare wavelet multiresolution analysis and factorial kriging. These results will be added to the paper presented at the International Geostatistics Congress in 2000 for publication in the International Journal of Remote Sensing.

PART II ANALYSIS OF SELECTED CLASSES OF GROUND COVER AT FORT A. P. HILL

Figure 1a shows the NIR values from the SPOT image of Fort A. P. Hill as a pixel map. Figure 1b, derived from Matlab, shows the location of the seven classes. By comparing the two maps it is clear that the classes relate to areas with identifiable levels of reflectance in the NIR waveband. Some classes are similar, but they are in different parts of the scene. Class 10 is the least homogeneous, which can be seen if Figure 1a is examined carefully. It incorporates both valley and spur components. Class 20 appears to be an open area from the topographic sheet and on a valley side between a spur or upland area and valley bottom. Classes 30 and 40 are upland or spur areas with low to intermediate reflectance values. Classes 50 and 60 are valley areas and appear to be more homogeneous than many of the other classes. Class 70 appears to be unwooded in part and on a spur.

Table 1 gives the summary statistics of the seven ground cover classes for near infra red (NIR)spectral values. Class 10 is the most variable class (see Figure 2a) and also in terms of the coefficient of variation. Classes 20 and 40 are the least variable, i.e. the most homogeneous (see Figures 3a and 5a). The remaining four classes have similar coefficients of variation, Table 1. The less variation there is within the class the greater its coherence. Classes 20 and 30 have similar mean values, as do classes 40 and 70, and 50 and 60. Class 10, as already noted, is different from the other classes and this is also the case with respect to the mean.

The histogram of class 10 suggests that the statistical distribution is bimodal. Again this shows its difference from the other classes and probably reflects the spur and valley components in the class. As a consequence it might have been beneficial to do the variogram analysis of the two strata separately. However, there were insufficient data for this. All of the other histograms show a unimodal distribution. The values for all classes have a near-normal distribution as shown by the histograms and the skewness values. Therefore, no transformation of the data was necessary.

Table 1: Summary statistics for the six spectral classes for Fort A. P. Hill.

Parameter	Classes						
	10	20	30	40	50	60	70
Number of observations	183	146	192	161	167	193	113
Mean	126.0	118.1	114.0	98.59	141.1	140.1	102.2
Median	128.0	119.0	113.0	99.0	142.0	141.0	103.0
Minimum	107.0	109.0	95.0	90.0	119.0	122.0	90.0
Maximum	148.0	125.0	131.0	110.0	166.0	169.0	116.0
Variance	102.9	13.62	60.67	15.33	78.06	68.03	28.38
Standard deviation	10.14	3.690	7.789	3.915	8.835	8.248	5.327
Coefficient of variation	8.048	3.127	6.832	3.971	6.266	5.891	5.223
Skewness	-0.160	-0.443	0.237	0.115	0.085	0.359	0.024
Kurtosis	-1.172	-0.134	-0.606	-0.098	0.053	0.934	-0.046

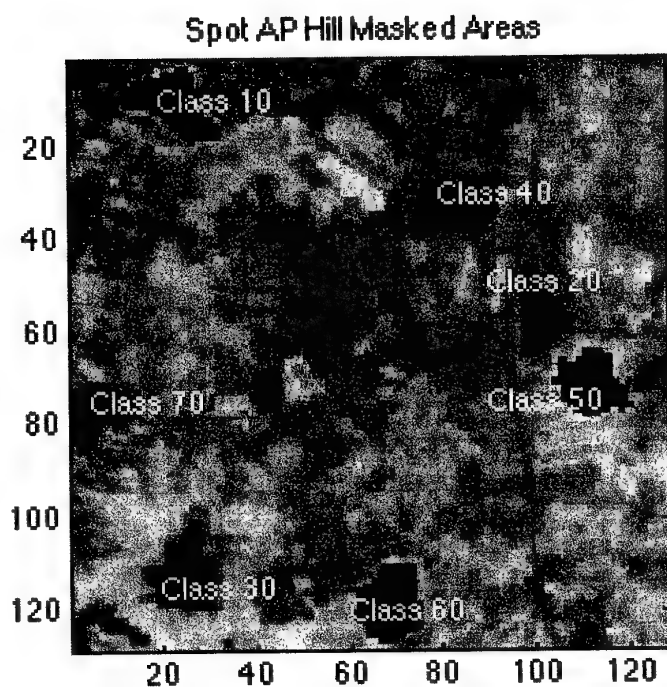
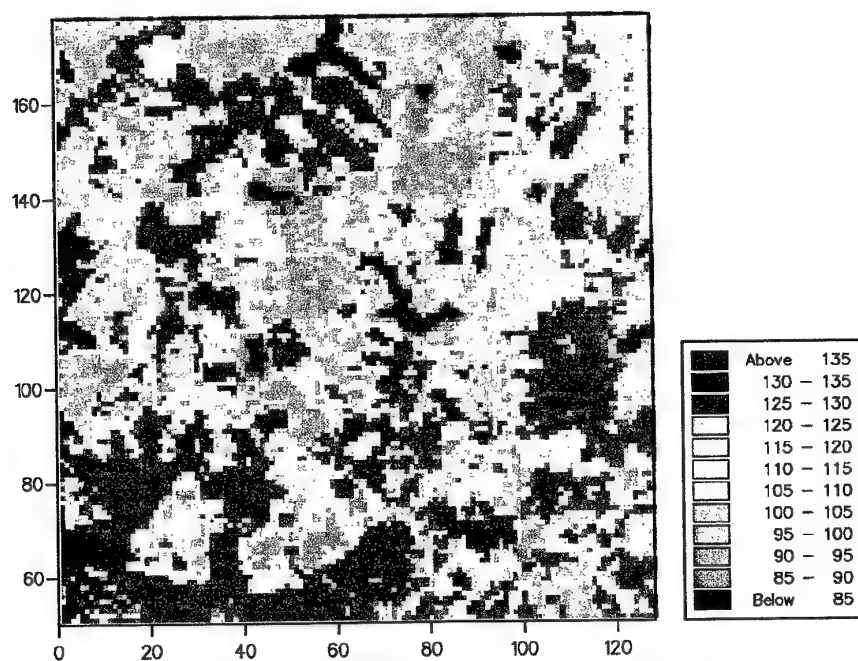


Figure 1. a) Part of SPOT image for Fort A. P. Hill, b) locations of six of the seven classes from the SPOT image of A. P. Hill.

Class 10

Figure 2a shows the pixel map of the NIR values, which cover a wide range. There is an upland area in the middle between two lowland or valley areas. The axes are pixels, each of which is 20 m \times 20 m. The variogram for class 10 was the most difficult to model. It is upwardly concave near to the origin suggesting the presence of local drift. A quadratic function fitted on the coordinates accounted for 46% of the variation. However, when the variogram was computed afresh on the residuals from the quadratic trend its shape remained the same. Therefore, the analysis was done on the raw data. The best fitting models were the circular and the stable exponential function. The latter aims to avoid the disadvantages of the Gaussian model. Visually the range of spatial dependence appears to be a little less than 199m as indicated by the circular model. The range for the stable exponential model is not sensible.

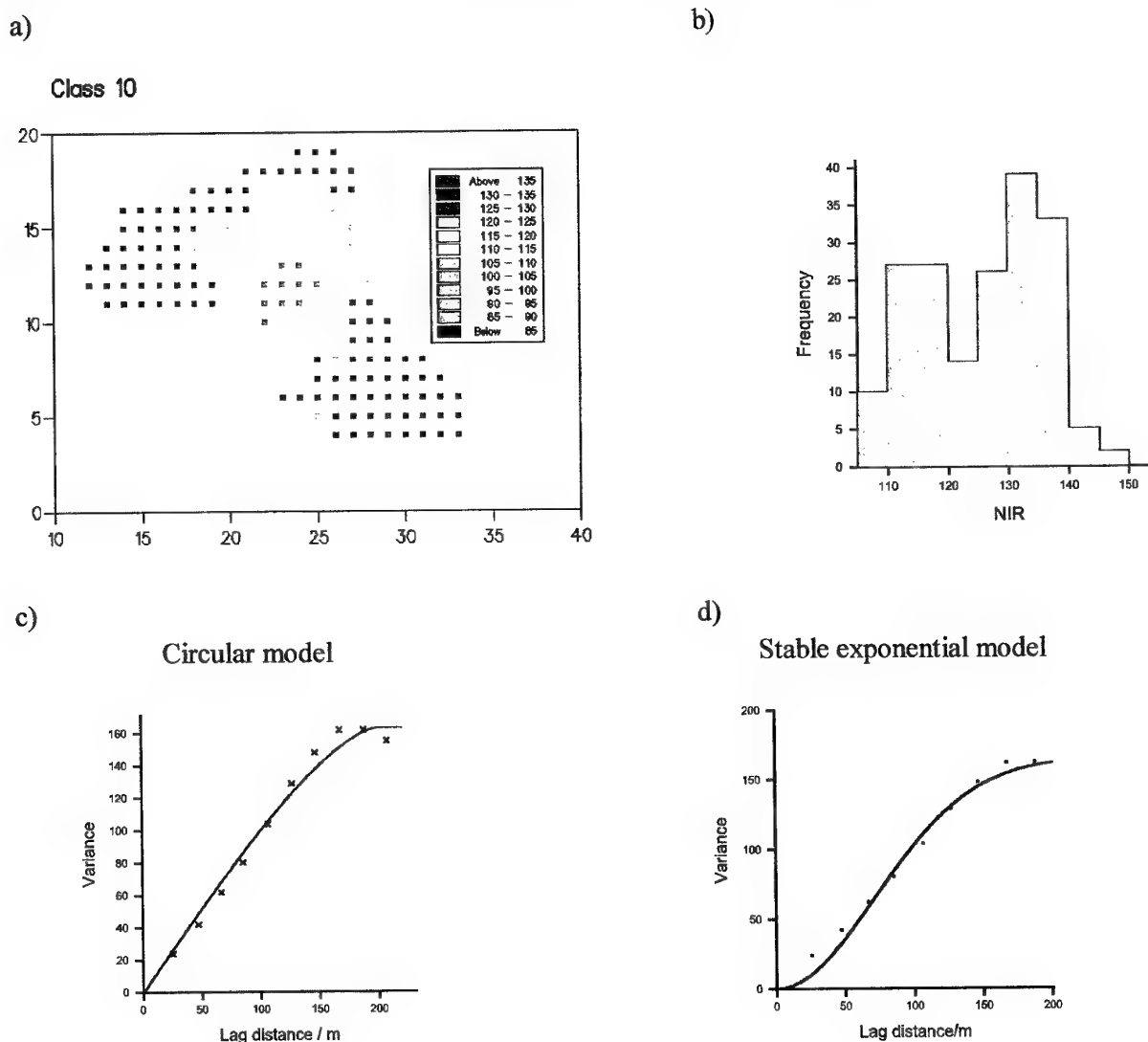


Figure 2. Class 10: a) pixel values of NIR, b) histogram, c) experimental variogram (symbols) circular variogram model, (line), d) experimental variogram (symbols) stable exponential variogram model.

Class 20

Figure 3a shows the NIR values plotted as a pixel map for class 20. It seems that this class might comprise a clearing between a valley and spur. The NIR values are in the upper part of the range. As before the pixels are 20 m \times 20 m Figure 3c shows the experimental variogram and Figure 3d the fitted circular model. It has a range of spatial dependence similar to that for class 10. The sill variance, however, is much smaller showing the effects of the smaller maximum reflectance values and smaller degree of variation present.

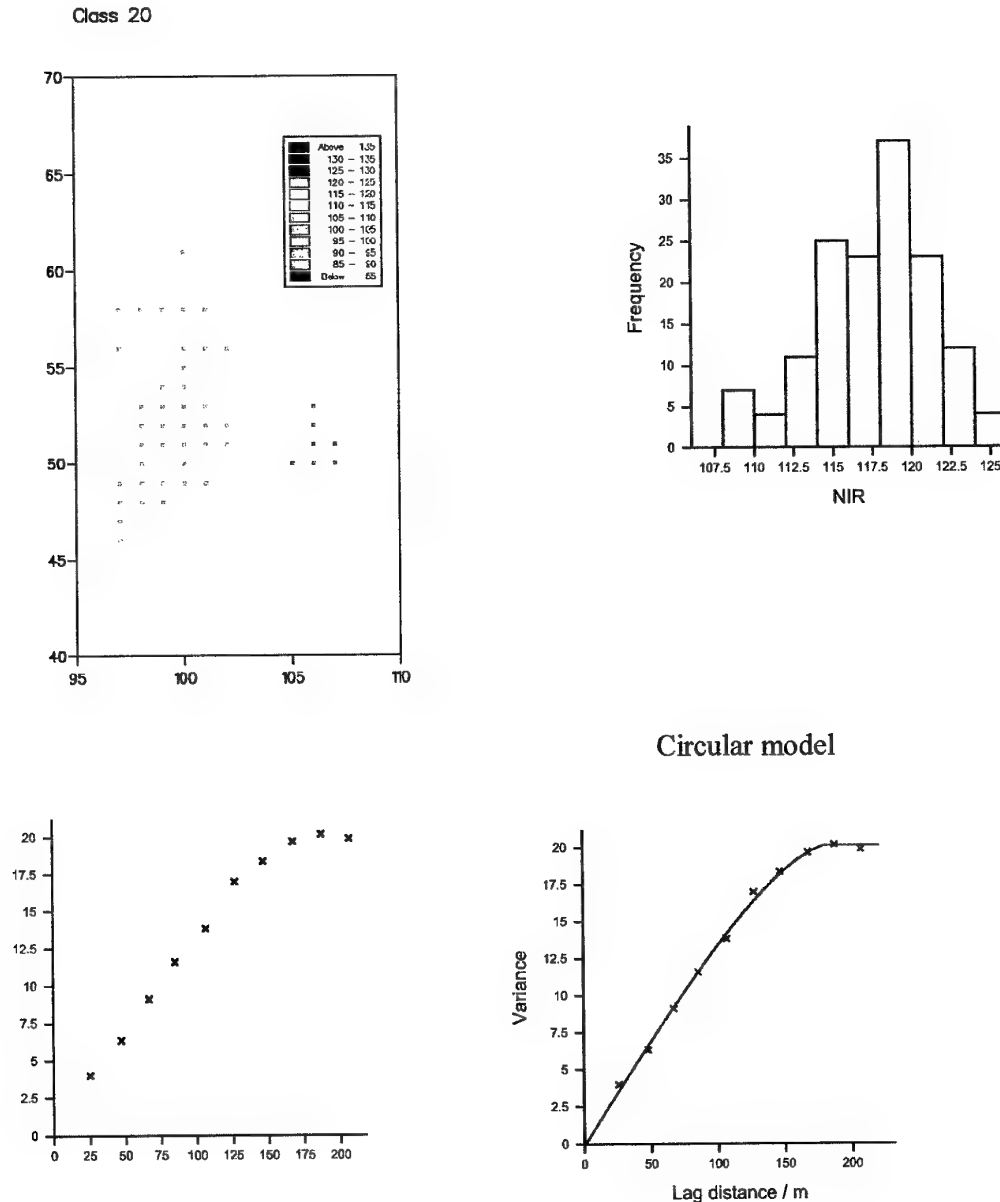


Figure 3. Class 20: a) pixel values of NIR, b) histogram, c) experimental variogram (symbols), d) experimental variogram (symbols) circular variogram model (line).

Class 30

Figure 4a of the pixel values shows that this class has a markedly patchy variation. It is largely an upland area, but possibly with small patches or lower lying areas within it. The NIR values are intermediate to large. The best fitting model was a nested spherical one with a short-range structure of about 68 m and a long-range structure of about 175 m. The latter is similar to the ranges for classes 10 and 20. This class is distinct from all of the others in having this nested variation which is typical of the whole image, but with larger ranges.

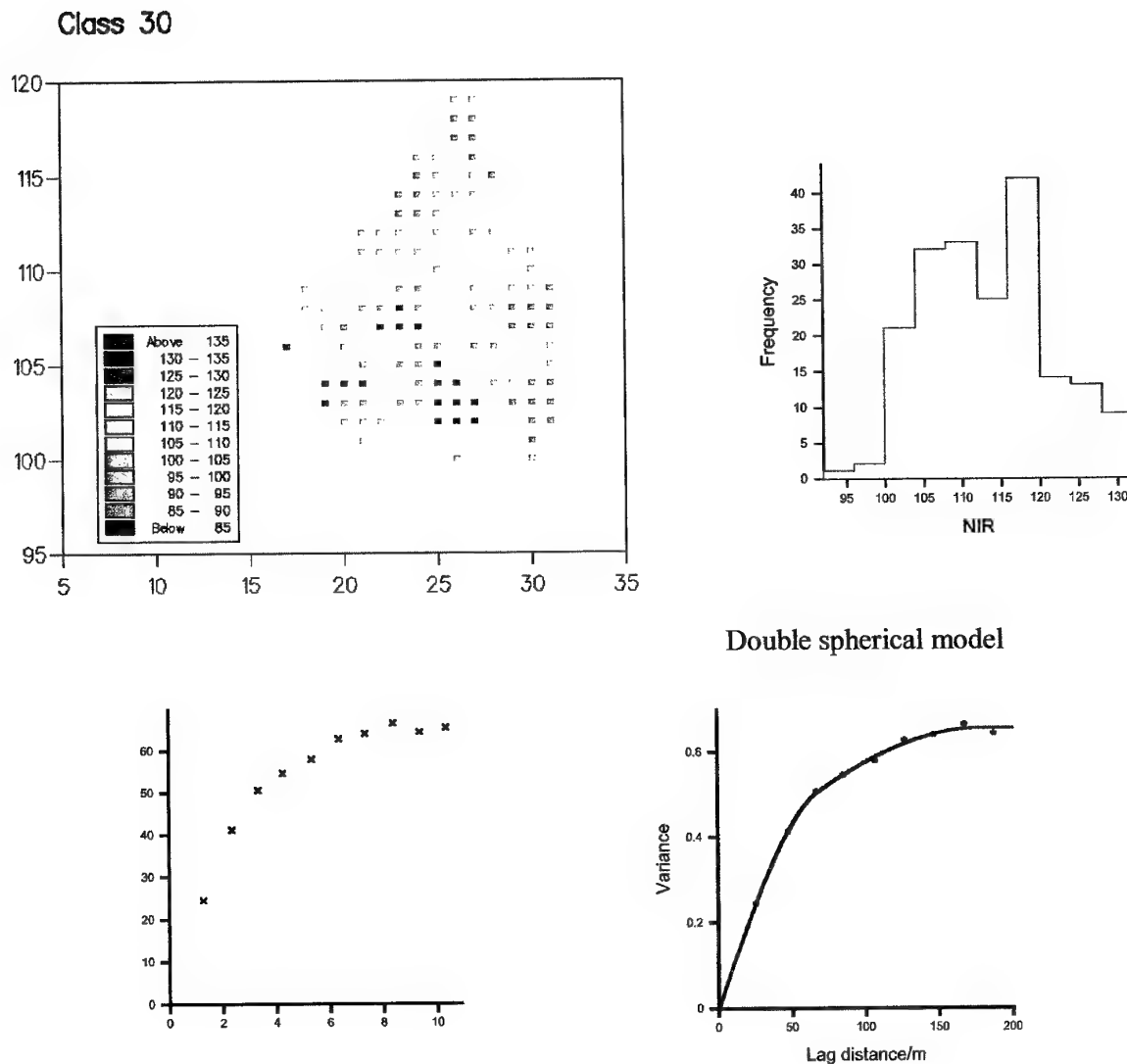


Figure 4. Class 30: a) pixel values of NIR, b) histogram, c) experimental variogram (symbols, d) experimental variogram (symbols) double spherical variogram model (line).

Class 40

Class 40 appears to be the most uniform (Figure 5a), however, its coefficient of variation is larger than for class 20. The NIR values are in the small to intermediate range. It is an upland area that appears to have been cleared of woodland. The variogram has the smallest sill variance, which supports the visual impression gained from this class. The variogram was fitted best by a pentaspherical model. Although the variation appeared to be the least, the variogram of this class has the shortest range of spatial dependence of all variograms, Table 2.

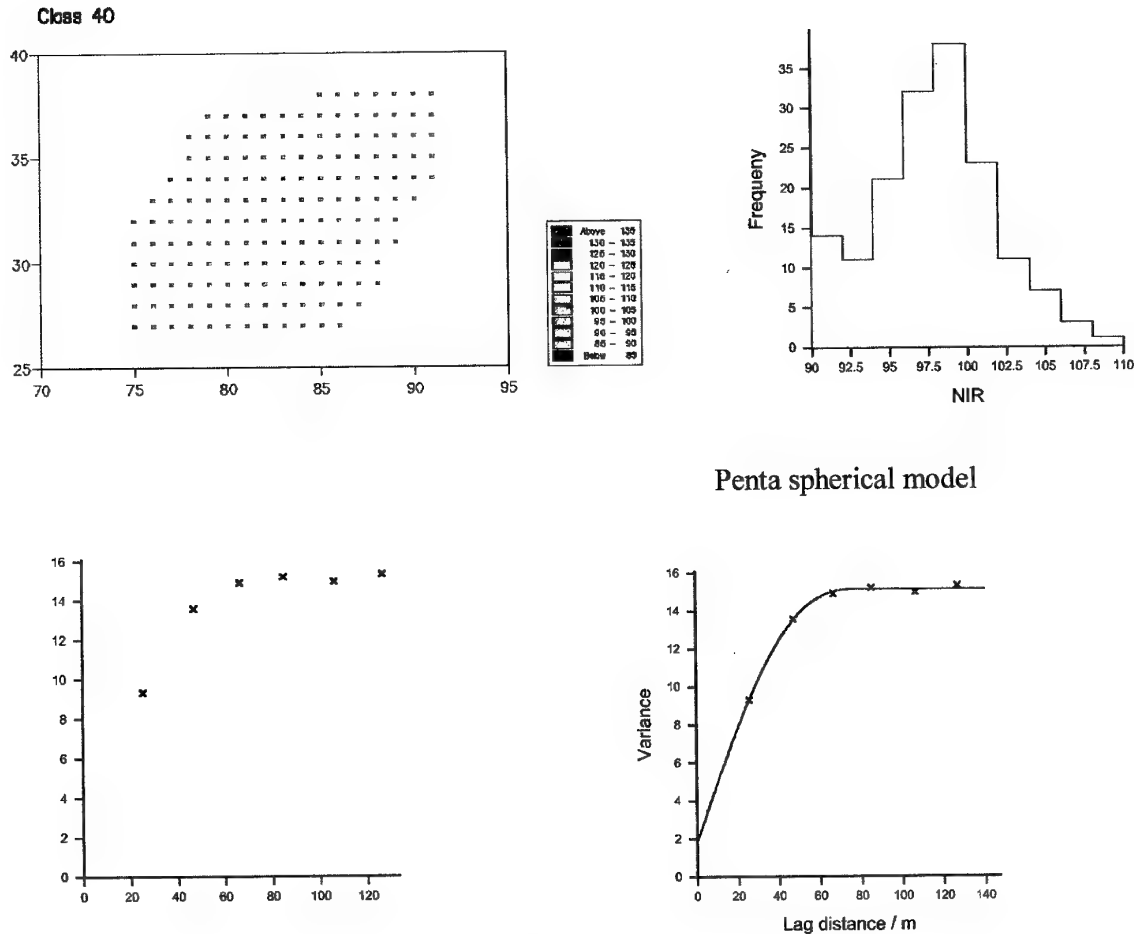


Figure 5. Class 40: a) pixel values of NIR, b) histogram, c) experimental variogram (symbols), d) experimental variogram (symbols) pentaspherical variogram model (line).

Class 50

This class also appears similar visually (Figure 6a) to class 60, although it is slightly more variable. They are both in valley locations. The NIR values are in the upper range. The sill variance of the variogram is relatively large and the range of spatial dependence is different from all other classes. It is intermediate at 117 m.

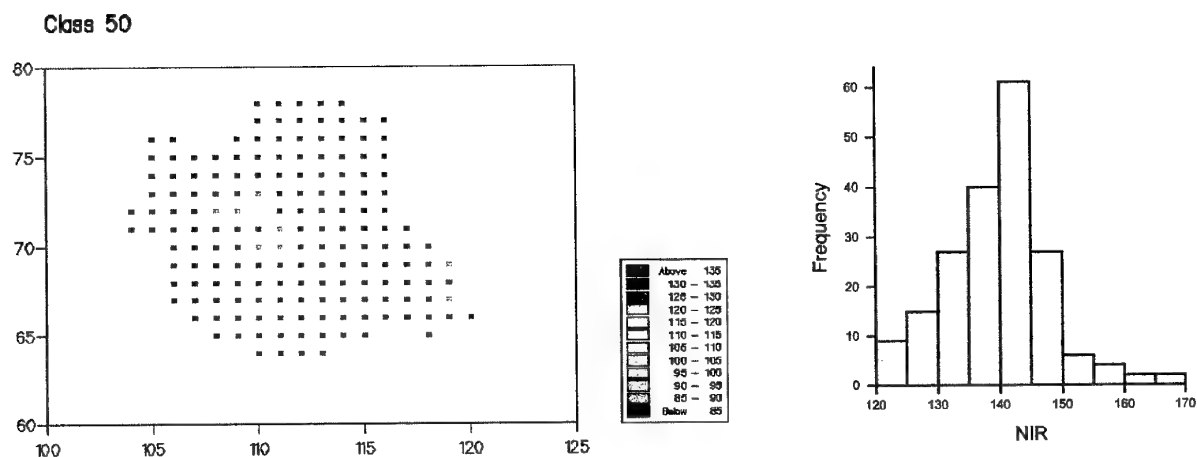


Figure 6. Class 50: a) pixel values of NIR, b) histogram, c) experimental variogram (symbols), d) experimental variogram (symbols) circular variogram model (line).

Class 60

Figure 7a shows the pixel values for class 60, which are in a similar range to those for class 50. It is a valley location. The variogram has an intermediate sill variance, which is similar to that for class 50. Its range of spatial dependence of 103 m is the second smallest. Therefore, although the pixel values are similar to class 50 the texture in the image defined by the range is different.

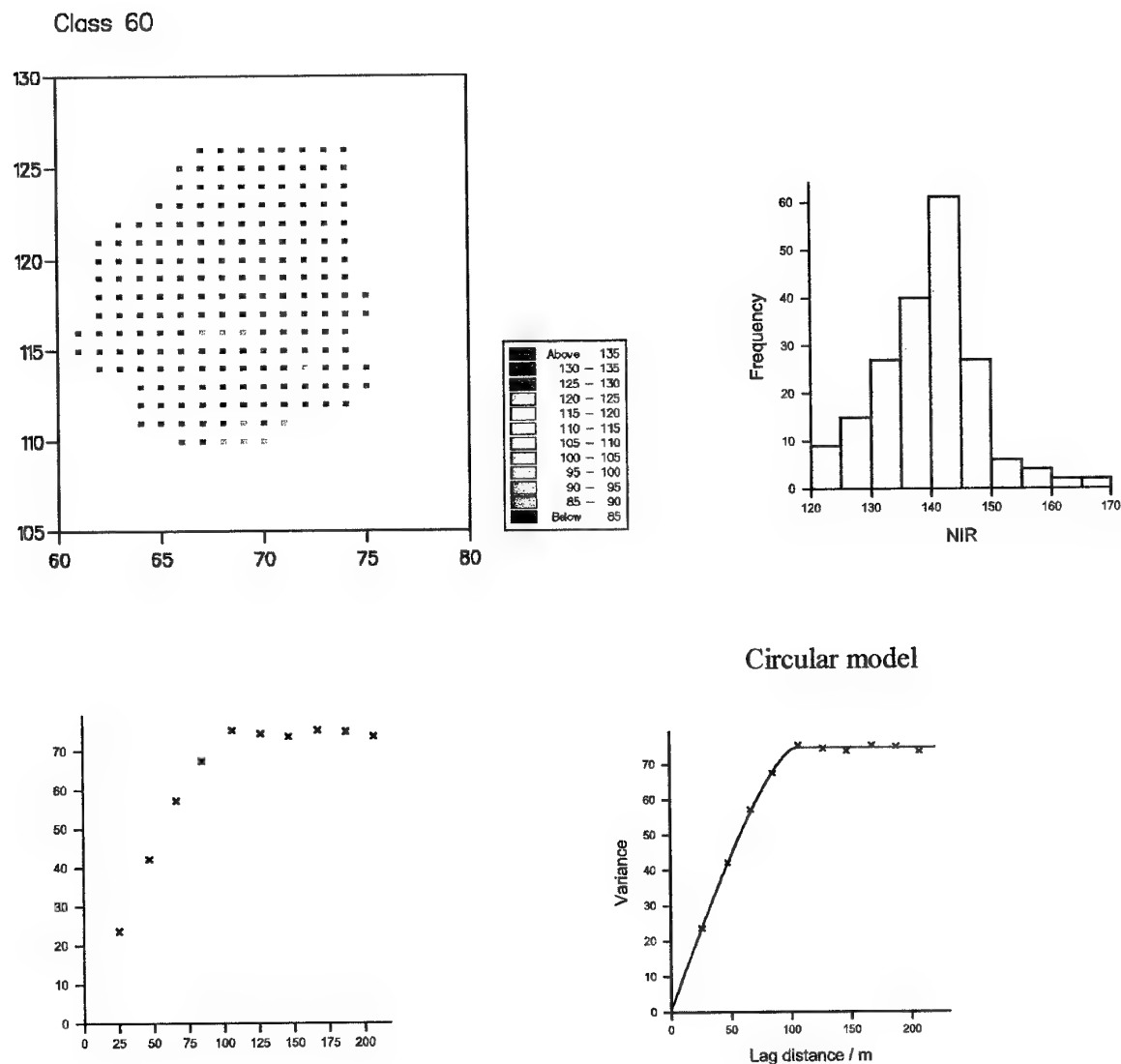


Figure 7. Class 60: a) pixel values of NIR, b) histogram, c) experimental variogram (symbols), d) experimental variogram (symbols) circular variogram model (line).

Class 70

Figure 8a shows the pixel map of NIR values, which are small to intermediate and similar to those of class 40. This class is in an upland area and there might be some unwooded area that give rise to the evident patchiness in the spatial distribution of NIR values. The variogram sill is modest and of a similar order of magnitude to those for classes 20 and 40, which are in similar landscape positions. The variogram range of 139 m is intermediate and different from all of the other classes.

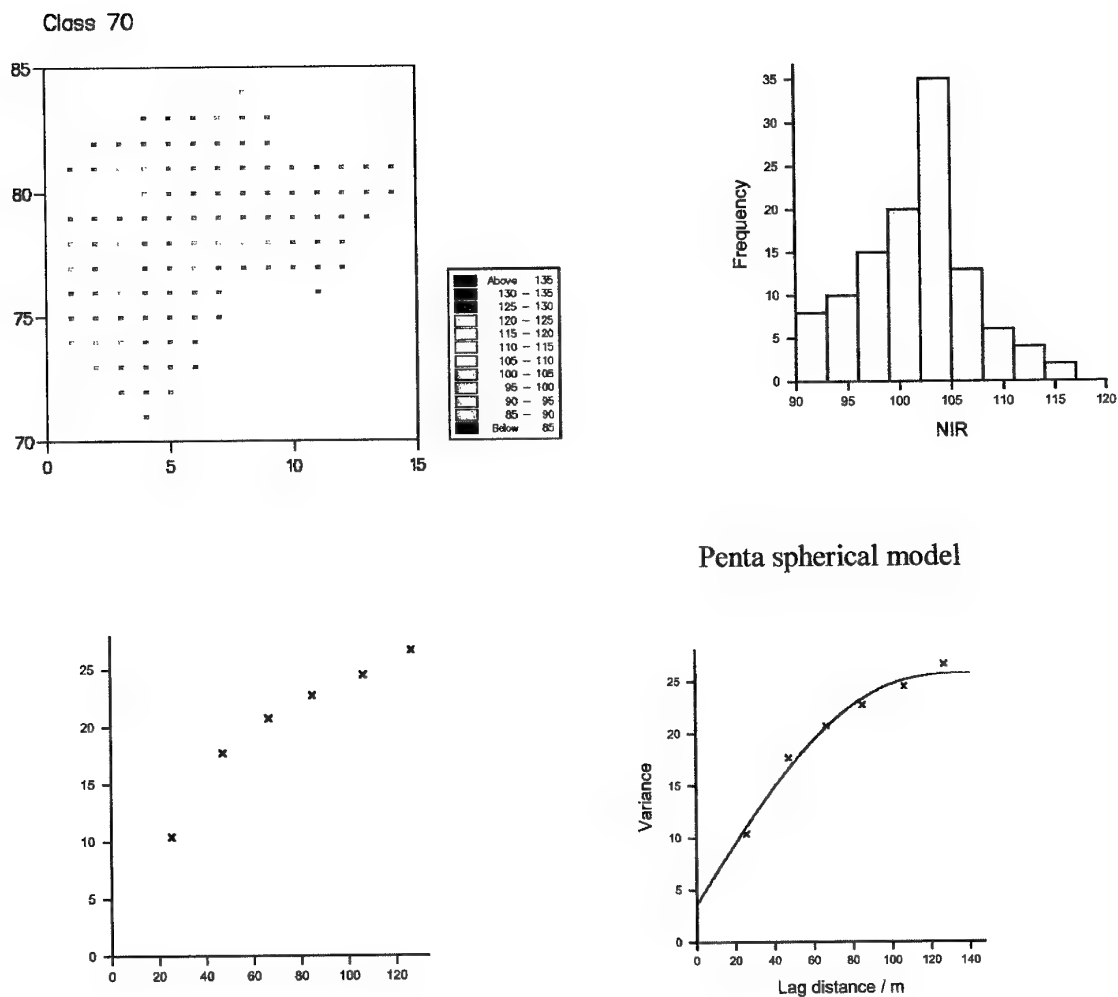


Figure 8. Class 70: a) pixel values of NIR, b) histogram, c) experimental variogram (symbols), d) experimental variogram (symbols) pentaspherical variogram model (line).

Table 2: Model parameters for the functions fitted to the experimental variograms of the six spectral classes for Fort A. P. Hill.

		Model parameter							
Class	Model type	Nugget variance	Sill variance	(1)	Sill variance	(2)	Range 1 (m)	Range 2 (m)	Exponent
Class 10	Circular	0	163.3				199.0		
"	Stable								
	exponential	0	165.1				309.9		1.973
Class 20	Circular	0	20.13				180.9		
Class 30	Double								
	spherical	0.1479	32.05		33.25		67.92	175.6	
Class 40	Penta-								
	spherical	3.288	12.36				90.86		
Class 50	Circular	0	95.31				117.4		
Class 60	Circular	0	74.46				102.6		
Class 70	Penta-								
	spherical	3.714	22.03				139.4		

Summary of analysis of classes

The variogram ranges identified for these classes relate to ones already described for the SPOT image and the 1-m CAMIS imagery. The short-range component of the variation identified in the SPOT image was 130 m, which relates to the variation described by class 70. The long-range component of 420 m was not present in any class which is as expected. The long-range component in the SPOT image represents the main physiographic elements and associated differences in ground cover. The short-range component identified in the variogram of class 30 of about 68 m was identified in the NIR waveband of the 1 in 15 selection from the 1-m imagery of 75 m for the average variogram (see Table 12 report N68171-97-C-9029). The group of ranges of about 100 m and 190 m were also detected in the 1-m imagery.

The results suggest that parts of the image associated with particular types of ground cover have a texture that can be described by the variogram ranges and the sill variances. Classes 30, 50 and 70 are different from each other and the other classes in terms of their sill variances and ranges of the variogram models. Classes 10 and 20 have similar ranges but very different variances; classes 40 and 60 have similar ranges, but again very different sill variances, reflectance values and they are in different landscape positions. Classes 50 and 60 have fairly similar variograms and reflectance values, but the variogram ranges are different. Classes 40 and 70 have similar nugget:sill ratios, similar reflectance values and landscape attributes. Nevertheless it seems that each of these classes can be distinguished from other classes either in terms of the variogram range or the sill variance.

PART III ANALYSIS OF HYPERSPECTRAL IMAGERY FROM FORT HOOD AND FORT A. P. HILL

The aims of this investigation were to examine the spectra of individual pixels from different types of ground cover to assess their similarity or otherwise, and to determine whether their variograms were distinctive. In addition a principal component analysis was done together with non-hierarchical classifications using the spectral values and the principal component scores. Spectral information from Fort Hood and Fort A. P. Hill were examined.

Fort Hood spectra

Pixels from a Hydice hyperspectral image of Fort Hood (Texas) near Clean were selected according to different types of ground cover comprising different types of vegetation, asphalt and soil. The image is shown in Figure 9a. The $3 \text{ m} \times 3 \text{ m}$ pixels in each of the six groups were contiguous and relate to the areas marked by the arrows. Figure 9b shows the relative sizes of the classes of pixels and their locations.

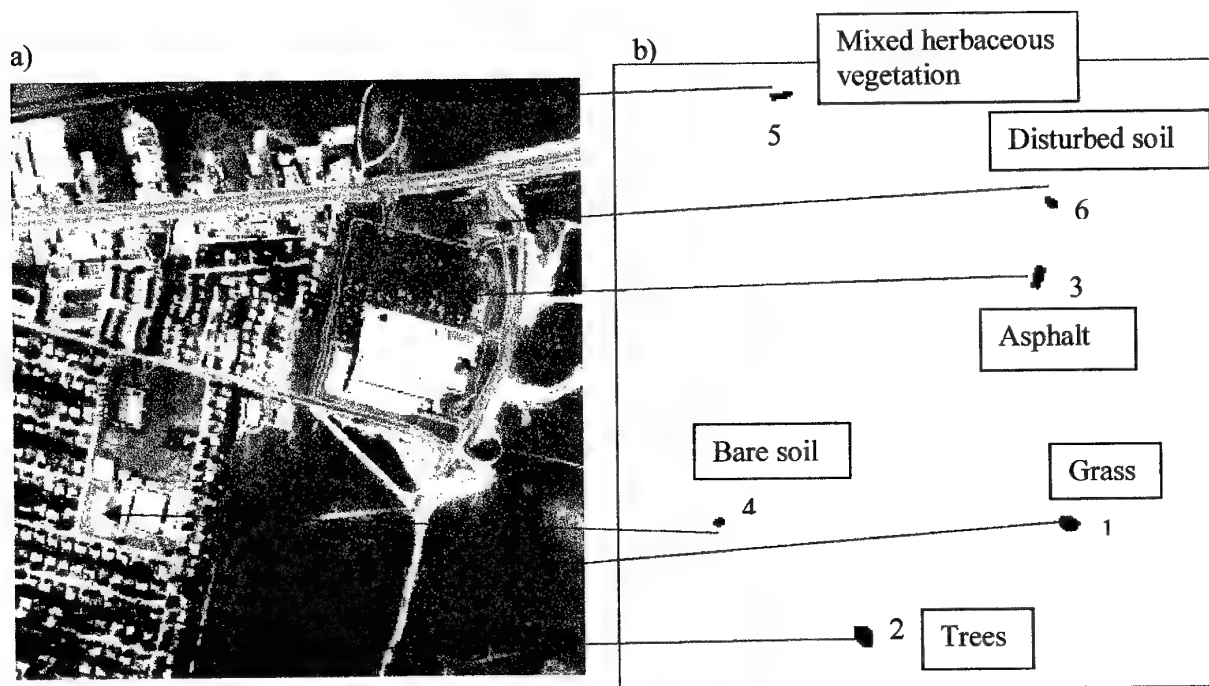


Figure 9. a) Colour image of part of Fort Hood and b) the locations and sizes of the classes of pixels.

There were 132 wavelength values (nm) in each spectrum and a total of 329 pixels. Table 3 gives the number of sites in each class and the associated ground cover class.

Table 3: Classes of different ground cover type and number of pixels in each for Fort Hood.

Class	Type of ground cover	Number of pixels	Pixel range
1	Grass	70	1 – 70
2	Trees	92	71 – 162
3	Asphalt	66	163 – 228
4	Bare soil	21	229 – 249
5	Mixed herbaceous vegetation	38	250 – 287
6	Disturbed soil	42	288 – 329

The spectrum for each pixel was plotted as a trace and examined for differences and similarities. Experimental variograms were computed from the spectra for each pixel. The full set of spectra and variograms can be provided, but to simplify interpretation we focus on selected ones with particular properties. This selection was based on the form of the spectrum and its variogram. This part of the investigation was done without reference to the classes of ground cover in case there were differences in the spectra for a given classes which might be overlooked by focusing on the classes only.

Spectra

The selected spectra for the six ground cover classes are shown in Figures 12 to 84. Some spectra have distinctly different forms, while others vary in the finer detail or in their maximum reflectance values.

A visual inspection of the spectra suggested the following similarities and differences for Fort Hood. The lists marked by **G** are spectra belonging to a pure and distinctive group, those marked by ☆ are similar although they belong to different ground cover classes.

Pixels:

G 1 – 70 (Class 1)

71 – 82

☆ { 83 – 84, 86 – 89, 94, 96 – 98, 103, 105 – 107, 112 – 113, 115 – 119, 121 – 123,
125 – 130,
146 – 152, 156, 158 – 160, 162.
250 – 264, 266 – 271, 273 – 283, 285 – 287, 265, 272, 284. (Class 5)
85, 93, 102.
90, 111.
91 – 92, 99 – 101
95
104, 108 – 110, 114, 120, 124, 143 – 145, 153 – 155, 157, 161.
131 – 133
134 – 139
140
141 – 142
163 – 228 (Class 3)
229 – 249 (Class 4)
288 – 325, 328 – 329 (Class 6)
326 – 327

(Class 2)

Variography

All of the experimental variograms showed evidence of trend with an upwardly concave slope near to the origin. Linear and quadratic functions were fitted to the wavelengths (one dimension only). In general the quadratic function accounted for more of the variance in the data than the linear one (see Table 4 for a summary of the trend analysis for the selected pixels). The percentage variance accounted for ranged from 20.9% for pixel 105 to 81.9% for pixel 25. The variograms of selected spectra were computed on the residuals from the trend – Table 4 describes whether the residuals from the linear or quadratic trend or the raw data were used. All of these variograms are periodic. The periodic function on its own and combined with other functions such as power, exponential and stable exponential functions were programmed in GenStat for this analysis. The stable exponential enables a concave shape near to the origin to be fitted satisfactorily. The program is given in Appendix I.

The simple periodic function is given by:

$$\gamma(h) = c_1 \cos\left(\frac{2\pi h}{\omega}\right) + c_2 \sin\left(\frac{2\pi h}{\omega}\right)$$

where ω is the wavelength, c_1 is the amplitude and c_2 is the phase. This model is valid in one dimension only, which means that we can apply it satisfactorily to the spectra.

The periodic with power function (PPF) is given by:

$$\gamma(h) = wh^\alpha + c_1 \cos\left(\frac{2\pi h}{\omega}\right) + c_2 \sin\left(\frac{2\pi h}{\omega}\right)$$

where w is the intensity of variation, and α is the exponent which describes the curvature.

The periodic function combined with an exponential one (PEF) is given by:

$$\gamma(h) = 1 - \exp\left\{\frac{-h}{r}\right\} + c_1 \cos\left(\frac{2\pi h}{\omega}\right) + c_2 \sin\left(\frac{2\pi h}{\omega}\right)$$

where r is the distance parameter of the exponential function.

Finally the periodic function combined with a stable exponential one (PES) is given by:

$$\gamma(h) = 1 - \exp\left\{\frac{-h^\alpha}{r^\alpha}\right\} + c_1 \cos\left(\frac{2\pi h}{\omega}\right) + c_2 \sin\left(\frac{2\pi h}{\omega}\right)$$

where α is the exponent. This model takes account of an upwardly concave slope in the experimental variogram near to the origin.

This suite of models was fitted each time and the function with the smallest residual sum of squares was selected. The one that fitted the most commonly was the periodic combined with a power function. Table 4 gives a summary of the variogram analysis, the data used, the type of model fitted and the model parameters.

Although all variograms showed evidence of trend and periodicity – there are still several different forms. For example some have a longer wavelength than others, others continue to increase while some flatten, some have larger variances and amplitudes. The variograms for pixels 1 and 25 are similar (as are their spectra), Figures 12a and 13a, but the amplitudes of the fitted models are different, Figures 12c and 13c. This also applies to pixels 71 and 85, Figures 15 and 22, respectively, where the amplitudes and variances are quite different, which reflect the differences in the spectra. Their variograms have similar shapes, however. Pixels 82 and 108, Figures 21c and 30c, have variograms with similar wavelengths, but very different amplitudes (Table 4), which are reflected in the differences in their spectra, Figures 21a and 30a. The variograms of pixels 1 and 95, Figures 12c and 25c, are different in form; the former has a longer wavelength, but both have similar amplitudes (Table 4). Pixel 163, Figure 50 b and c, has a very different variogram from all of the others. That computed on the residuals has a single large peak and is fitted by a simple periodic

function with a shorter wavelength than those above. Pixel 230 has a distinctive variogram with a long wavelength of about 735 nm and a small amplitude, Figure 65 c and Table 4. Pixel 250 has a similar variogram and spectrum to of pixel 82, Figures 68 and 21, respectively. Pixel 266, Figure 73, has a variogram with a similar wavelength to that of 272, Figure 76, but their amplitudes are different and there are subtle differences in their spectra. The variograms of pixels 288 and 317, Figures 81 and 83, respectively, have similar wavelengths, but different amplitudes which are reflected by small differences in their spectra. Pixels 323 and 327 have some differences in their spectra, although they are similar and this is reflected by the different wavelengths of the variograms (Figures 84 and 85, and Table 4). The wavelength for the former is 776 nm and the latter 254 nm, Figures 84 and 85.

Visual appraisal of ground cover class spectra and variograms

The spectra and variograms for classes 1, 4, 5 and 6 are distinctive. There are small differences within these classes that are evident in both differences in the spectra and the variogram model parameters. The spectra of class 2 are more heterogeneous. The overall shapes of the spectra are similar – differences relate to different reflectance maxima and subtle differences in the sharpness of the peaks in the central section. Class 5 has similar spectra to some of those in class 2 – see the list above.

Multivariate analysis of Fort Hood spectra

Principal component analysis

A principal components analysis was done using all of the pixels and the spectral values. Table 5 gives the latent roots and vectors of the first three principal components, which account for 99.5% of the variance. Eigenvector values greater than 0.1 are in bold. For PC 1 these are for wavebands 22 to 34, and 45. For PC 2 they are 6, 48 to 49, 50 to 57, 60 to 79, and for PC 3 1 to 4, 6 to 12, 49 to 57 and 82 to 100. Figure 10 shows the pixels plotted in the projection of PC1 and PC 2, using the PC scores. There are four well-defined and coherent groups, 1, 3, 4 and 6 which accords with the visual observations of the spectra and the variograms. Class 4 is the most distinct and this has spectra with large average reflectance values – these relate to the bare ground class cover. Class 2 is diffuse and merges with class 5, which again was apparent from the visual appraisal. Classes 2 and 5 have a larger extent on axis 2 than on axis 1, although both have larger extents on PC 1 than any other class.

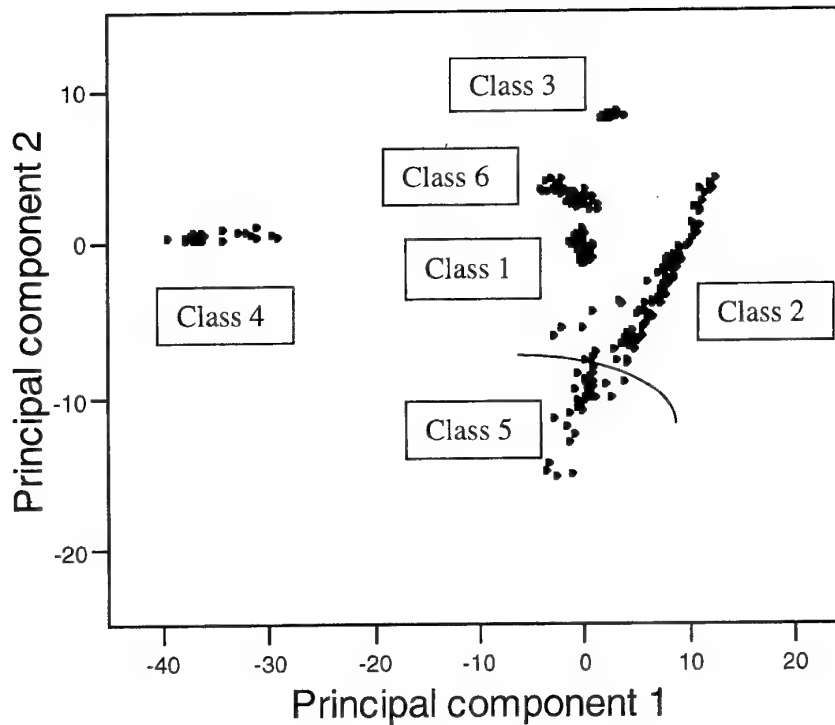


Figure 10. Plot of individual pixels in the projection of principal components 1 and 2 using the PC scores. The ground cover classes are shown near to the relevant group of pixels, and the line shows the approximate separation between classes 2 and 5.

Non-hierarchical k -means dynamic clustering

This is an alternative approach to classification compared with the more commonly used hierarchical methods. Webster and Oliver (1990) describe the method. Non-hierarchical classification is also known as dynamic clustering. The population is subdivided at a single level into as many classes as desired. The approach subdivides a set of individuals into two or more disjoint groups. Each individual belongs to one, *and only one*, group. The general aim is to subdivide the population optimally such that there is minimum variation within the classes and the difference between them is maximised.

A mathematical criterion is chosen as a basis for optimising the subdivision, such as the within groups sums of squares or Wilks' criterion (L) to measure the dispersion within groups, or Trace $W^{-1}B$ to measure the separation between groups. The population can be divided into an arbitrary number of groups at the outset or the number could be based on information from another analysis. The test criterion is calculated, and individuals are then moved from group to group and the criterion recalculated. If the change improves the criterion the move is retained, otherwise it is not. There are different ways of moving individuals from group to group in an iterative way to try to obtain an optimum (Webster and Oliver, 1990). In general, the optimal number of groups to subdivide the population into is unlikely to be known, therefore more groups than are likely are chosen at first. The number of groups can then be reduced one at a time by fusing the two most similar groups and recalculating the criterion. Individuals are then moved as before.

Non-hierarchical classification has an additional advantage compared with the hierarchical ones in that once individuals are assigned to groups they can still be moved. This means that as the groups change character as individuals are removed or added others can be moved to optimise the criterion. Once an individual is grouped in a hierarchical method it is irrevocable.

One of the difficulties with non-hierarchical methods is that it is sometimes difficult to decide how many groups is optimal. Groups tend to be of a similar size and shape, and weak clusters might not be isolated as distinct classes. There is a solution to this that uses Wilks' criterion, L , and g^2L is plotted against g , where g , is the number of classes.

I applied this method clustering to the pixels from the Fort Hood image. There were too many wavebands for the method to work successfully – the large number caused instability in the matrices. Therefore, I did the analysis on the scores of the first three principal components, and on 50% and 25% of the wavebands. The sums of squares criterion provided the most stable results. Starting with 10 groups, the pixels were reclassified until three groups remained. It was not possible to calculate Wilks' criterion, therefore I plotted the sums of squares criterion against g for each data set. Figure 11 shows the results for the three data sets. The most likely number of groups is shown where the graph goes below the general trend. Based on this the analyses using the raw spectra suggest that five groups is optimal, whereas for the PC scores 6 groups is optimal. Figure 10 of the scores plotted in the plane of components 1 and 2 shows five separate groups. Nevertheless, it is evident that groups 2 and 5 although part of a continuum, do occupy distinctive parts of this projection.

Table 6 gives the classes to which each pixel belongs for the three sets of data. For the 66 wavebands both the 5-group and 6-group classifications are given for comparison with the six classes from the PCA scores. There are minor differences between the six classes for the raw data and the PC scores in ground cover class 2. The bold lines show the limit of each of the six ground cover classes. The comparison below uses the results of the optimal classifications for the raw data with 66 bands (5 groups) and the PC scores (6 groups).

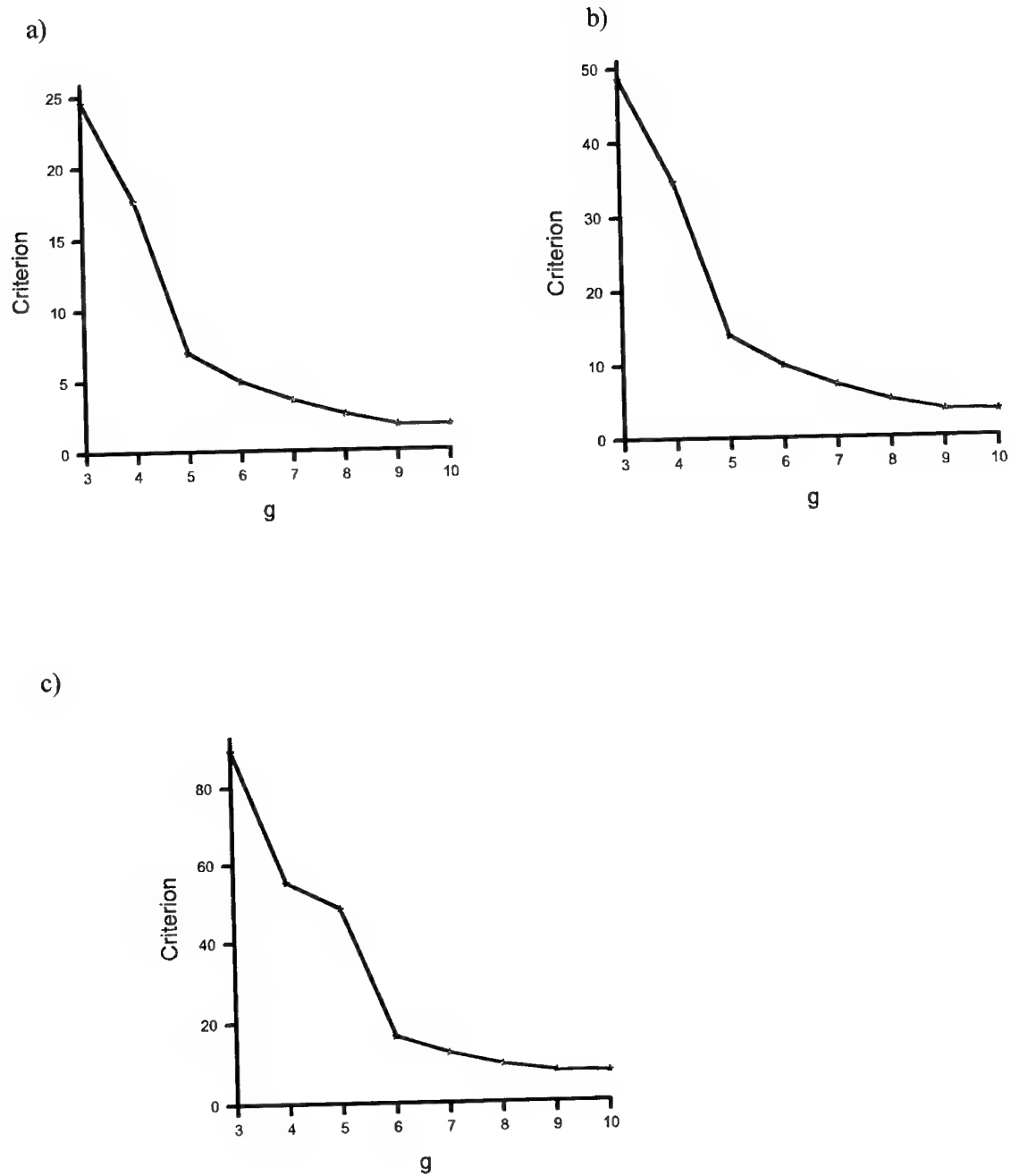


Figure 11 Sum of squares criterion $\times g$ plotted against g (number of groups) for:
a) 33 wavebands, b) 66 wavebands, and c) the scores of the first five principal components.

Class 1 pixels

For class 1 the classification results for the three analyses show that the 70 pixels belong to the same group. The group is pure and this reflects the homogeneity of the spectra and the variograms from a visual appraisal. The largest reflectance values in this class are about 300 nm. The ground cover for this class is grass.

The variograms of the raw data are markedly concave near to the origin. Figures 12b and 13b of the raw variograms of pixels 1 and 25 show that they are similar. The variograms were computed again from the quadratic residuals, Figures 12c and 13 c for pixels 1 and 25, again they are very similar. They were fitted best by a periodic with power function (PPF) and they have a wavelength of about 500 nm, and amplitudes between 600 and just over 1000. Table 4 gives the parameters of the best fitting models.

Class 2 pixels

This is the largest class with 92 individuals and the ground cover comprises trees interspersed with herbaceous ground cover plants. It does not appear to be the kind of dense woodland that occurs at Fort A. P. Hill. The spectra for this ground cover class are very different in shape from those of class 1, Figures 15a and 48a. The classification in all cases shows that this is a heterogeneous group. For both the raw data and the PC scores the class comprises three groups from the non-hierarchical classification, but there are differences between them. For the raw data the class comprises mainly groups 3 (26 pixels) and 4 (59 pixels), with only seven pixels belonging to group 5. The pixels of the latter group are scattered within the class. Those for groups 3 and 4 are similar in shape, but the reflectance values for group 3 are larger (a maximum of over 400, compared with about 300 for group 4). The spectra for group 5 also have a similar shape to groups 3 and 4, but their reflectance values are much smaller, i.e. reaching a maximum of about 130. The six-group classification using PC scores has 6 pixels only in group 3; these have spectra with the largest reflectance values in this ground cover class. There are 47 pixels in group 4 (more or less equivalent to group 3 for the raw data with 5 groups) and 39 in group 5 (more or less equivalent to group 4 for the raw data with 5 groups). The six-group classifications for the raw data and the PC scores are similar.

The experimental variograms of the raw data are distinctively different from those of class 1, Figures 15b to 48b. The variograms were recomputed on the residuals and modelled by the periodic with power function. The model parameters for selected pixels are given in Table 4. All of the models have wavelengths of between 465 nm and 476 nm. Pixels 107 and 140 belong to group 3 for the raw data and the PCA scores. They have the largest amplitudes of the variograms in this class – over 5555, Figures 29 and 40. Pixels 71, 77 and 82, Figures 15, 17 and 21, respectively, belong to group 3 for the raw data and 4 for the PC scores. They have large amplitudes of between 3669 and 4881. Pixels 85 and 128 (Figures 22 and 36) belong to group 4 for the raw data and the PC scores. Their amplitudes are intermediate with values of about 2600. Pixels 90, 91 and 162 (Figures 23, 24 and 48) belong to group 4 for the raw data and group 6 for the PC scores. They have a small amplitude of between 1090

and 2197. Finally pixel 104 belongs to group5 for both the raw data and PC scores – it has the smallest amplitude. Nevertheless the variograms have a consistent form. The differences in the amplitudes of the periodic component of the fitted models reinforce the fact that this group has differences in the magnitude of the reflectances.

The complexity of this ground cover class is not surprising because trees result in variable reflectances associated with the shadows created by their crowns and their different heights and extents. In the 1-metre imagery described in Appendix (II – the paper submitted to the International Journal of Remote Sensing) these effects could be seen as ‘pock-marks’.

Class 3 pixels

The spectra of this class are very different from the previous classes. They are flatter, and the reflectance increases gradually from the small wavelengths to the longer ones where they become more bulbous in shape. The spectra have small maximum reflectance values of about 130. The class is well defined visually and in the classifications. The six-group classifications for both the raw data and the PC scores distinguish the class from pixels in class 2, whereas the five-group classification of the raw data links these pixels with the low reflectance pixels (group 5) in class 2. This ground cover class is asphalt and there should be no overlap with class 2 spectra. The group 5 pixels in class 2 do not have a similar shape to the spectra of this class; they simply have small maximum reflectance values. This suggests that the optimal classification into six groups based on the PC scores is more powerful in terms of discrimination than that using the raw data.

This group could also be discriminated on the basis that a linear trend accounted for most of the variance in the data (81.6% to 89%), whereas for the majority of the spectra most of the variance was accounted for by a quadratic function. The experimental variograms of the raw data and those computed from the linear residuals are different from those for classes 1 and 2. The variograms of the residuals are a single peak and were fitted best by a simple periodic function. Figures 49 to 64 shows a selection and Table 4 gives the model parameters. They have a wavelength of about 350 nm, and a small amplitude of about 20.

Class 4 pixels

This class is well defined both visually and by the classifications. It is pure and clearly discriminated. The ground cover is bare soil and the maximum reflectance values are large, close to 500. The spectra have an overall bulbous shape with less defined peaks and troughs than many of the other spectra.

The variograms were computed from the quadratic residuals. Figures 65 and 66 (pixels 230 and 234) show that the wavelengths are close to 700 nm and the amplitudes are small, about 150. For pixel 242, Figure 67 and Table 4, the wavelength is smaller – about 450 nm.

Class 5 pixels

This ground cover class is mixed herbaceous vegetation. The spectra have a similar general shape to those of class 2. For the five-group classification this class overlaps with the 26 pixels in group 3, i.e. the ones with the larger reflectance values. For the six-group classification the overlap is much less – for the PC scores it is with six pixels only. This latter seems more reasonable in that it is likely that there are herbaceous plants between the trees in places in class 2. These results support the statement above that the classification using the PC scores is more discriminatory.

The variograms of this class were computed on the quadratic residuals. The wavelengths of the periodic with power functions are about 470 nm, which is close to those for class 2 for which the spectra are also similar. The raw variograms and those on the residuals have a similar shapes also, Figures 68 to 80. The amplitudes of these functions are large, up to 12 000nm, Table 4. However, there is a considerable range in amplitude from 2993 (pixel 159) to 12 487 (pixel 284). The pixels belong to group 3 for both the raw data and PC scores and have similar properties to pixels in this group for class 2. This ground cover class has the largest amplitudes for the variogram models.

Class 6 pixels

This groundcover class is disturbed soil, but it is a well-defined group using the raw data and PC scores. Visually these spectra are also different, yet the classifications indicate an overlap with class 1. The spectra in these classes have similar peaks and troughs, but they are less defined and have smaller maximum reflectance values.

This ground cover class has distinctive variograms, as well as distinctive spectra, Figures 82 to 85. The experimental variograms of the raw data have a marked unbounded form. A quadratic trend accounted for a larger percentage of the variance than for any other class. Variograms were computed on the residuals from this trend. The best fitting model was also different from the other classes, being a periodic with exponential function in the main. The wavelength is about 300 nm on average, which is smaller than those for the other classes. The amplitude is also the smallest being about 50 on average. Table 4 gives the model parameters of the variograms. Figures 81 to 85 show selected variograms from the raw data and the quadratic residuals.

Summary of results

For ground cover classes 1, 3, 4 and 6 the results show a clear distinction between them in terms of their spectra. They occupy well-defined parts of the property space in the projection of the first two principal components. A comparison of the classification results using the raw data and the PC scores suggest that the PC score enable a better discrimination between the spectra. However, for the 5-group classification using the raw data and the 6-groups classification using the PC scores (the optimal classifications) classes 1 (grass) and 6 (disturbed soil), which have different spectra, have been placed in the same multivariate group as each other by both classifications. Since the PC scores provided the basis for good discrimination, they were classified into 7 groups to see whether there was any explanation for the overlap between classes 1 and 6. At the 7-group level class 6 is now distinct from class 1. All of the other classes remain similar. It seems that the variation in the spectra of class 2 is greater than that between classes 1 and 6. Therefore, caution is required in taking the prescribed route through the analysis. The other puzzle is the overlap between classes 2 and 5 which possibly relates to the fact that there is ground vegetation between the trees.

In spite of some anomalies the analyses suggest that a combination of visual inspection, multivariate classification and ordination, and variography enable us to distinguish between different kinds of ground cover class in terms of their hyperspectral information. The spectra of classes 1, 3, 4 and 6 were clearly different. The complexity of class 2 spectra can probably be explained by the texture in the pixels arising from different tree heights, extents and proximity, with areas of ground cover vegetation interspersed and showing through in parts.

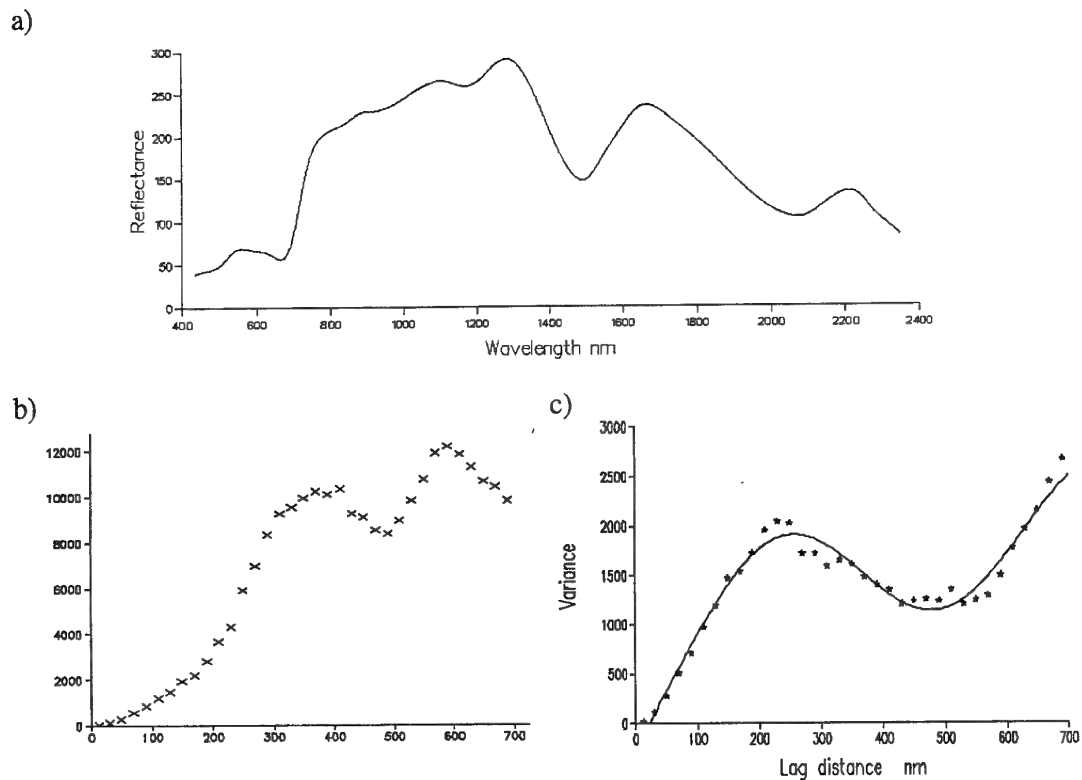


Figure 12. Ft Hood: pixel 1: a) spectrum, b) experimental variogram of raw values, and c) experimental variogram and fitted model (PPF) of quadratic residuals.

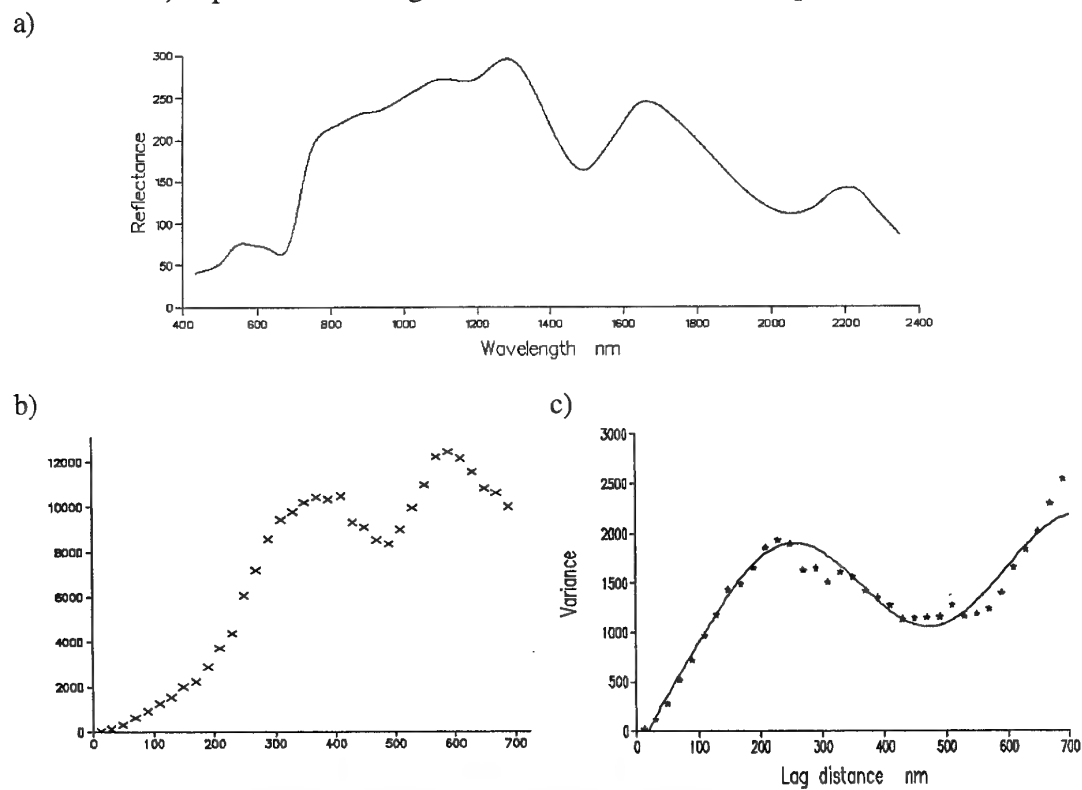


Figure 13. Ft Hood: pixel 25: a) spectrum, b) experimental variogram of raw values, and c) experimental variogram and fitted model (PES) of quadratic residuals.

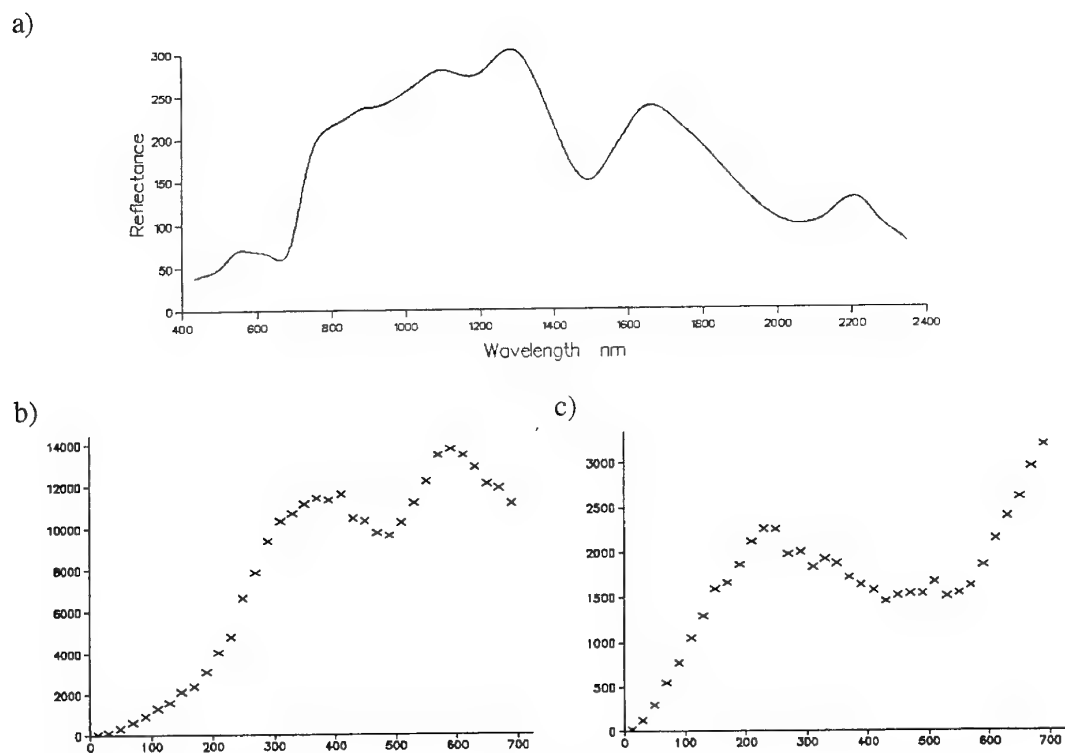


Figure 14 . Ft Hood: pixel **50**: a) spectrum, b) experimental variogram of raw values, and c) experimental variogram of quadratic residuals.

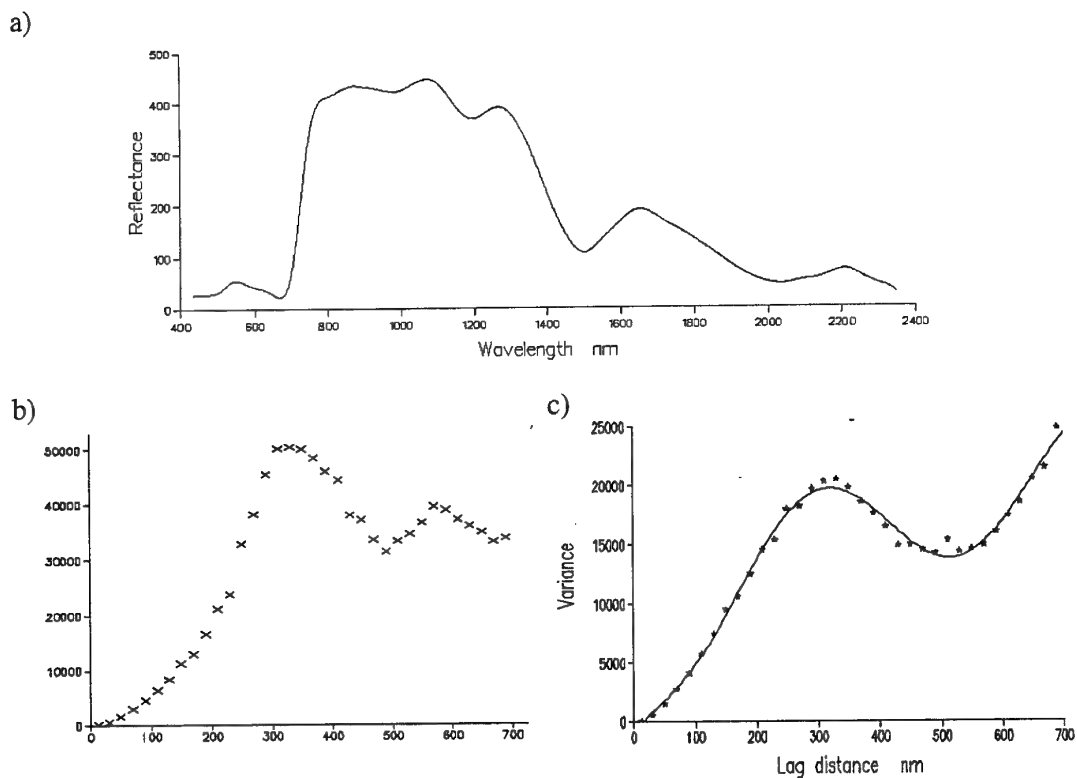


Figure 15. Ft Hood: pixel 71: a) spectrum, b) experimental variogram of raw values, and c) experimental variogram and fitted model (PPF) of quadratic residuals.

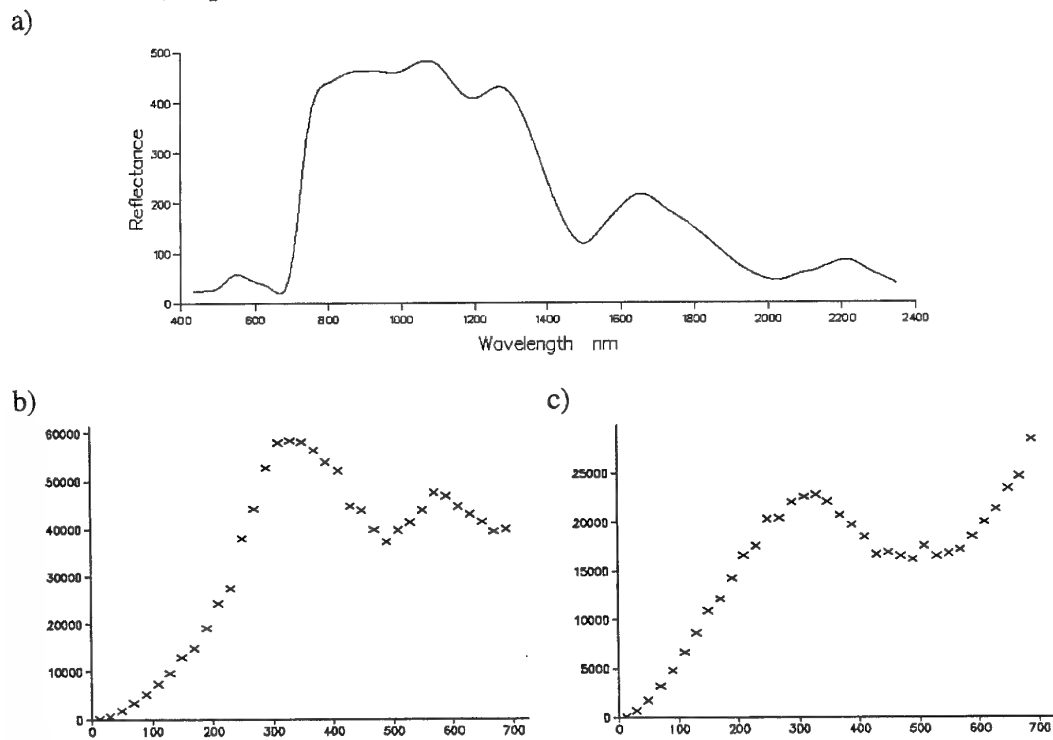
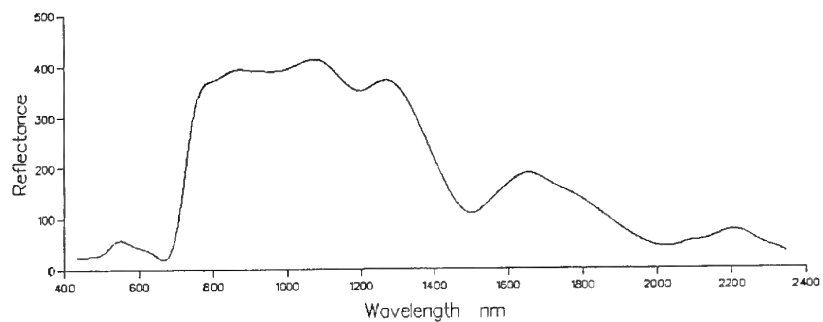


Figure 16. Ft Hood: pixel 76: a) spectrum, b) experimental variogram of raw values, and c) experimental variogram of quadratic residuals.

a)



b)

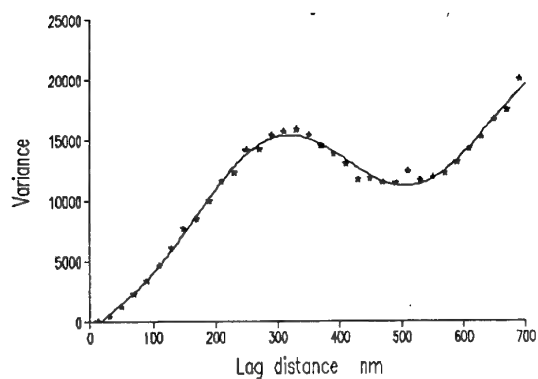
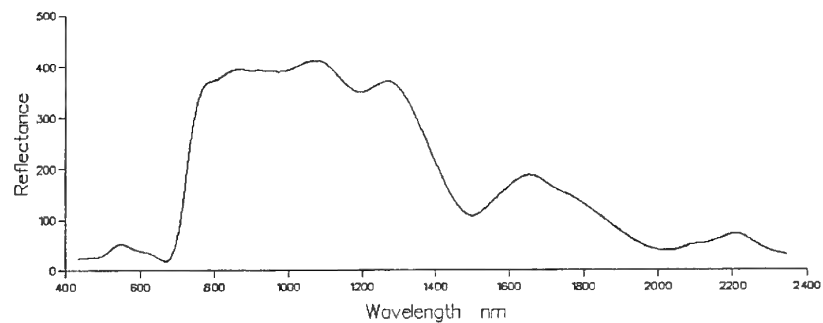


Figure 17. Ft Hood: pixel **77**: a) spectrum, b) experimental variogram and fitted model (PPF) of quadratic residuals.

a)



b)

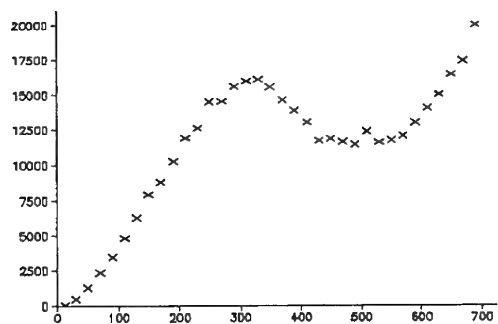
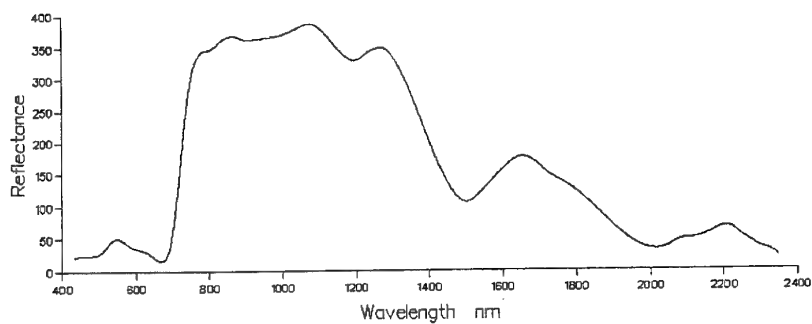


Figure 18. Ft Hood: pixel **78**: a) spectrum, b) experimental variogram of quadratic residuals.

a)



b)

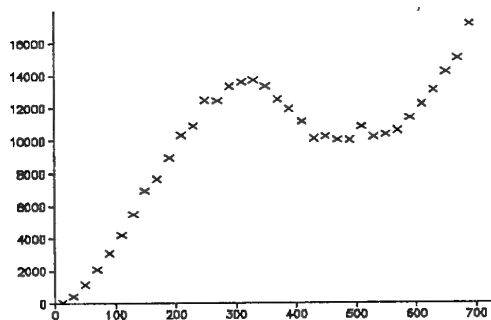
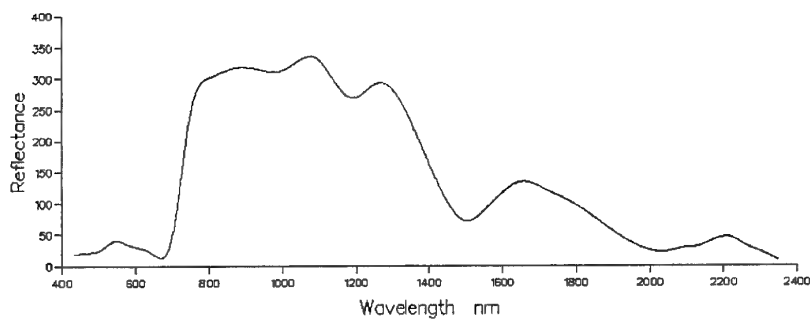


Figure 19. Ft Hood: pixel **79**: a) spectrum, b) experimental variogram of quadratic residuals.

a)



b)

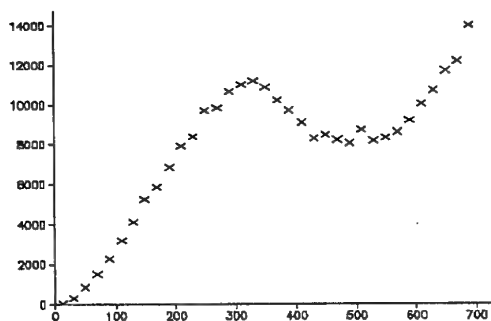


Figure 20 Ft Hood: pixel **80**: a) spectrum, b) experimental variogram of quadratic residuals.

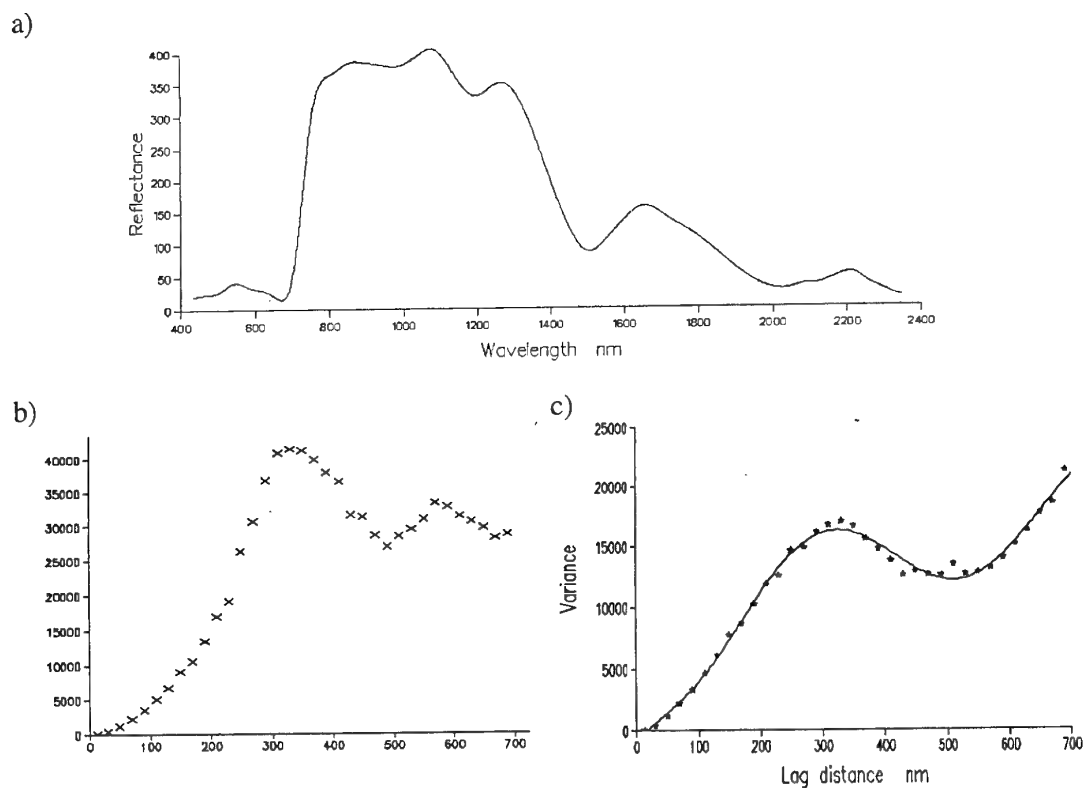


Figure 21. Ft Hood: pixel **82**: a) spectrum, b) experimental variogram of raw values, and c) experimental variogram and fitted model (PPF) of quadratic residuals.

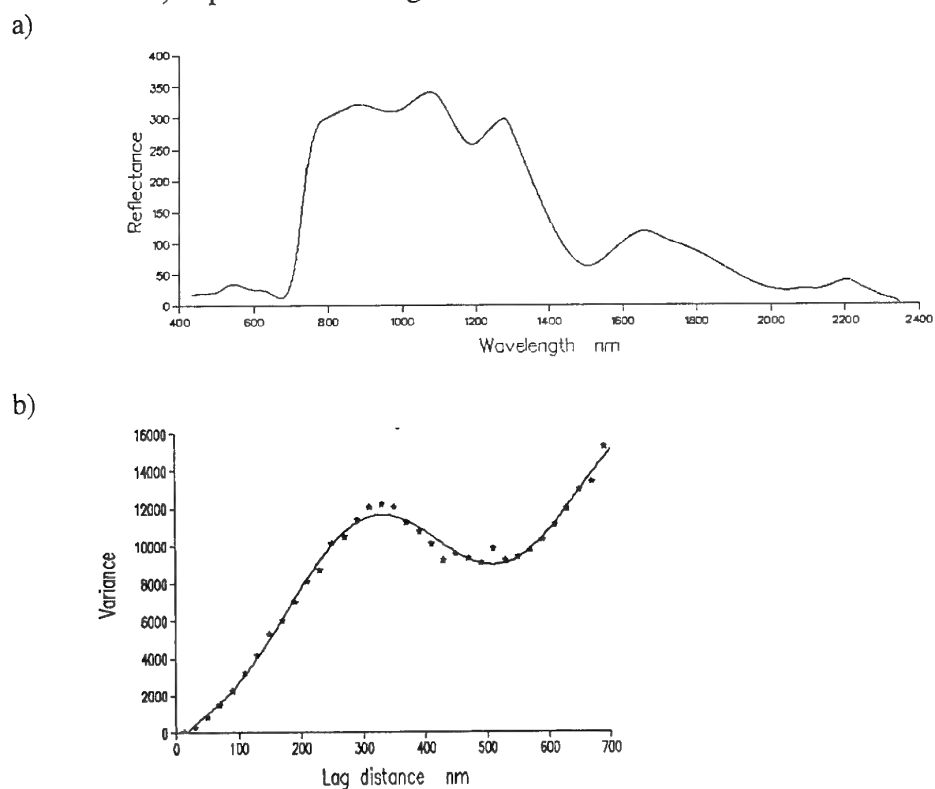


Figure 22. Ft Hood: pixel **85**: a) spectrum, b) experimental variogram and fitted model (PPF) of quadratic residuals.

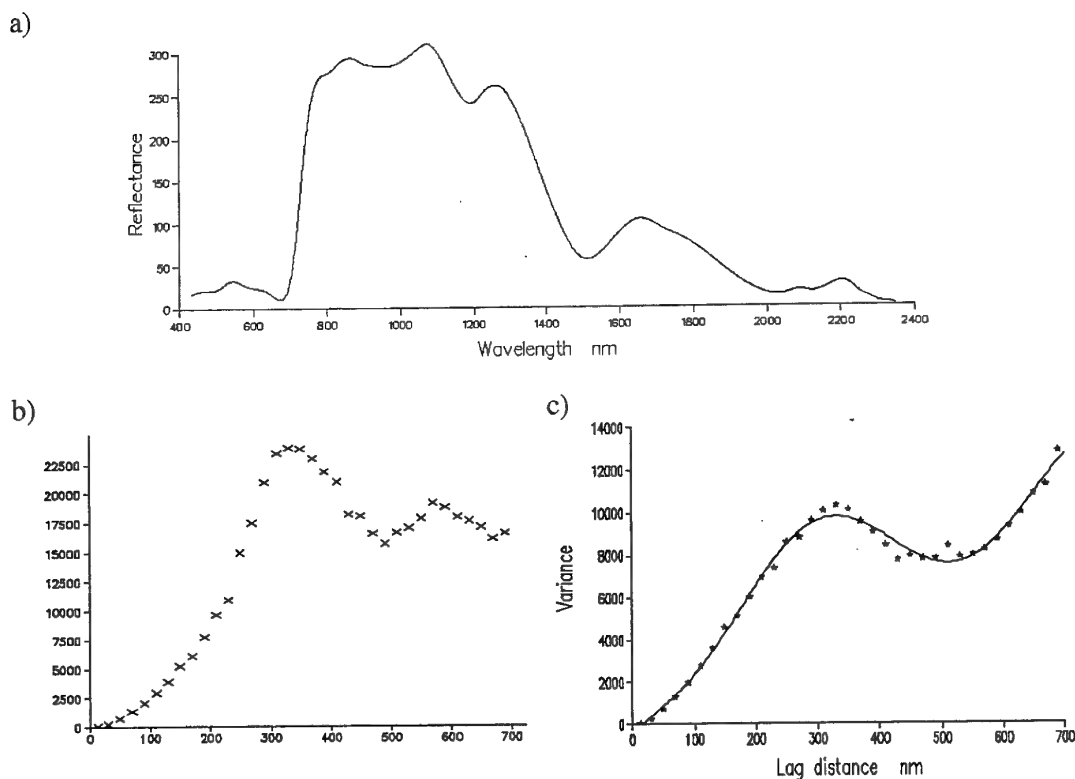


Figure 23. Ft Hood: pixel 90: a) spectrum, b) experimental variogram of raw values, and c) experimental variogram and fitted model (PPF) of quadratic residuals.

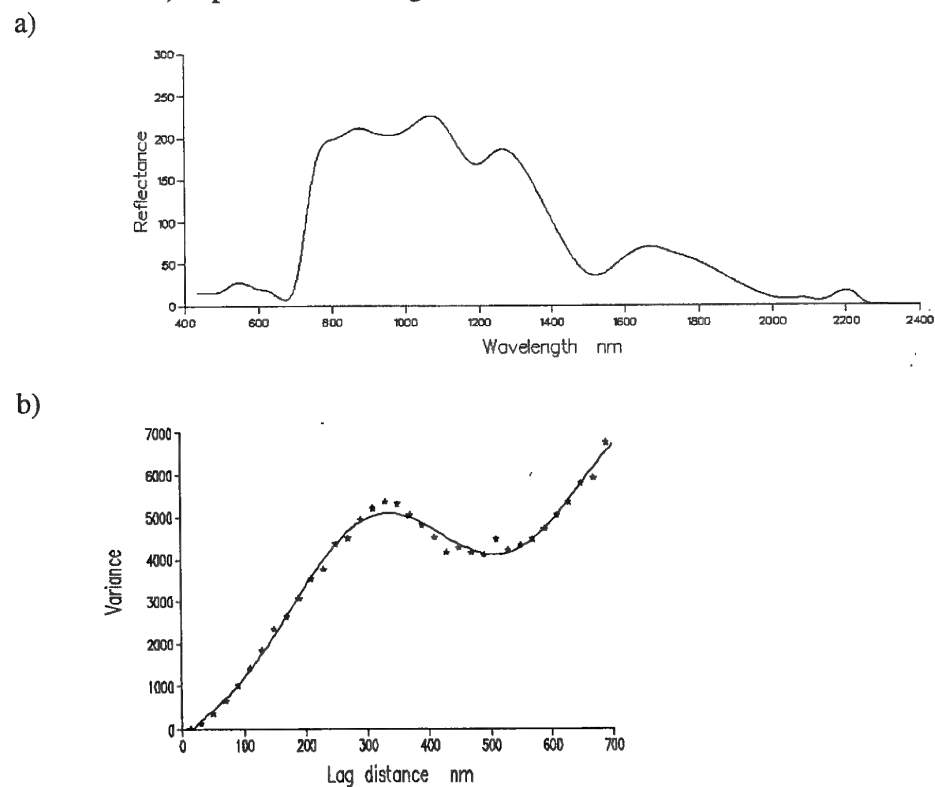


Figure 24. Ft Hood: pixel 91: a) spectrum, b) experimental variogram and fitted model (PPF) of quadratic residuals.

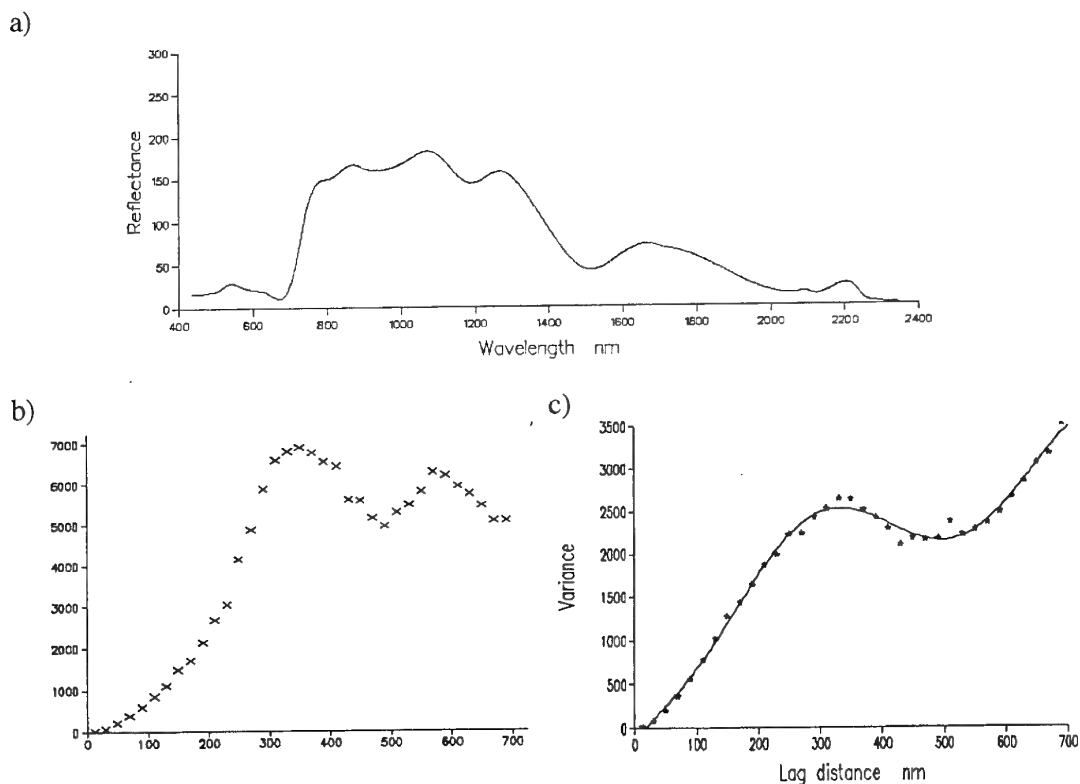


Figure 25. Ft Hood: pixel **95**: a) spectrum, b) experimental variogram of raw values, and c) experimental variogram and fitted model (PPF) of quadratic residuals.

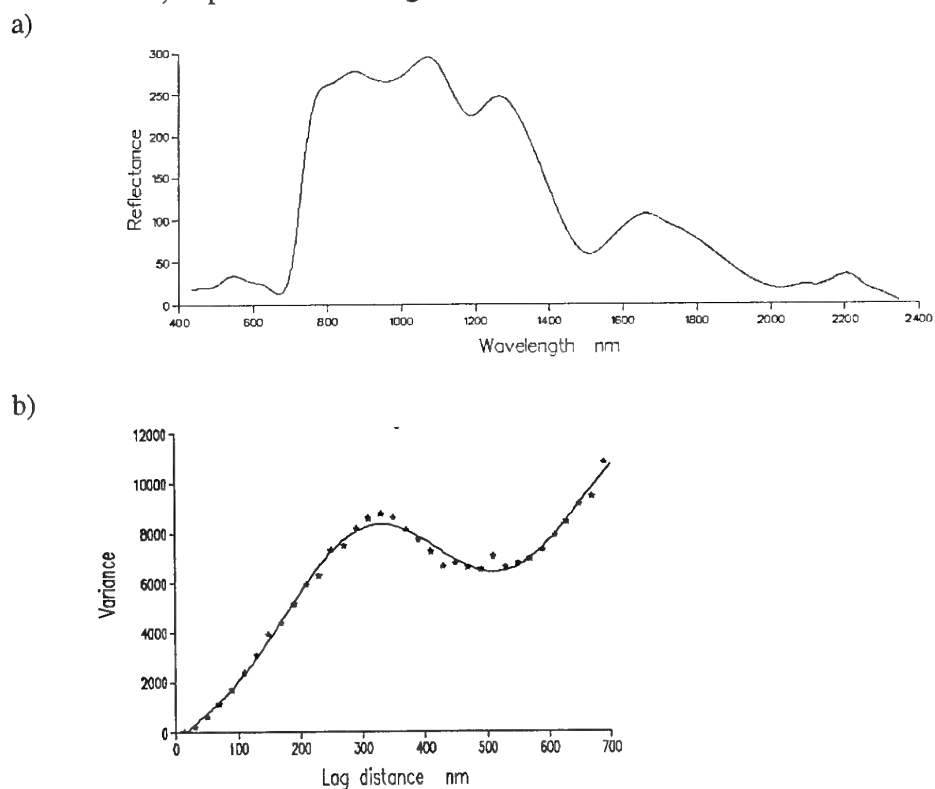


Figure 26. Ft Hood: pixel **96**: a) spectrum, b) experimental variogram and fitted model (PPF) of quadratic residuals.

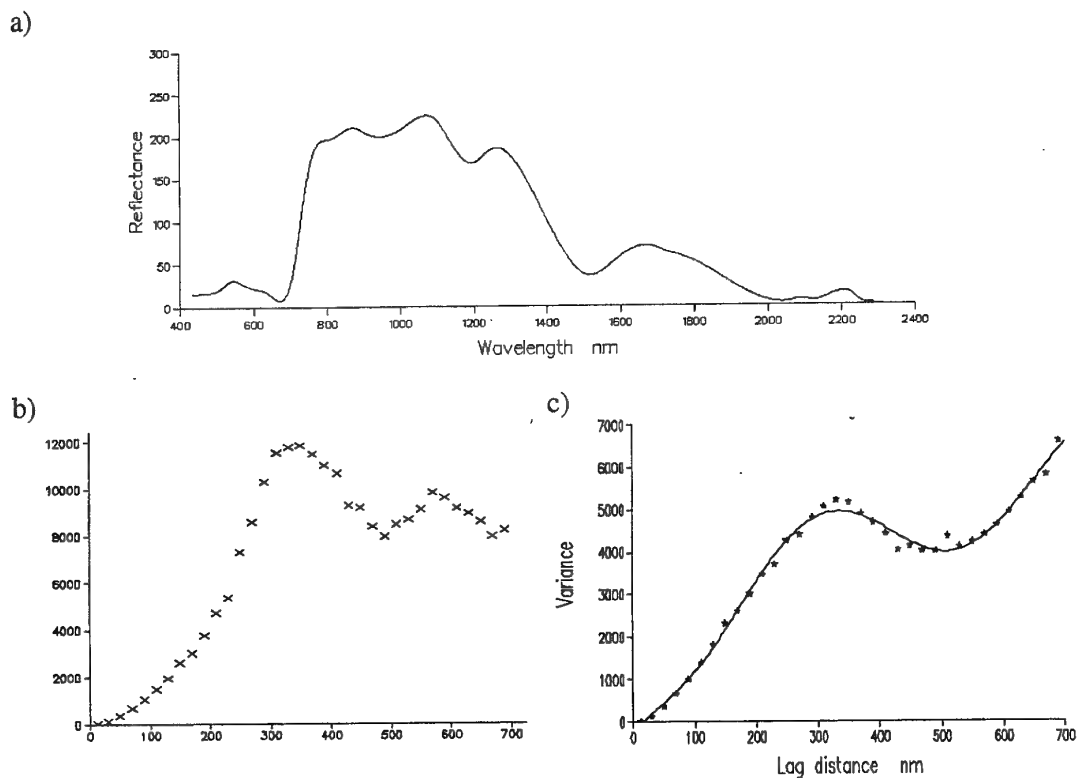


Figure 27. Ft Hood: pixel **100**: a) spectrum, b) experimental variogram of raw values, and c) experimental variogram and fitted model (PPF) of quadratic residuals.

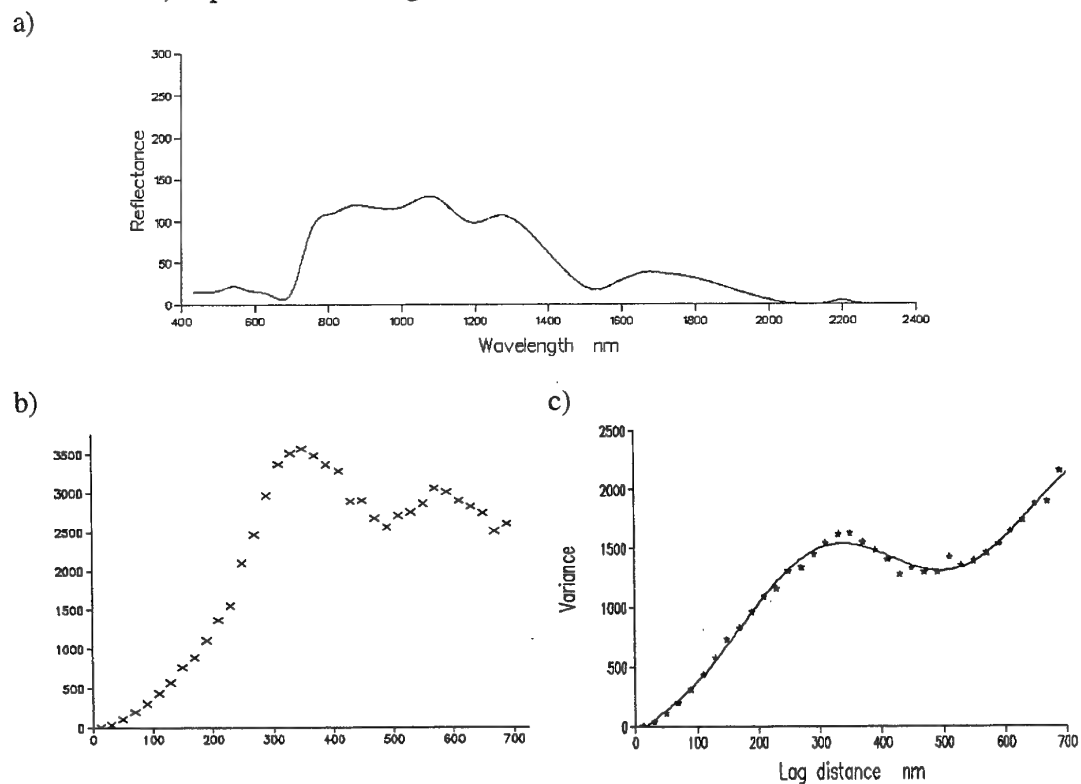


Figure 28. Ft Hood: pixel **104**: a) spectrum, b) experimental variogram of raw values, and c) experimental variogram and fitted model (PPF) of quadratic residuals.

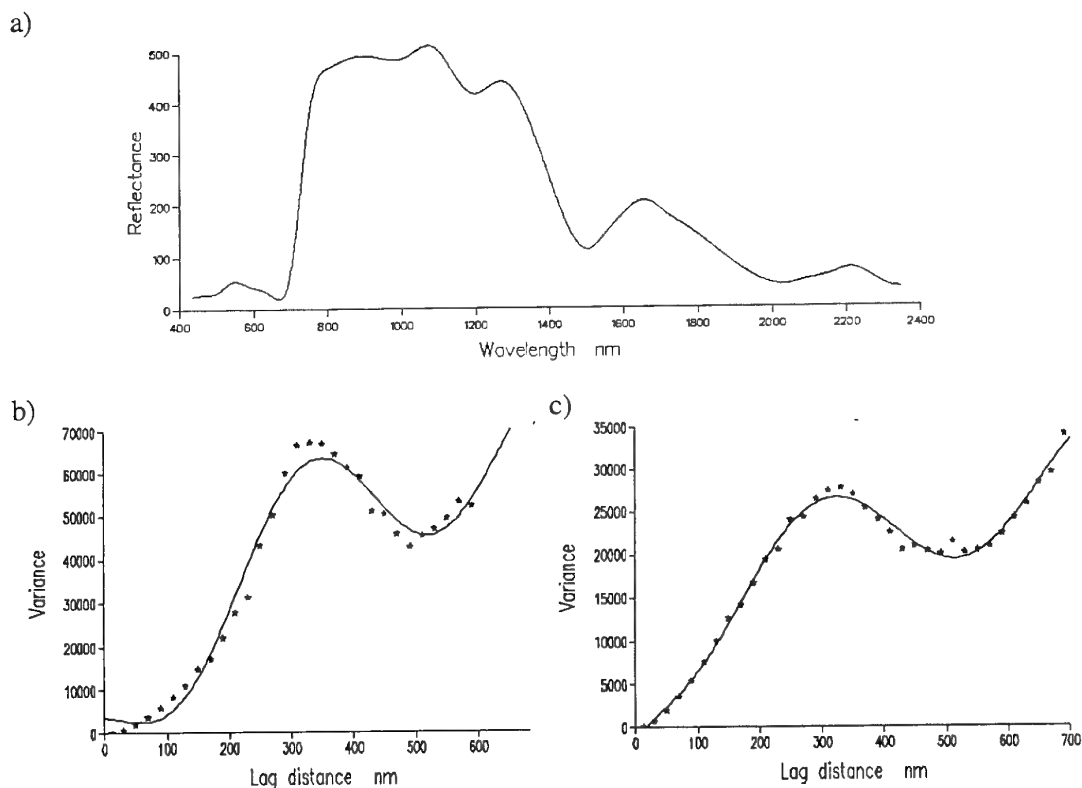


Figure 29. Ft Hood: pixel **107**: a) spectrum, b) variogram and fitted model (PEF) of raw values clipped, c) variogram and fitted model (PPF) of quadratic residuals.

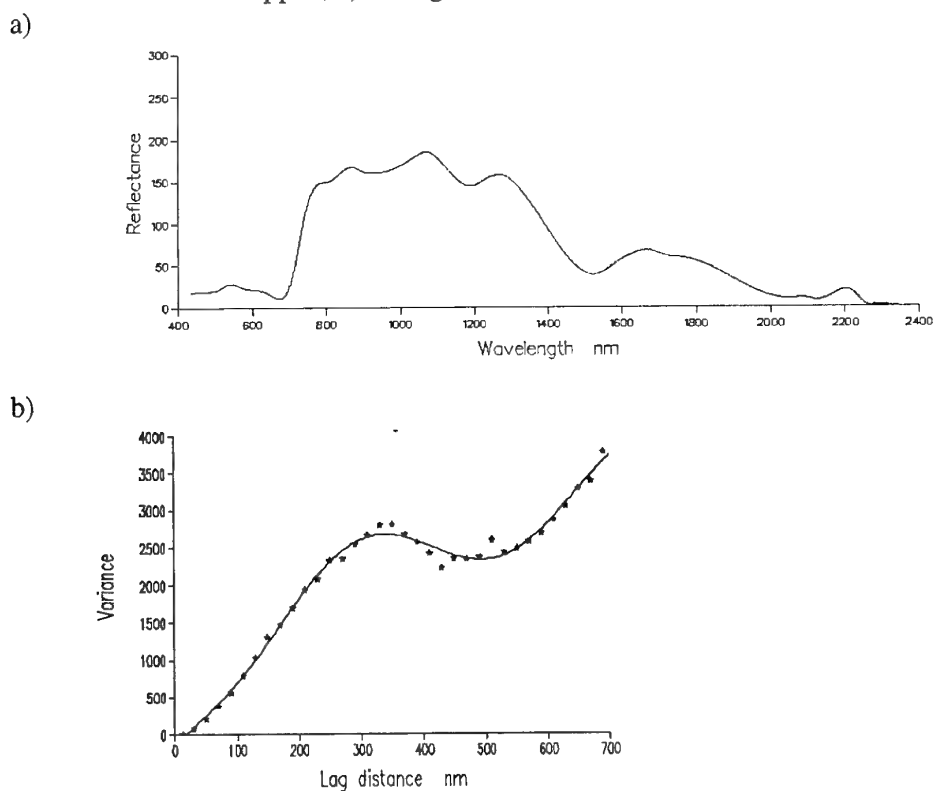


Figure 30. Ft Hood: pixel **108**: a) spectrum, b) experimental variogram and fitted model (PPF) of quadratic residuals.

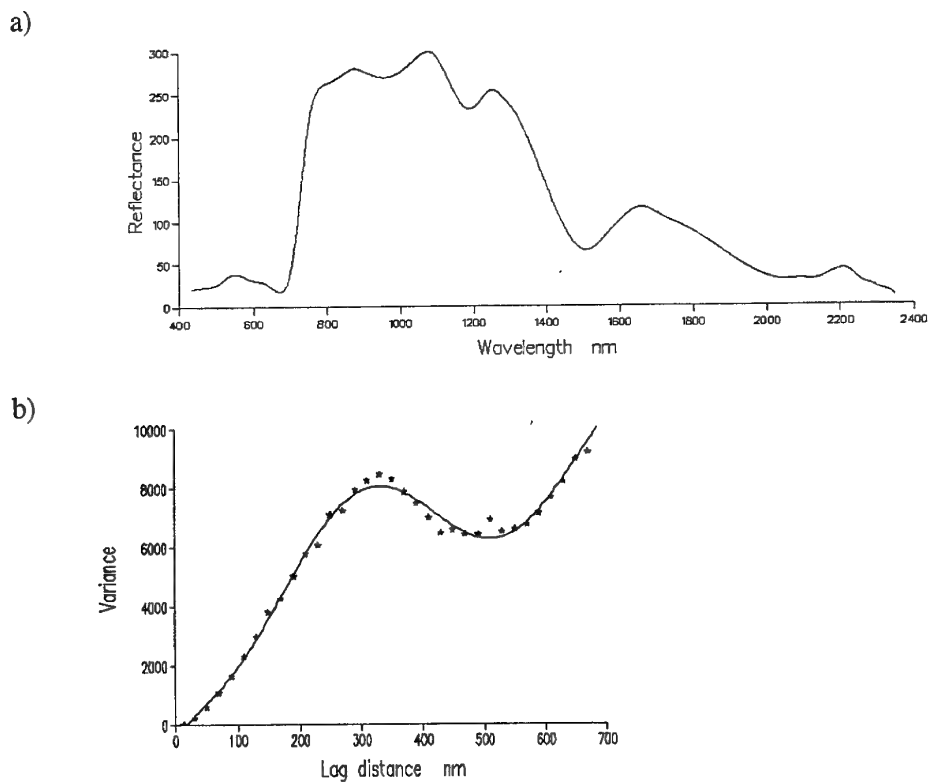


Figure 31 Ft Hood: pixel **111**: a) spectrum, b) experimental variogram and fitted model (PPF) of quadratic residuals.

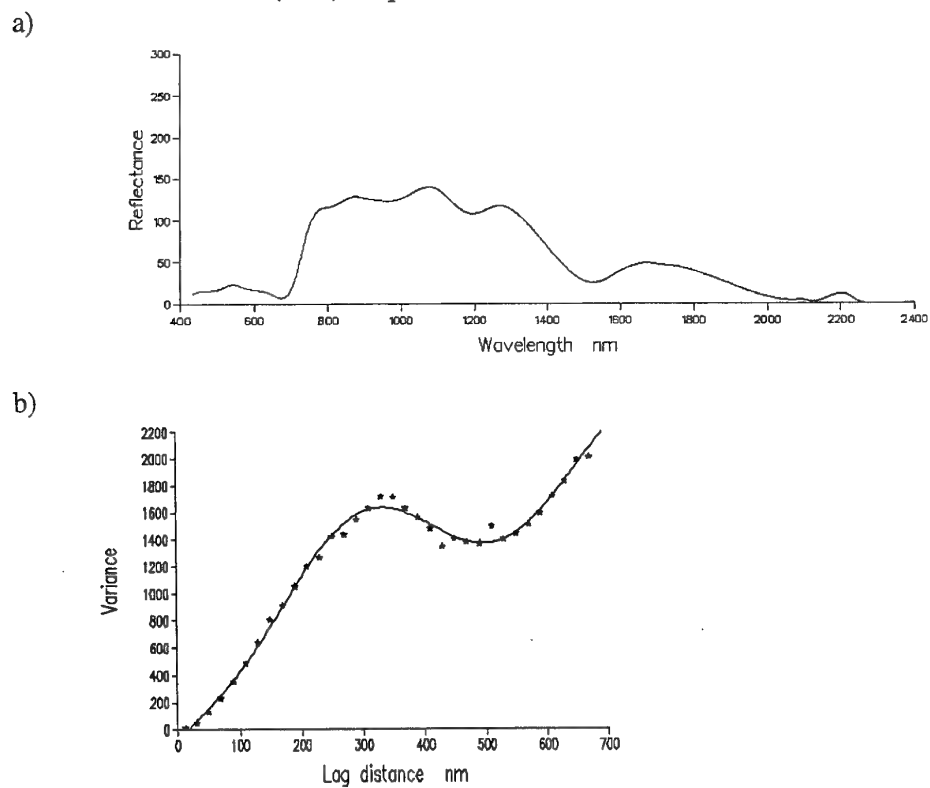
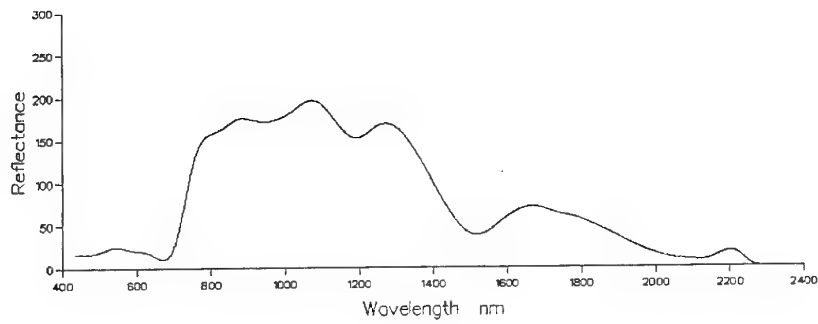
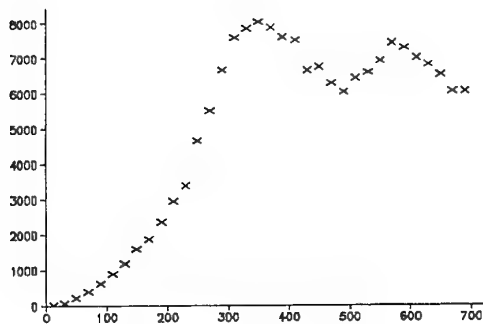


Figure 32 Ft Hood: pixel **114**: a) spectrum, b) experimental variogram and fitted model (PPF) of quadratic residuals.

a)



b)



c)

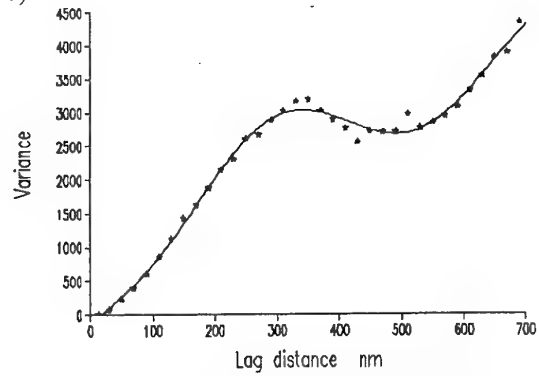
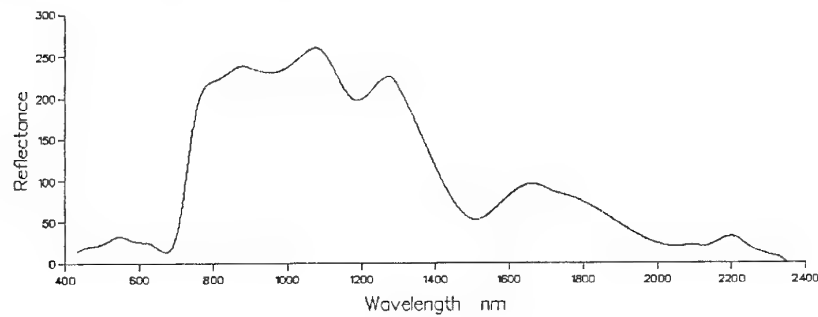


Figure 33. Ft Hood: pixel **120**: a) spectrum, b) experimental variogram of raw values, and c) experimental variogram and fitted model (PPF) of quadratic residuals.

a)



b)

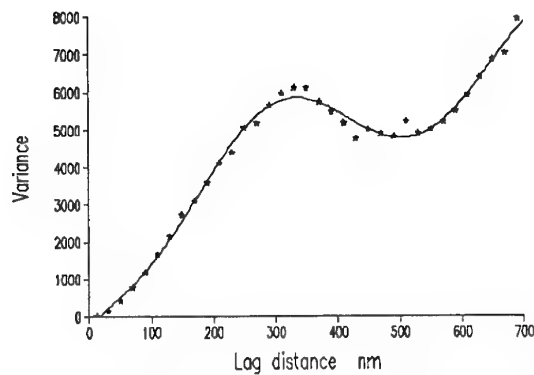
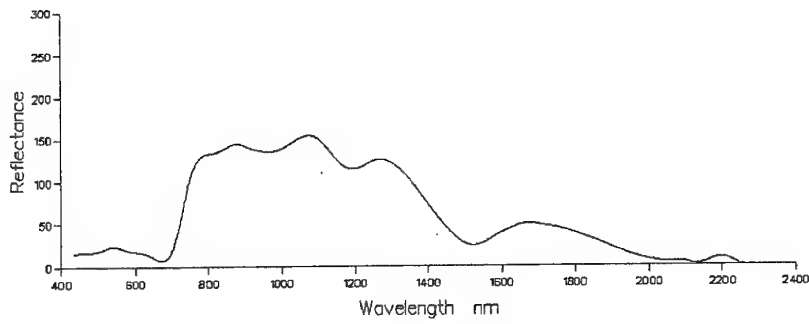
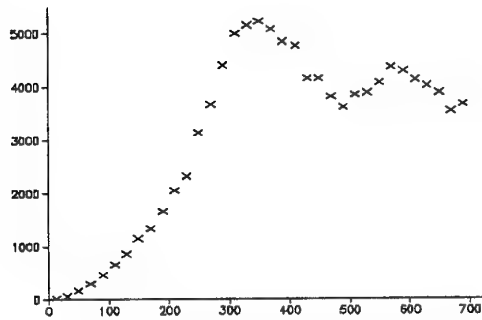


Figure 34. Ft Hood: pixel **121**: a) spectrum, b) experimental variogram and fitted model (PPF) of quadratic residuals.

a)



b)



c)

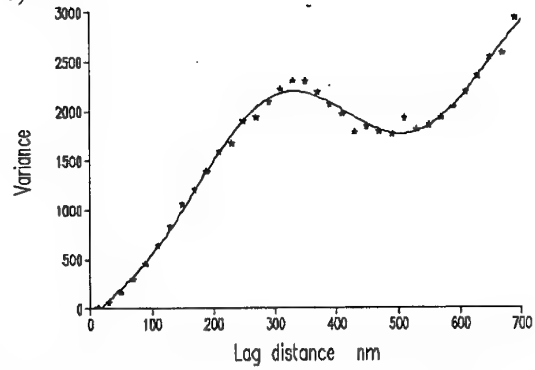
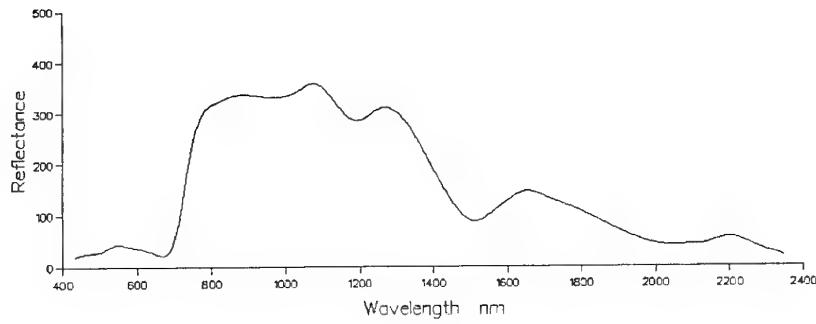
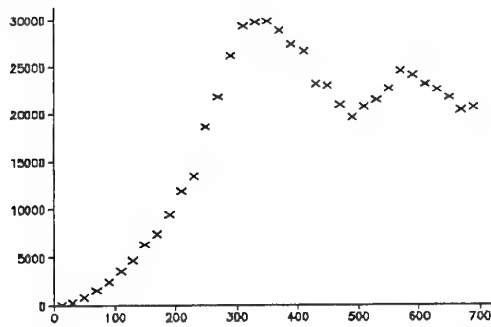


Figure 35. Ft Hood: pixel **124**: a) spectrum, b) experimental variogram of raw values and c) experimental variogram and fitted model (PPF) of quadratic residuals.

a)



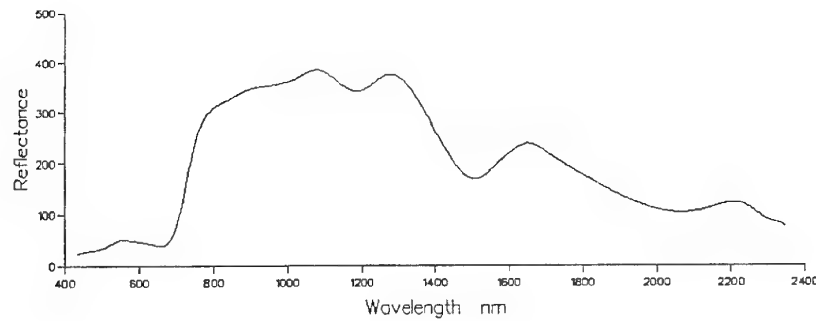
b)



c)

Figure 36. Ft Hood: pixel **128** a) spectrum, b) experimental variogram of raw values, and c) experimental variogram and fitted model (PPF) of quadratic residuals.

a)



b)

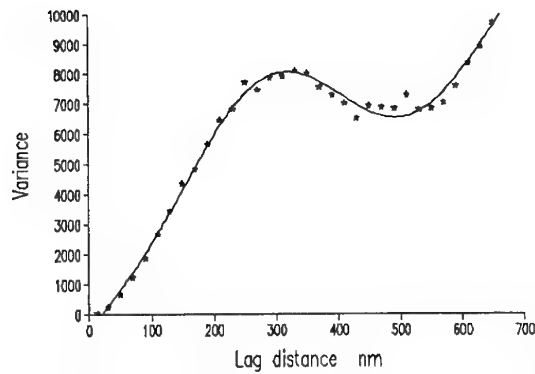


Figure 37. Ft Hood: pixel **131** a) spectrum, b) experimental variogram and fitted model (PPF) of quadratic residuals.

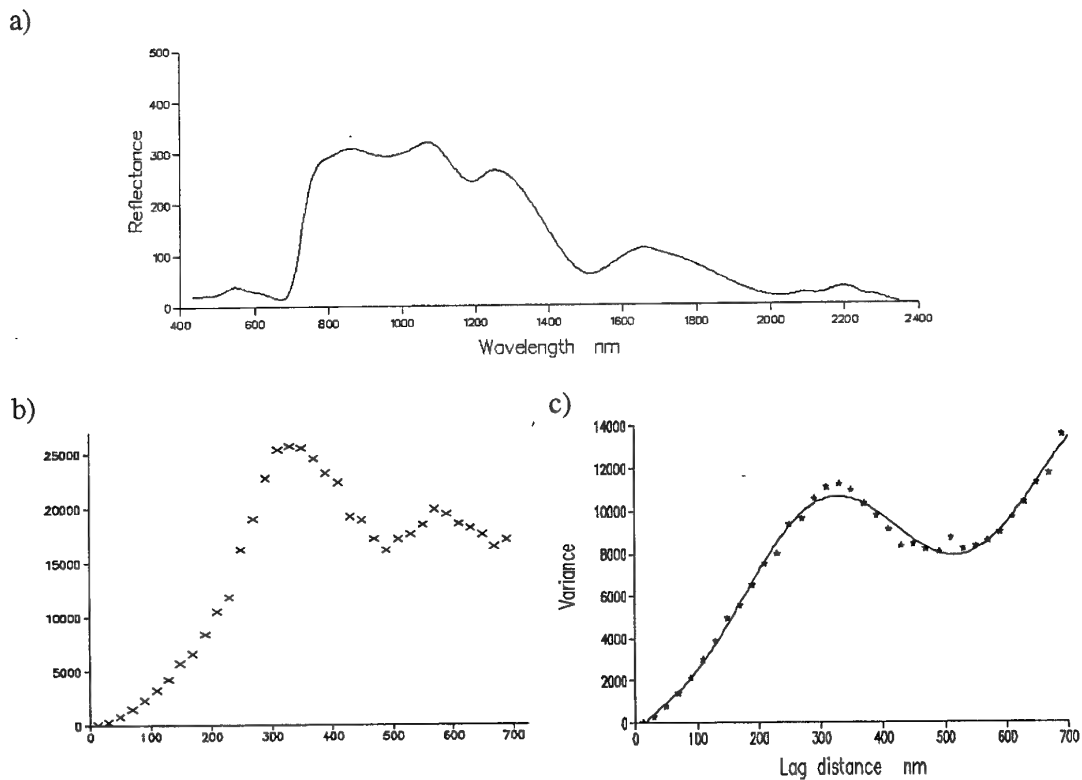


Figure 38. Ft Hood: pixel **134**: a) spectrum, b) experimental variogram of raw values, and c) experimental variogram and fitted model (PPF) of quadratic residuals.

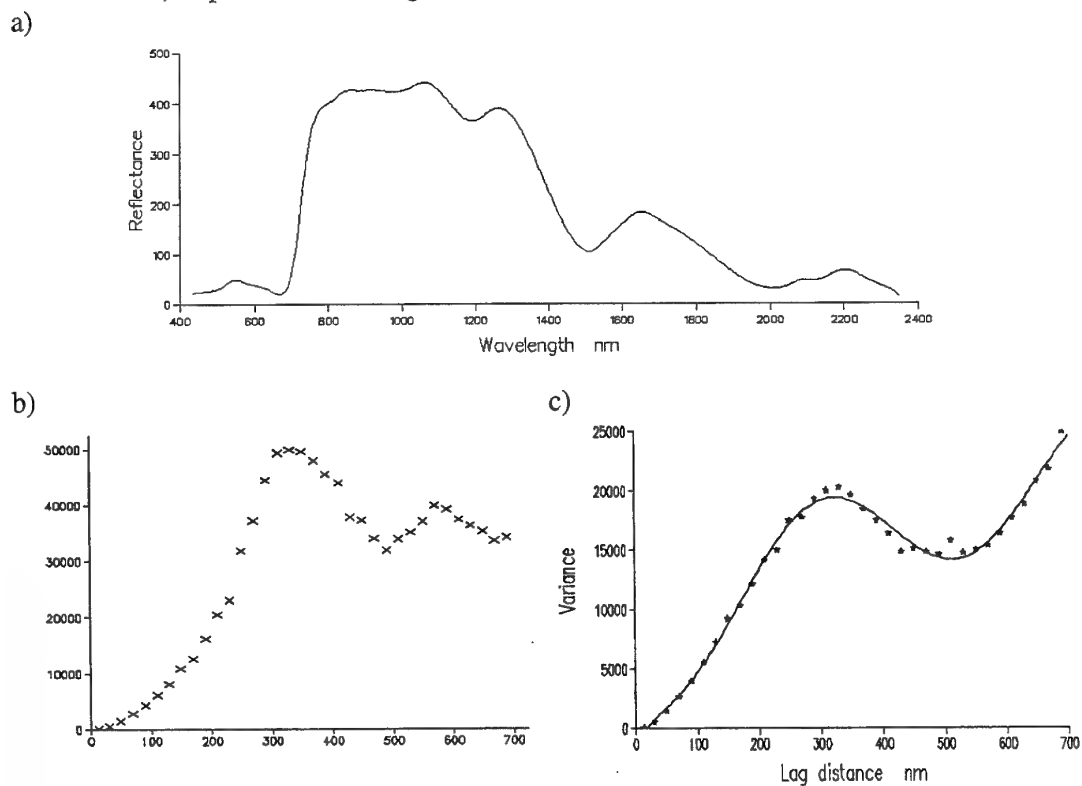
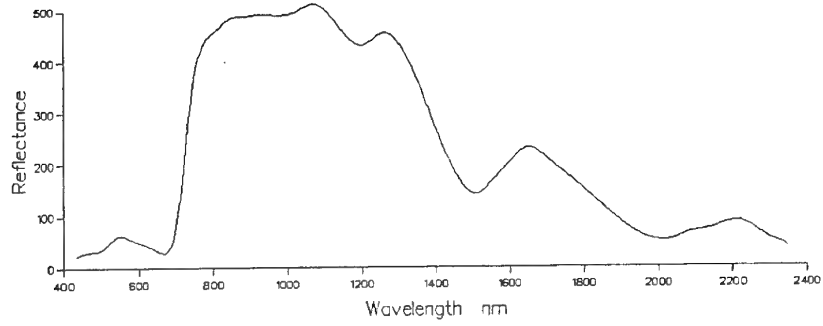


Figure 39. Ft Hood: pixel **139**: a) spectrum, b) experimental variogram of raw values, and c) experimental variogram and fitted model (PPF) of quadratic residuals.

a)



b)

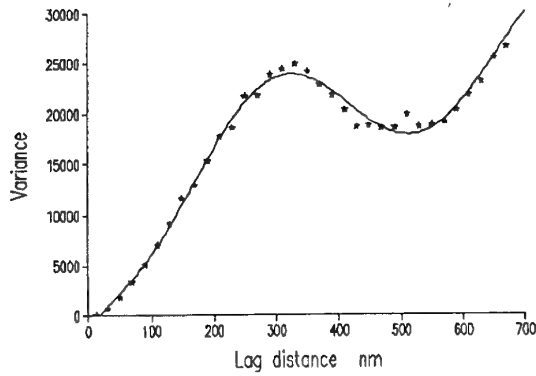
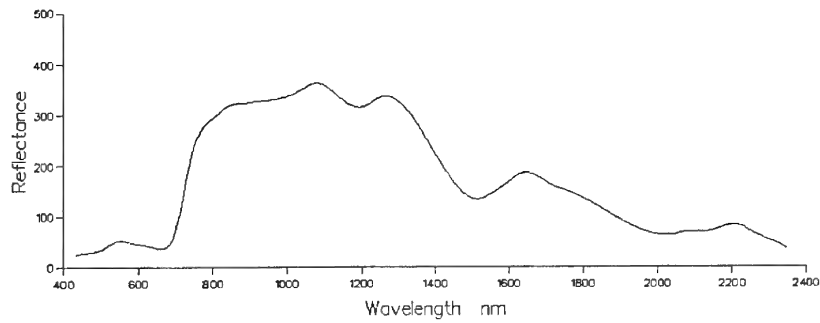


Figure 40. Ft Hood: pixel **140**: a) spectrum, b) experimental variogram and fitted model (PPF) of quadratic residuals.

a)



b)

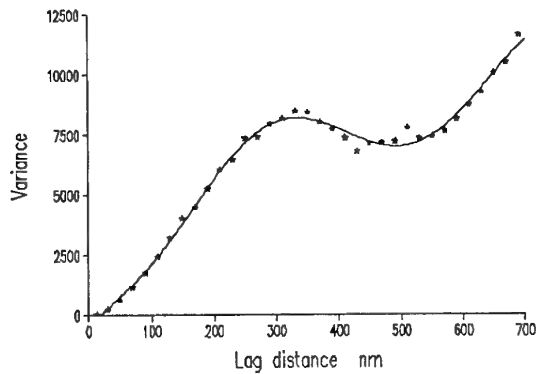
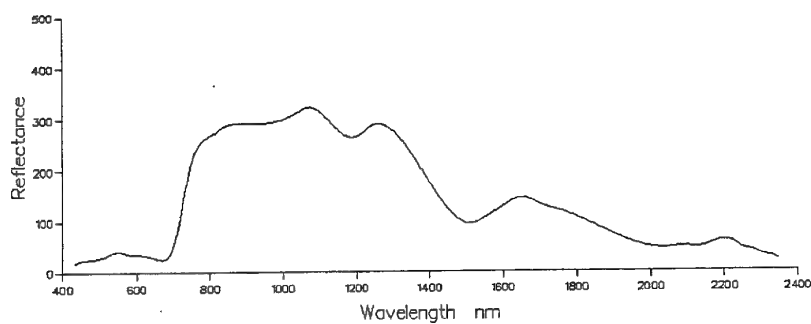


Figure 41. Ft Hood: pixel **141** a) spectrum, b) experimental variogram and fitted model (PPF) of quadratic residuals.

a)



b)

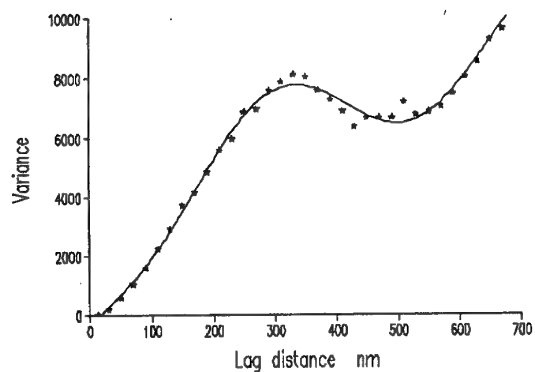
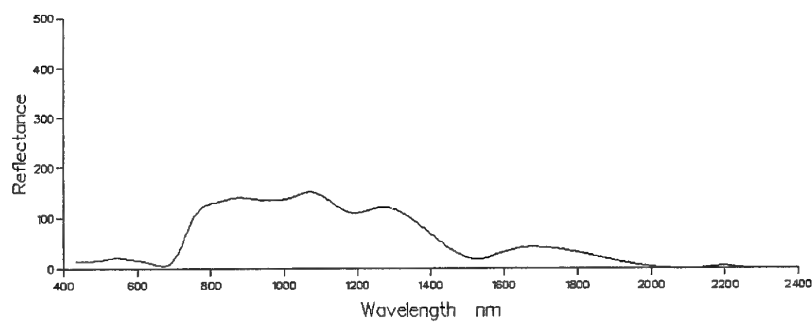


Figure 42. Ft Hood: pixel **142**: a) spectrum, b) experimental variogram and fitted model (PPF) of quadratic residuals.

a)



b)

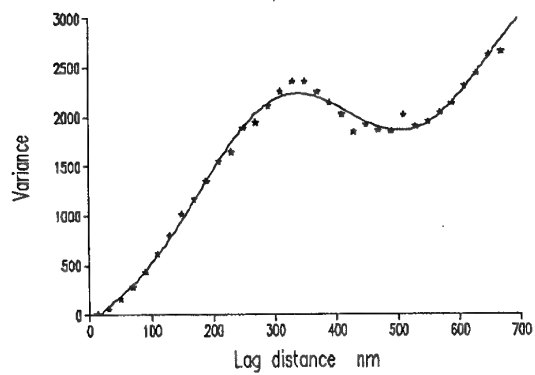
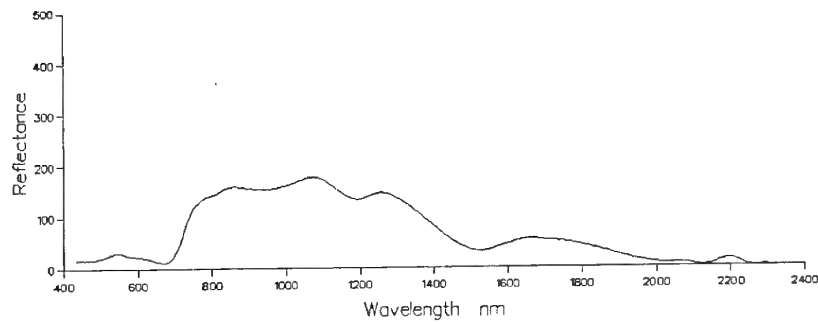


Figure 43. Ft Hood: pixel **143**: a) spectrum, b) experimental variogram and fitted model (PPF) of quadratic residuals.

a)



b)

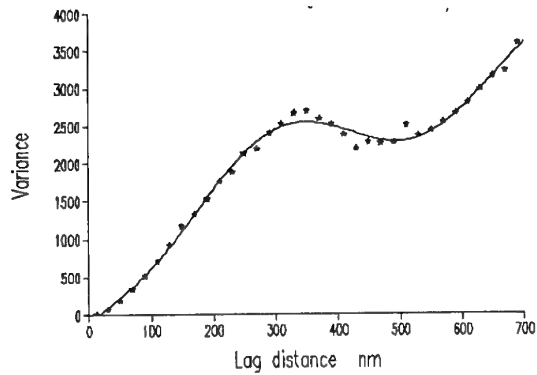
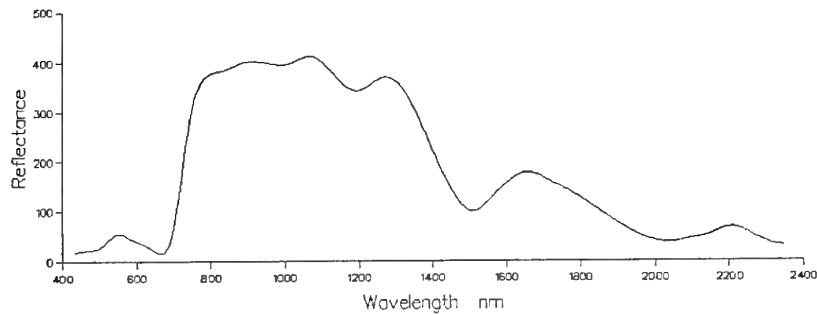
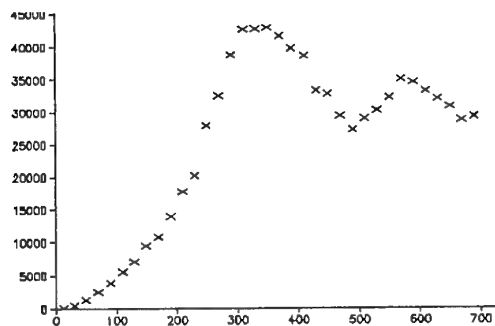


Figure 44. Ft Hood: pixel **140**: a) spectrum, b) experimental variogram and fitted model (PPF) of quadratic residuals.

a)



b)



c)

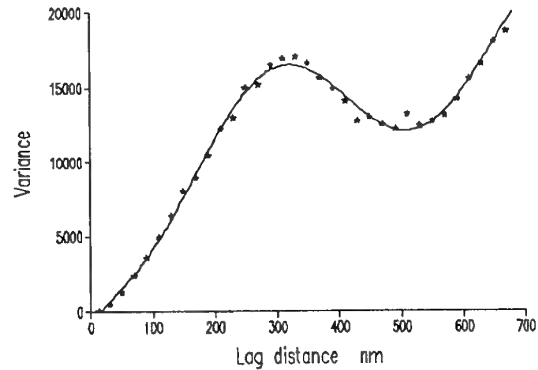
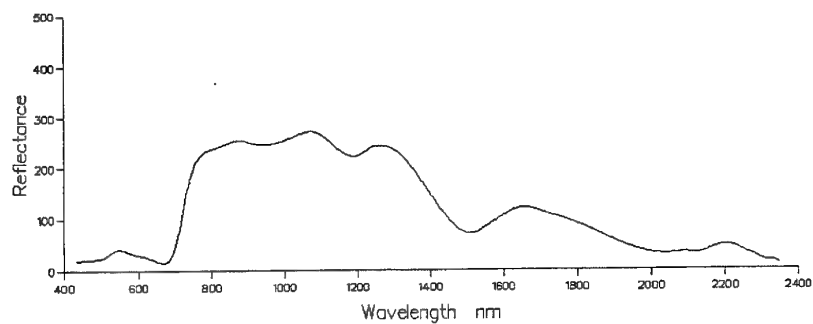


Figure 45. Ft Hood: pixel **159**: a) spectrum, b) experimental variogram of raw values, and c) experimental variogram and fitted model (PPF) of quadratic residuals.

a)



b)

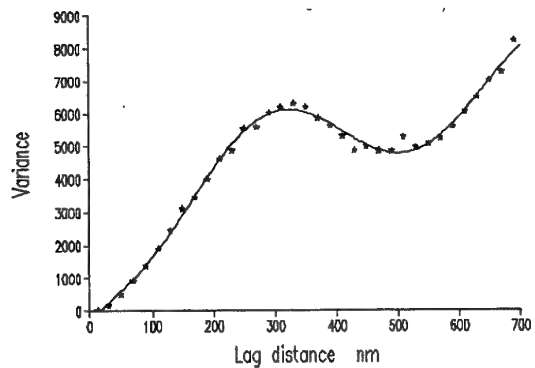
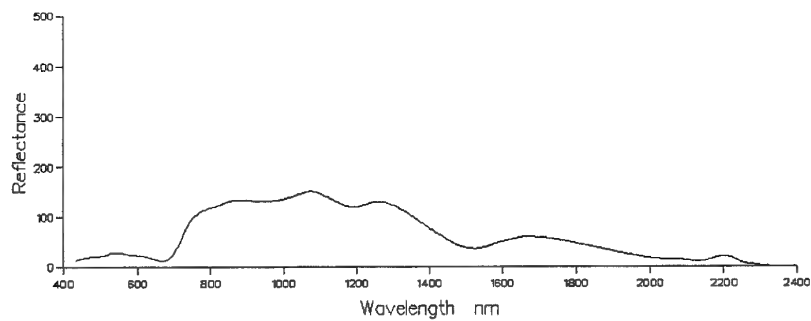


Figure 46. Ft Hood: pixel **160**: a) spectrum, b) experimental variogram and fitted model (PPF) of quadratic residuals.

a)



b)

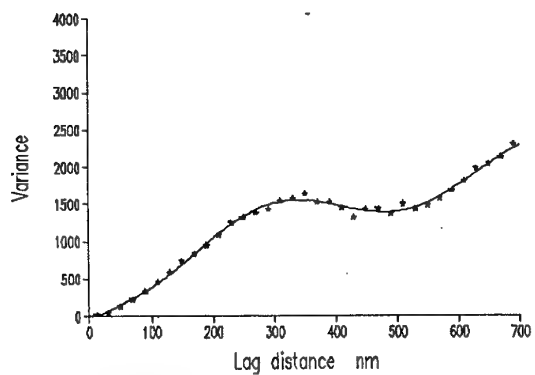
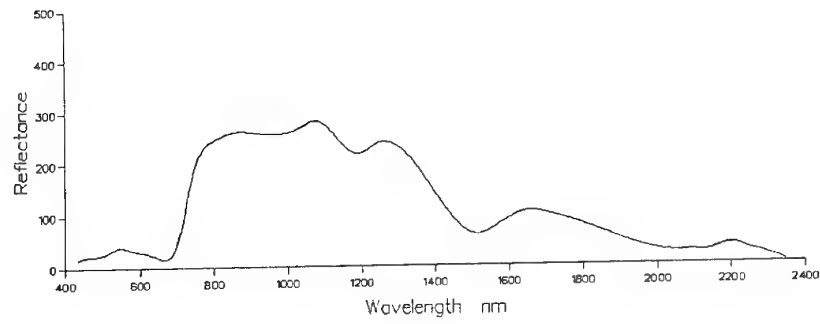
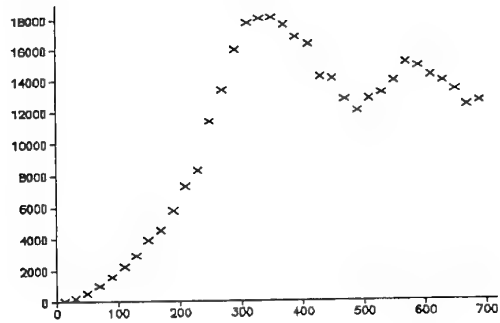


Figure 47. Ft Hood: pixel **161**: a) spectrum, b) experimental variogram and fitted model (PPF) of quadratic residuals.

a)



b)



c)

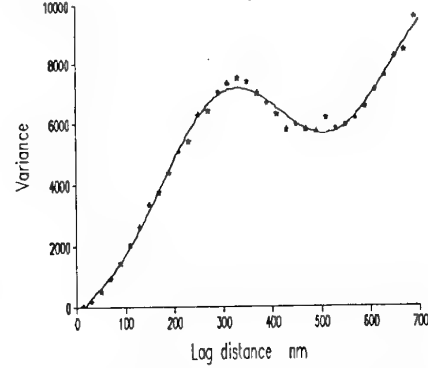


Figure 48. Ft Hood: pixel **162**: a) spectrum, b) experimental variogram of raw values, and c) experimental variogram and fitted model (PPF) of quadratic residuals.

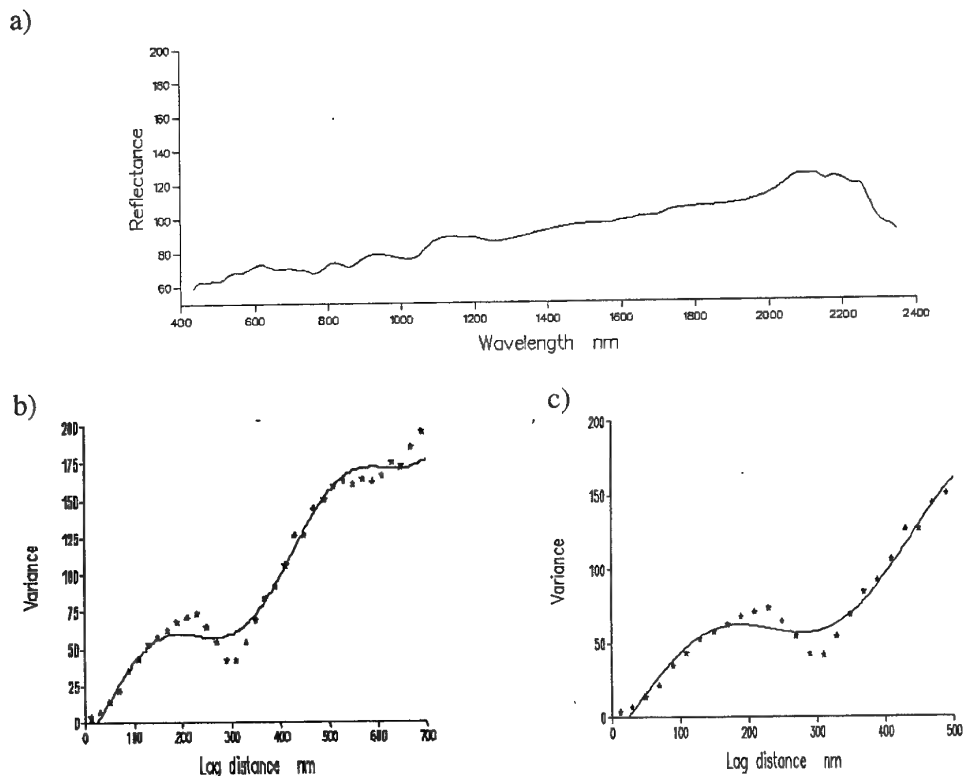


Figure 49. Ft Hood: pixel **163**: a) spectrum, b) experimental variogram and fitted model (PPF) of raw values, and c) as b) but clipped at 500 nm lag distance.

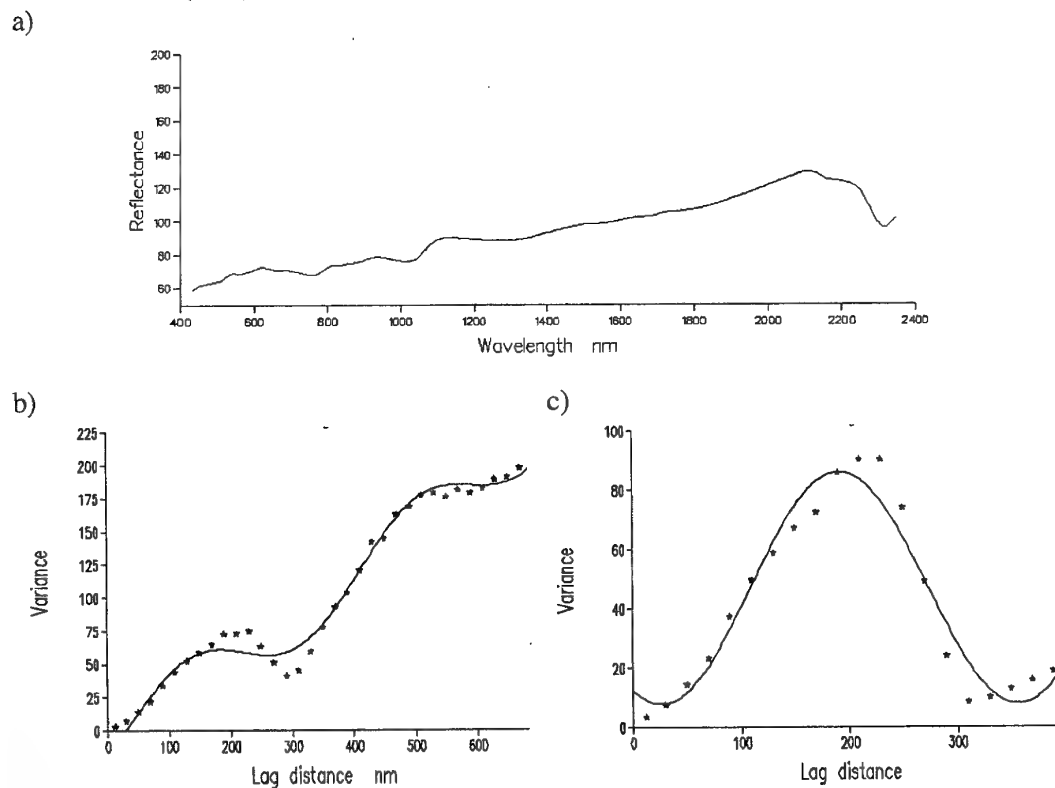
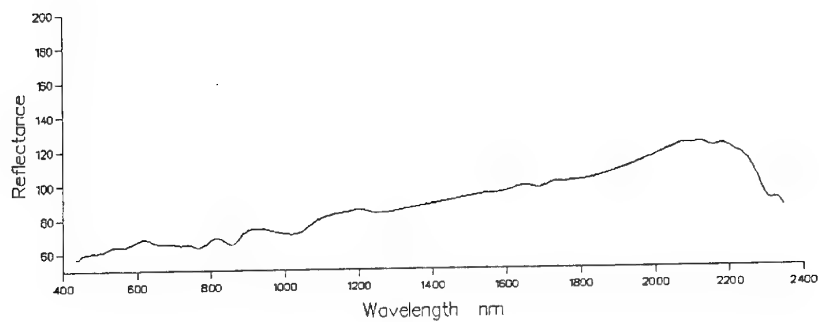


Figure 50. Ft Hood: pixel **163** a) spectrum, b) variogram and fitted model (PPF) of raw values, c) variogram and model (periodic) of linear residuals, clipped.

a)



b)

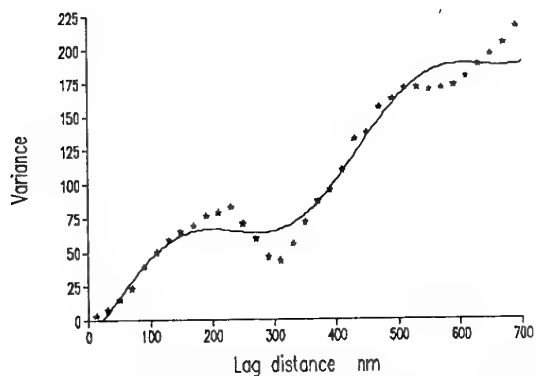
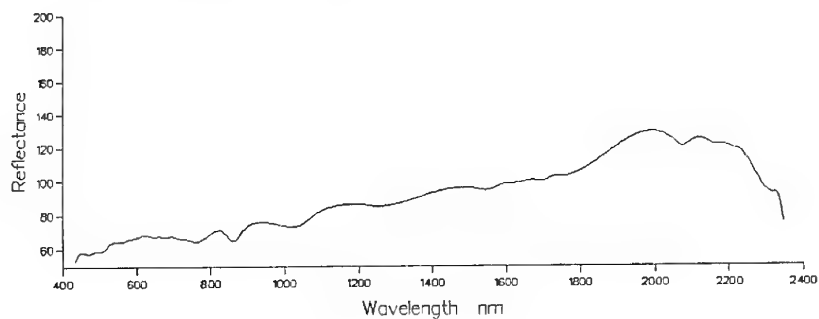


Figure 51 Ft Hood: pixel **167**: a) spectrum, b) experimental variogram and fitted model (PPF) of raw values.

a)



b)

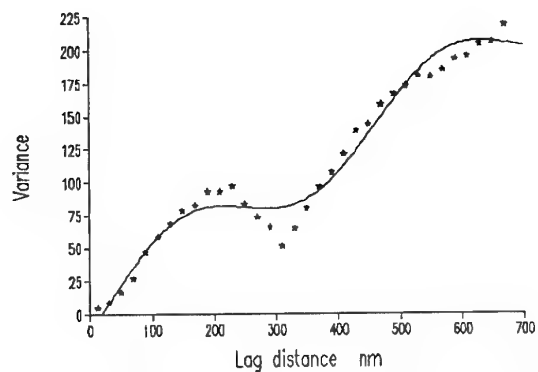
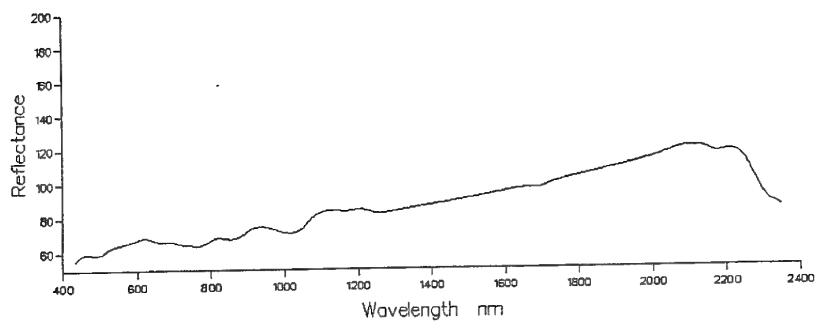


Figure 52. Ft Hood: pixel **168**: a) spectrum, b) experimental variogram and fitted model (PPF) of raw values.

a)



b)

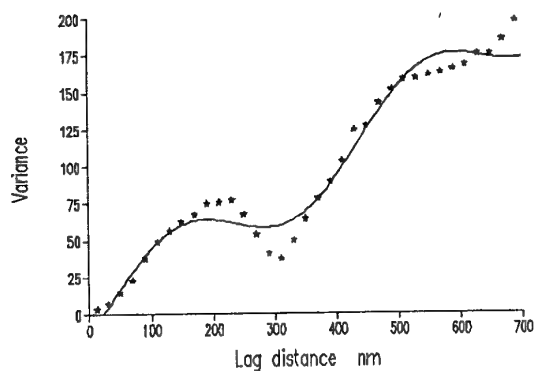
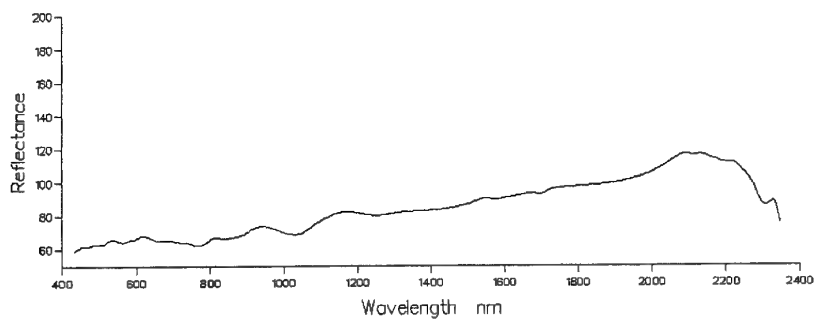


Figure 53. Ft Hood: pixel **169**: a) spectrum, b) experimental variogram and fitted model (PPF) of raw values.

a)



b)

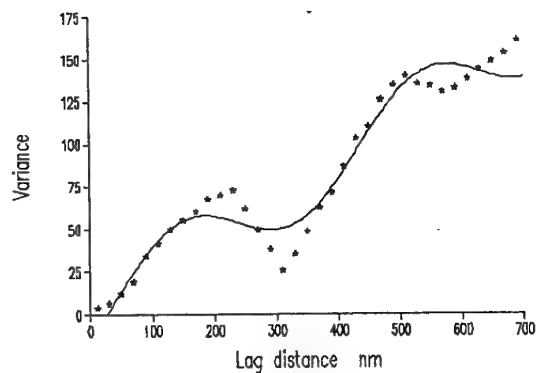
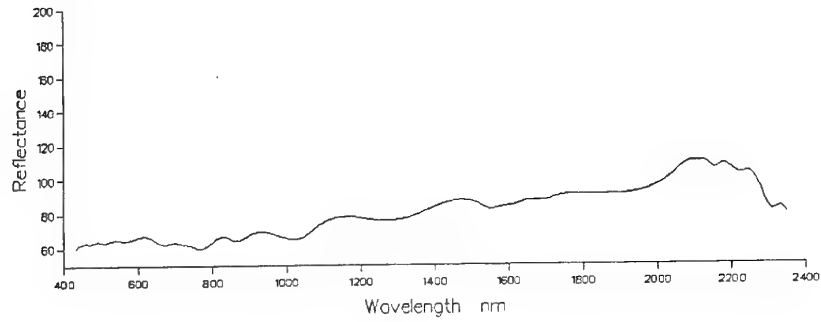


Figure 54. Ft Hood: pixel **171**: a) spectrum, b) experimental variogram and fitted model (PPF) of raw values.

a)



b)

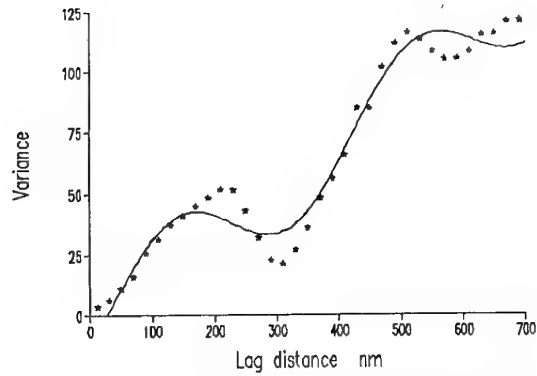
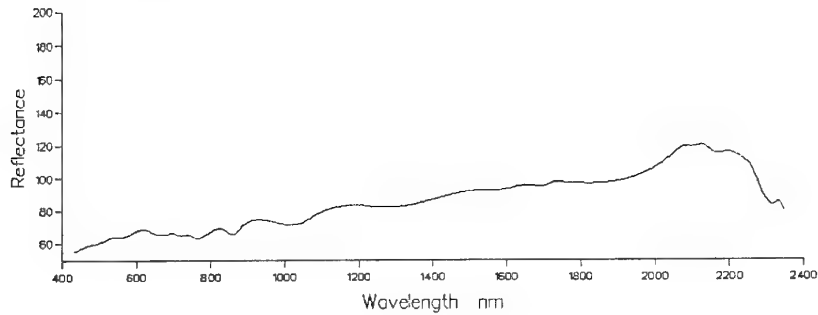


Figure 55. Ft Hood: pixel **188**: a) spectrum, b) experimental variogram and fitted model (PPF) of raw values.

a)



b)

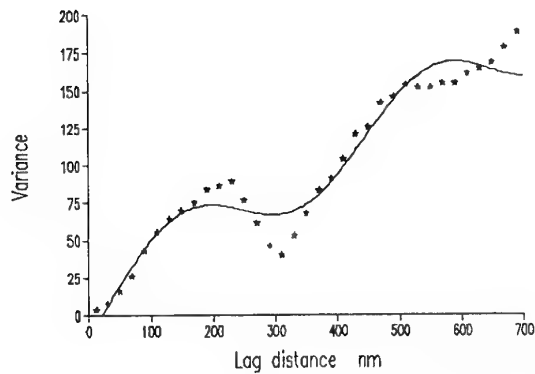
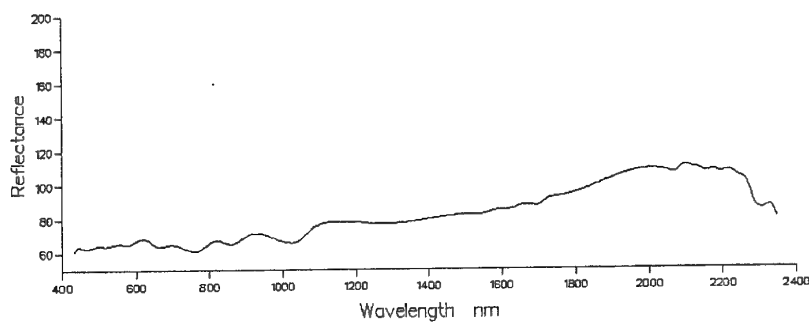


Figure 56. Ft Hood: pixel **190**: a) spectrum, b) experimental variogram and fitted model (PPF) of raw values.

a)



b)

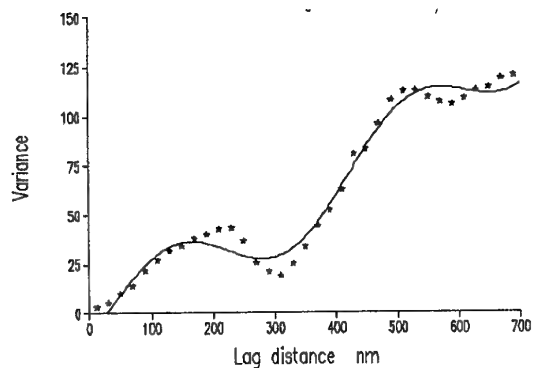
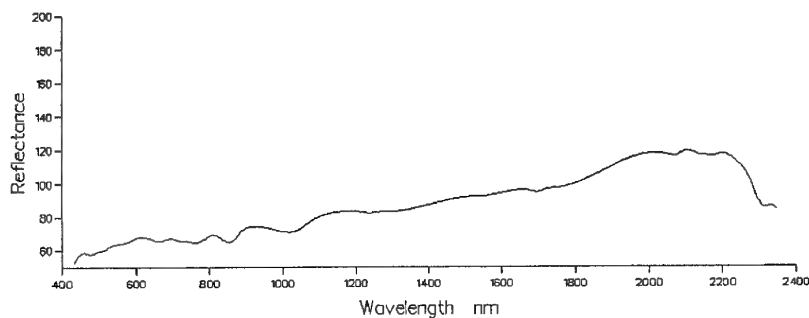
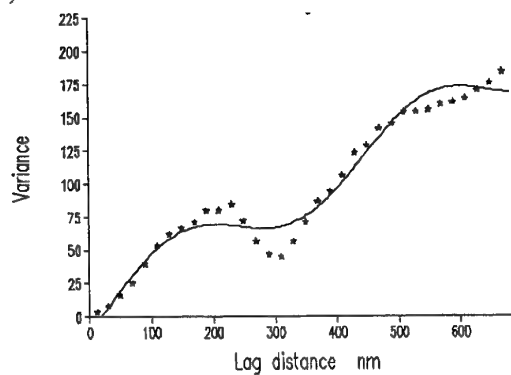


Figure 57. Ft Hood: pixel **193**: a) spectrum, b) experimental variogram and fitted model (PPF) of raw values.

a)



b)



c)

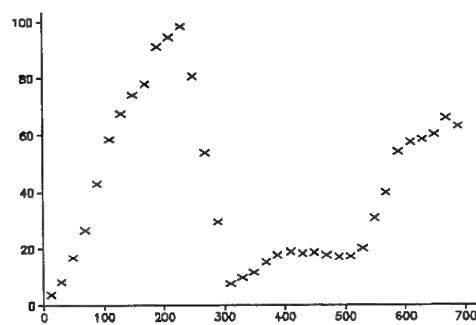
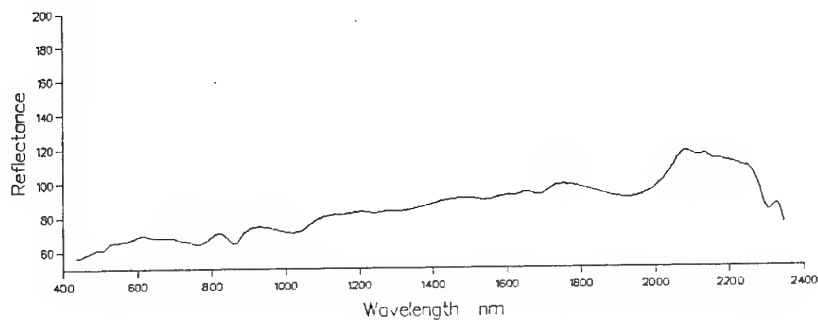


Figure 58. Ft Hood: pixel **195**: a) spectrum, b) experimental variogram and fitted model (PPF) of raw values, and c) variogram of linear residuals.

a)



b)

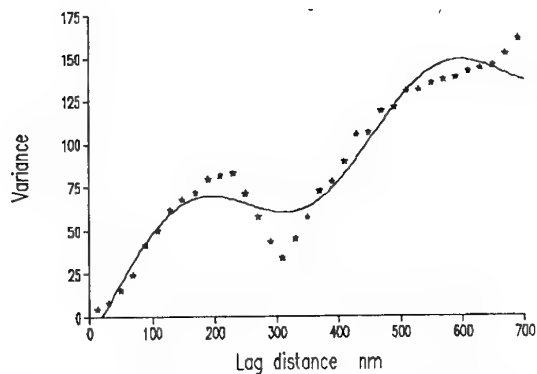
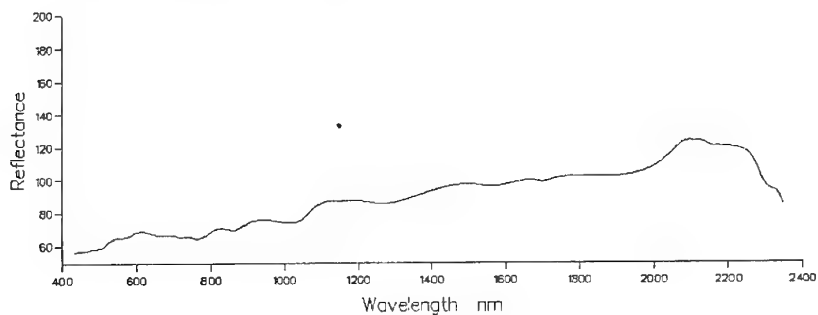


Figure 59. Ft Hood: pixel **198**: a) spectrum, b) experimental variogram and fitted model (PPF) of raw values.

a)



b)

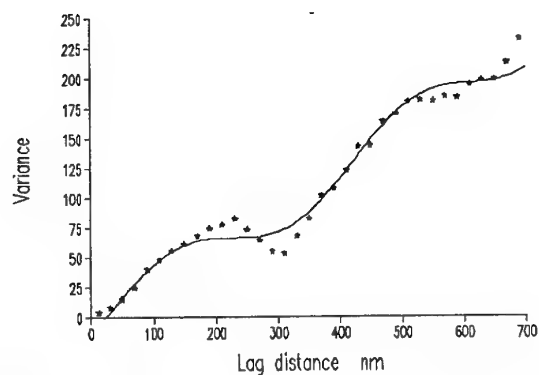
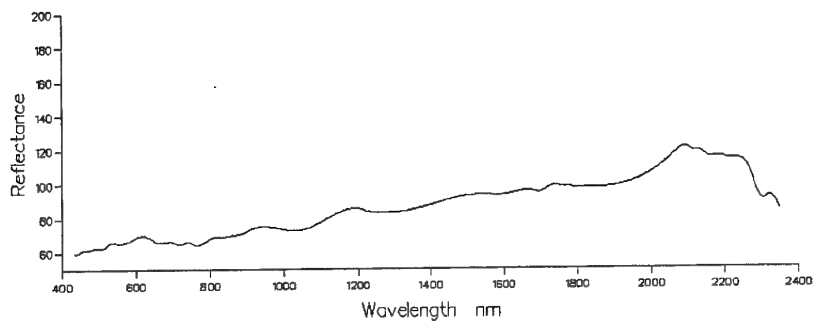


Figure 60. Ft Hood: pixel **204**: a) spectrum, b) experimental variogram and fitted model (PPF) of raw values.

a)



b)

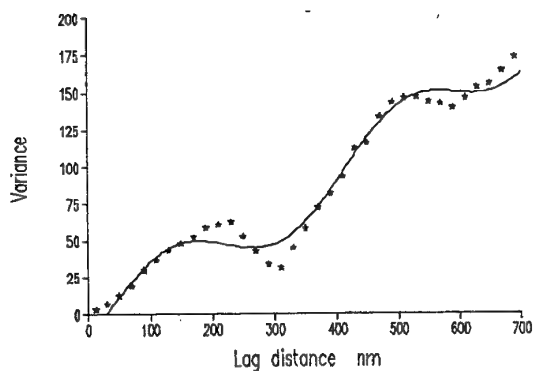
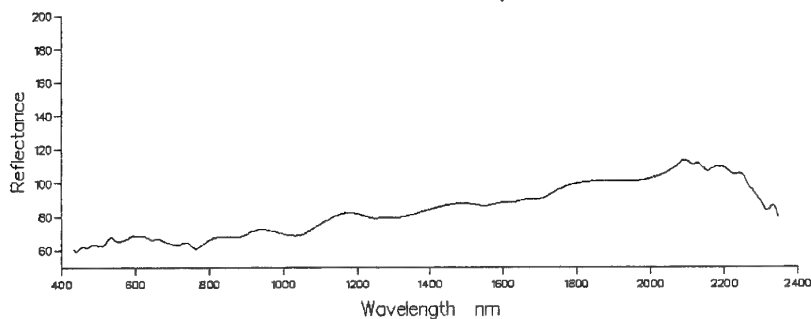


Figure 61. Ft Hood: pixel **206**: a) spectrum, b) experimental variogram and fitted model (PPF) of raw values.

a)



b)

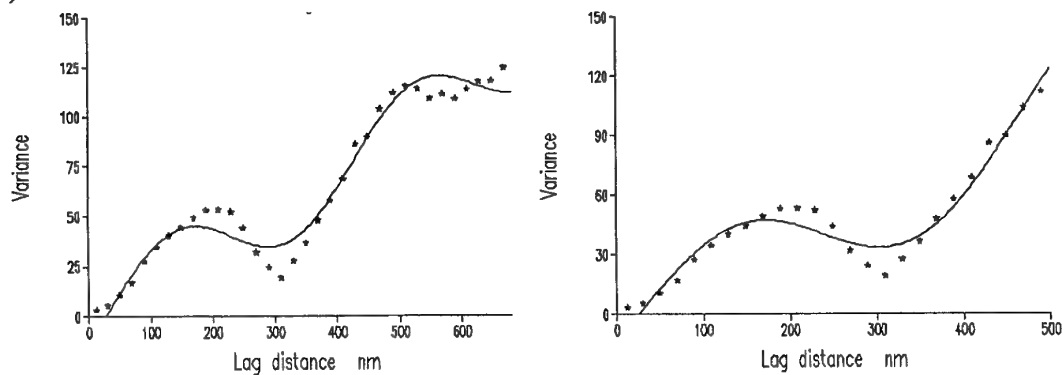


Figure 62. Ft Hood: pixel **207**: a) spectrum, b) experimental variogram and fitted model (PPF) of raw values, c) as b) but clipped at 500 nm lag distance.

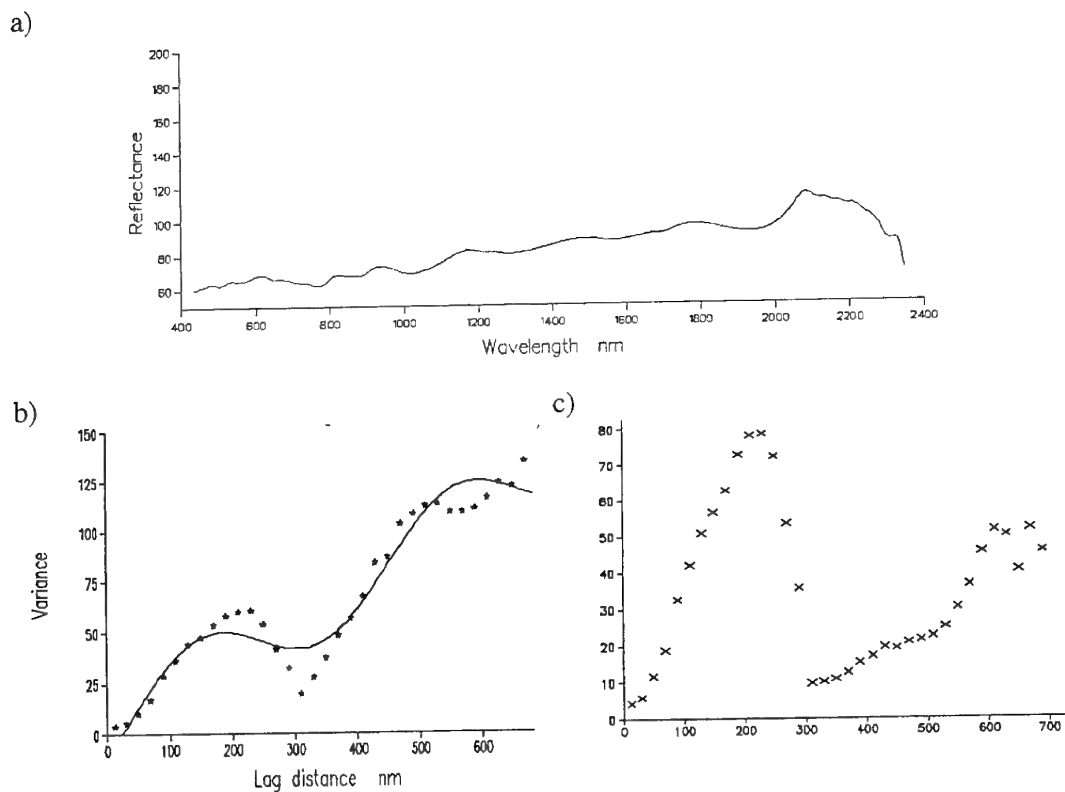


Figure 63. Ft Hood: pixel **213**: a) spectrum, b) experimental variogram and fitted model (PPF) of raw values, and c) variogram of linear residuals.

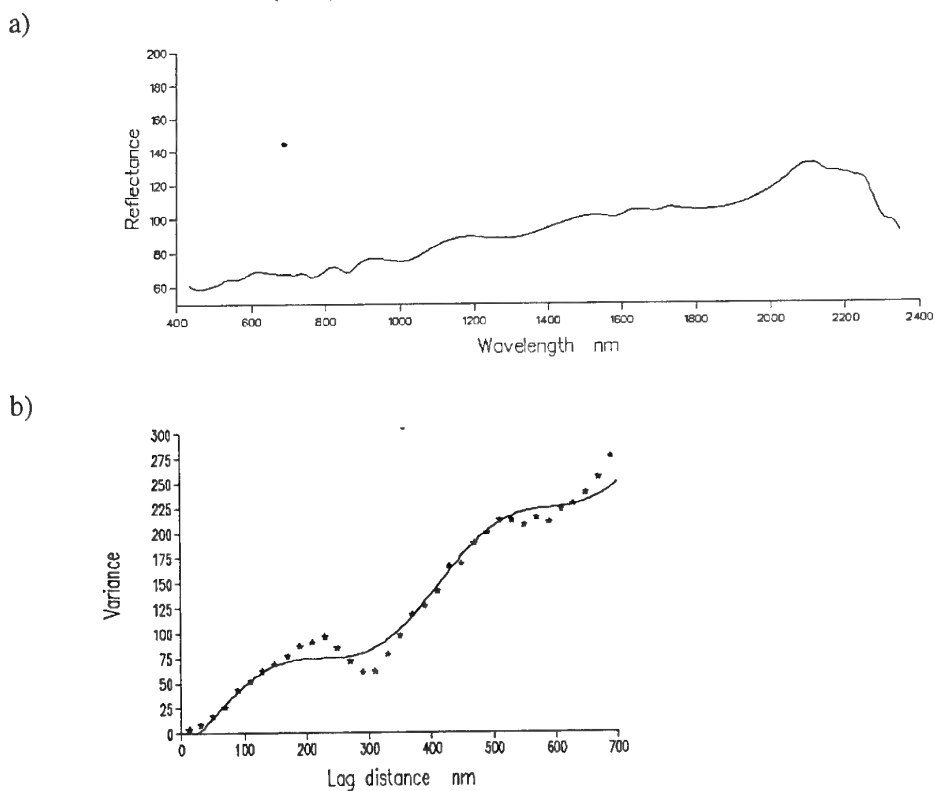


Figure 64. Ft Hood: pixel **214**: a) spectrum, b) experimental variogram and fitted model (PPF) of raw values.

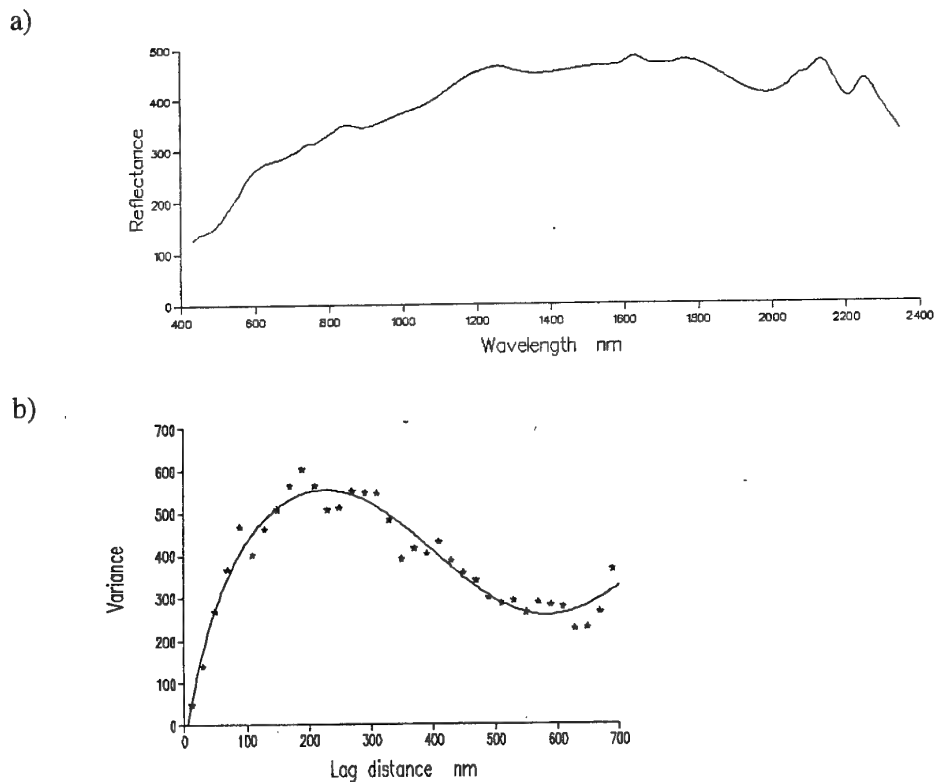


Figure 65. Ft Hood: pixel **230**: a) spectrum, b) experimental variogram and fitted model (PEF) of quadratic residuals.

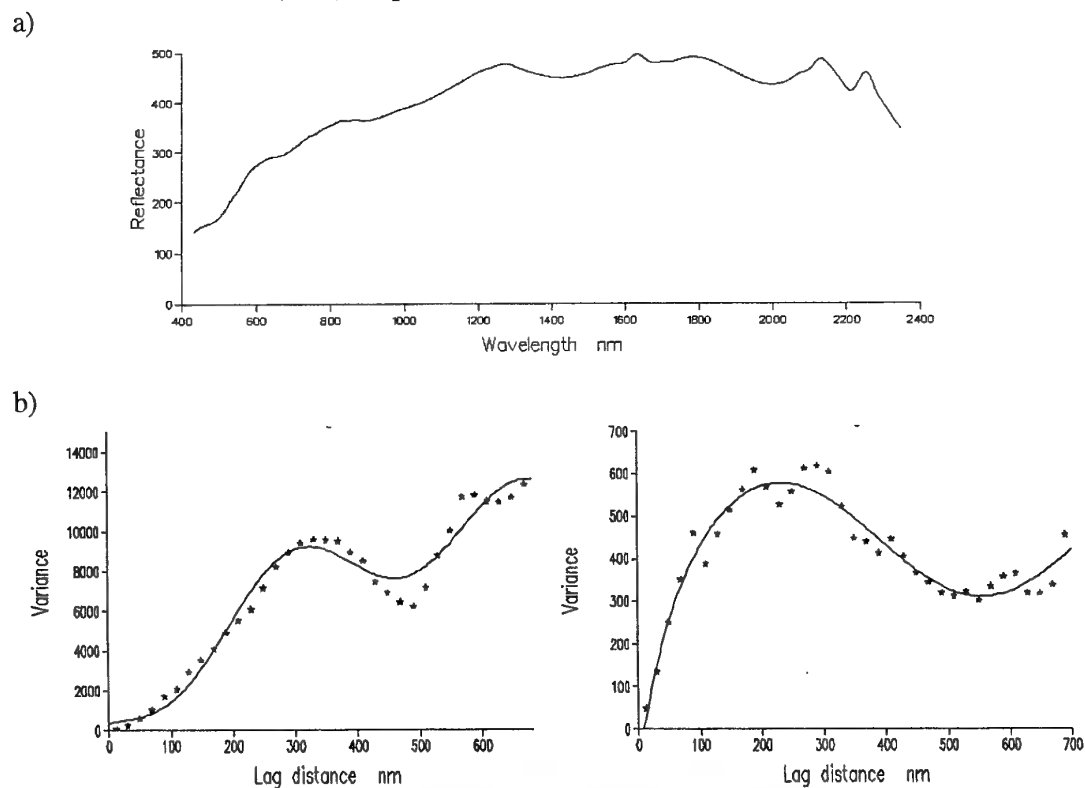


Figure 66. Ft Hood: pixel **234**: a) spectrum, b) variogram and fitted model (PEF) of raw values, c) variogram and fitted model (PEF) of quadratic residuals.

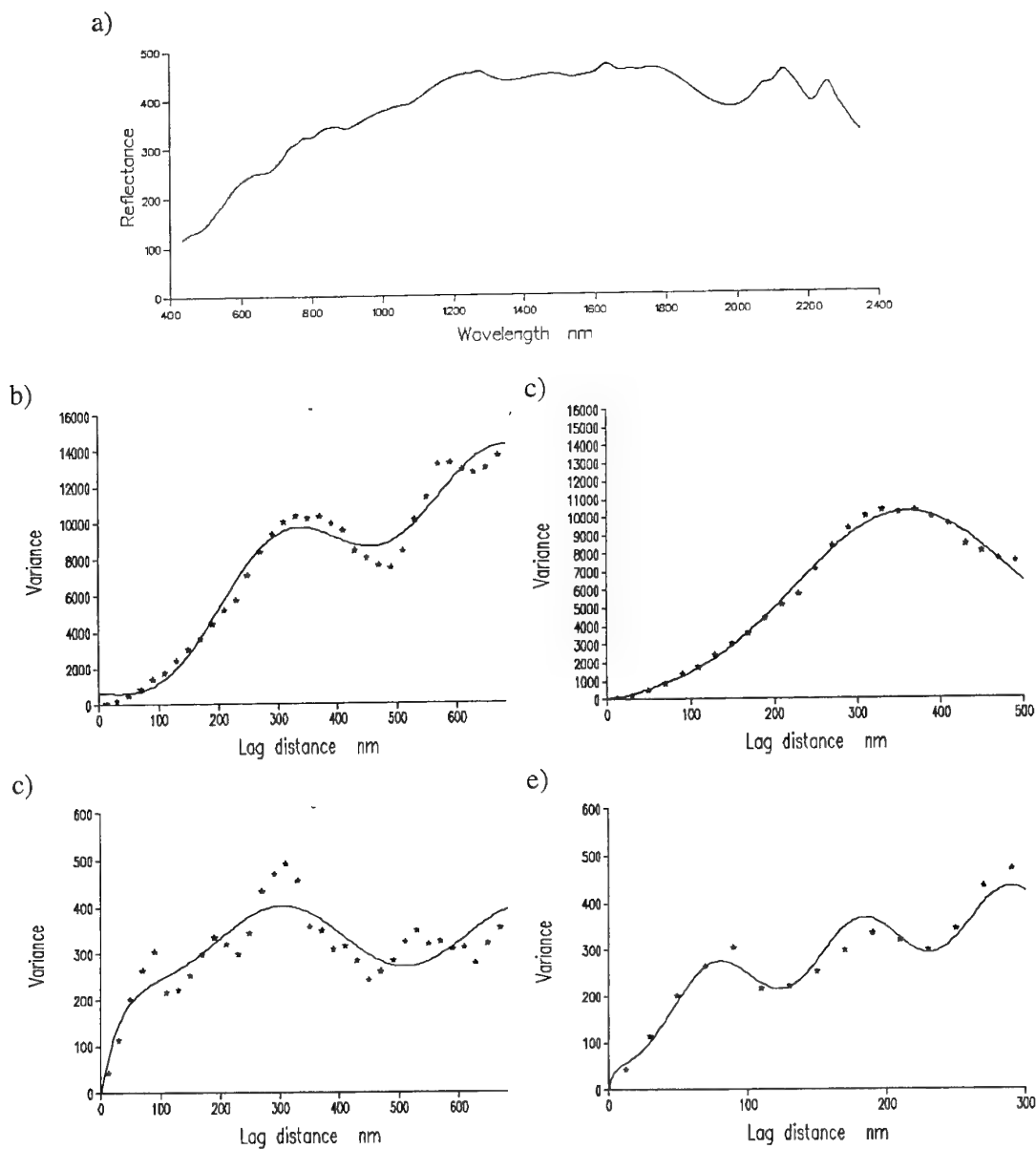


Figure 67. Ft Hood: pixel **242**: a) spectrum, b) experimental variogram and fitted model (PES) of raw values, c) experimental variogram and fitted model (PEF) of raw values, clipped at 500nm lag distance, d) experimental variogram and fitted model (PEF) of quadratic residuals and e) experimental variogram and fitted model (PPF) of quadratic residuals, clipped at 300 nm lag distance.

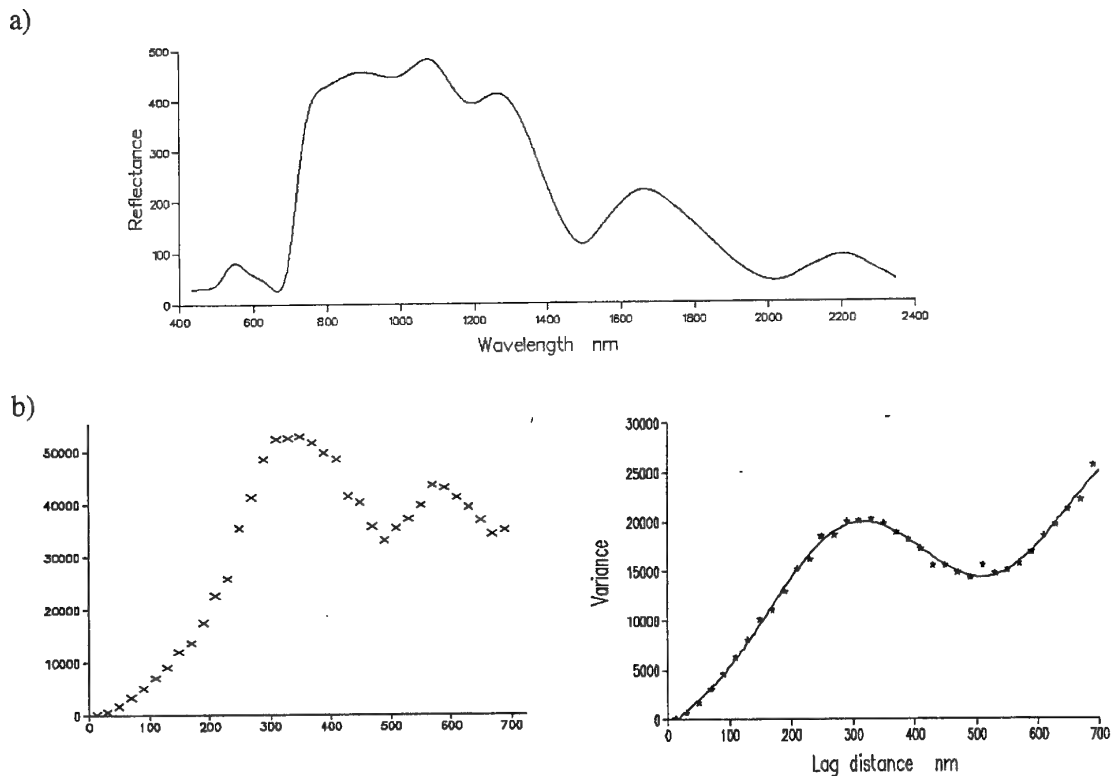


Figure 68. Ft Hood: pixel **250**: a) spectrum, b) experimental variogram of raw values, and c) experimental variogram and fitted model (PPF) of quadratic residuals.

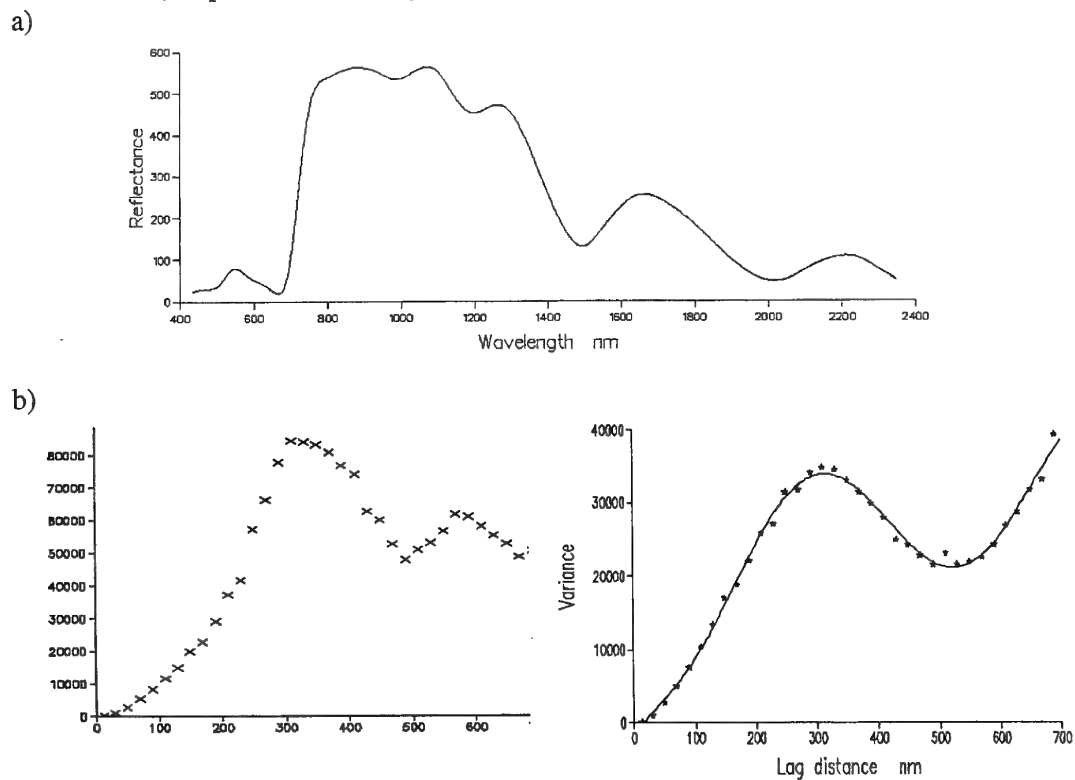


Figure 69. Ft Hood: pixel **255**: a) spectrum, b) experimental variogram of raw values, and c) experimental variogram and fitted model (PPF) of quadratic residuals.

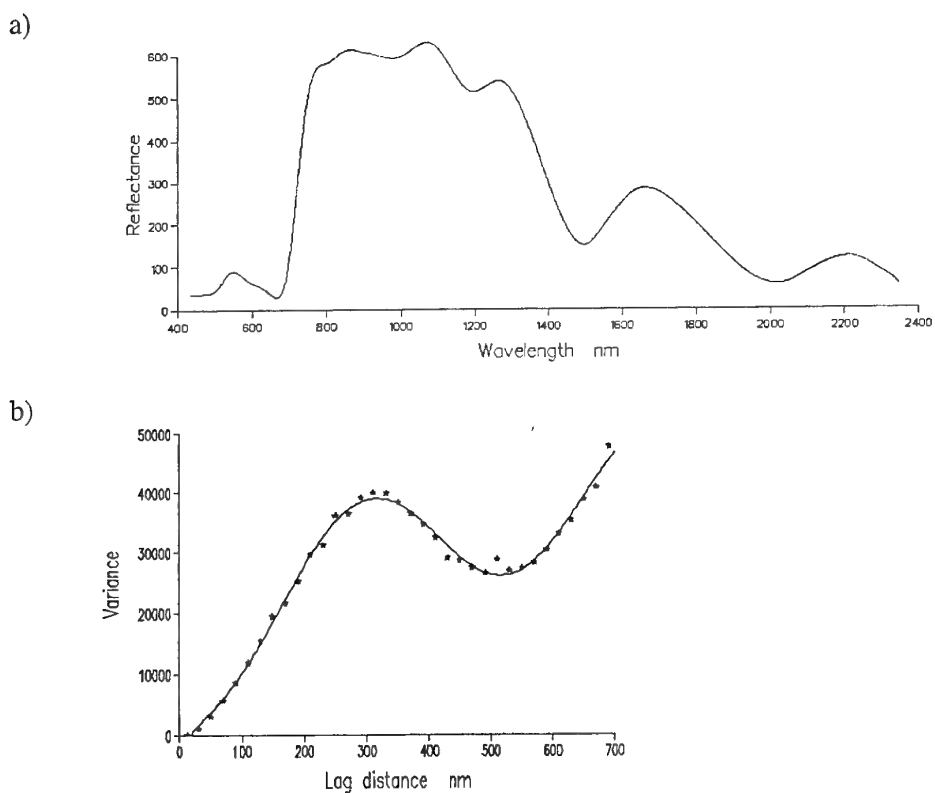


Figure 70. Ft Hood: pixel **257**: a) spectrum, b) experimental variogram of raw values, and c) experimental variogram and fitted model (PPF) of quadratic residuals.

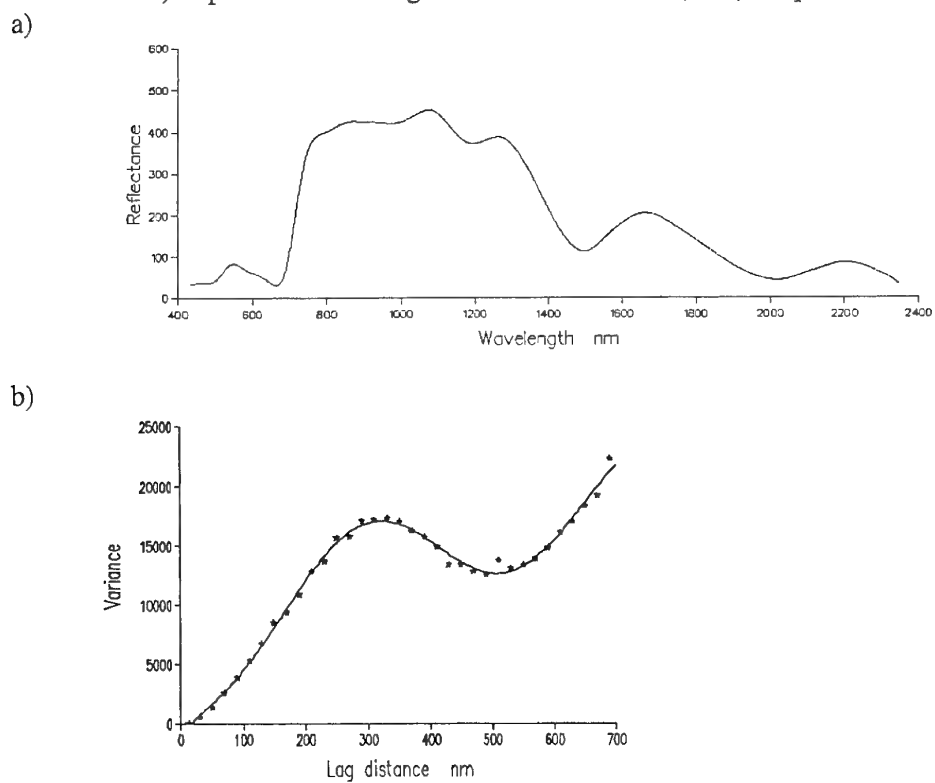


Figure 71. Ft Hood: pixel **260**: a) spectrum, b) experimental variogram and fitted model (PPF) of quadratic residuals.

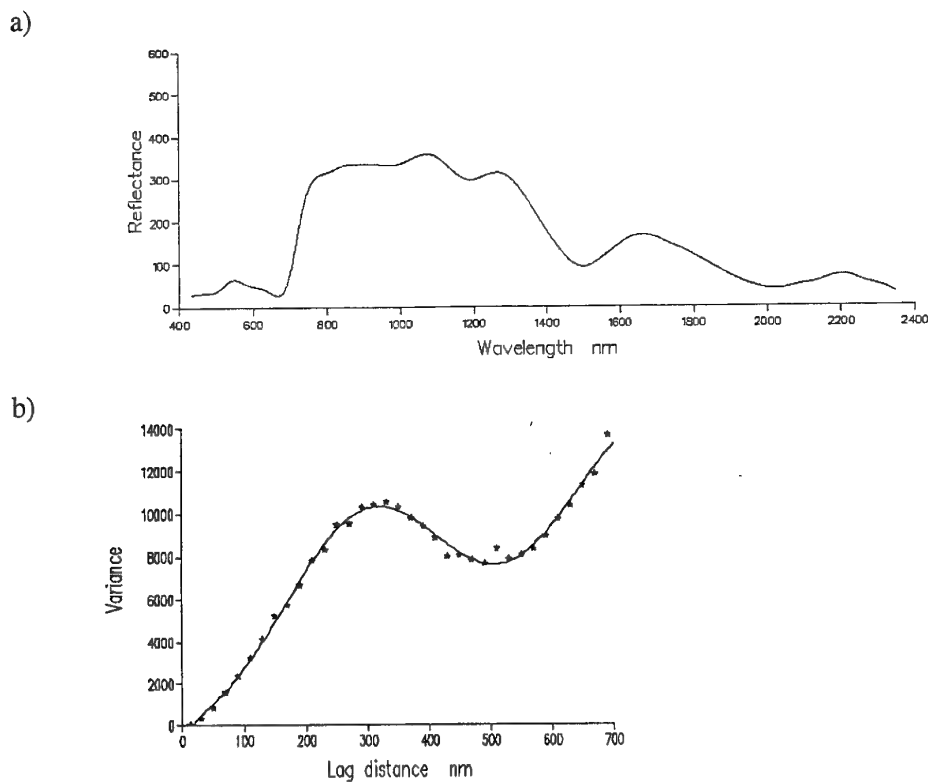


Figure 72. Ft Hood: pixel **261**: a) spectrum, b) experimental variogram and fitted model (PPF) of quadratic residuals.

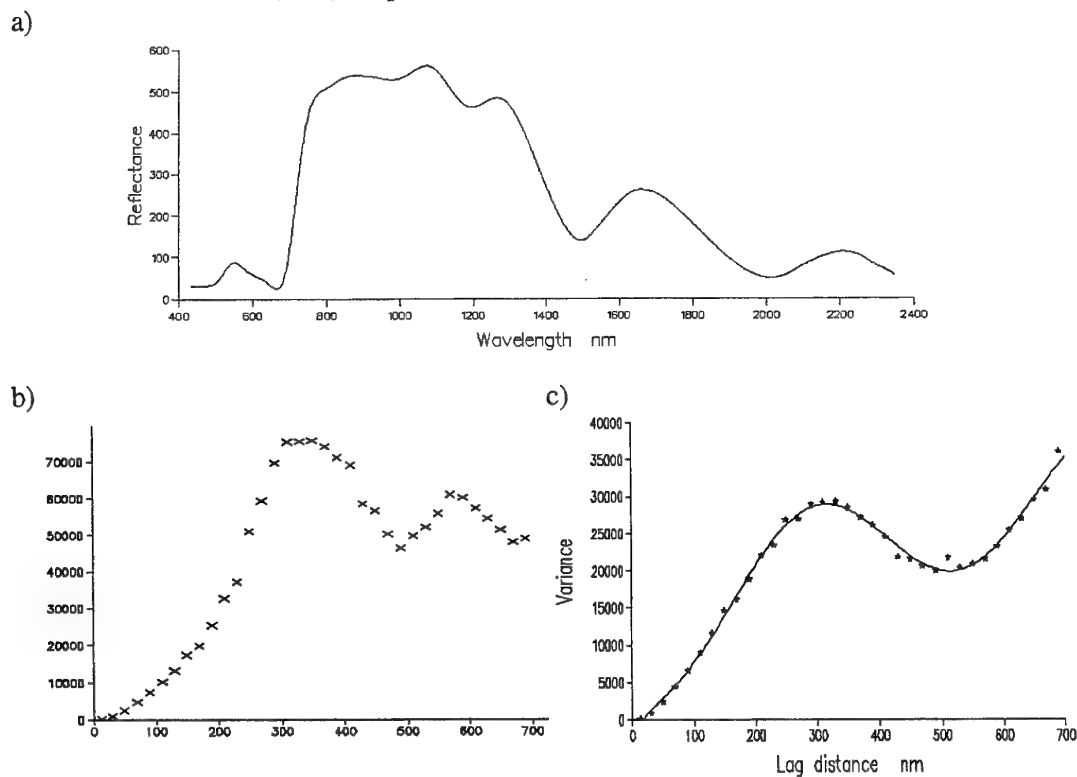
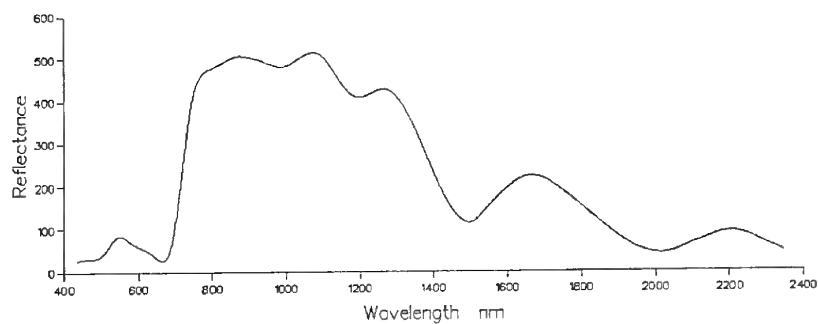


Figure 73. Ft Hood: pixel **266**: a) spectrum, b) experimental variogram of raw values, and c) experimental variogram and fitted model (PPF) of quadratic residuals.

a)



b)

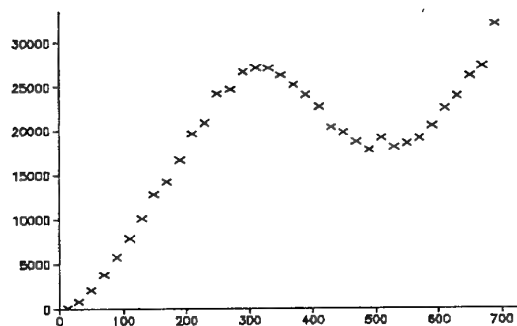
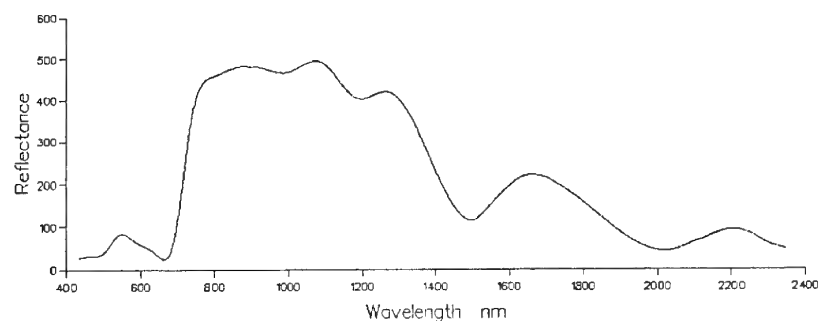


Figure 74. Ft Hood: pixel **268**: a) spectrum, b) experimental variogram of quadratic residuals.

a)



b)

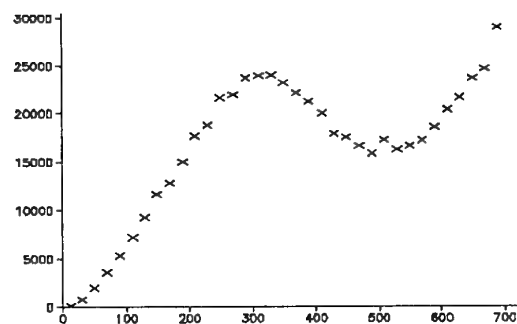


Figure 75. Ft Hood: pixel **269**: a) spectrum, b) experimental variogram of quadratic residuals.

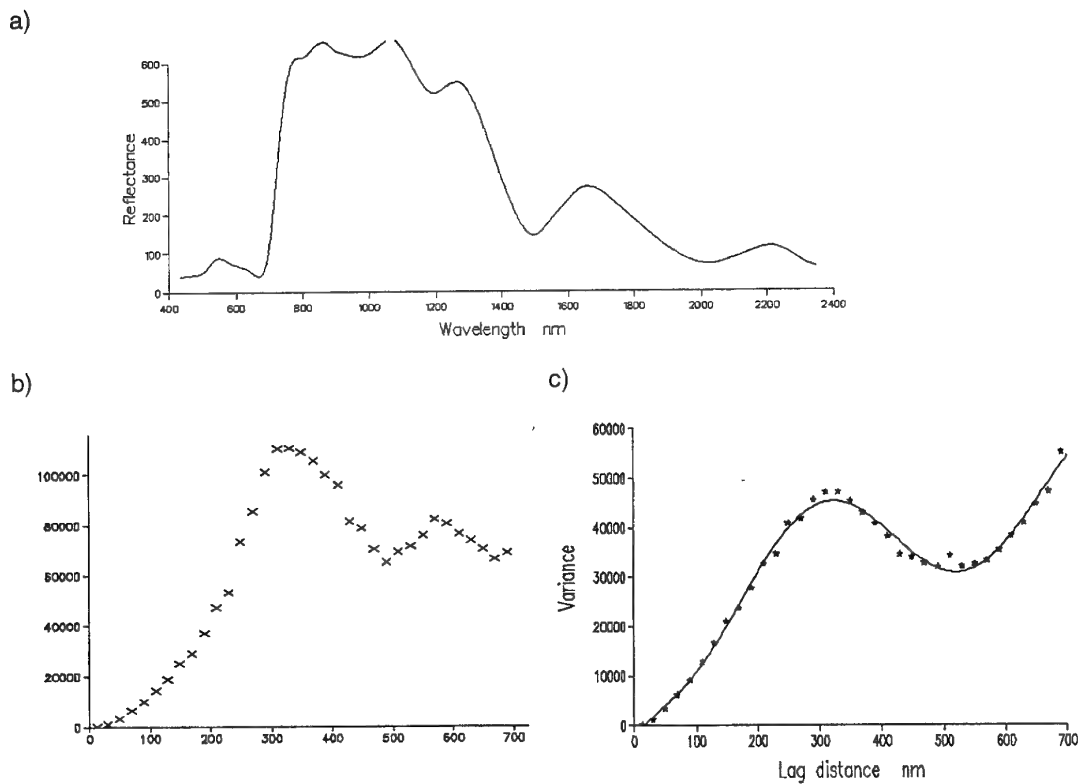


Figure 76. Ft Hood: pixel **272**: a) spectrum, b) experimental variogram of raw values and c) experimental variogram and fitted model (PPF) of quadratic residuals.

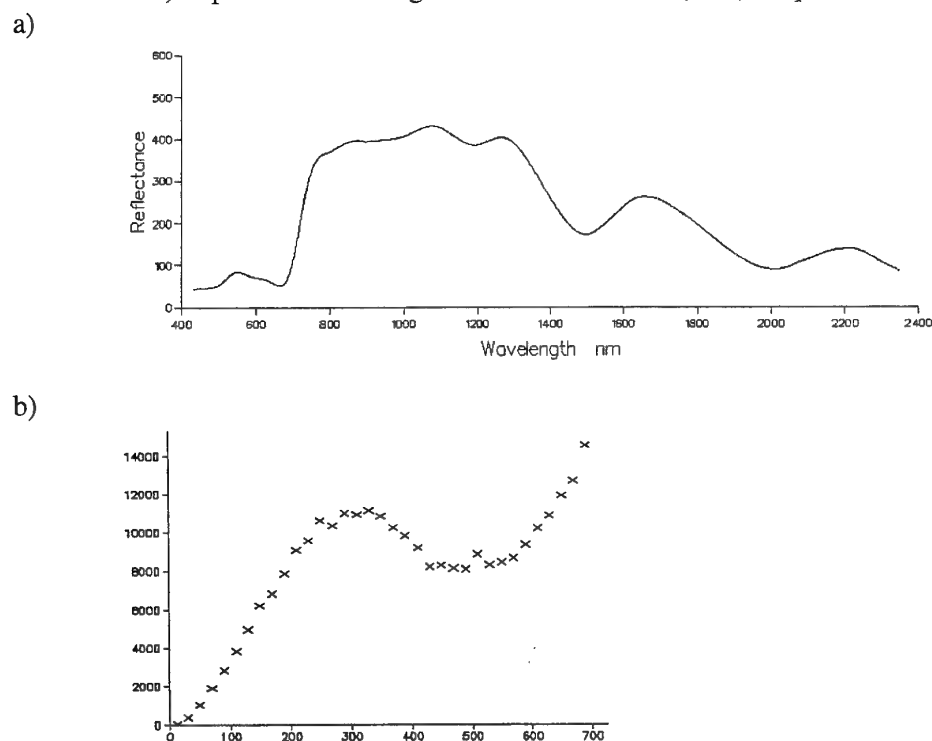


Figure 77. Ft Hood: pixel **273**: a) spectrum, b) experimental variogram of quadratic residuals.

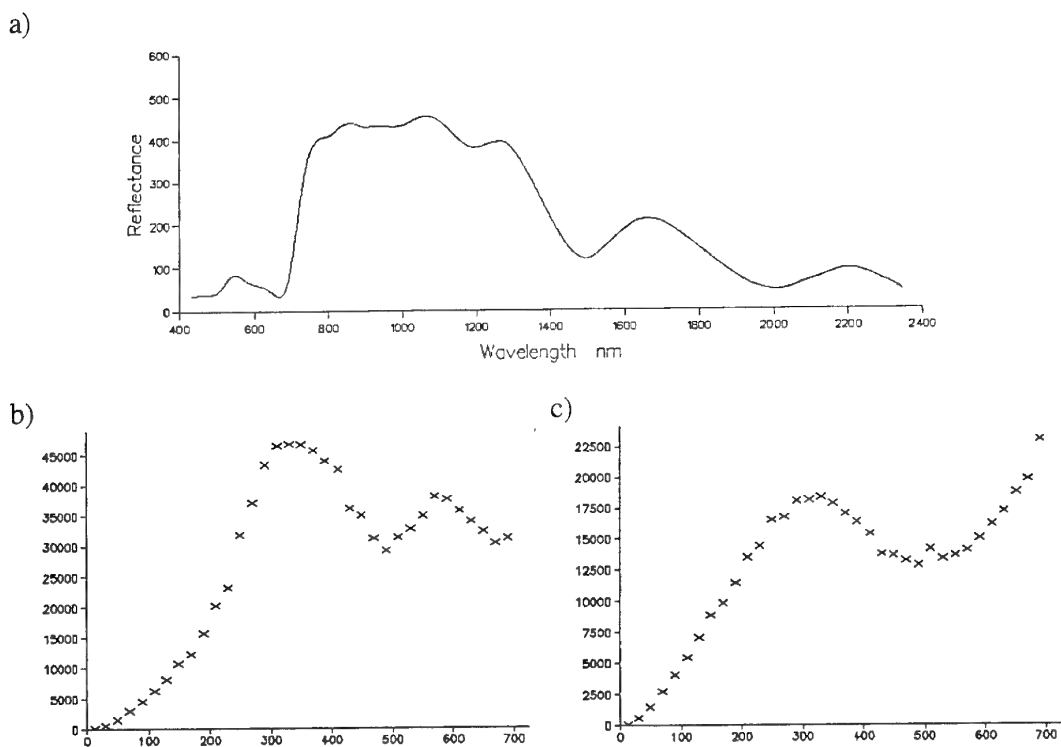


Figure 78. Ft Hood: pixel **278**: a) spectrum, b) experimental variogram of raw values and c) experimental variogram of quadratic residuals.

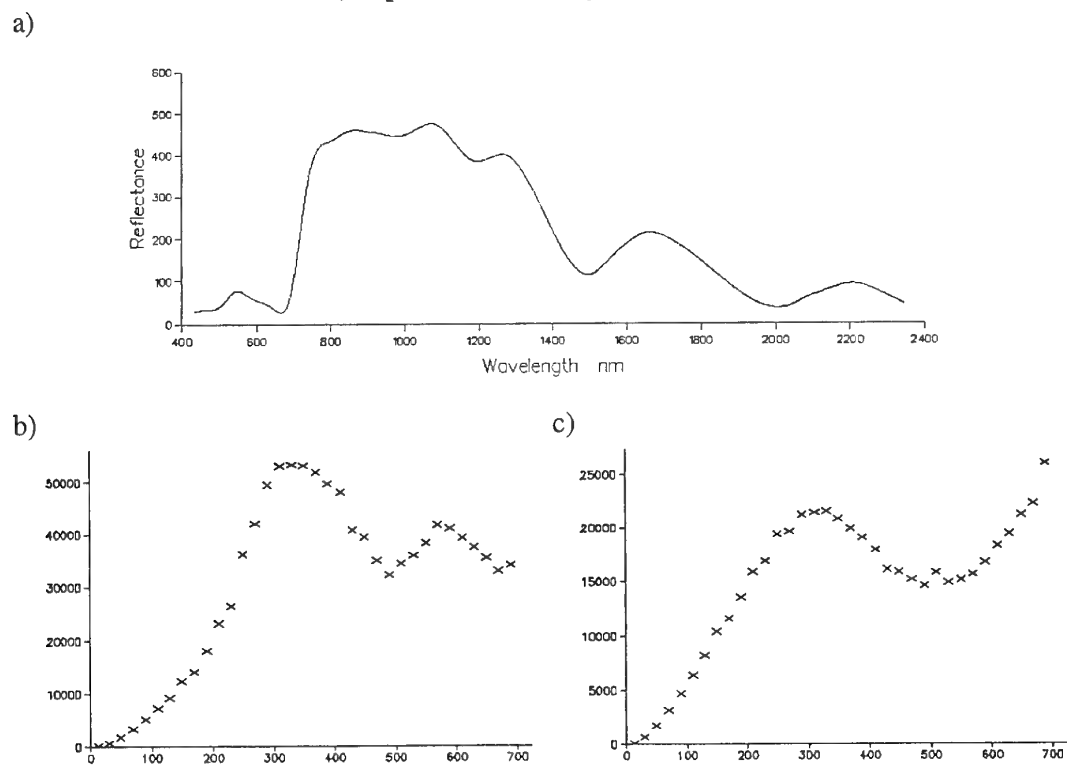


Figure 79. Ft Hood: pixel **282**: a) spectrum, b) experimental variogram of raw values and c) experimental variogram of quadratic residuals.

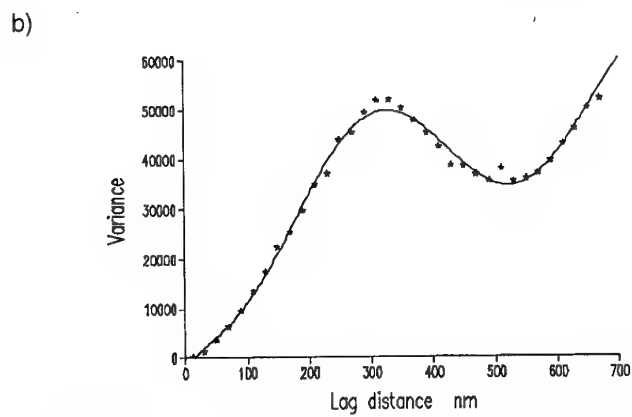
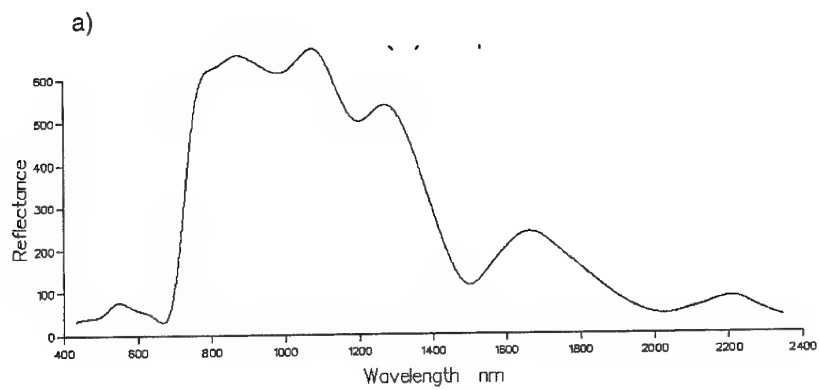
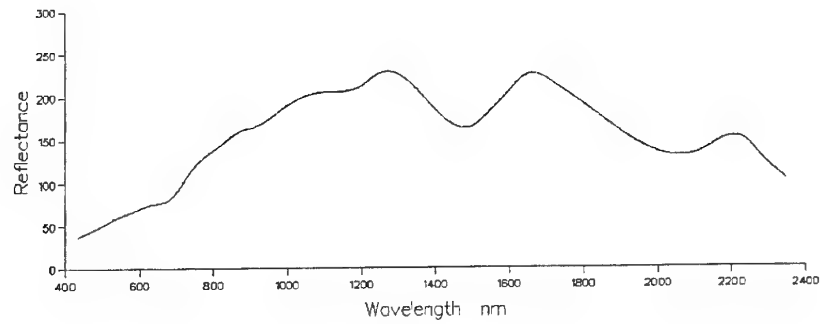
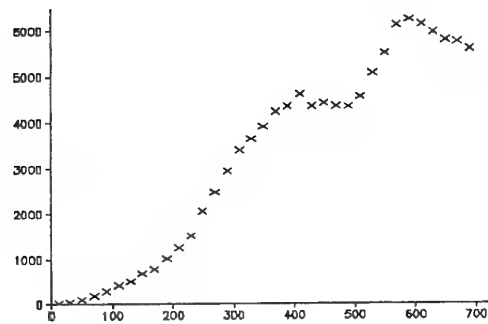


Figure 80. Ft Hood: pixel **284**: a) spectrum, b) experimental variogram and fitted model (PPF) of quadratic residuals

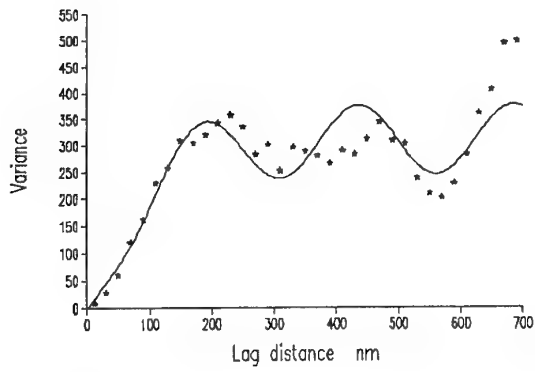
a)



b)



c)



d)

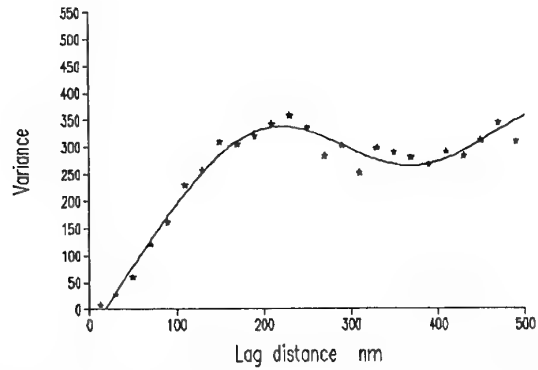


Figure 81. Ft Hood: pixel **288**: a) spectrum, b) experimental variogram of raw values, c) experimental variogram and fitted model (PEF) of quadratic residuals, d) variogram and fitted model (PEF) of quadratic residuals clipped at 500 nm.

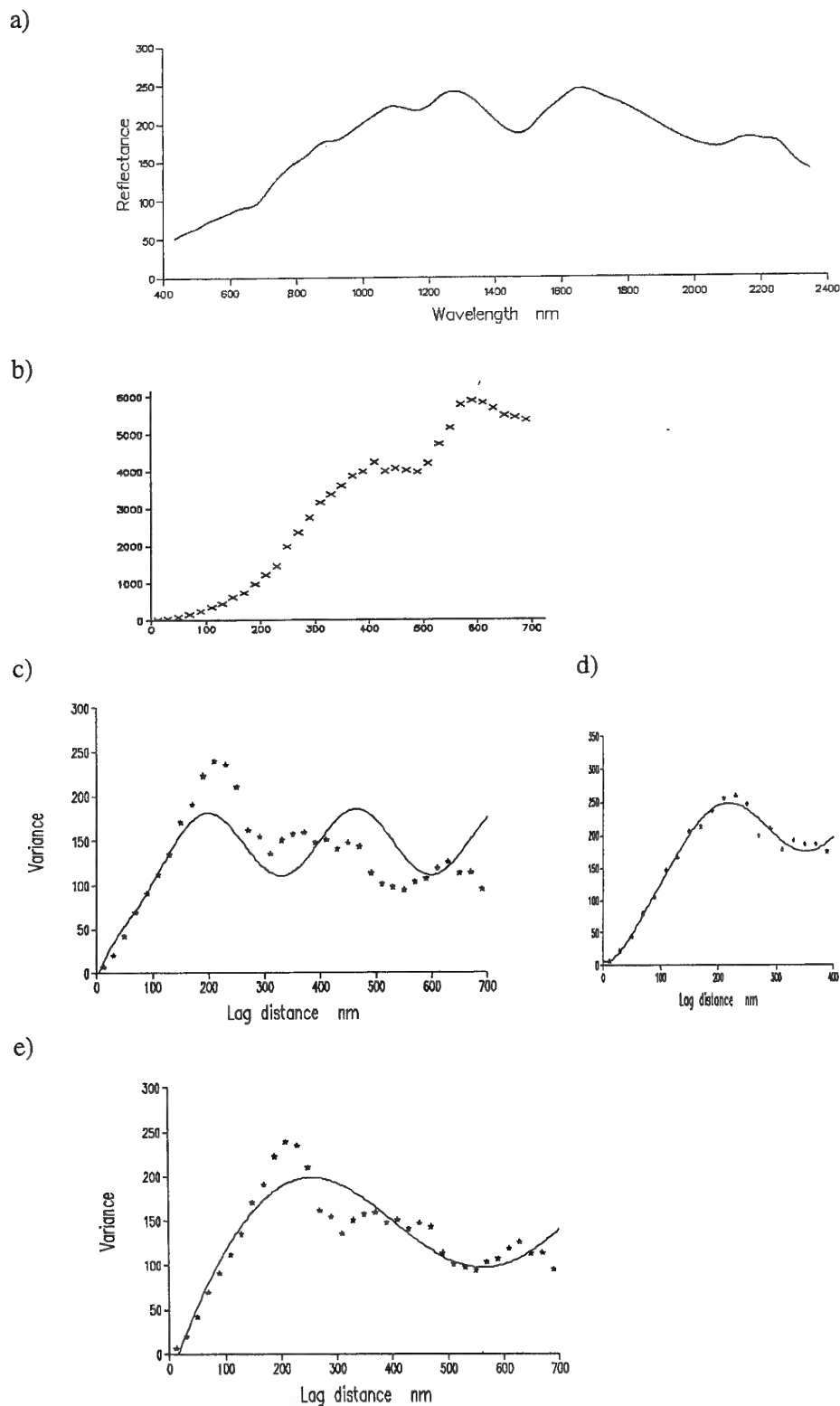
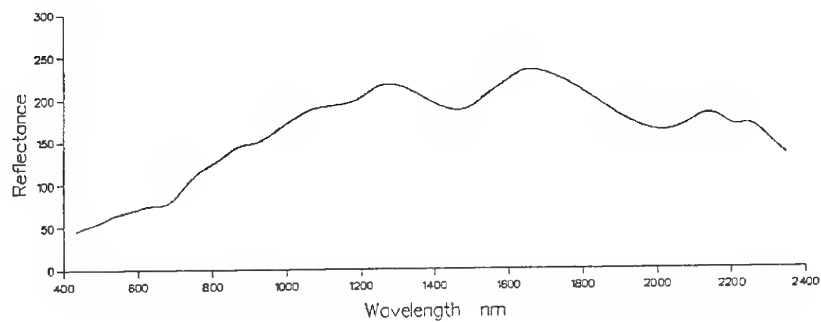
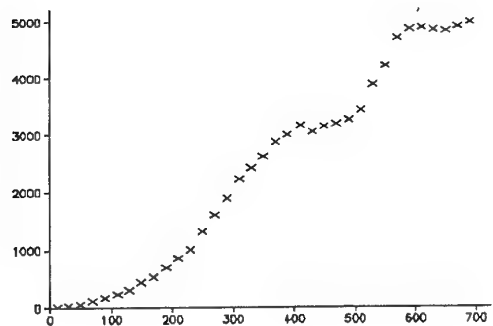


Figure 82. Ft Hood: pixel **300**: a) spectrum, b) experimental variogram of raw values, c) experimental variogram and fitted model (PEF) of quadratic residuals, d) variogram and fitted model (PES) of quadratic residuals clipped at 500 nm, e) variogram and fitted *long wavelength* model (PPF) of quadratic residuals.

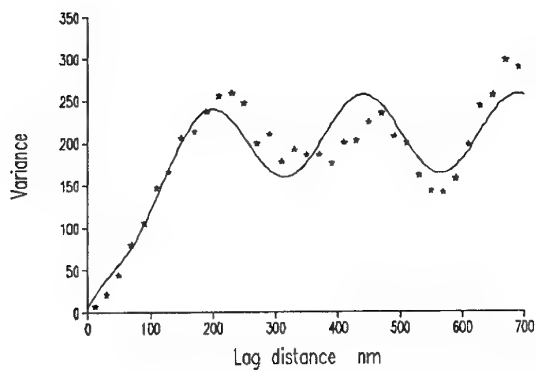
a)



b)



c)



d)

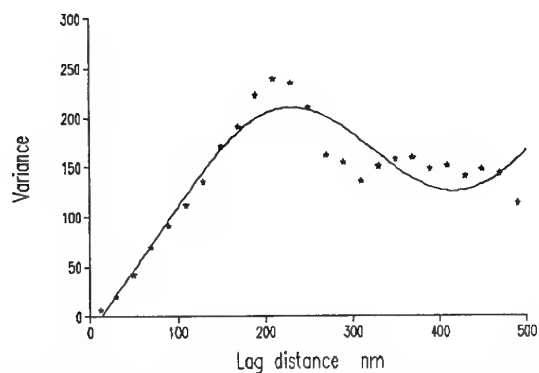


Figure 83. Ft Hood: pixel **317**: a) spectrum, b) experimental variogram of raw values, c) experimental variogram and fitted model (PPF) of quadratic residuals, d) variogram and fitted model (PEF) of quadratic residuals clipped at 500 nm.

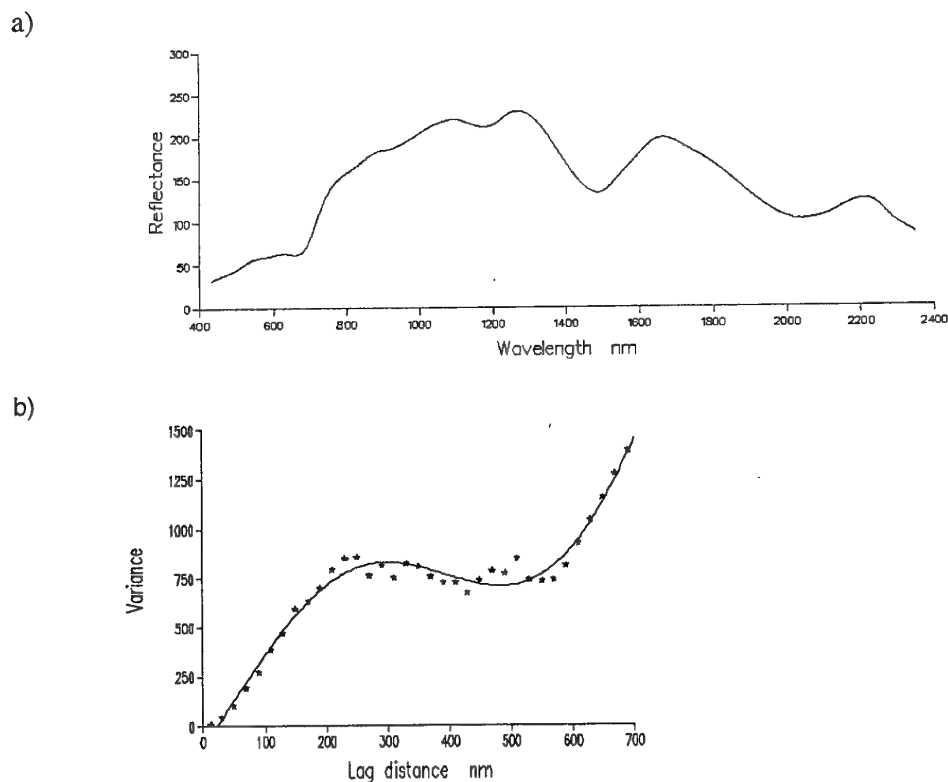


Figure 84. Ft Hood: pixel **323**: a) spectrum, b) experimental variogram and fitted *long wavelength* model (PPF) of quadratic residuals.

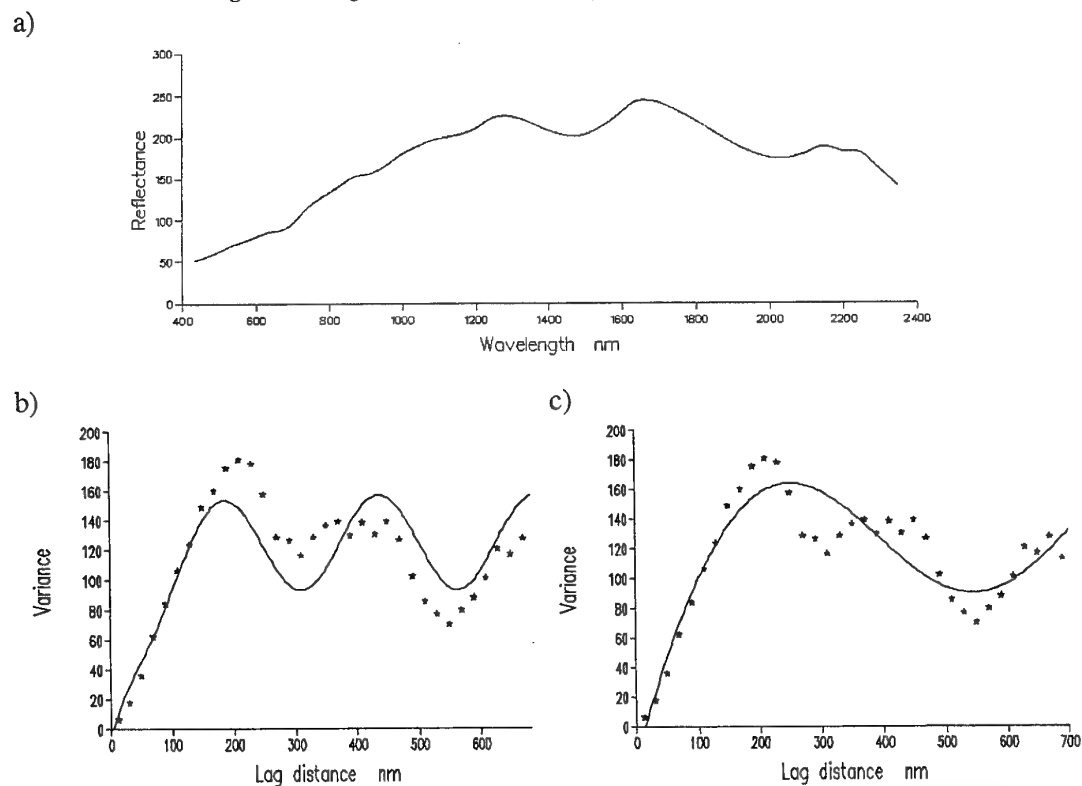


Figure 85. Ft Hood: pixel **327**: a) spectrum, b) experimental variogram and fitted model (PEF) of quadratic residuals, c) as b) fitted to *long wavelength* model (PEF).

Table 4: Summary of trend analysis and model parameters of variograms for selected pixels for Fort Hood

Pixel	% trend removed		Trend	Model Fitted	Model Parameters							
	linear	quadratic	Used	PPF PES PEF	Nugget	Sill	Distance	Gradient	Exponent	Wavelength	Amplitude	Phase
1	6.4	80.6	Q	F	0			129.3	0.4205	527.6	605.6	2.747
25	7.2	81.9	Q	F	0	1808	130.6			473.7	525.1	3.090
71	0.2	53.0	Q	F	0			1194	0.4399	472.4	4881	2.358
77	0.0	55.5	Q	F	0			886.7	0.4514	470.7	3669	2.397
82	0.7	53.0	Q	F	0			821.5	0.4743	469.7	3818	2.323
85	1.4	51.4	Q	F	0			497.4	0.5041	465.5	2637	2.232
90	2.2	51.6	Q	F	0			428.8	0.5000	469.5	2197	2.281
91	3.8	51.4	Q	F	0			193.5	0.5263	467.6	1090	2.238
95	2.5	57.6	Q	F	0			90.74	0.5411	469.7	501.7	2.371
96	1.7	52.4	Q	F	0			375.3	0.4954	470.7	1887	2.288
100	4.1	51.6	Q	F	0			190.8	0.5240	467.1	1057	2.252
104	7.2	51.5	Q	F	0			48.82	0.5615	463.1	305.6	2.254
107	0.2	52.3	Q	F	0			1425	0.4626	471.8	6373	2.331
"			None	F	0			64010	259.6	472.0	14336	1.624
108	3.7	56.3	Q	F	0			82.99	0.5672	467.8	509.4	2.332
111	1.1	53.1	Q	F	0			354.2	0.4997	471.0	1794	2.301
114	5.2	54.7	Q	F	0			58.79	0.5397	466.0	331.5	2.327
120	3.0	56.5	Q	F	0			84.09	0.5860	463.7	569.9	2.269
121	1.6	54.1	Q	F	0			217.7	0.5352	465.1	1227	2.254
124	5.6	52.4	Q	F	0			87.69	0.5184	469.7	468.6	2.312
128	0.3	53.9	Q	F	0			519.1	0.4939	466.9	2621	2.773
131	1.0	67.1	Q	F	0			356.4	0.5052	475.0	1723	2.555
134	2.2	51.1	Q	F	0			535.2	0.4735	471.3	2517	2.281
139	0.4	53.5	Q	F	0			1032	0.4645	469.7	4634	2.323
140	0.0	55.4	Q	F	0			1241	0.4691	476.2	5555	2.381
141	0.0	62.4	Q	F	0			271.5	0.5555	465.9	1621	2.345
142	0.0	58.0	Q	F	0			271.3	0.5439	467.0	1587	2.305
143	6.4	49.8	Q	F	0			73.55	0.5527	465.5	460.1	2.218
157	5.6	54.4	Q	F	0			65.16	0.5997	465.8	461.6	2.228
159	0.1	53.9	Q	F	0			902.2	0.4607	467.0	3934	2.333
160	0.3	53.6	Q	F	0			290.2	0.4886	469.8	1346	2.401
161	3.6	59.0	Q	F	0			40.68	0.5993	447.6	281.5	2.173
162	1.6	53.2	Q	F	0			293.7	0.5126	465.1	1570	2.259
163	87.7	88.4	None	F	0			0.1532	1.0930	385.2	20.38	2.199
"	87.7	88.4	None	F	0			0.1178	1.1400	400.8	24.34	2.12
164	88.7	89.3	Lin	Periodic	0					330.0	39.15	2.654
"	88.7	89.3	None	F	0			0.098	1.1820	367.0	22.86	2.266
167	86.2	87.0	None	F	0			0.1983	1.0660	399.3	22.42	2.141
168	85.4	86.9	None	F	0			0.462	0.9367	422.5	23.77	2.136

F is best fitting model

PPF periodic with power function

PES periodic with stable function

PEF periodic exponential function

Q quadratic detrend

Lin linear detrend

L fitted model with longer wavelength

C fitted model with shorter lag distance

Table 4: Summary of trend analysis and model parameters of variograms for selected pixels for Fort Hood (continued)

Pixel	% trend removed		Trend	Model Fitted		Model Parameters								
	linear	quadratic		Used	PPF	PES	PEF	Nugget	Sill	Distance	Gradient	Exponent	Wavelength	Amplitude
169	86.1	86.9	None	F			0			0.2001	1.0480	400.3	23.16	3.145
171	83.1	83.3	None	F			0			0.2163	1.0080	390.3	21.54	2.264
188	82.0	81.9	None	F			0			0.0923	1.1070	385.4	18.78	2.171
190	81.6	82.1	None	F			0			0.5801	0.8736	400.8	22.47	2.254
193	84.8	84.8	None	F			0			0.0311	1.2780	385.6	18.15	2.113
195	85.5	86.8	None	F			0			0.4117	0.9324	404.8	20.78	2.167
198	82.3	83.8	None	F			0			0.8126	0.7941	412.2	21.71	2.256
204	88.0	89.2	None	F			0			0.1689	1.1010	381.9	19.52	2.192
206	87.3	87.6	None	F			0			0.0761	1.1880	370.7	19.81	2.226
207	84.1	84.2	None	F			0			0.1049	1.0910	387.0	19.93	2.181
"	84.1	84.2	None	F			0			0.0193	1.3890	429.3	26.52	1.985
213	82.5	83.0	None	F			0			0.2171	0.9736	410.8	18.96	2.166
214	87.9	88.8	None	F			0			0.1531	1.1420	367.1	21.61	2.315
230	60.4	97.0	Q		F		0	409.8	52.89			734.6	150.7	1.855
234	61.5	96.7	Q		F		0	449.7	58.03			669.5	138.4	2.063
"	61.5	96.7	None		F		0	12719	348.30			373.9	1775	1.637
242	60.8	97.7	Q		F		0	336.6	39.34			411.5	65.93	1.643
"	60.8	97.7	Q	F			0			37.07	0.4111	106.1	54.13	1.892
"	60.8	97.7	None			F	0	15395	423.00		1.1020	367.2	1733	1.169
"	60.8	97.7	None		F		0	7804	126.90			476.3	2860	1.649
250	0.0	54.5	Q	F			0			1228	0.4397	472.7	4823	2.409
255	0.0	51.7	Q	F			0			2919	0.3735	483.5	9268	2.464
257	0.0	52.6	Q	F			0			2814	0.4079	477.8	10054	2.433
260	0.2	54.6	Q	F			0			956.1	0.4575	471.2	3993	2.383
261	0.1	55.3	Q	F			0			578.8	0.4572	470.0	2420	2.398
266	0.0	54.1	Q	F			0			1984	0.4187	476.3	7277	2.436
272	0.2	50.2	Q	F			0			2885	0.4289	475.1	11555	2.326
274	0.0	57.6	Q	F			0			1315	0.4071	480.5	4497	2.555
284	1.2	48.4	Q	F			0			2848	0.4475	472.8	12487	2.268
288	29.0	93.0	Q		F		0	311.3	83.19			250.1	65.78	1.640
"	29.0	93.0	Q		F		0	325.0	100.30			349.2	52.31	2.712
"	29.0	93.0	Q	F			0			0.132	1.2890	759.6	198.5	1.647
300	40.8	95.9	Q		F		0	210.3	78.43			248.5	46.78	1.436
"	40.8	95.9	Q			F	0	213.0	81.98		1.578	274.4	37.62	1.373
"	40.8	95.9	Q	F			0			0.9401	0.9040	724.8	108.8	1.749
317	52.3	96.9	Q		F		0	148.1	53.86			269.1	37	1.748
"	52.3	96.9	Q	F			0			24.68	0.3342	429.2	60.6	3.122
"	52.3	96.9	Q		F		0	164.4	139.40			697.1	64.28	1.962
323	57.2	84.7	Q	F			0			0.037	1.6480	776.1	491.8	1.757

F is best fitting model

PPF periodic with power function

PES periodic with stable function

PEF periodic exponential function

L fitted model with longer wavelength

C fitted model with shorter lag distance

Q quadratic detrend
Lin linear detrend

Table 4: Summary of trend analysis and model parameters of variograms for selected pixels for Fort Hood (continued)

Pixel	% trend removed		Trend	Model Fitted			Model Parameters					
	linear	quadratic		PPF	PES	PEF	Nugget	Sill	Distance	Gradient Exponent	Wavelength	Amplitude Phase
326	55.5	97.2	Q	F			0	147.5	59.83		271.6	31.56 1.782
"	55.5	97.2	Q	F			0	199.0	104.60		272.2	37.52 1.604 C
"	55.5	97.2	Q	F			0	164.8	158.80		758.3	65.12 1.900 L
327	52.6	97.3	Q	F			0	125.5	52.21		253.5	31.74 1.755
"	52.6	97.3	Q	F			0	140.3	130.10		673.4	47.6 1.972 L
329	30.9	93.8	Q	F			0	282.7	75.50		250.8	65.93 1.650

F is best fitting model

PPF periodic with power function

PES periodic with stable function

PEF periodic exponential function

Q quadratic detrend

Lin linear detrend

L fitted model with longer wavelength

C fitted model with shorter lag distance

Table 5. Eigenvalues and eigenvectors for Fort Hood using all spectra

Component Eigenvalue	PC1 96.69	PC2 32.33	PC3 2.42			
Percentage variance	73.25	24.41	1.84			
Waveband				Waveband	Waveband	Waveband
v1	-0.0913	0.0660	0.1349	v21	-0.0996	0.0240
v10	-0.0945	0.0578	0.1042	v22	-0.1001	0.0130
v100	-0.0976	-0.0307	-0.1408	v23	-0.1002	0.0044
v101	-0.0971	0.0504	-0.0080	v24	-0.1002	0.0002
v102	-0.0977	0.0468	0.0026	v25	-0.1002	-0.0036
v103	-0.0980	0.0450	0.0084	v26	-0.1002	-0.0046
v104	-0.0981	0.0444	0.0066	v27	-0.1002	-0.0049
v105	-0.0983	0.0433	0.0052	v28	-0.1006	0.0008
v106	-0.0986	0.0409	0.0053	v29	-0.1007	0.0092
v107	-0.0988	0.0399	0.0018	v3	-0.0932	0.0606
v108	-0.0991	0.0378	0.0004	v30	-0.1006	0.0133
v109	-0.0993	0.0360	-0.0050	v31	-0.1004	0.0187
v11	-0.0950	0.0553	0.1021	v32	-0.1002	0.0217
v110	-0.0995	0.0345	-0.0131	v33	-0.1001	0.0227
v111	-0.0997	0.0330	-0.0214	v34	-0.1000	0.0244
v112	-0.0998	0.0320	-0.0269	v35	-0.0998	0.0275
v113	-0.0998	0.0309	-0.0326	v36	-0.0995	0.0303
v114	-0.0998	0.0309	-0.0381	v37	-0.0995	0.0312
v115	-0.0998	0.0305	-0.0438	v38	-0.0994	0.0320
v116	-0.0997	0.0295	-0.0503	v39	-0.0991	0.0352
v117	-0.0997	0.0289	-0.0537	v4	-0.0929	0.0615
v118	-0.0998	0.0283	-0.0562	v40	-0.0987	0.0375
v119	-0.0998	0.0286	-0.0531	v41	-0.0983	0.0399
v12	-0.0951	0.0556	0.1003	v42	-0.0980	0.0420
v120	-0.0998	0.0294	-0.0464	v43	-0.0980	0.0418
v121	-0.0999	0.0300	-0.0348	v44	-0.0991	0.0342
v122	-0.0999	0.0304	-0.0259	v45	-0.1011	0.0111
v123	-0.0999	0.0303	-0.0200	v46	-0.0982	-0.0383
v124	-0.0999	0.0300	-0.0188	v47	-0.0843	-0.0916
v125	-0.0997	0.0315	-0.0280	v48	-0.0579	-0.1399
v126	-0.0995	0.0331	-0.0343	v49	-0.0402	-0.1586
				PC3	PC2	PC1
				0.0866	0.0240	-0.0996
				0.0881	0.0130	-0.1001
				0.0875	0.0044	-0.1002
				0.0842	0.0002	-0.1002
				0.0875	-0.0036	-0.1002
				0.0839	-0.0046	-0.1002
				0.0759	-0.0049	-0.1002
				0.0760	0.0008	-0.1006
				0.0687	0.0092	-0.1007
				0.1224	0.0606	-0.0932
				0.0670	0.0133	-0.1006
				0.0630	0.0187	-0.1004
				0.0589	0.0217	-0.1002
				0.0578	0.0227	-0.1001
				0.0540	0.0244	-0.1000
				0.0476	0.0275	-0.0998
				0.0445	0.0303	-0.0995
				0.0408	0.0312	-0.0995
				0.0369	0.0320	-0.0994
				0.0321	0.0352	-0.0991
				0.1235	0.0615	-0.0929
				0.0317	0.0375	-0.0987
				0.0317	0.0399	-0.0983
				0.0304	0.0420	-0.0980
				0.0272	0.0418	-0.0980
				0.0154	0.0342	-0.0991
				0.0267	0.0111	-0.1011
				0.0233	-0.0383	-0.0982
				0.0331	-0.0916	-0.0843
				0.0878	-0.1399	-0.0579
				0.1038	-0.1586	-0.0402
				PC3	PC2	PC1
				0.0875	-0.1688	-0.0251
				0.0334	-0.1676	-0.0305
				0.0322	-0.1677	-0.0304
				0.0333	-0.1680	-0.0298
				0.0307	-0.1684	-0.0291
				0.0292	-0.1685	-0.0290
				0.0252	-0.1686	-0.0287
				0.1089	0.0590	-0.0940
				0.0241	-0.1680	-0.0299
				-0.0273	-0.1488	-0.0541
				-0.0325	-0.1475	-0.0552
				-0.0371	-0.1468	-0.0557
				-0.0450	-0.1481	-0.0544
				-0.0533	-0.1494	-0.0529
				-0.0597	-0.1502	-0.0519
				-0.0538	-0.1502	-0.0520
				-0.0614	-0.1494	-0.0523
				-0.0752	-0.1475	-0.0537
				0.1165	0.0552	-0.0947
				-0.0717	0.0008	-0.1007
				-0.0967	-0.0059	-0.1004
				-0.1117	-0.0124	-0.0998
				-0.1194	-0.0190	-0.0993
				-0.1267	-0.0254	-0.0986
				-0.1338	-0.0316	-0.0978
				-0.1383	-0.0376	-0.0969
				-0.1488	-0.0417	-0.0959
				-0.1551	-0.0464	-0.0949
				-0.1591	-0.0493	-0.0942
				0.1016	0.0592	-0.0942
				-0.1670	-0.0517	-0.0934

Table 5. Continued.

Waveband	PC1	PC2	PC3	Waveband	PC1	PC2	PC3	Waveband	PC1	PC2	PC3
v127	-0.0995	0.0334	-0.0321	v5	-0.0935	0.0601	0.1164	v91	-0.0924	-0.0545	-0.1765
v128	-0.0992	0.0357	-0.0297	v50	-0.0316	-0.1646	0.1092	v92	-0.0922	-0.0546	-0.1800
v129	-0.0990	0.0373	-0.0292	v51	-0.0282	-0.1661	0.1162	v93	-0.0923	-0.0542	-0.1793
v13	-0.0950	0.0564	0.0941	v52	-0.0270	-0.1664	0.1208	v94	-0.0929	-0.0525	-0.1747
v130	-0.0986	0.0400	-0.0255	v53	-0.0264	-0.1672	0.1126	v95	-0.0935	-0.0499	-0.1707
v131	-0.0979	0.0443	-0.0320	v54	-0.0261	-0.1675	0.1085	v96	-0.0943	-0.0465	-0.1670
v132	-0.0979	0.0439	-0.0289	v55	-0.0257	-0.1679	0.1036	v97	-0.0951	-0.0424	-0.1629
v14	-0.0954	0.0551	0.0917	v56	-0.0261	-0.1674	0.1108	v98	-0.0962	-0.0388	-0.1495
v15	-0.0957	0.0539	0.0888	v57	-0.0258	-0.1676	0.1082	v99	-0.0969	-0.0352	-0.1441
v16	-0.0960	0.0527	0.0849	v58	-0.0251	-0.1686	0.0947				
v17	-0.0963	0.0516	0.0805	v59	-0.0247	-0.1689	0.0914				
v18	-0.0970	0.0473	0.0856	v6	-0.0941	0.0578	0.1154				
v19	-0.0980	0.0412	0.0810	v60	-0.0245	-0.1691	0.0876				
v2	-0.0914	0.0666	0.1298	v61	-0.0240	-0.1698	0.0753				
v20	-0.0987	0.0349	0.0809	v62	-0.0243	-0.1696	0.0766				

Table 6. Classes from the non-hierarchical classification of Fort Hood spectra using 66 wavebands and the first three principal components

Site No	g5-66	g5-pca	g6-66	g6-pca	g7-pca	Site No	g5-66	g5-pca	g6-66	g6-pca	g7-pca	Site No	g5-66	g5-pca	g6-66	g6-pca	g7-pca
1	2	2	1	2	2	111	4	5	4	5	5	221	5	2	6	6	6
2	2	2	1	2	2	112	4	4	4	4	4	222	5	2	6	6	6
3	2	2	1	2	2	113	3	4	4	4	4	223	5	2	6	6	6
4	2	2	1	2	2	114	5	5	5	5	5	224	5	2	6	6	6
5	2	2	1	2	2	115	4	5	5	5	5	225	5	2	6	6	6
6	2	2	1	2	2	116	4	4	4	4	4	226	5	2	6	6	6
7	2	2	1	2	2	117	3	4	4	4	4	227	5	2	6	6	6
8	2	2	1	2	2	118	4	4	4	4	4	228	5	2	6	6	6
9	2	2	1	2	2	119	4	5	5	5	5	229	1	1	2	1	7
10	2	2	1	2	2	120	4	5	5	5	5	230	1	1	2	1	7
11	2	2	1	2	2	121	4	5	5	5	5	231	1	1	2	1	7
12	2	2	1	2	2	122	3	4	4	4	4	232	1	1	2	1	7
13	2	2	1	2	2	123	3	4	4	4	4	233	1	1	2	1	7
14	2	2	1	2	2	124	5	5	5	5	5	234	1	1	2	1	7
15	2	2	1	2	2	125	4	4	4	4	4	235	1	1	2	1	7
16	2	2	1	2	2	126	4	4	4	4	4	236	1	1	2	1	7
17	2	2	1	2	2	127	3	4	4	4	4	237	1	1	2	1	7
18	2	2	1	2	2	128	4	4	4	4	4	238	1	1	2	1	7
19	2	2	1	2	2	129	4	4	4	4	4	239	1	1	2	1	7
20	2	2	1	2	2	130	3	4	4	4	4	240	1	1	2	1	7
21	2	2	1	2	2	131	3	4	4	4	4	241	1	1	2	1	7
22	2	2	1	2	2	132	3	3	3	3	3	242	1	1	2	1	7
23	2	2	1	2	2	133	3	3	3	3	3	243	1	1	2	1	7
24	2	2	1	2	2	134	4	4	4	4	4	244	1	1	2	1	7
25	2	2	1	2	2	135	4	5	4	5	5	245	1	1	2	1	7
26	2	2	1	2	2	136	4	4	4	4	4	246	1	1	2	1	7
27	2	2	1	2	2	137	4	5	5	5	5	247	1	1	2	1	7
28	2	2	1	2	2	138	4	4	4	4	4	248	1	1	2	1	7
29	2	2	1	2	2	139	3	4	4	4	4	249	1	1	2	1	7
30	2	2	1	2	2	140	3	3	3	3	3	250	3	3	3	3	3
31	2	2	1	2	2	141	4	4	4	4	4	251	3	3	3	3	3
32	2	2	1	2	2	142	4	4	4	4	4	252	3	3	3	3	3
33	2	2	1	2	2	143	5	5	5	5	5	253	3	3	3	3	3
34	2	2	1	2	2	144	4	5	5	5	5	254	3	3	3	3	3
35	2	2	1	2	2	145	4	5	5	5	5	255	3	3	3	3	3
36	2	2	1	2	2	146	4	5	4	5	5	256	3	3	3	3	3
37	2	2	1	2	2	147	4	4	4	4	4	257	3	3	3	3	3
38	2	2	1	2	2	148	4	4	4	4	4	258	3	3	3	3	3
39	2	2	1	2	2	149	4	5	5	5	5	259	3	3	3	3	3
40	2	2	1	2	2	150	4	5	5	5	5	260	3	3	3	3	3
41	2	2	1	2	2	151	4	4	4	4	4	261	4	4	4	4	4
42	2	2	1	2	2	152	4	4	4	4	4	262	3	3	3	3	3
43	2	2	1	2	2	153	4	5	5	5	5	263	3	3	3	3	3
44	2	2	1	2	2	154	4	5	5	5	5	264	3	3	3	3	3

Table 6. Continued.

Site No	g5-66	g5-pca	g6-66	g6-pca	g7-pca	Site No	g5-66	g5-pca	g6-66	g6-pca	g7-pca	Site No	g5-66	g5-pca	g6-66	g6-pca	g7-pca	g5-66	g5-pca	g6-66	g6-pca	g7-pca
45	2	2	1	2	2	155	4	5	5	5	5	265	3	3	3	3	3	3	3	3	3	3
46	2	2	1	2	2	156	4	4	4	4	4	266	3	3	3	3	3	3	3	3	3	3
47	2	2	1	2	2	157	4	5	5	5	5	267	3	3	3	3	3	3	3	3	3	3
48	2	2	1	2	2	158	4	4	4	4	4	268	3	3	3	3	3	3	3	3	3	3
49	2	2	1	2	2	159	3	4	4	4	4	269	3	3	3	3	3	3	3	3	3	3
50	2	2	1	2	2	160	4	5	5	5	5	270	3	3	3	3	3	3	3	3	3	3
51	2	2	1	2	2	161	5	5	5	5	5	271	3	3	3	3	3	3	3	3	3	3
52	2	2	1	2	2	162	4	5	5	5	5	272	3	3	3	3	3	3	3	3	3	3
53	2	2	1	2	2	163	5	2	2	6	6	273	3	3	3	3	3	3	3	3	3	3
54	2	2	1	2	2	164	5	2	2	6	6	274	3	3	3	3	3	3	3	3	3	3
55	2	2	1	2	2	165	5	2	2	6	6	275	3	3	3	3	3	3	3	3	3	3
56	2	2	1	2	2	166	5	2	2	6	6	276	3	3	3	3	3	3	3	3	3	3
57	2	2	1	2	2	167	5	2	2	6	6	277	3	3	3	3	3	3	3	3	3	3
58	2	2	1	2	2	168	5	2	2	6	6	278	3	3	3	3	3	3	3	3	3	3
59	2	2	1	2	2	169	5	2	2	6	6	279	3	3	3	3	3	3	3	3	3	3
60	2	2	1	2	2	170	5	2	2	6	6	280	3	3	3	3	3	3	3	3	3	3
61	2	2	1	2	2	171	5	2	2	6	6	281	3	3	3	3	3	3	3	3	3	3
62	2	2	1	2	2	172	5	2	2	6	6	282	3	3	3	3	3	3	3	3	3	3
63	2	2	1	2	2	173	5	2	2	6	6	283	3	3	3	3	3	3	3	3	3	3
64	2	2	1	2	2	174	5	2	2	6	6	284	3	3	3	3	3	3	3	3	3	3
65	2	2	1	2	2	175	5	2	2	6	6	285	3	3	3	3	3	3	3	3	3	3
66	2	2	1	2	2	176	5	2	2	6	6	286	3	3	3	3	3	3	3	3	3	3
67	2	2	1	2	2	177	5	2	2	6	6	287	3	3	3	3	3	3	3	3	3	3
68	2	2	1	2	2	178	5	2	2	6	6	288	2	2	1	2	2	2	2	2	2	2
69	2	2	1	2	2	179	5	2	2	6	6	289	2	2	1	2	2	2	2	2	2	2
70	2	2	1	2	2	180	5	2	2	6	6	290	2	2	1	2	2	2	2	2	2	2
71	3	4	3	4	4	181	5	2	2	6	6	291	2	2	1	2	2	2	2	2	2	2
72	4	4	4	4	4	182	5	2	2	6	6	292	2	2	1	2	2	2	2	2	2	2
73	4	4	4	4	4	183	5	2	2	6	6	293	2	2	1	2	2	2	2	2	2	2
74	4	4	4	4	4	184	5	2	2	6	6	294	2	2	1	2	2	2	2	2	2	2
75	4	4	4	4	4	185	5	2	2	6	6	295	2	2	1	2	2	2	2	2	2	2
76	3	3	3	3	3	186	5	2	2	6	6	296	2	2	1	2	2	2	2	2	2	2
77	3	4	4	4	4	187	5	2	2	6	6	297	2	2	1	2	2	2	2	2	2	2
78	3	4	4	4	4	188	5	2	2	6	6	298	2	2	1	2	2	2	2	2	2	2
79	3	4	4	4	4	189	5	2	2	6	6	299	2	2	1	2	2	2	2	2	2	2
80	4	4	4	4	4	190	5	2	2	6	6	300	2	2	1	2	2	2	2	2	2	2
81	3	4	4	4	4	191	5	2	2	6	6	301	2	2	1	2	2	2	2	2	2	2
82	3	4	4	4	4	192	5	2	2	6	6	302	2	2	1	2	2	2	2	2	2	2
83	4	4	4	4	4	193	5	2	2	6	6	303	2	2	1	2	2	2	2	2	2	2
84	4	4	4	4	4	194	5	2	2	6	6	304	2	2	1	2	2	2	2	2	2	2
85	4	4	4	4	4	195	5	2	2	6	6	305	2	2	1	2	2	2	2	2	2	2
86	4	5	5	5	5	196	5	2	2	6	6	306	2	2	1	2	2	2	2	2	2	2
87	4	5	5	5	5	197	5	2	2	6	6	307	2	2	1	2	2	2	2	2	2	2
88	4	4	4	4	4	198	5	2	2	6	6	308	2	2	1	2	2	2	2	2	2	2

Table 6. Continued.

Site No	g5-66	g5-pca	g6-66	g6-pca	g7-pca	Site No	g5-66	g5-pca	g6-66	g6-pca	g7-pca	Site No	g5-66	g5-pca	g6-66	g6-pca	g7-pca	g5-66	g5-pca	g6-66	g6-pca	g7-pca
89	3	4	4	4	4	199	5	2	6	6	6	309	2	2	1	2	1	1	2	2	2	1
90	4	5	4	5	5	200	5	2	6	6	6	310	2	2	1	2	1	1	2	2	2	1
91	4	5	5	5	5	201	5	2	6	6	6	311	2	2	1	2	1	1	2	2	2	1
92	4	5	5	5	5	202	5	2	6	6	6	312	2	2	1	2	1	1	2	2	2	1
93	4	5	5	5	5	203	5	2	6	6	6	313	2	2	1	2	1	1	2	2	2	1
94	3	4	3	4	4	204	5	2	6	6	6	314	2	2	1	2	1	1	2	2	2	1
95	4	5	5	5	5	205	5	2	6	6	6	315	2	2	1	2	1	1	2	2	2	1
96	4	5	5	5	5	206	5	2	6	6	6	316	2	2	1	2	1	1	2	2	2	1
97	3	4	4	4	4	207	5	2	6	6	6	317	2	2	1	2	1	1	2	2	2	1
98	3	3	3	3	3	208	5	2	6	6	6	318	2	2	1	2	1	1	2	2	2	1
99	4	5	5	5	5	209	5	2	6	6	6	319	2	2	1	2	1	1	2	2	2	1
100	4	5	5	5	5	210	5	2	6	6	6	320	2	2	1	2	1	1	2	2	2	1
101	4	5	5	5	5	211	5	2	6	6	6	321	2	2	1	2	1	1	2	2	2	1
102	4	5	5	5	5	212	5	2	6	6	6	322	2	2	1	2	1	1	2	2	2	1
103	3	4	4	4	4	213	5	2	6	6	6	323	2	2	1	2	1	1	2	2	2	1
104	5	5	5	5	5	214	5	2	6	6	6	324	2	2	1	2	1	1	2	2	2	1
105	4	5	5	5	5	215	5	2	6	6	6	325	2	2	1	2	1	1	2	2	2	1
106	3	4	4	4	4	216	5	2	6	6	6	326	2	2	1	2	1	1	2	2	2	1
107	3	3	3	3	3	217	5	2	6	6	6	327	2	2	1	2	1	1	2	2	2	1
108	4	5	5	5	5	218	5	2	6	6	6	328	2	2	1	2	1	1	2	2	2	1
109	5	5	5	5	5	219	5	2	6	6	6	329	2	2	1	2	1	1	2	2	2	1
110	5	5	5	5	5	220	5	2	6	6	6											

g5-66 represents the classification using 66 spectra and a 5-group subdivision.
g5-pca represents the classification using the first three principal components a 5-group subdivision.
g6-66 represents the classification using 66 spectra and a 6-group subdivision.
g6-pca represents the classification using the first three principal components a 6-group subdivision.
g7-pca represents the classification using the first three principal components a 7-group subdivision.

Fort A. P. Hill

Pixels from a hyperspectral image of Fort A. P. Hill (Virginia) were selected according to different types of ground cover comprising different types of vegetation, trees, soil and water. The image is shown in Figure 86a. The six groups of pixels were contiguous and relate to the areas marked by the arrows. Figure 86b shows the relative sizes of the classes of pixels and their locations.

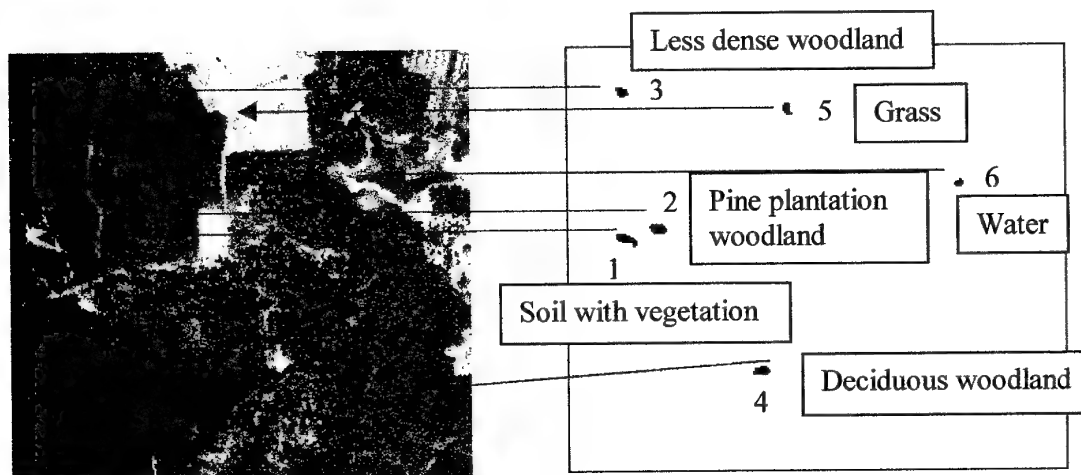


Figure 86. a) Colour image of part of Fort A. P. Hill, and b) the locations and sizes of the classes of pixels.

There were 126 wavelength values (nm) in each spectrum and a total of 172 pixels of about $3 \text{ m} \times 3 \text{ m}$. Table 7 gives the number of sites in each class and the associated ground cover class.

Table 7. Classes of different ground cover type and number of pixels in each for Fort A. P. Hill.

Class	Type of ground cover	Number of pixels	Pixel range
1	Soil with vegetation	43	1 – 43
2	Plantation woodland?	36	44 – 79
3	Shrubs?	24	80 – 103
4	Mixed woodland?	35	104 – 138
5	Grass	21	139 – 159
6	Water	13	160 – 172

As for Fort Hood the spectrum for each pixel was plotted as a trace and examined for differences and similarities. Experimental variograms were computed from the spectral data for each pixel. The full set of spectra and variograms can be provided, but to simplify interpretation we focus on selected ones with particular properties. This selection was based on the form of the spectrum and its variogram. This part of the investigation was done without reference to the classes of ground cover in case there were differences in the spectra for a given classes which might be overlooked by focusing on the classes only.

Spectra

Most of the spectra for Fort A. P. Hill have a similar form – the main differences relate to the fine detail and in particular their maximum reflectance values. The spectra for class 6 (water) are distinctly different from the others and from any of the spectra of Fort Hood. Selected spectra are shown in Figures 89 to 115.

A visual inspection of the spectra suggests that 1 to 159 have a similar overall shape. Some, such as pixel 40, Figure 91, have a larger spike at about 1300 nm than others such as pixel 4, Figure 90. The other main difference apart from small details in the shape is the average reflectance value. For class 1 the average spectral value is about 1800, for class 2 it is about 1100, for class 3 it is 1400, for class 4 which has the widest range in mean values for the spectrum it is about 1700, for class 5 it is about 2100, and for class 6 it is 160. Thus there is a considerable range in reflectance values and apart from class 6 it is likely to be the main basis for discrimination.

Variography

All of the experimental variograms showed weak evidence of trend with their unbounded form. Linear and quadratic functions were fitted to the wavelengths (one dimension only). The quadratic function accounted for more of the variance in the data than the linear one (see Table 8 for a summary for the selected pixels). It ranged from 41% for pixel 107 to 59% for pixel 160. The variograms of selected spectra were computed on the residuals from quadratic trend function. For pixels 1-159 they have a similar form. It was possible to fit a periodic function with a short wavelength as well as one with a longer wavelength to all of the variograms, Figure 89 for example. Most of the models with a short wavelength were the periodic with exponential or stable exponential function (PEF and PES, respectively). In general the shorter wavelength is about 250 nm, and the longer one varies between 520 nm to 790 nm. The latter were generally associated with the periodic with power function (PPF). The main difference between the variograms of the different classes of ground cover relates to the amplitudes of the fitted models.

Principal component analysis

A principal components analysis was done using all of the pixels and the spectral values. Table 9 gives the latent roots and vectors of the first three principal components, which account for 96.4% of the variance. Large eigenvector values are in bold. For PC 1 (\bullet 0.0975) these are for wavebands 70 to 93. For PC 2 (\bullet 0.13) they are for 11 to 17, and 22 to 33, and for PC 3 (\bullet 0.4) wavebands 63 to 65. Figure 87 shows the pixels plotted in the projection of PC1 and PC 2 using the PC scores. There are three well-defined and coherent groups, 1, 5 and 6. Class 6 is the most distinct and this has spectra with the smallest average reflectance values. Classes 2, 3 and 4 merge in the centre of the figure. Nevertheless, based on the PC scores, they occupy a distinct part of the space.

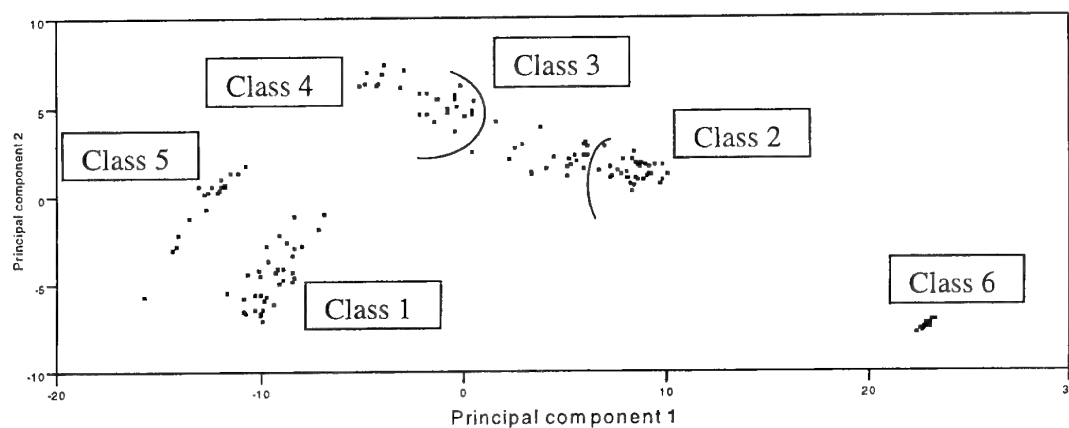


Figure 87. Plot of individual pixels in the projection of principal components 1 and 2 using the PC scores. The ground cover classes are shown near to the relevant group of pixels, and the lines shows the approximate separation between classes 2, 3 and 4.

Non-hierarchical *k*-means dynamic clustering

I applied this method clustering to the pixels from the Fort A. P. Hill image. There were too many wavebands for the method to work successfully as before. Therefore, I did the analysis on the scores of the first three principal components, and on 63 (alternate) wavebands. The sums of squares criterion provided the most stable results. Starting with 10 groups, the pixels were reclassified until three groups remained. As it was not possible to calculate Wilks' criterion, I plotted the sums of squares criterion against g for each data set. Figure 88 shows the results for the two data sets. The most likely number of groups is shown where the graph goes below the general trend. Based on this the analysis using the raw spectra the graph suggests that four or seven groups is optimal, whereas for the PC scores 6 groups is optimal. Figure 87 of the scores plotted in the plane of components 1 and 2 shows four separate groups. Nevertheless, it is evident that groups 2 to 4 form a continuum in this projection.

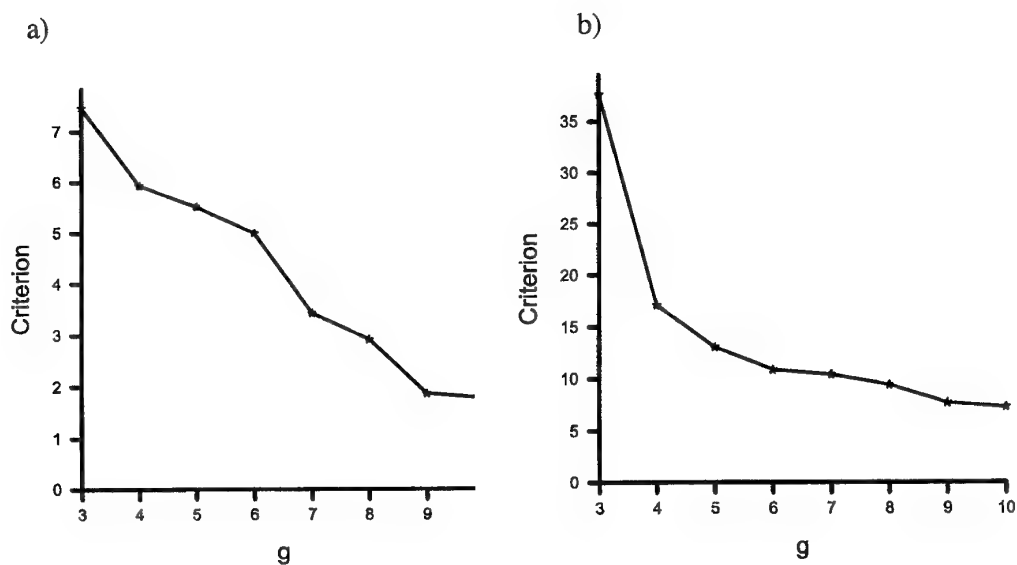


Figure 88 Sum of squares criterion $\times g^2$ plotted against g (number of groups) for:
a) 63 wavebands, and b) the scores of the first five principal components

Table 10 gives the classes to which each pixel belongs for the two sets of data. For the 63 wavebands both the 6-group and 7-group classifications are given for comparison with the six classes from the PCA scores. In general the 7-group classification does not improve the discrimination between classes, therefore it is not discussed below in detail. The bold lines show the extent of each of the six ground cover classes.

Class 1 pixels

Ground cover class 1 is soil with vegetation. For the PCA 6-group classification based on the scores it is a pure group. For the raw spectra six pixels belong to another group that overlaps with class 4. This class occupies a distinct part of the property space projection, Figure 85. It has the second largest reflectance values. Figures 89 to 91 show the spectra for pixels 1, 4 and 40.

The variograms of pixels 1 and 40 have a wavelength of about 250 nm for the shorter wavelength and over 700 nm for the longer periodic function. The amplitudes of the models for this class are the second largest, Table 8.

Class 2 pixels

This ground cover class appears to be dense pine plantation woodland. For the classification based on PC scores six pixels belong to group 6 and the rest to group 4 of the multivariate classification. For the raw spectra the class is less pure having three groups present (six pixels belong to group 4, five to group 6 and the rest to group 5). Figures 92 to 99 show the spectra selected to represent this class. There is more variation present than in class 1.

The wavelengths of the variogram models fitted with the longer period range between about 558 nm and 750 nm, Table 8. The amplitudes are intermediate in terms of the full data, but it is evident that as the wavelength increases so does the amplitude, Table 8.

Class 3 pixels

This is the least pure class for the classification based on PC scores. There are three multivariate groups in this class: six pixels belong to group 4, one to group 5 and the rest to group 6. For the raw spectra the distribution of classes is similar to that for the PC scores. In property space this ground cover class is transitional to classes 2 and 4. It appears to be less dense vegetation than that of class 2 – it is possibly young pine plantation. Figures 100 and 101 are examples of the spectra of this class.

The variograms have been fitted by models with a short and a long wavelength, Figures 100 and 101. The former is about 250 nm and the longer one is 750 nm. These variograms have a larger amplitude than those of class 2, Table 8.

Class 4 pixels

This ground cover class is deciduous woodland. For the PC scores the class is almost pure with just two pixels belonging to another group. For the raw spectra there are three groups present, with 13 pixels belonging to groups other than the dominant one. Figures 102 to 108 are examples of spectra belonging to this group. Their overall shapes are similar, but the height of the peak at 1400 nm varies.

The variograms of this class have wavelengths for the longer periodic function of between 522 nm and 789 nm. Their amplitudes are larger than for classes 2 and 3,

Table 8. The approximate wavelength of the shorter fitting periodic function is about 250 nm.

Class 5 pixels

This ground cover class is grass and it is clearly distinct in the property space projection from all of the other classes. For the PC scores the group is pure. It is reasonably coherent for the raw spectra, however, the majority of pixels belong to the same group as the majority of pixels in class 1. There is some similarity between these ground cover classes in the image, Figure 1. However, the intensity of vegetation cover is less in class 1.

Figures 109 and 110 are examples of the spectra for this class. The variograms in this class Figures 109 and 110 and Table 8 have the largest amplitudes and wavelengths of between 615 nm and 714 nm. There is also a shorter fitting periodic function with a wavelength of about 250 nm.

Class 6 pixels

This is the most distinctive class in terms of the raw spectra, Figures 111 to 168, and the variograms. It is water and the reflectance values are the smallest. The multivariate classifications have resulted in pure classes for both the PC scores and the raw spectra.

The variograms have a large wavelength (for the longer fitting periodic function) and the smallest amplitude, Figures 111 to 168 and Table 8. The wavelength of the shorter fitting function is about 250 nm.

Summary of results

The classification based on the PC scores has produced more coherent and pure classes than that using the raw data. The spectra for Fort A. P. Hill are more similar in form for classes 1 to 5 than those for Fort Hood. Nevertheless the classes are distinguishable by multivariate classification using the PC scores. The data reduction to three components compared with half of the spectra clearly refines the analysis. The shapes of the variograms for these data are less distinctive between ground cover classes, but the amplitudes of the periodic functions could be used for discrimination. The variogram for the water is distinguishable from all of the others.

Conclusions

This project has analysed pixel information for selected classes of ground cover in two ways. Part II of the report analysed a set of pixels belonging to a coherent ground cover class using NIR. The results show that the classes had distinguishable characteristics that could be identified from the structure of the variogram. The suggestion is that the texture of a ground cover class in an image has an identifiable form.

Part III of the report describes the investigation of the hyperspectral data for individual pixels. The results show that certain ground cover classes have very distinctive spectra, for instance at Fort Hood. However when the ground cover classes are different kinds of trees the distinction is less clear from the spectra alone. The variograms provide clues as to the differences in terms of the sizes of the variances, in particular. However for some classes the spectra have distinct wavelengths for the periodic functions. The principal component analyses have been particularly effective in concentrating the vital information and in so doing enable better discrimination between the ground cover classes in terms of the spectral values. The non-hierarchical multivariate classifications using the PC scores are powerful in distinguishing the classes.

The results suggest that PCA with the non-hierarchical classification provides a rapid means of discrimination. The variograms, although distinctive for certain ground cover types, do not provide a rapid means of discrimination because the differences are often more subtle. For example at Fort A. P. Hill for classes 1 to 5 the difference in the variograms according to the classes was the amplitudes of the fitted periodic functions.

Acknowledgement

I thank Dr Stephen Heming for his input into this work on the hyperspectral data and Mr Bosch for his close support.

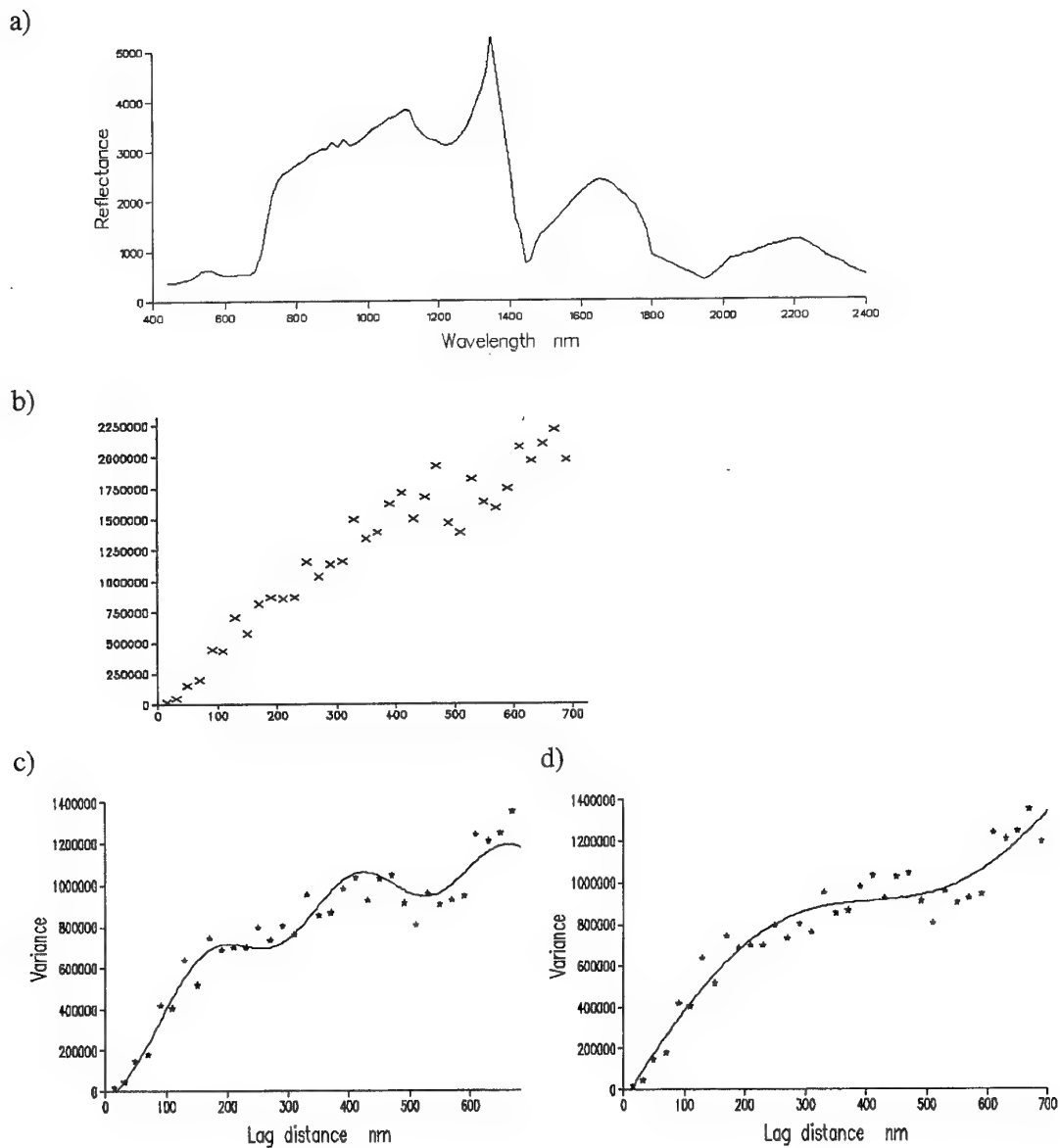


Figure 89. A.P. Hill: pixel 1: a) spectrum, b) experimental variogram of raw values, c) and d) experimental variogram and fitted models of quadratic residuals - short wavelength PES and long wavelength PPF, respectively.

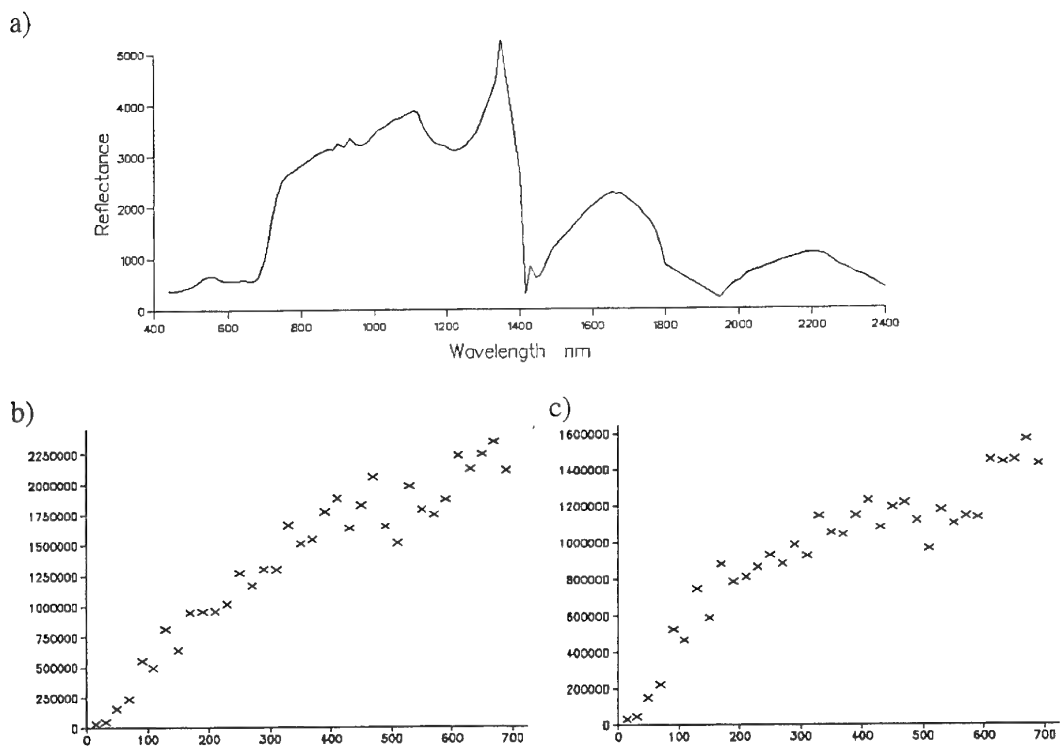


Figure 90. A.P. Hill: pixel 4: a) spectrum, b) experimental variogram of raw values and c) experimental variogram of quadratic residuals.

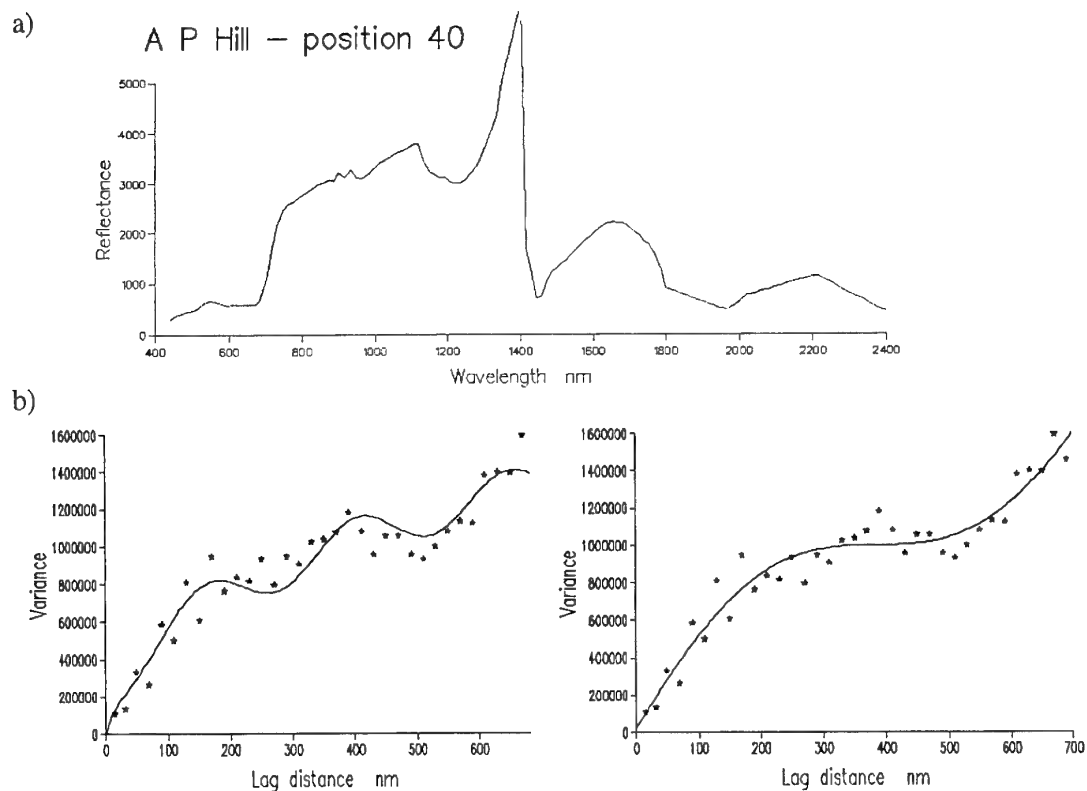


Figure 91. A.P. Hill: pixel 40: a) spectrum, b) and c) experimental variogram and fitted models of quadratic residuals - short and long wavelength PPF model.

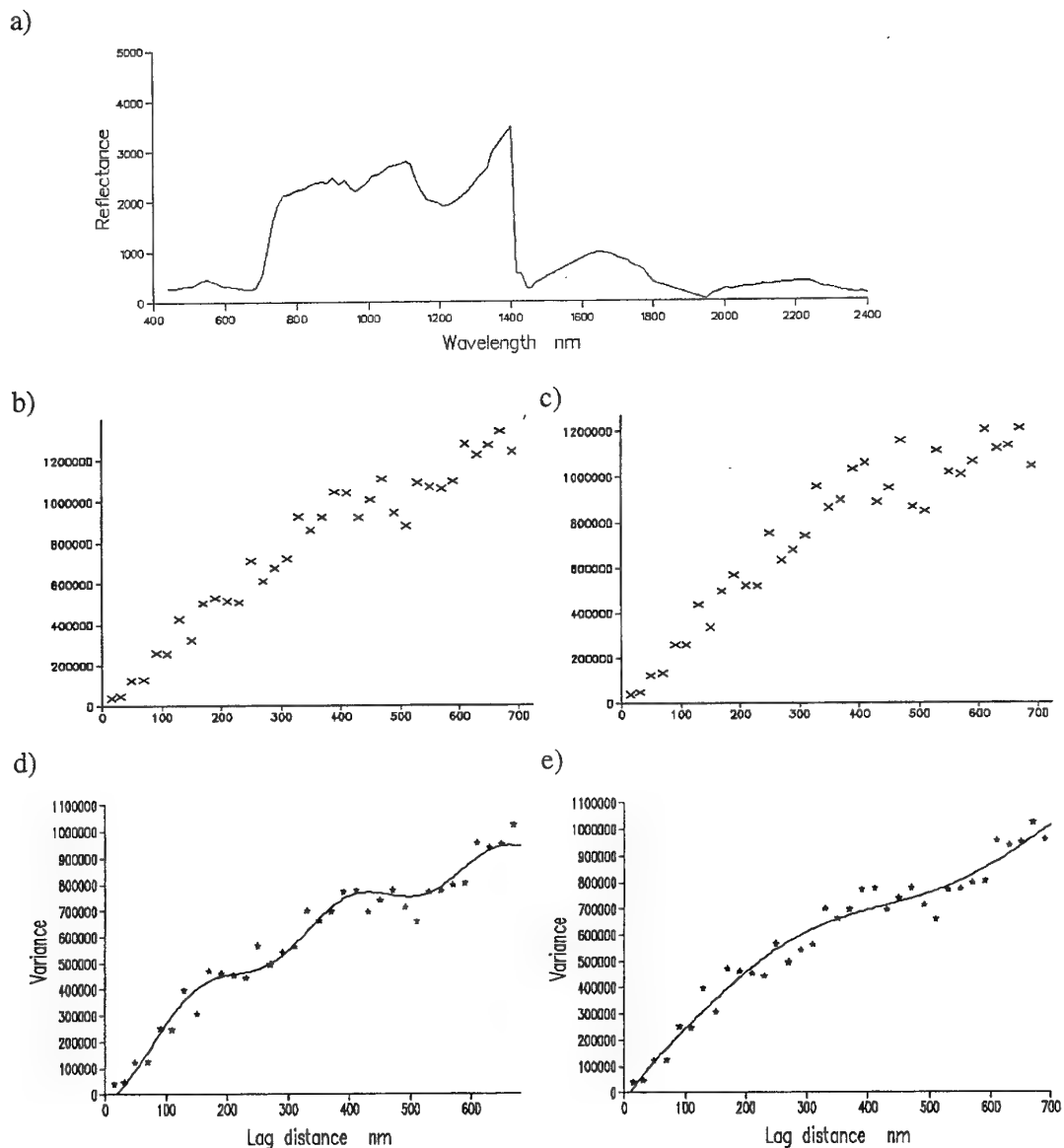


Figure 92. A.P. Hill: pixel 44: a) spectrum, b) experimental variogram of raw values, c) experimental variogram of linear residuals, d) and e) experimental variogram and fitted models of quadratic residuals - short wavelength PEF and long wavelength PPF, respectively.

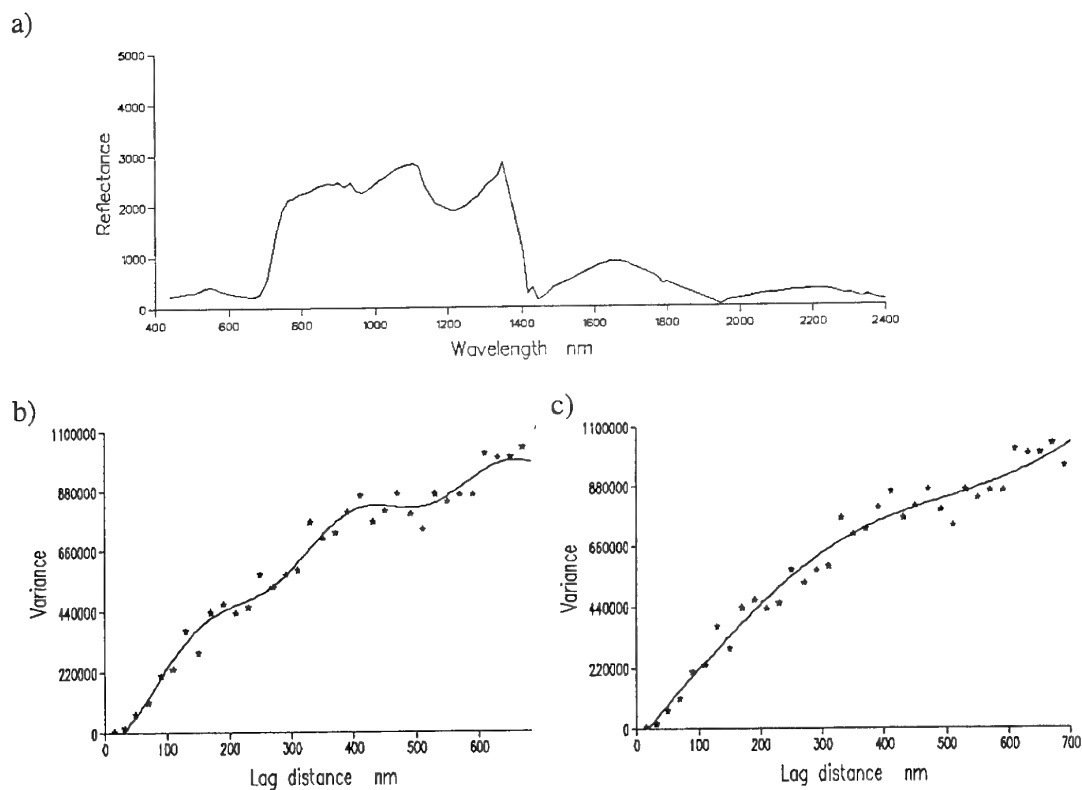


Figure 93. A.P. Hill: pixel **50**: a) spectrum, b) & c) experimental variogram and fitted models of quadratic residuals - short PES and long wavelength PPF model.

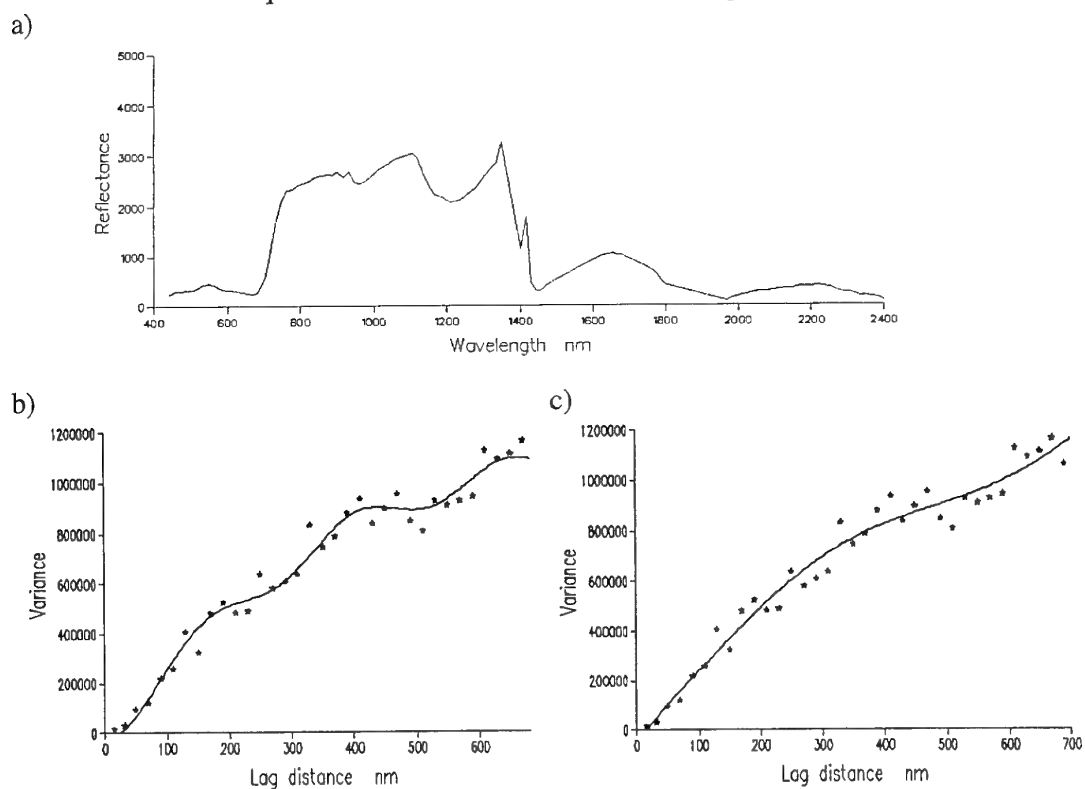


Figure 94. A.P. Hill: pixel **54**: a) spectrum, b) & c) experimental variogram and fitted models of quadratic residuals - short (PES) and long wavelength (PPF model).

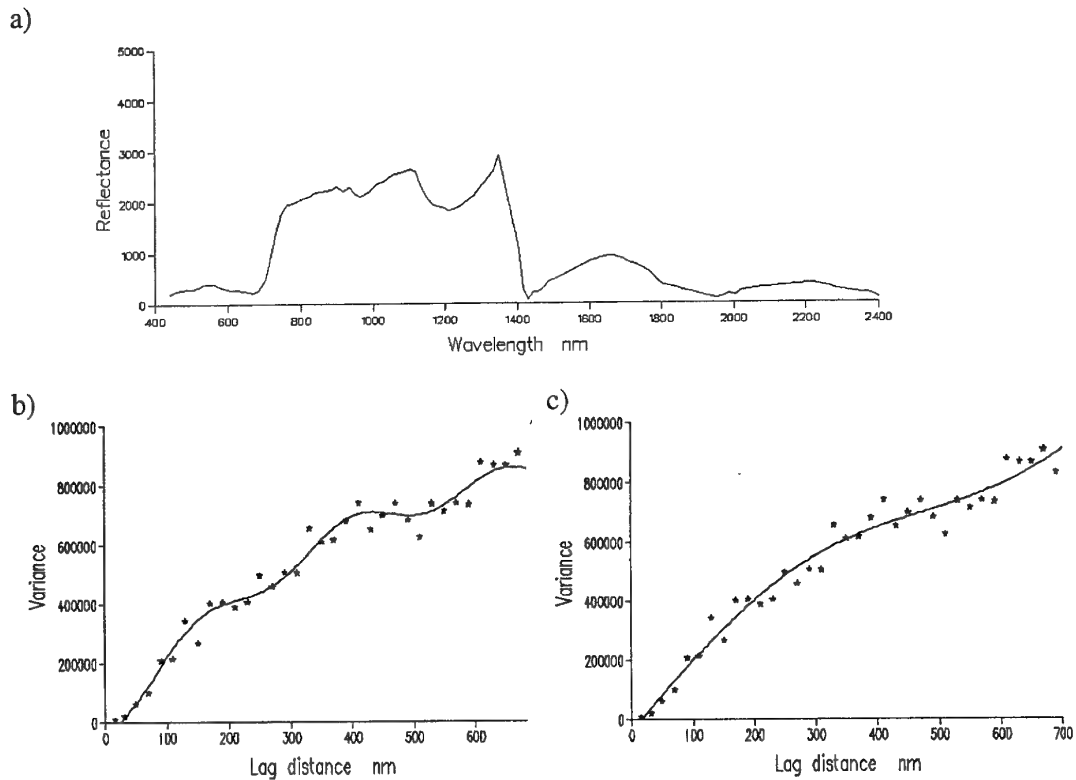


Figure 95. A.P. Hill: pixel **65**: a) spectrum, b) and c) experimental variogram and fitted models of quadratic residuals – short PES and long wavelength PPF model.

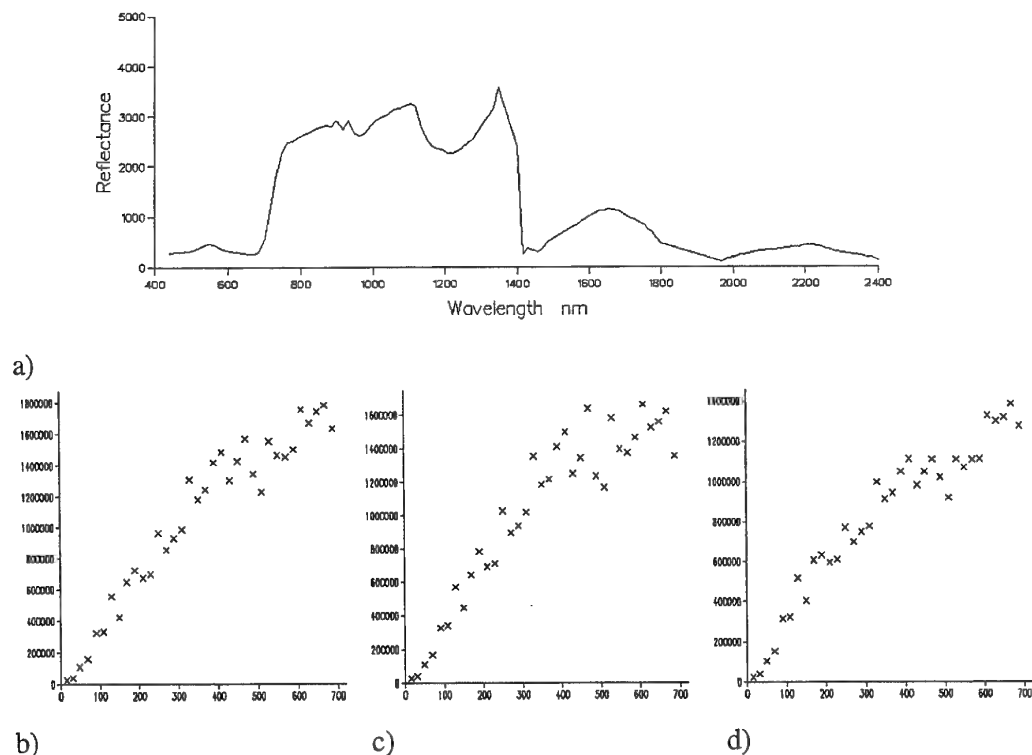


Figure 96. A.P. Hill: pixel **70**: a) spectrum, b) experimental variogram of raw values, c) variogram of linear residuals and d) variogram of quadratic residuals.

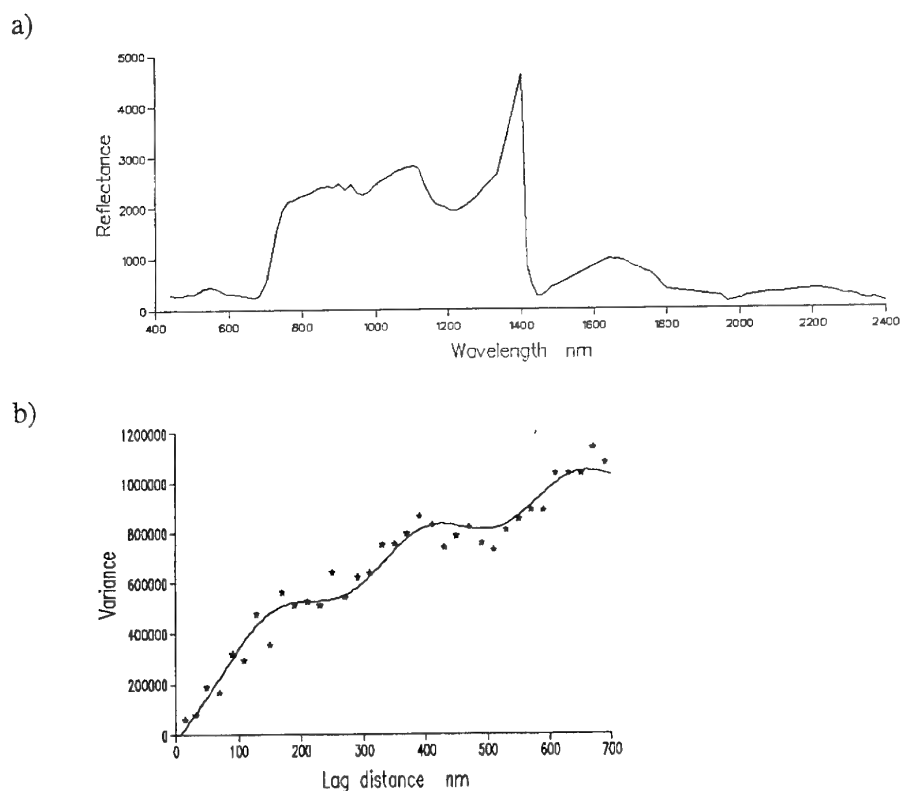


Figure 97. A.P. Hill: pixel **75**: a) spectrum, b) experimental variogram and fitted model of quadratic residuals (short wavelength PES model).

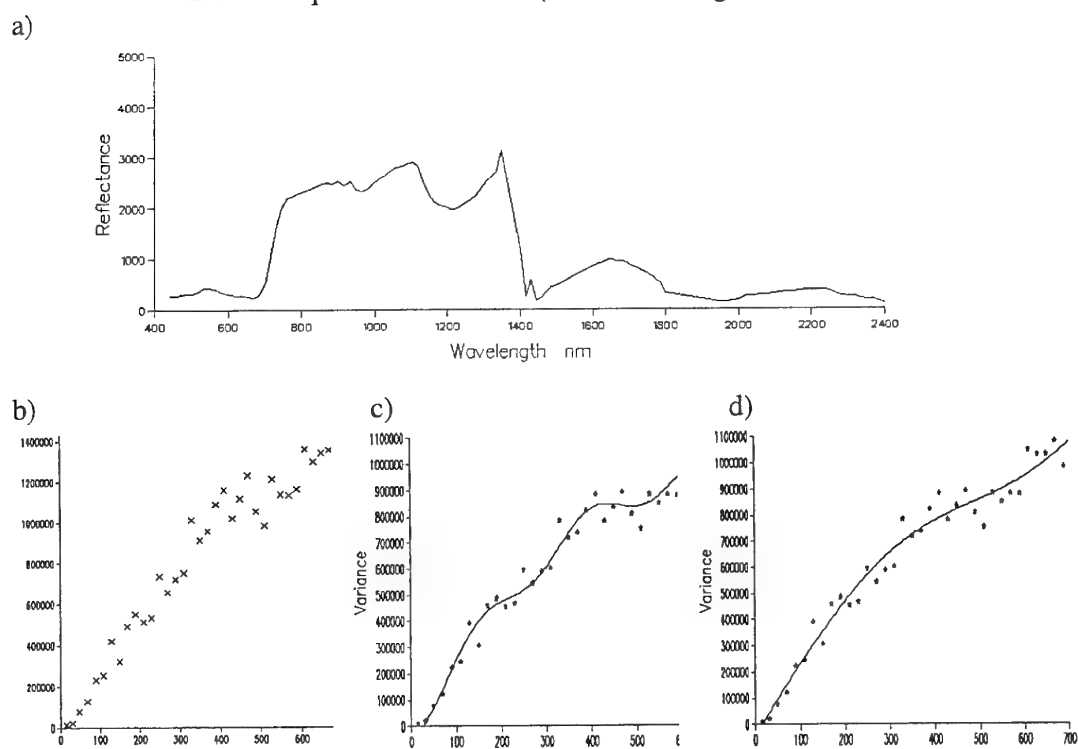
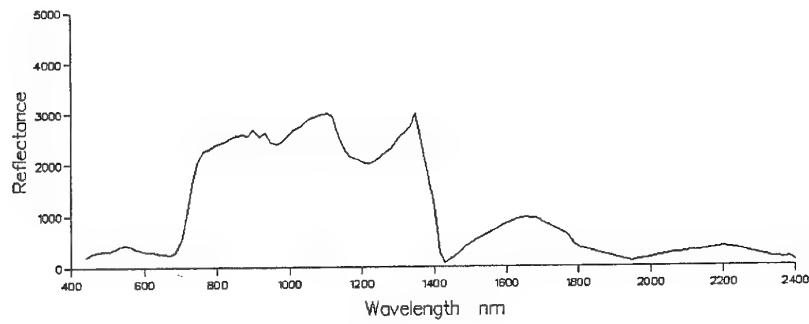
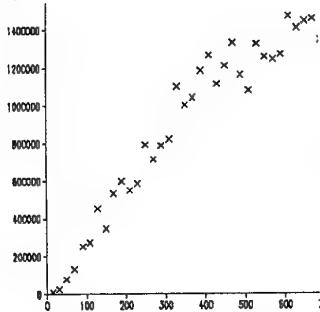


Figure 98. A.P. Hill: pixel **76**: a) spectrum, b) experimental variogram of raw values, c) and d) variograms and fitted models of quadratic residuals - short wavelength PES model and long wavelength PPF model.

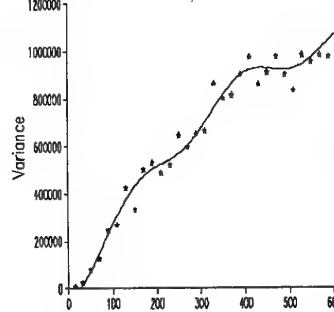
a)



b)



c)



d)

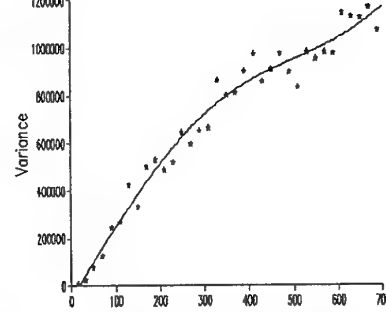


Figure 99. A.P. Hill: pixel 79: a) spectrum, b) experimental variogram of raw values, c) and d) variograms and fitted models of quadratic residuals - short wavelength PES model and long wavelength PPF model.

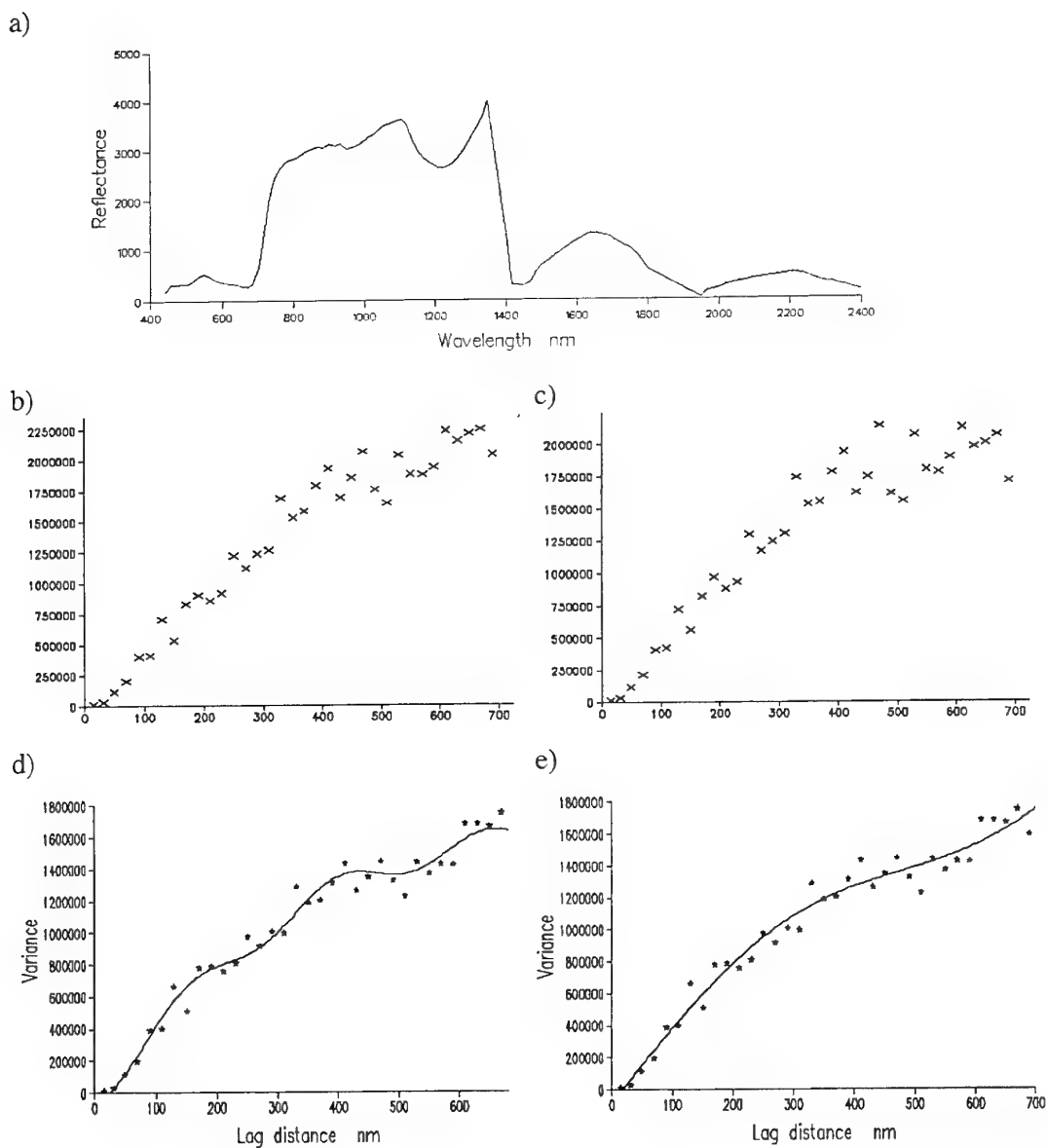
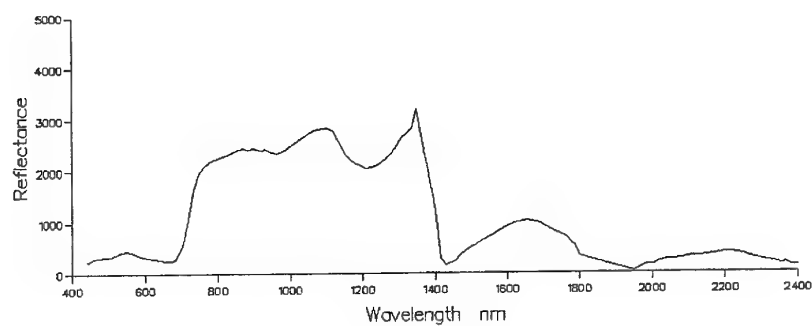


Figure 100. A.P. Hill: pixel **87** a) spectrum, b) experimental variogram of raw values, c) experimental variogram of linear residuals, d) and e) experimental variogram and fitted models of quadratic residuals - short wavelength PES and long wavelength PPF, respectively.

a)



b)

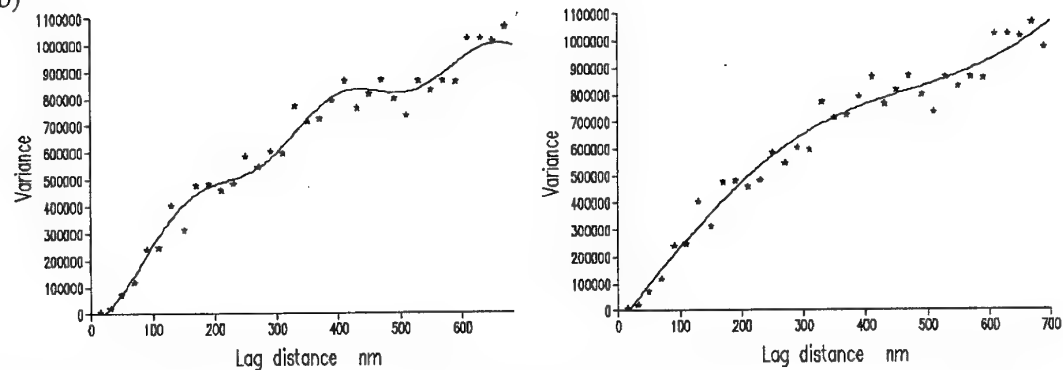


Figure 101. A.P. Hill: pixel 90: a) spectrum, b) and c) experimental variogram and fitted models of quadratic residuals - short PES and long wavelength PPF model.

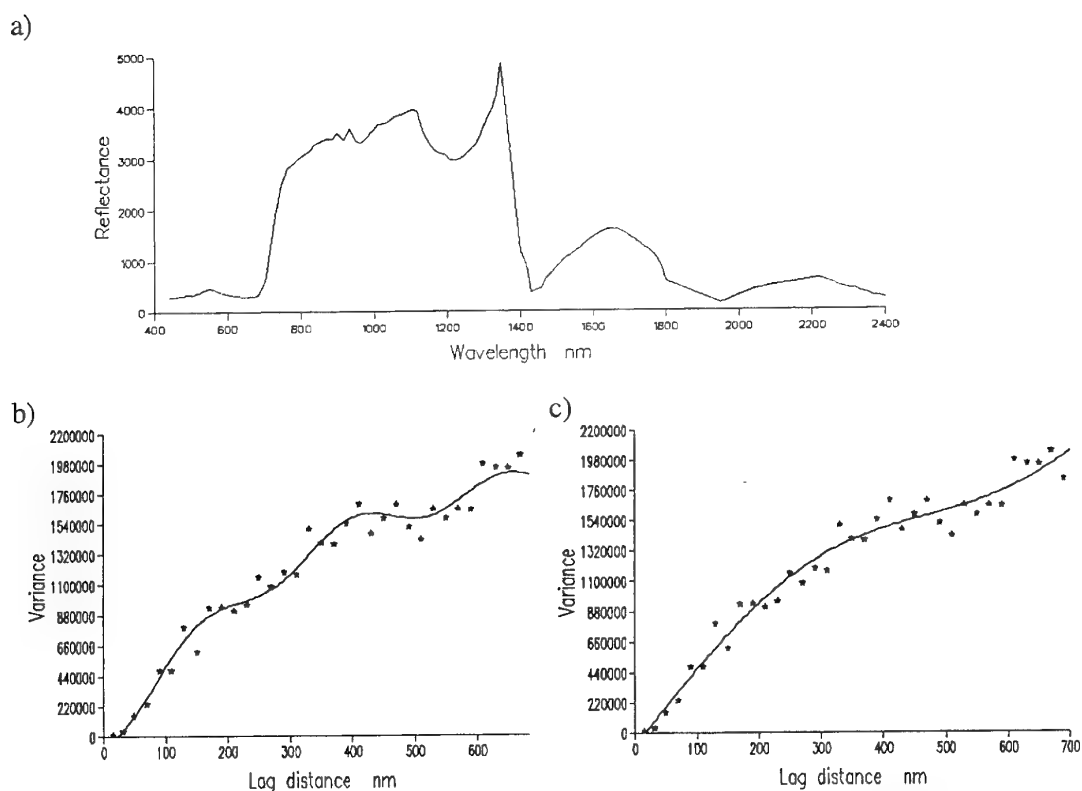


Figure 102. A.P. Hill: pixel **104**: a) spectrum, b) and c) experimental variogram and fitted models of quadratic residuals - short PES and long wavelength PPF model.

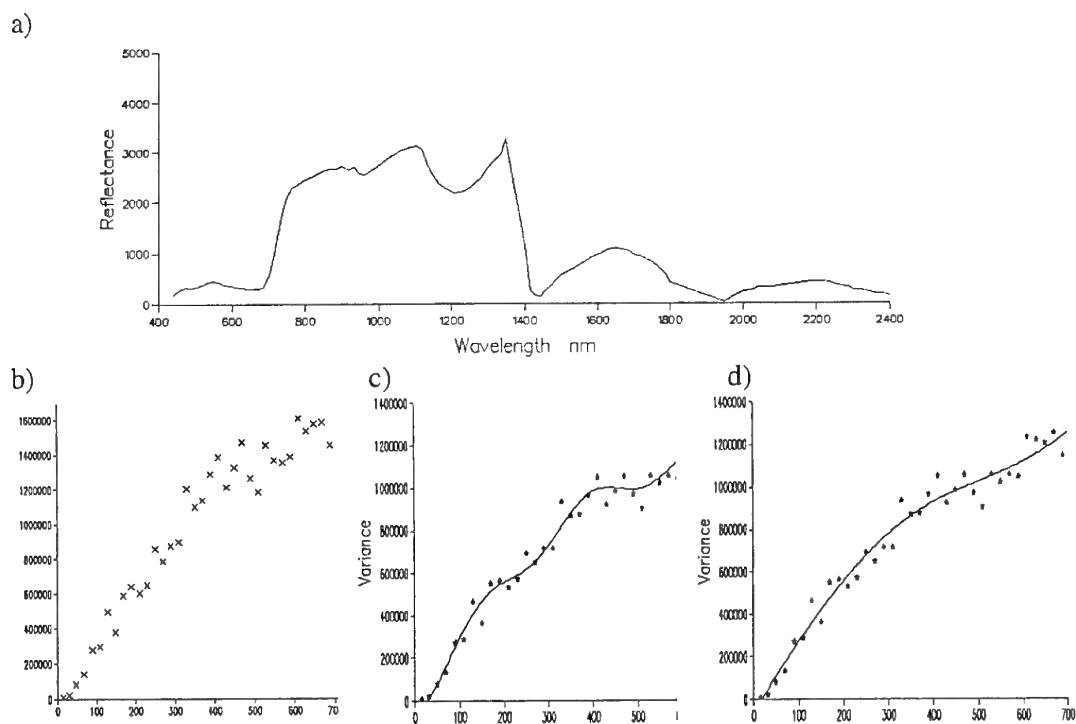


Figure 103. A.P. Hill: pixel **107**: a) spectrum, b) variogram of raw values, c) & d) variogram and fitted models of quadratic residuals - short PES and long wave PPF.

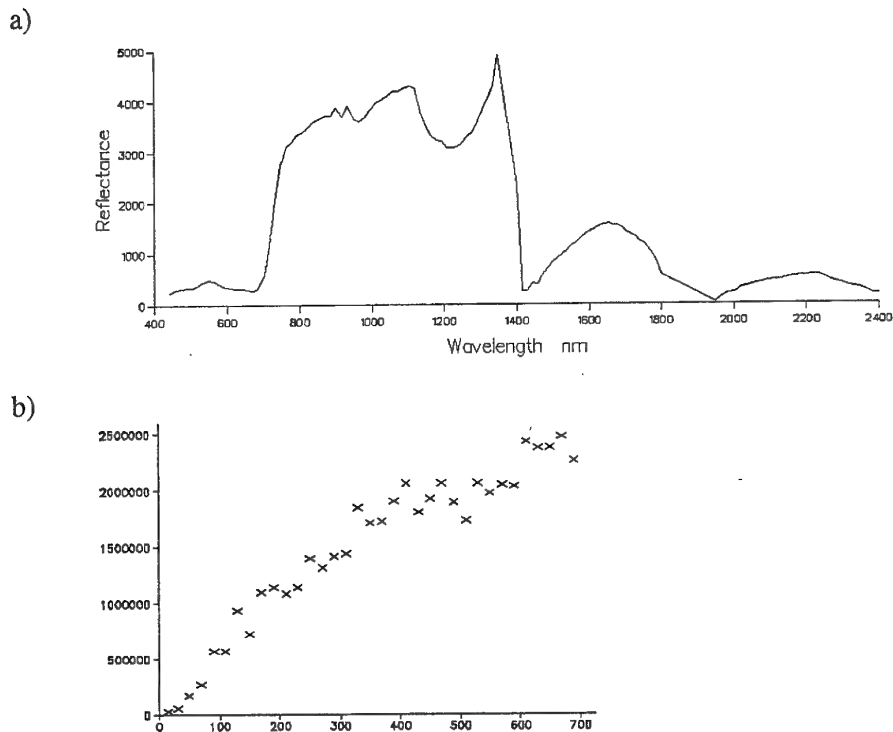


Figure 104. A.P. Hill: pixel **108**: a) spectrum, b) experimental variogram of quadratic residuals.

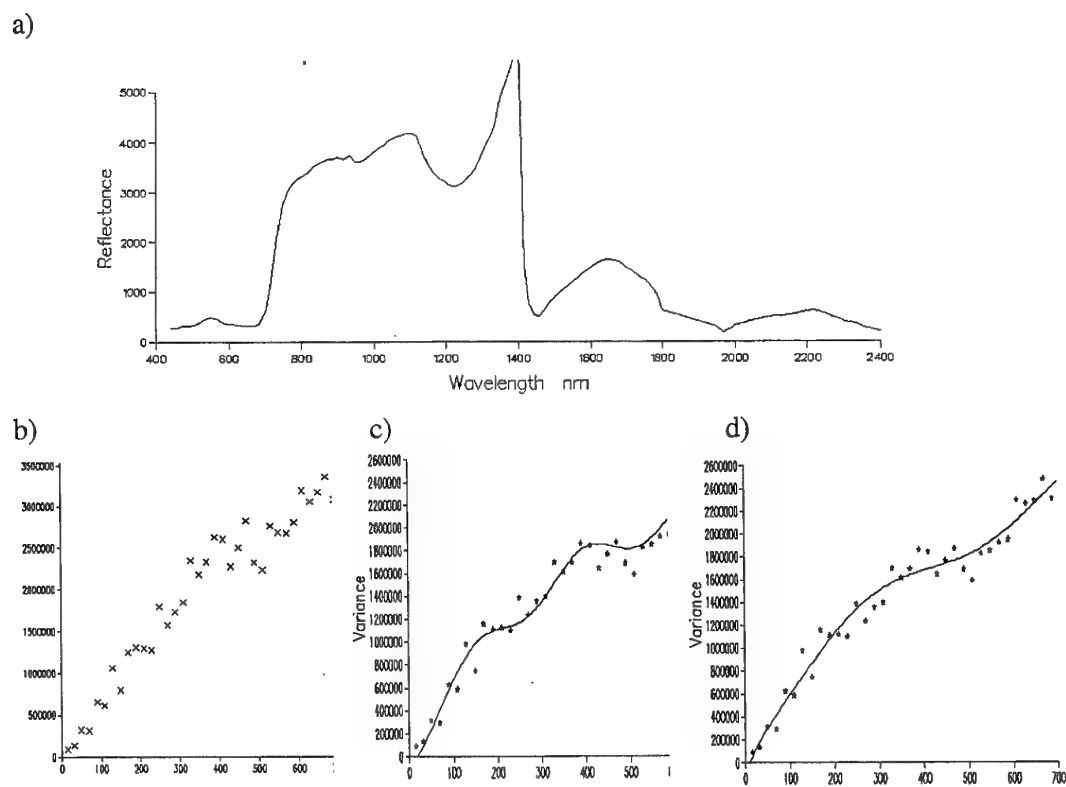


Figure 105 .A. P. Hill: pixel **115**: a) spectrum, b) experimental variogram of raw values, c) & d) experimental variogram and fitted models of quadratic residuals - short wavelength PEF and long wavelength PPF model.

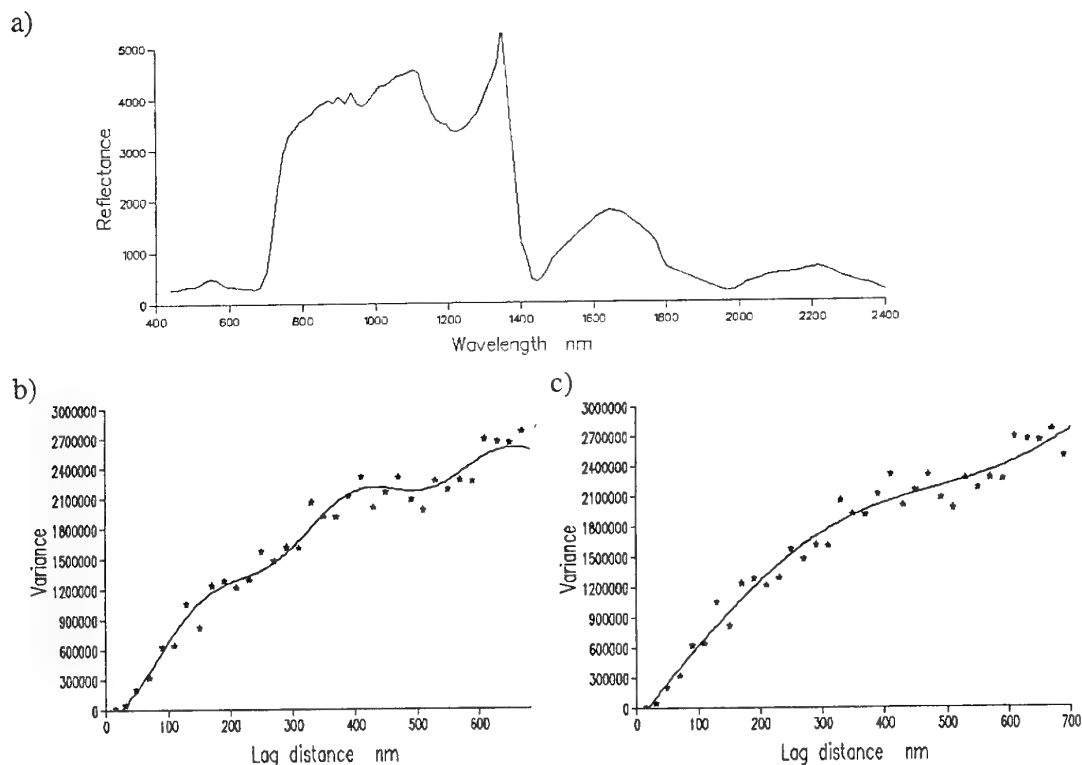


Figure 106. A.P. Hill: pixel **119**: a) spectrum, b) & c) experimental variogram and fitted models of quadratic residuals - short PES and long wavelength PPF model.

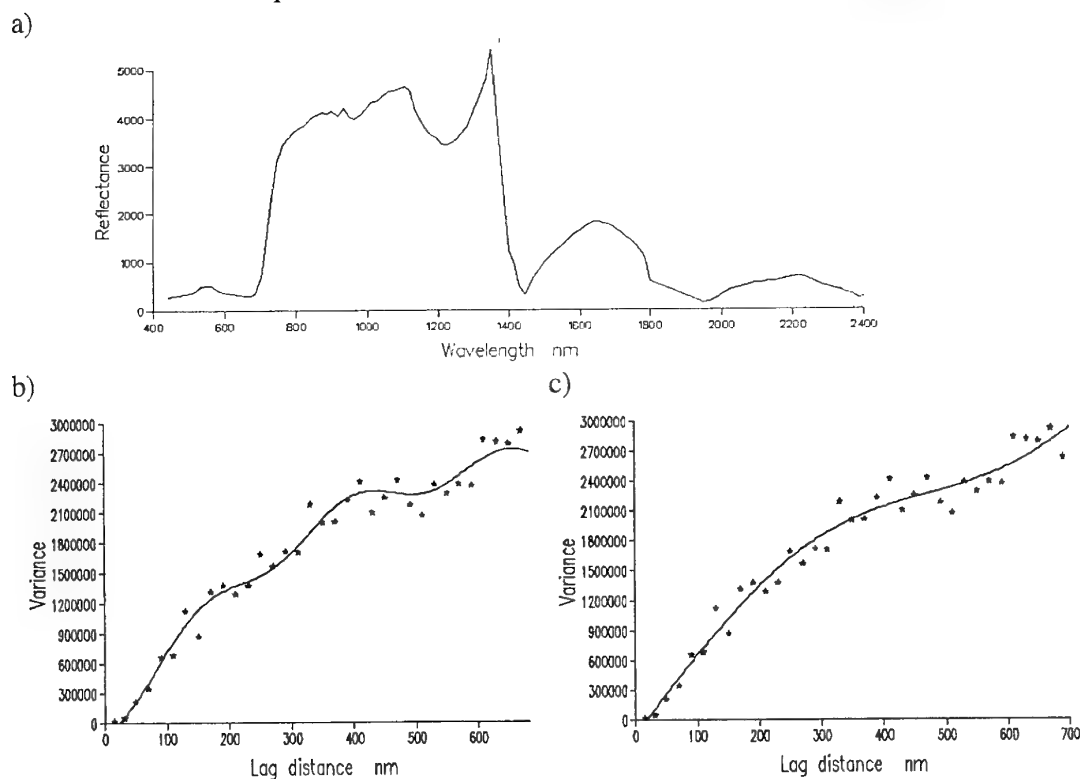


Figure 107. A.P. Hill: pixel **120**: a) spectrum, b) & c) experimental variogram and fitted models of quadratic residuals - short PES and long wavelength PPF model.

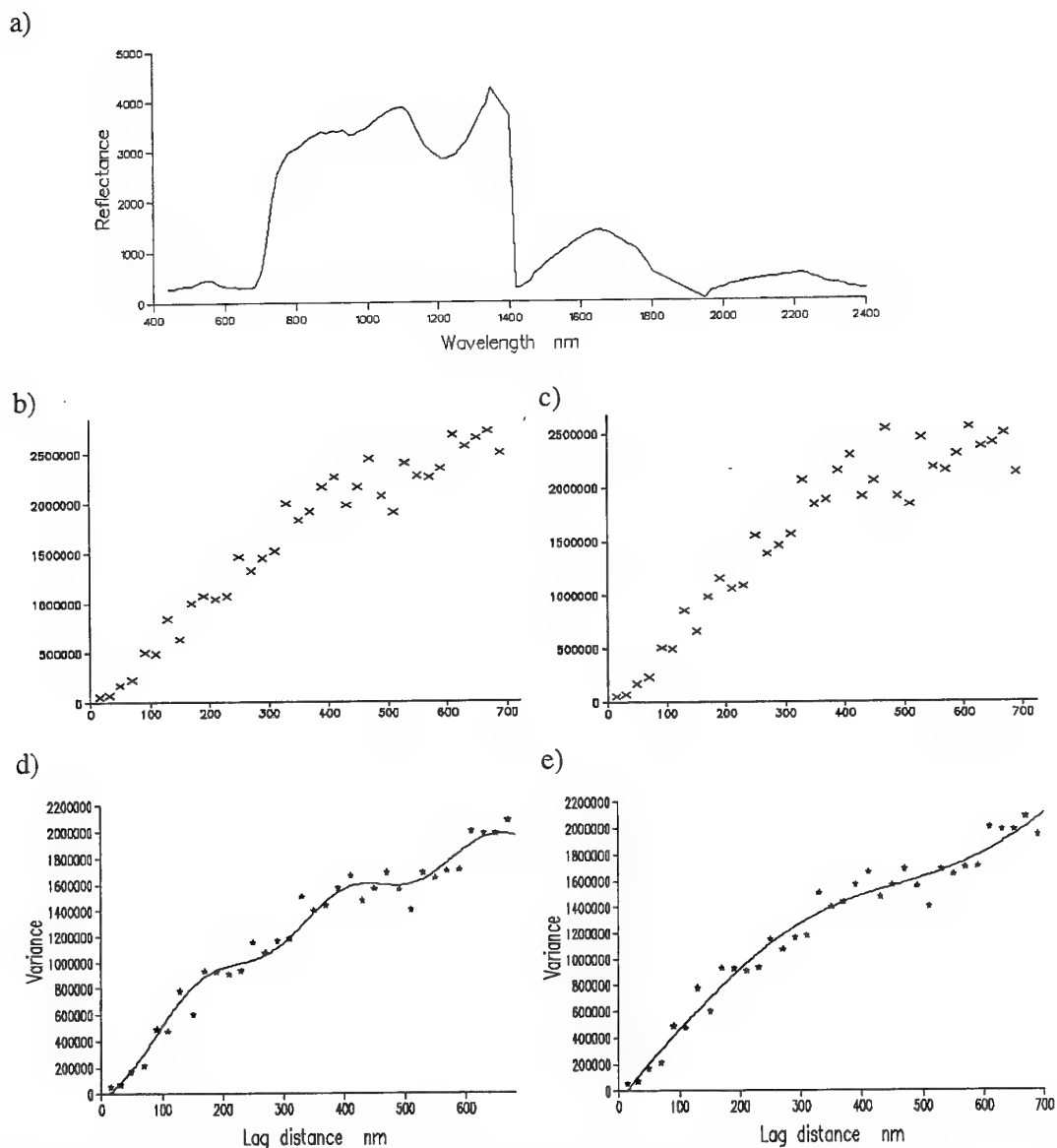
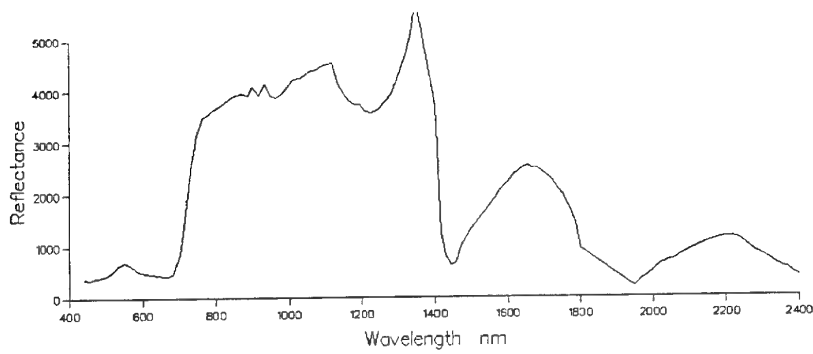
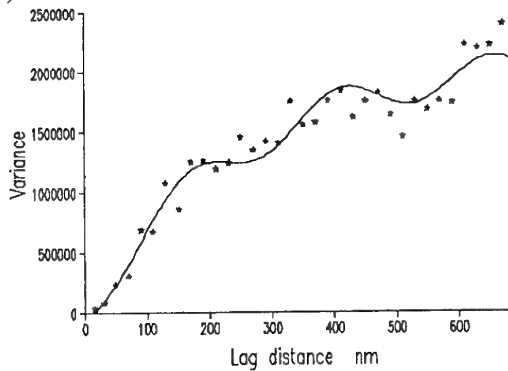


Figure 108. A.P. Hill: pixel **133** a) spectrum, b) experimental variogram of raw values, c) experimental variogram of linear residuals, d) & e) experimental variogram and fitted models of quadratic residuals - short wavelength PEF and long wavelength PPF, respectively.

a)



b)



c)

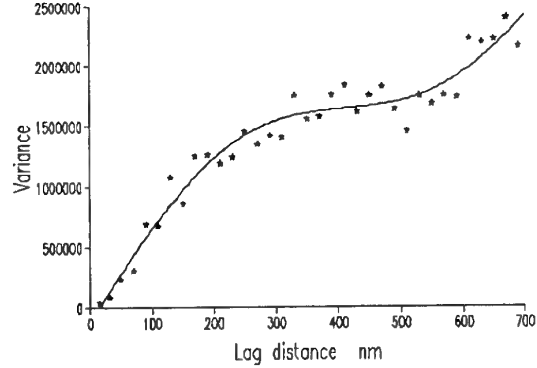
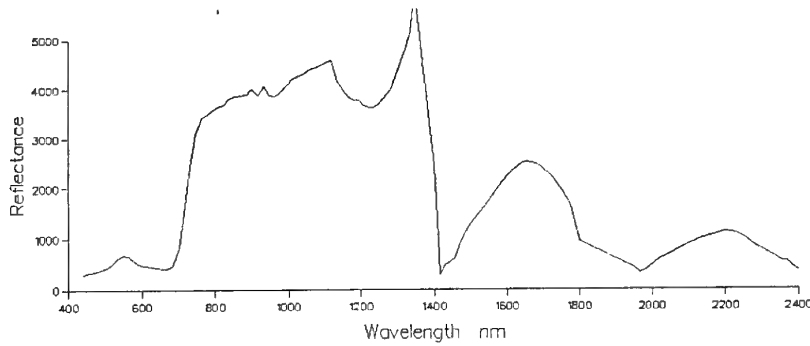
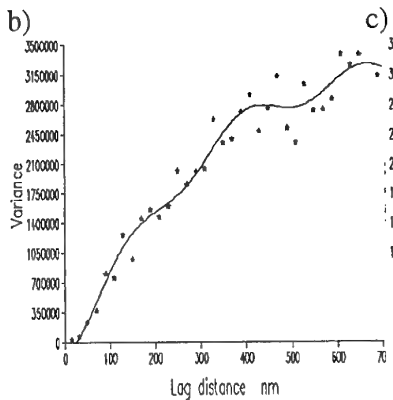


Figure 109. A.P. Hill: pixel **139**: a) spectrum, b) & c) experimental variogram and fitted models of quadratic residuals - short PEF and long wavelength PPF model.

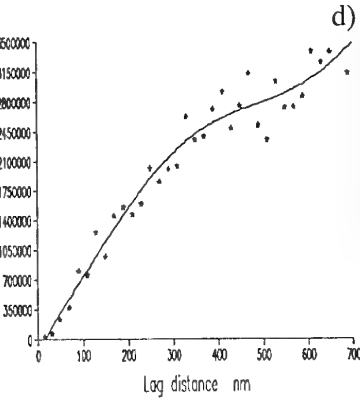
a)



b)



c)



d)

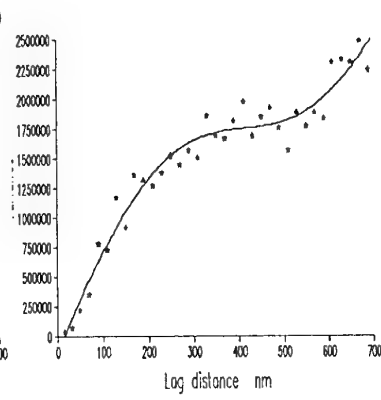
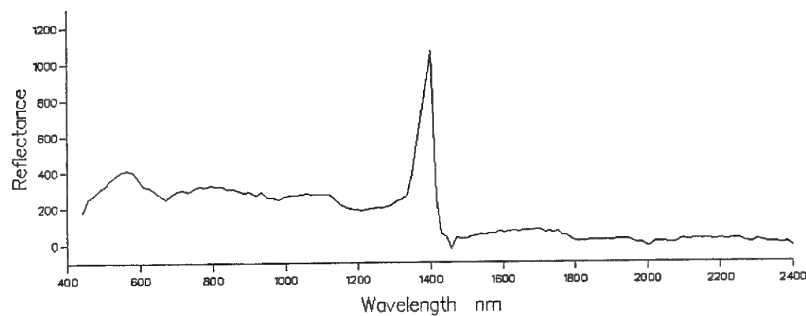
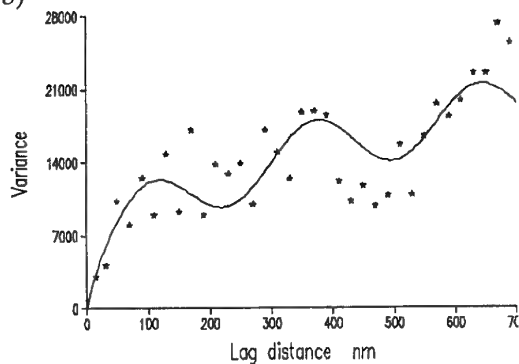


Figure 110. A.P. Hill: pixel **141**: a) spectrum, b) & c) variogram and fitted models of raw data, short PES and long PPF, d) variogram of quadratic residuals (PPF).

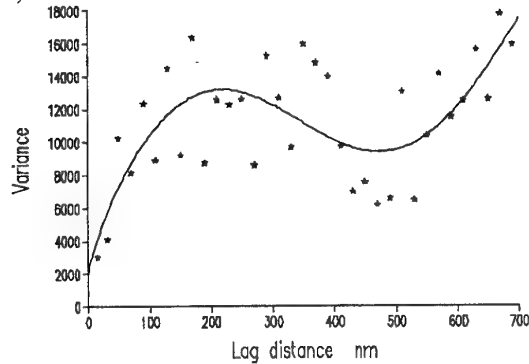
a)



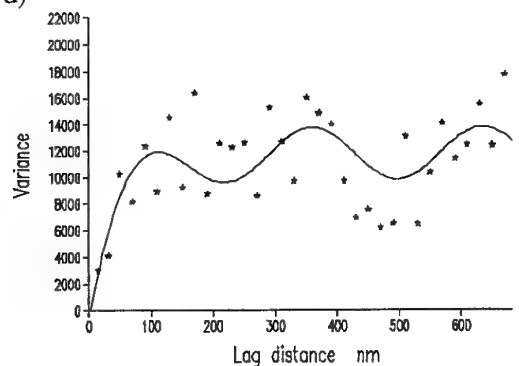
b)



c)



d)



e)

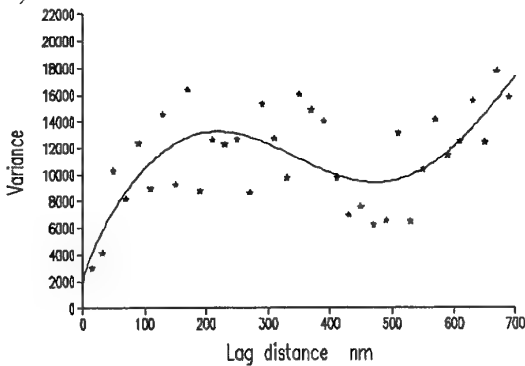


Figure 111. A.P. Hill: pixel **160** a) spectrum, b) experimental variogram and fitted model (PPF) of raw values c) experimental variogram and fitted model of linear residuals, long wavelength PPF, and d) & e) experimental variogram and fitted models of quadratic residuals - short wavelength PPF and long wavelength PPF, respectively.

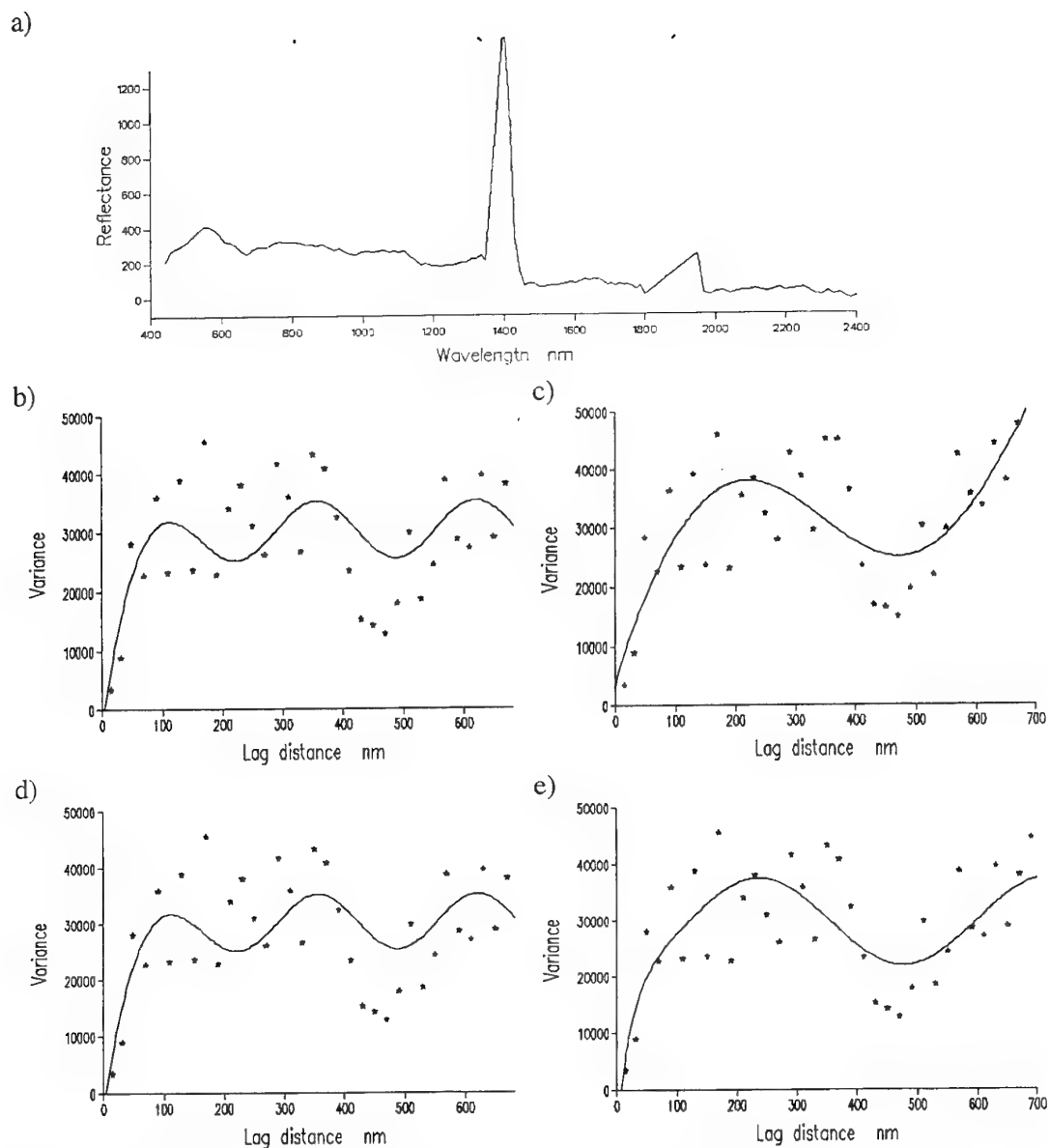


Figure 112. A.P. Hill: pixel **165** a) spectrum, b) & c) experimental variogram and fitted models of raw values, short and long wavelength d) & e) experimental variogram and fitted models of linear residuals - short wavelength PEF and long wavelength PPF, respectively.

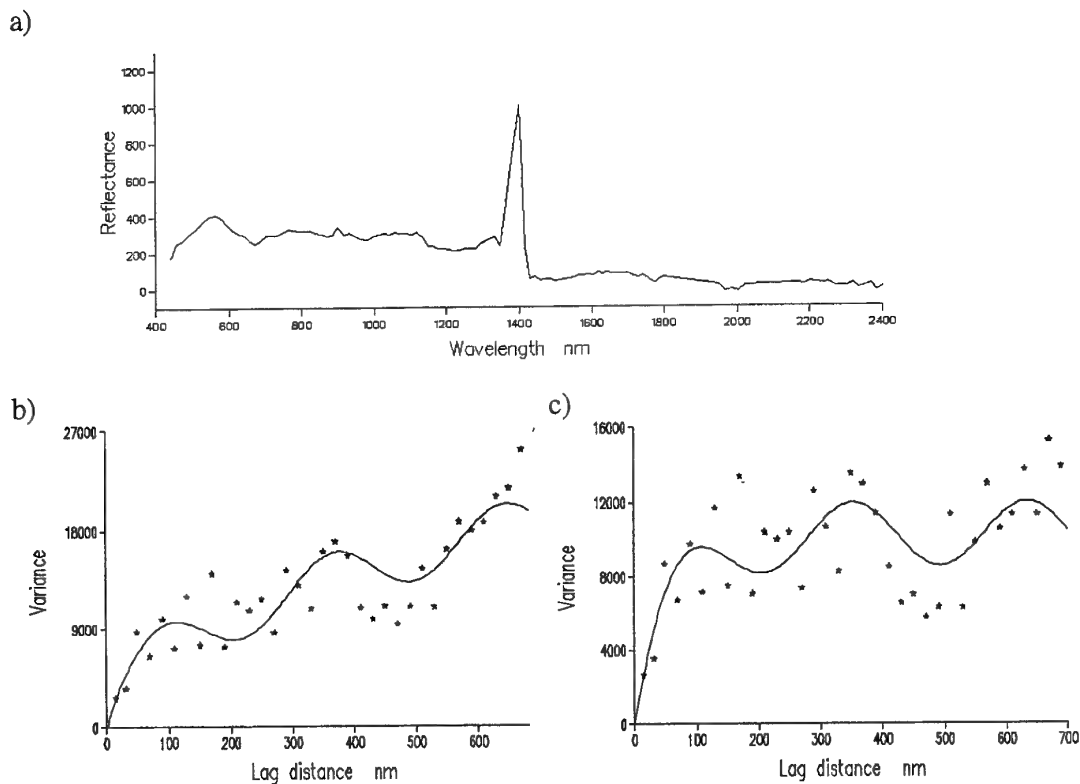


Figure 113. A.P. Hill: pixel **166**: a) spectrum, b) experimental variogram and fitted models of raw data, short wavelength PPF model and c) experimental variogram and fitted models of linear residuals, short wavelength PEF.

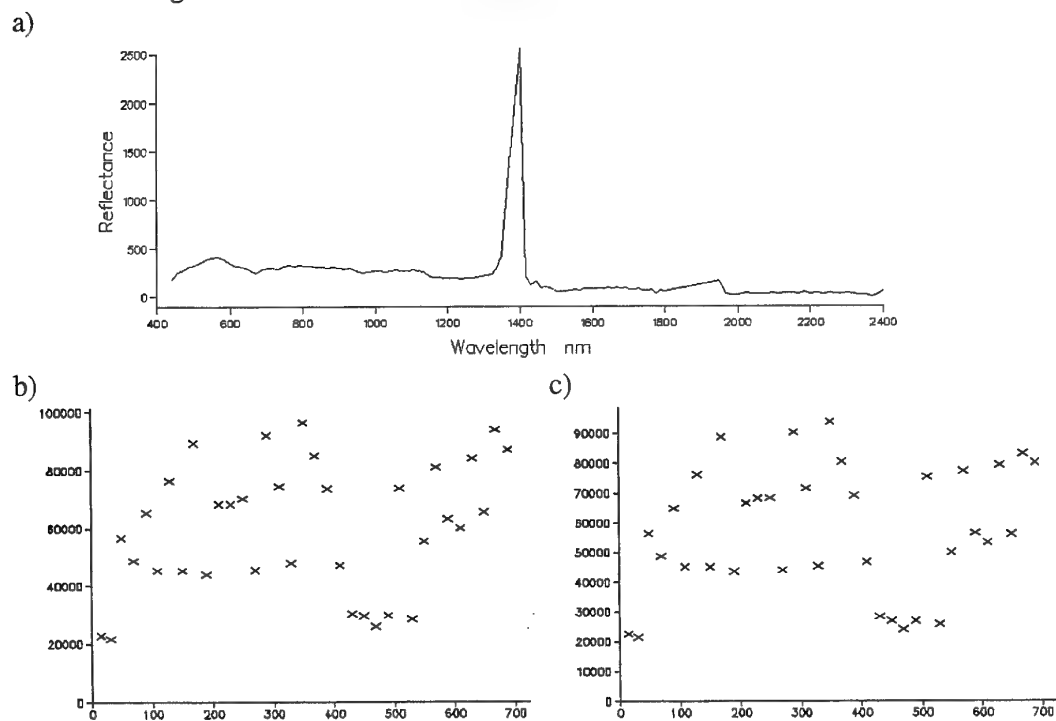
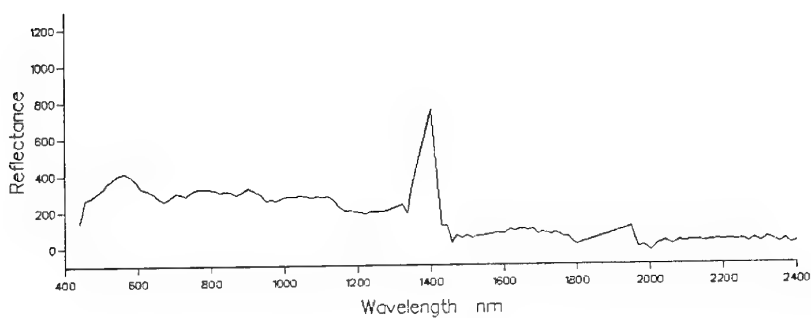
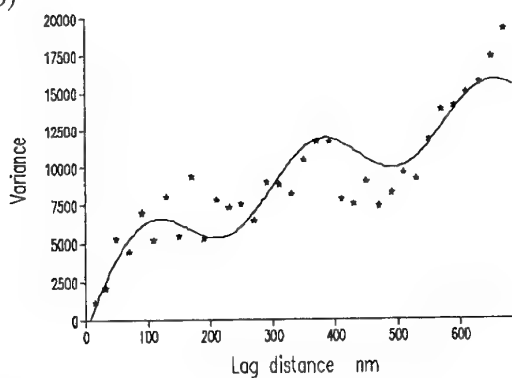


Figure 114. A.P. Hill: pixel **167**: a) spectrum, b) experimental variogram of raw data c) experimental variogram of linear residuals.

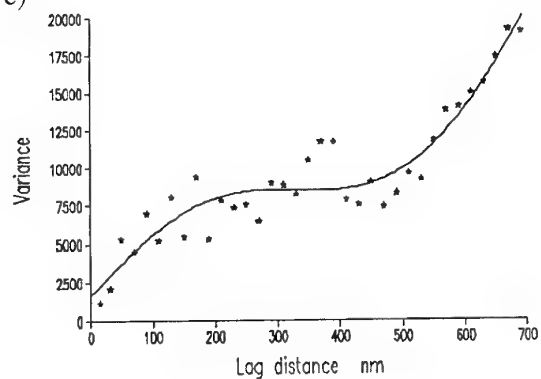
a)



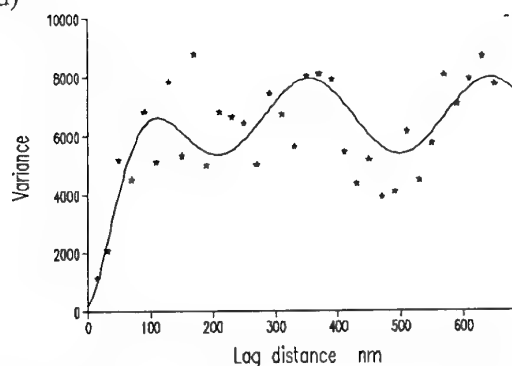
b)



c)



d)



e)

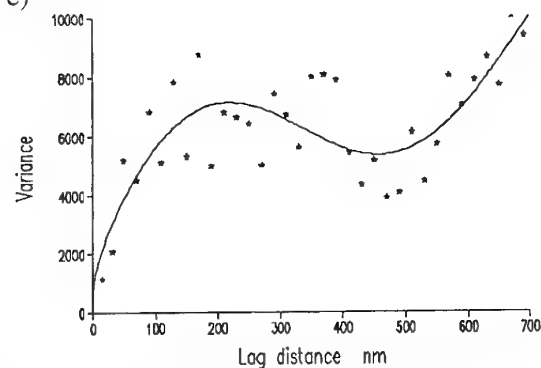


Figure 115. A.P. Hill: pixel **168**: a) spectrum, b) & c) experimental variogram and fitted models (PPF) of raw values, short and long wavelength d) & e) experimental variogram and fitted models of linear residuals - short wavelength PES and long wavelength PPF, respectively.

Table 8: Summary of trend analysis and model parameters of variograms for selected pixels for Fort A.P. Hill

Pixel	% trend removed		Trend	Model Fitted		Model Parameters								
	linear	quadratic				Used	PPF	PES	PEF	Nugget	Sill	Distance	Gradient	Exponent
1	9.2	52.3	Q			F	0	1.2E+06	239.6			248.3	96874	2.197
"	9.2	52.3	Q	F			0			6095	0.8349	726.1	195679	1.911
40	9.9	48.6	Q	F			0			69229	0.4522	244.1	114515	2.229
"	9.9	48.6	Q	F			0			3552	0.9490	783.4	307081	1.491
44	20.0	42.3	Q			F	0	1.1E+06	389.8			250.1	51297	2.574
"	20.0	42.3	Q	F			0			10679	0.6948	558.5	50849	3.103
50	21.4	40.6	Q			F	0	1.0E+06	313.9		1.2630	249.6	46023	2.620
"	21.4	40.6	Q	F			0			6392	0.7865	693.7	69732	2.819
54	20.9	43.1	Q			F	0	1.2E+06	344.2		1.1720	245.0	52823	2.267
"	20.9	43.1	Q	F			0			7959	0.7668	629.0	66375	3.075
65	19.8	41.1	Q			F	0	9.1E+05	327.4		1.1590	249.4	42694	2.562
"	19.8	41.1	Q	F			0			4399	0.8243	744.3	72047	2.349
75	19.1	40.8	Q			F	0	1.8E+06	905.2		0.7433	244.7	57908	2.392
76	20.8	40.9	Q			F	0	1.1E+06	324.3		1.2100	250.2	49225	2.599
"	20.8	40.9	Q	F			0			6387	0.7918	700.7	72066	2.689
79	21.3	40.2	Q			F	0	1.2E+06	313.3		1.2550	249.5	50889	2.659
"	21.3	40.2	Q	F			0			6351	0.8069	748.2	86600	2.562
87	18.9	41.6	Q			F	0	1.7E+06	308.4		1.2040	248.9	75989	2.538
"	18.9	41.6	Q	F			0			8137	0.8317	750.0	152570	2.355
90	20.5	42.0	Q			F	0	1.1E+06	326.4		1.1530	247.7	49035	2.453
"	20.5	42.0	Q	F			0			4657	0.8408	750.8	91291	2.287
104	16.4	42.9	Q			F	0	2.0E+06	301.0		1.1680	248.2	94916	2.493
"	16.4	42.9	Q	F			0			10754	0.8120	733.6	181498	2.347
107	19.8	40.8	Q			F	0	1.2E+06	308.6		1.2530	248.8	54333	2.624
"	19.8	40.8	Q	F			0			5839	0.8323	789.1	106535	2.366
115	19.3	43.6	Q			F	0	2.6E+06	372.5			250.2	119159	2.619
"	19.3	43.6	Q	F			0			30773	0.6661	521.9	129584	2.921
119	16.7	42.1	Q			F	0	2.7E+06	295.3		1.2160	248.5	121633	2.558
"	16.7	42.1	Q	F			0			14801	0.8100	743.8	242183	2.400
120	17.0	41.9	Q			F	0	2.8E+06	295.9		1.1990	247.4	126810	2.493
"	17.0	41.9	Q	F			0			15870	0.8081	725.4	258755	2.421
133	17.9	41.8	Q			F	0	2.4E+06	420.5			239.7	89353	2.085
"	17.9	41.8	Q	F			0			16544	0.7444	613.2	122421	3.009
139	12.6	46.9	Q			F	0	2.2E+06	258.2			243.8	146716	2.075
"	12.6	46.9	Q	F			0			10405	0.8425	714.0	340547	1.993
141	12.1	44.8	Q	F			0			15438	0.7878	698.8	336947	2.089
"	12.1	44.8	None			F	0	3.3E+06	287.7		1.3160	259.6	144847	3.011
"	12.1	44.8	None	F			0			29940	0.7338	615.5	232984	3.029
160	59.1	58.9	Q			F	0	1.2E+04	53.6			275.7	1983	1.894
"	59.1	58.9	Q	F			0			342.4	0.6043	757.5	5253	1.210
"	59.1	58.9	Lin			F	0	1.2E+04	53.9			275.9	1989	1.890
"	59.1	58.9	Lin	F			0			325.6	0.6130	758.2	5293	1.203
"	59.1	58.9	None	F			0			1618	0.3777	269.8	2826	2.279

F is best fitting model

PPF periodic with power function

PES periodic with stable function

PEF periodic exponential function

Q quadratic detrend

Lin linear detrend

L fitted model with longer wavelength

C fitted model with shorter lag distance

Table 8: Summary of trend analysis and model parameters of variograms for selected pixels for Fort A.P. Hill (continued)

Pixel	% trend removed		Trend	Model Fitted			Model Parameters							
	linear	quadratic		Used	PPF	PES	PEF	Nugget	Sill	Distance	Gradient	Exponent	Wavelength	Amplitude
165	34.4	34.1	Lin			F	0	3.0E+04	47.4			265.3	4921	2.134
"	34.4	34.1	Lin			F	0	3.0E+04	24.2			480.2	7768	3.090
"	34.4	34.1	None			F	0	3.0E+04	47.4			265.3	4921	2.134
"	34.4	34.1	None	F			0			544.2	0.6967	723.8	16742	1.371
166	63.9	63.6	Lin			F	0	1.0E+04	62.8			281.7	1719	1.576
"	63.9	63.6	Lin	F			0			308.7	0.5969	757.1	3905	1.162
"	63.9	63.6	None	F			0			752.5	0.4882	275.7	2444	1.968
168	70.7	70.6	Lin			F	0	6.7E+03	69.3		1.74	289.5	1274	1.385
"	70.7	70.6	Lin	F			0			235.7	0.57	722.6	2586	1.272
"	70.7	70.6	None	F			0			282.1	0.60	274.0	1911	2.153
"	70.7	70.6	None	F			0			2.581	1.39	800.0	4389	1.167

Q quadratic detrend
Lin linear detrend

F is best fitting model
PPF periodic with power function
PES periodic with stable function
PEF periodic exponential function

L fitted model with longer wavelength
C fitted model with shorter lag distance

Table 9. Eigenvalues and eigenvectors for Fort A. P. Hill using all spectra

Component Eigenvalue	PC1	PC2	PC3												
Percentage variance	81.0	13.8	1.6												
Waveband	PC1	PC2	PC3	Waveband	PC1	PC2	PC3	Waveband	PC1	PC2	PC3	Waveband	PC1	PC2	PC3
v1	-0.0785	-0.0273	-0.0193	v26	-0.0797	0.1412	0.0153	v67	-0.0959	-0.0342	-0.1003				
v10	-0.0792	-0.1287	0.0733	v27	-0.0798	0.1410	0.0139	v68	-0.0965	-0.0330	-0.0843				
v100	-0.0935	-0.0728	-0.0135	v28	-0.0800	0.1406	0.0129	v69	-0.0976	-0.0298	-0.0465				
v101	-0.0944	-0.0679	-0.0151	v29	-0.0801	0.1401	0.0122	v7	-0.0867	-0.0942	0.0898				
v102	-0.0951	-0.0635	-0.0085	v3	-0.0847	-0.1120	0.0495	v70	-0.0980	-0.0253	-0.0244				
v103	-0.0953	-0.0626	-0.0030	v30	-0.0806	0.1387	0.0113	v71	-0.0982	-0.0216	-0.0170				
v104	-0.0952	-0.0629	0.0025	v31	-0.0806	0.1386	0.0114	v72	-0.0983	-0.0182	-0.0131				
v105	-0.0952	-0.0629	0.0052	v32	-0.0815	0.1354	0.0129	v73	-0.0985	-0.0150	-0.0127				
v106	-0.0953	-0.0621	0.0058	v33	-0.0823	0.1325	0.0117	v74	-0.0985	-0.0131	-0.0086				
v107	-0.0953	-0.0612	0.0087	v34	-0.0832	0.1294	0.0119	v75	-0.0986	-0.0112	-0.0060				
v108	-0.0953	-0.0601	0.0063	v35	-0.0845	0.1243	0.0098	v76	-0.0986	-0.0099	-0.0055				
v109	-0.0957	-0.0576	0.0047	v36	-0.0849	0.1226	0.0082	v77	-0.0987	-0.0088	-0.0030				
v11	-0.0764	-0.1430	0.0674	v37	-0.0852	0.1214	0.0080	v78	-0.0987	-0.0078	-0.0020				
v110	-0.0960	-0.0547	0.0024	v38	-0.0852	0.1214	0.0103	v79	-0.0879	-0.0835	0.0913				
v111	-0.0960	-0.0547	0.0064	v39	-0.0853	0.1213	0.0116	v8	-0.0879	-0.0835	0.0913				
v112	-0.0959	-0.0552	0.0042	v4	-0.0826	-0.1233	0.0602	v80	-0.0987	-0.0070	0.0001				
v113	-0.0957	-0.0577	0.0033	v40	-0.0850	0.1223	0.0124	v81	-0.0987	-0.0072	-0.0003				
v114	-0.0955	-0.0601	0.0019	v41	-0.0848	0.1231	0.0127	v82	-0.0987	-0.0084	0.0026				
v115	-0.0951	-0.0630	0.0061	v42	-0.0846	0.1236	0.0136	v83	-0.0986	-0.0095	0.0045				
v116	-0.0949	-0.0647	0.0000	v43	-0.0846	0.1235	0.0135	v84	-0.0986	-0.0102	0.0025				
v117	-0.0949	-0.0649	0.0007	v44	-0.0850	0.1219	0.0142	v85	-0.0986	-0.0121	0.0081				
v118	-0.0945	-0.0675	0.0101	v45	-0.0856	0.1192	0.0144	v86	-0.0985	-0.0146	0.0062				
v119	-0.0941	-0.0697	0.0026	v46	-0.0869	0.1138	0.0143	v87	-0.0984	-0.0163	0.0097				
v12	-0.0781	-0.1400	0.0585	v47	-0.0881	0.1085	0.0085	v88	-0.0984	-0.0176	0.0115				
v120	-0.0930	-0.0749	-0.0022	v48	-0.0900	0.0992	0.0087	v89	-0.0984	-0.0176	0.0082				
v121	-0.0929	-0.0769	-0.0131	v49	-0.0912	0.0925	0.0058	v9	-0.0859	-0.0956	0.0839				
v122	-0.0910	-0.0808	-0.0202	v5	-0.0816	-0.1291	0.0618	v90	-0.0983	-0.0186	0.0052				
v123	-0.0899	-0.0863	0.0019	v50	-0.0919	0.0886	0.0071	v91	-0.0984	-0.0181	0.0028				
v124	-0.0877	-0.0828	-0.0063	v51	-0.0924	0.0851	0.0074	v92	-0.0983	-0.0175	0.0034				
v125	-0.0792	-0.0889	-0.0422	v52	-0.0927	0.0835	0.0080	v93	-0.0982	-0.0182	-0.0079				
v126	-0.0281	-0.0543	0.0699	v53	-0.0925	0.0848	0.0090	v94	-0.0965	-0.0173	-0.0021				
v13	-0.0766	-0.1452	0.0488	v54	-0.0921	0.0873	0.0087	v95	-0.0511	-0.0801	-0.2146				
v14	-0.0761	-0.1463	0.0452	v55	-0.0919	0.0882	0.0081	v96	-0.0876	-0.0967	-0.0508				
v15	-0.0770	-0.1435	0.0346	v56	-0.0919	0.0882	0.0091	v97	-0.0891	-0.0932	-0.0224				
v16	-0.0784	-0.1395	0.0259	v57	-0.0920	0.0877	0.0086	v98	-0.0910	-0.0815	-0.0394				
v17	-0.0797	-0.1345	0.0282	v58	-0.0923	0.0854	0.0083	v99	-0.0926	-0.0773	-0.0279				
v18	-0.0904	-0.0737	0.0484	v59	-0.0929	0.0819	0.0072								
v19	-0.0955	-0.0120	0.0540	v6	-0.0820	-0.1237	0.0749								
v2	-0.0850	-0.1020	0.0595	v60	-0.0936	0.0767	0.0055								

Table 9. Continued

Waveband	PC1	PC2	PC3	Waveband	PC1	PC2	PC3	Waveband	PC1	PC2	PC3
v20	-0.0900	0.0905	0.0429	v61	-0.0945	0.0698	0.0054				
v21	-0.0828	0.1280	0.0302	v62	-0.0947	0.0663	0.0010				
v22	-0.0798	0.1398	0.0231	v63	-0.0216	0.0137	-0.5719				
v23	-0.0788	0.1434	0.0185	v64	-0.0386	-0.0176	-0.5346				
v24	-0.0790	0.1432	0.0180	v65	-0.0657	-0.0171	-0.4417				
v25	-0.0793	0.1423	0.0170	v66	-0.0909	-0.0305	-0.1851				

Table 10 Classes from the non-hierarchical classification of Fort A. P. Hill spectra using 63 wavebands and the first three principal components

Pixel No	g7-63	g6-63	g6-pca	Pixel No	g7-63	g6-63	g6-pca	Pixel No	g7-63	g6-63	g6-pca
1	2	2	1	61	5	5	4	121	7	2	5
2	2	2	1	62	6	6	6	122	7	2	5
3	2	2	1	63	6	6	6	123	7	2	5
4	2	2	1	64	5	5	4	124	7	2	5
5	2	2	1	65	5	5	4	125	1	1	5
6	2	2	1	66	5	5	4	126	7	2	5
7	2	2	1	67	6	6	6	127	7	2	5
8	2	2	1	68	6	6	6	128	7	2	5
9	1	1	1	69	4	4	4	129	7	2	5
10	1	1	1	70	6	6	6	130	7	2	5
11	2	2	1	71	5	5	4	131	7	2	5
12	2	2	1	72	5	5	4	132	1	1	5
13	2	2	1	73	5	5	4	133	1	1	5
14	2	2	1	74	5	5	4	134	1	1	5
15	2	2	1	75	4	4	4	135	7	1	5
16	2	2	1	76	5	5	4	136	7	1	5
17	2	2	1	77	5	5	4	137	7	2	5
18	2	2	1	78	4	4	4	138	7	2	5
19	1	1	1	79	5	5	4	139	1	2	2
20	2	2	1	80	6	6	6	140	7	2	2
21	2	2	1	81	6	6	6	141	7	2	2
22	2	2	1	82	6	6	6	142	7	2	2
23	1	1	1	83	6	6	6	143	7	2	2
24	2	2	1	84	6	6	6	144	7	2	2
25	2	2	1	85	6	6	6	145	7	2	2
26	2	2	1	86	6	6	6	146	7	2	2
27	7	2	1	87	6	6	6	147	7	2	2
28	2	2	1	88	5	5	4	148	7	1	2
29	2	2	1	89	6	6	6	149	7	2	2
30	2	2	1	90	5	5	4	150	7	2	2
31	2	2	1	91	6	6	6	151	2	2	2
32	2	2	1	92	6	6	6	152	7	2	2
33	2	2	1	93	1	1	5	153	7	2	2
34	2	2	1	94	6	6	6	154	7	1	2
35	7	2	1	95	5	5	4	155	7	2	2
36	2	2	1	96	6	6	6	156	7	2	2
37	2	2	1	97	5	5	4	157	7	2	2
38	2	2	1	98	5	5	4	158	7	2	2
39	2	2	1	99	6	6	6	159	7	2	2
40	1	1	1	100	6	6	6	160	3	3	3
41	2	2	1	101	5	5	4	161	3	3	3
42	2	2	1	102	6	6	6	162	3	3	3
43	2	2	1	103	6	6	6	163	3	3	3
44	4	4	4	104	2	2	5	164	3	3	3

Table 10. Continued

Pixel No	g7-63	g6-63	g6-pca	Pixel No	g7-63	g6-63	g6-pca	Pixel No	g7-63	g6-63	g6-pca	Pixel No	g7-63	g6-63	g6-pca	g6-63	g6-pca	g6-63	g6-pca	g6-63	g6-pca
45	5	5	4	105	1	1	5	165	3	3	5	165	3	3	5	3	3	3	3	3	3
46	5	5	4	106	6	6	4	166	3	3	6	166	3	3	6	3	3	3	3	3	3
47	5	5	4	107	6	6	4	167	3	3	6	167	3	3	6	3	3	3	3	3	3
48	5	5	4	108	7	2	4	168	3	2	5	168	3	3	5	3	3	3	3	3	3
49	4	4	4	109	7	2	4	169	3	2	5	169	3	3	5	3	3	3	3	3	3
50	5	5	4	110	7	2	4	170	3	2	5	170	3	3	5	3	3	3	3	3	3
51	5	5	4	111	1	1	4	171	3	1	5	171	3	3	5	3	3	3	3	3	3
52	5	5	4	112	7	2	4	172	3	2	5	172	3	3	5	3	3	3	3	3	3
53	5	5	4	113	7	2	4														
54	5	5	4	114	7	2	4														
55	5	5	4	115	1	1	4														
56	5	5	4	116	7	2	4														
57	4	4	6	117	7	1	6														
58	5	5	4	118	7	2	4														
59	5	5	4	119	7	2	4														
60	5	5	4	120	7	2	4														

g7-63 represents the classification using 63 spectra and a 7-group subdivision.

g6-63 represents the classification using 63 spectra and a 6-group subdivision.

g6-pca represents the classification using the first three principal components a 6-group subdivision.

APPENDIX I

This is a GenStat program to fit periodic models to the variogram. This was written to fit models to the spectra in the preceding report. The following functions can be fitted:

- a) simple periodic, b) periodic with phase shift, c) periodic with power function, d) periodic with exponential function, and e) periodic with stable exponential function.

A file with variogram values is appended so that the program can be tested.

```

job 'variogram fitting'
scalar a1, top, bot, pi
scalar rex, nugg, wave, cfun, sfun, grad, alpha
calc pi=3.14159

calc bot=0
calc top=100
calc top=top*(top.gt.0)
text [nval=2] title
text [nval=1] label
frame window=1,2,3,4; ylower=0.20,0.12,0.32,0.52; \
  yupper=0.8,0.47,0.87,0.87; \
  xlower=0.1,0.48,0.10,0.48; xupper=0.9,0.93,0.8,0.93

variate [nval=201] dpar2, dpar1, ypow, yper, yabs
variate [nval=201] xlag; values=!(1...201)
variate [nval=201] yvar
variate [nval=2] xdv,ydv
  calc rex=400
  calc xlag=(xlag-1.0)*rex/200
  calc xdv$[1]=0
  calc xdv$[2]=rex

"
open 'testper.gra'; channel=4 ; filetype=graphics
device 4
"

open '2fthd_37n.gam'; channel=2
read [channel=2] title
print title
read [channel=2] label
print label
read [channel=2; setnvalues=y; skip=*] lag, gam, wt
graph[nr=19; nc=45] gam;lag;meth=p

print 'Model: unbounded linear'
model [weights=wt] gam; residuals=R; fittedvalues=F
fit lag

print '***** Periodic model with phase *****'
print ' weights = npairs '
expression periodic[1,2]; \
value=!e(c1 = (cos(2*pi*lag/a1))), \

```

DRAFT

```

!e(c2 = (sin(2*pi*lag/a1)))
model [weights=wt; distribution=normal] gam; fittedvalues=F
rcycle a1; initial = 300; upper=500; lower=50
fitnonlinear [print=monitoring; calculation=periodic[]] c1,c2

rkeep estimates=kest
print kest
calc wave=kest$[1]
calc cfun=kest$[2]
calc sfun=kest$[3]
calc nugg=kest$[4]
calc hypo=sqrt(sfun*sfun+cfun*cfun)
calc phi=arccos(cfun/hypo)
calc amp=cfun/cos(phi)
print amp, phi
calc yabs=0
calc dpar2=2*pi*xlag/wave
calc yper=cfun*(cos(dpar2))+sfun*(sin(dpar2))
calc yvar=yper+nugg
pen 19; size=1.0
axes window=1; pen=19; \
  xtitle='Lag distance'; \
  ytitle='Variance'; \
  ylower=bot; yupper=top; xlower=0; xupper=rex; \
  xmarks=!(0,100...300) ; ymarks=!(0,20...100)
"    ylabels=!t('0','1.0','2.0','3.0') "
"    ylabels=!t('0','0.2','0.4','0.6','0.8','1.0')"

pen 1,2; linestyle=1,0; colour=1; method=monotonic, point; \
  symbols=0,4; thickness=2.0; size=0.7
dgraph [window=1; keywindow=0; title='Variogram'] \
  y=yvar, gam; x=xlag, lag; pen=1,2

print '***** Periodic model *****'
print ' weights = npairs '
expression periodic[1]; \
value=!e(c1 = (cos(2*pi*lag/a1)))
model [weights=wt; distribution=normal] gam; fittedvalues=F
rcycle a1; initial = 300; upper=500; lower=50
fitnonlinear [print=monitoring; calculation=periodic[]] c1
rkeep estimates=kest
print kest
calc wave=kest$[1]
calc cfun=kest$[2]
calc sfun=0

calc nugg=kest$[3]
calc hypo=sqrt(sfun*sfun+cfun*cfun)
calc phi=arccos(cfun/hypo)
calc amp=cfun/cos(phi)
print amp, phi
calc yabs=0
calc dpar2=2*pi*xlag/wave
calc yper=cfun*(cos(dpar2))+sfun*(sin(dpar2))
calc yvar=yper+nugg
pen 19; size=1.0
axes window=1; pen=19; \
  xtitle='Lag distance'; \
  ytitle='Variance'; \
  ylower=bot; yupper=top; xlower=0; xupper=rex; \
  xmarks=!(0,100...300) ; ymarks=!(0,20...100); \
"    ylabels=!t('0.2','0.4','0.6','0.8','1.0')"
pen 1,2; linestyle=1,0; colour=1; method=monotonic, point; \
  symbols=0,4; thickness=2.0; size=0.7

```

DRAFT

```
dgraph [window=1;keywindow=0;title='Variogram'] \
  y=yvar,gam; x=xlag,lag; pen=1,2

print '*** Periodic model with phase shift and power function ***'
print ' weights = npairs '
expression periodicpower[1,2,3]; \
value=!e(c1 = (cos(2*pi*lag/a1))), \
      !e(c2 = (sin(2*pi*lag/a1))), \
      !e(c3=((lag**a2)))

model [weights=wt; distribution=normal] gam; fittedvalues=F
rcycle a1,a2; initial = 400, 1.0; upper=800,1.9; lower=5,0.1
fitnonlinear [constant=omit;\
  calculation=periodicpower[]] c1,c2,c3

rkeep estimates=kest
print kest
calc wave=kest$[1]
calc cfun=kest$[3]
calc sfun=kest$[4]
calc nugg=0
calc grad=kest$[5]
calc alpha=kest$[2]

calc hypo=sqrt(sfun*sfun+cfun*cfun)
calc phi=arccos(cfun/hypo)
calc amp=cfun/cos(phi)

print amp, phi, nugg, wave, grad, alpha

calc yabs=0
calc dpar2=2*pi*xlag/wave
calc yper=cfun*(cos(dpar2))+sfun*(sin(dpar2))
calc ypow=grad*xlag**alpha
calc yvar=nugg+ypow+yper

pen 19; size=1.0
axes window=1; pen=19; \
  xtitle='Lag distance'; \
  ytitle='Variance'; \
  ylower=bot; yupper=top; xlower=0; xupper=rex; \
  xmarks=!(0,100...700) ; ymarks=!(0,2000...8000)
"
; \
  ylabel=!(t('0','1.0','2.0','3.0'))
"

pen 1,2; linestyle=1,0; colour=1;method=monotonic,point; \
  symbols=0,4; thickness=2.0; size=0.7
dgraph [window=1;keywindow=0;title='Variogram'] \
  y=yvar,gam; x=xlag,lag; pen=1,2

print '***** Periodic model with phase and exponential
function*****'
print ' weights = npairs '
expression periodicexp[1,2,3]; \
value=!e(c1 = (cos(2*pi*lag/a1))), \
      !e(c2 = (sin(2*pi*lag/a1))), \
      !e(c3=(1.0-exp(-(lag/a2))))

model [weights=wt; distribution=normal] gam; fittedvalues=F
rcycle a1,a2; initial = 400,100; upper=900,500; lower=5,1
```

DRAFT

```

fitnonlinear [constant=omit; calculation=periodicexp[]] \
              c1,c2,c3
rkeep estimates=kest
print kest
calc wave=kest$[1]
calc cfun=kest$[3]
calc sfun=kest$[4]
calc nugg=0
calc dist=kest$[2]
calc sill=kest$[5]

calc hypo=sqrt(sfun*sfun+cfun*cfun)
calc phi=arccos(cfun/hypo)
calc amp=cfun/cos(phi)

print sill, dist, amp, cfun, sfun, wave

calc yabs=0

calc dpar2=2*pi*xlag/wave
calc yper=cfun*(cos(dpar2))+sfun*(sin(dpar2))
calc dpar1=xlag/dist
calc yexp=sill*(1.0-exp(-dpar1))

calc yvar=nugg+yexp+yper

pen 19; size=1.0
axes window=1; pen=19; \
  xtitle='Lag distance'; \
  ytitle='Variance'; \
  ylower=bot; yupper=top; xlower=0; xupper=rex; \
  xmarks=!(0,100...700) ; ymarks=!(0,1000...7000)
"  ylabels=!(t('0','1.0','2.0','3.0')) "
pen 1,2; linestyle=1,0; colour=1; method=monotonic,point; \
  symbols=0,4; thickness=2.0; size=0.7
dgraph [window=1; keywindow=0; title='Variogram'] \
  y=yvar,gam; x=xlag,lag; pen=1,2

"
print '*** Periodic model with phase shift and stable function ***'
print ' weights = npairs '
expression periodicexpst[1,2,3]; \
value=!e(c1 = (cos(2*pi*lag/a1))), \
      !e(c2 = (sin(2*pi*lag/a1))), \
      !e(c3=(1.0-exp(-(lag/a2))))

model [weights=wt; distribution=normal] gam; fittedvalues=F
rcycle a1,a2; initial = 400,100; upper=800,1000; lower=5,1
fitnonlinear [constant=omit; \
              calculation=periodicexpst[]] c1,c2,c3
"
print '*** Periodic model with phase shift and stable function ***'
print ' weights = npairs '
expression periodicexpst[1,2,3]; \
value=!e(c1 = (cos(2*pi*lag/a1))), \
      !e(c2 = (sin(2*pi*lag/a1))), \
      !e(c3=(1.0-exp(-((lag*a3)/(a2**a3)))))

model [weights=wt; distribution=normal] gam; fittedvalues=F
rcycle a1,a2,a3; initial = 400,100,1; upper=800,1000,2;
lower=5,0.1,0.1;\
step=0.1,0.1,0.01
fitnonlinear [const=omit; \

```


DRAFT

```
calculation=periodicexpst[] c1,c2,c3
rkeep estimates=kest
print kest
calc wave=kest$[1]
calc cfun=kest$[4]
calc sfun=kest$[5]
calc nugg=0
calc alpha=kest$[3]
calc dist=kest$[2]
calc sill=kest$[6]

calc hypo=sqrt(sfun*sfun+cfun*cfun)
calc phi=arccos(cfun/hypo)
calc amp=cfun/cos(phi)

print sill, dist, amp, cfun, sfun, wave, alpha

calc yabs=0

calc dpar2=2*pi*xlag/wave
calc yper=cfun*(cos(dpar2))+sfun*(sin(dpar2))
calc dpar1=xlag**alpha/dist**alpha
calc yexps=sill*(1.0-exp(-dpar1))

calc yvar=nugg+yexps+yper

pen 19; size=1.0
axes window=1; pen=19; \
  xtitle='Lag distance'; \
  ytitle='Variance'; \
  ylower=bot; yupper=top; xlower=0; xupper=rex; \
  xmarks=!(0,100...700) ; ymarks=!(0,1000...8000)
" ylabels=t('0','1.0','2.0','3.0') "
pen 1,2; linestyle=1,0; colour=1; method=monotonic, point; \
  symbols=0,4; thickness=2.0; size=0.7
dgraph [window=1;keywindow=0;title='Variogram'] \
  y=yvar,gam; x=xlag,lag; pen=1,2

stop
```

Variogram values

Lag[0]	Vgram[0]	Count[0]
Fort Hood 2		
:		
Position 37		
:		
12.0	3.52	234.0

DRAFT

29.6	7.45	278.0
49.4	14.58	249.0
69.4	23.31	235.0
89.4	37.41	208.0
109.5	49.72	201.0
129.6	58.94	177.0
149.3	67.37	169.0
169.6	72.55	163.0
189.5	86.05	141.0
209.3	90.44	135.0
229.5	90.36	122.0
249.3	74.24	108.0
269.5	49.30	101.0
289.6	24.11	94.0
309.9	8.45	91.0

:

APPENDIX II

Paper submitted to International Journal of Remote Sensing – please do not quote from this or use the information therein.

Using the Variogram to Explore Imagery of Two Different Spatial Resolutions

M. A. OLIVER¹, J. A. SHINE² and K. R. SLOCUM²

¹ Department of Soil Science, University of Reading, Whiteknights, Reading RG6 6DW, United Kingdom.

² United States Army Topographic Engineering Center, 7701 Telegraph Road, Alexandria, Virginia 22315-3864, USA

Abstract. The resolution of remotely sensed data is becoming increasingly fine, and there are now many sources of data with a pixel size of 1 m × 1 m. This produces huge amounts of data that have to be stored, processed and transmitted. For environmental applications this resolution possibly provides far more data than are needed; data overload. This poses the question: how much is too much? We have explored two resolutions of data, 1-m pixel CAMIS data and 20-m pixel SPOT data, using the variogram of geostatistics. For both we used the normalized difference vegetation index (NDVI). It is clear that there is more information in the 1-m data and three scales of spatial variation were identified: a short scale of about 25 m, an intermediate one of about 150 m and a much longer one of about 600 m. We sub-sampled the 1-m data and identified an additional scale of variation of about 300 m. The latter and the short spatial scale were identified consistently until the sub-sample was 1 pixel in 15 for each row and column (or 1 pixel in 225). At this stage spatial scales of about 100 m and 600 m were described, which suggested that only now was there a real difference in the amount of information available. We compared the results of this analysis with the variogram of the SPOT data. Similar spatial scales to those from the sub-sampled 1-m data were identified. From this analysis it seems that a pixel size of 20-m is adequate for many environmental applications, and that if more detail is required the 1-m data could be sub-sampled to 1 pixel in 10 for every row and column without any serious loss of information. This reduces significantly the amount of data that needs to be stored, transmitted and analysed and has important implications for data compression.

1. Introduction

The applications of remotely sensed imagery are constantly increasing as are the capabilities for increasingly fine spatial resolution. Aerial images contain large amounts of information, both spatial (pixels) and spectral (wavebands) data. As the resolution increases this results in vastly more information: imagery with a spatial resolution of 1 m × 1 m per pixel contains 400 times as much data as that with a pixel size of 20 m × 20 m. A wide variety of satellite sensors will provide information at 1-m or near 1-m resolution in the next few years (Aplin *et al.*, 1997). Sensor systems such as IKONOS (Space Imaging, Corp., panchromatic channel) and CAMIS

(Computerized Airborne Multispectral Imaging System) already achieve this resolution (Carder, 1993; Baker, 1999). Hyperspectral imagery, such as HYDICE, has many more wavebands than the conventional imagery of SPOT (4 bands) or Landsat TM (7 Bands). For example SEBASS thermal hyperspectral imagery has 128 wavebands. With such data, if the spatial resolution is the same as that for a SPOT image, then there are almost 42 times more data. In this paper we consider the spatial resolution of the data only.

If both the resolution and spectral information are increased then it is clear how the amount of information will expand. There are consequences of this for data storage, transfer and analysis. It is evident that 1-m imagery contains more information than that at coarser resolutions, such as the 20-m SPOT data, but this raises two questions. How much of the additional information is of real use? What are the relative costs of obtaining, analysing and storing the extra data? Acquiring and storing 1-m data may entail a significant cost, even in an era of cheaper hardware and constantly increasing memory availability. The speed and accuracy with which data can be transferred and processed will be improved by reducing the data optimally for future use. The extent of data compression will depend on the degree of redundancy present in the data and what the future uses are likely to be. By examining 1-m imagery at a range of resolutions it might determine the stages at which crucial spatial information is lost and, therefore, whether processing the full set of data is worthwhile.

Geostatistics has been applied successfully to remotely sensed data in a range ways, for example to improve image classification (Abarca-Hernandez and Chica-Olmo, 1999), to monitor crop growth (Erickson *et al.*, 1999), and to design optimal sampling schemes for ground surveys (Oliver *et al.*, 2000). In this paper we use the variogram of Regionalized Variable Theory to compare the data from a SPOT satellite image and 1-m CAMIS imagery over eastern Virginia in the United States. The 1-m data were sub-sampled to explore a range of distances between pixels, but less than that of the SPOT 20-m pixel. The analysis used the normalized difference vegetation index (NDVI) for both sets of data. The NDVI is related to the proportion of photosynthetically absorbed radiation and it is therefore useful for identifying changes in ground cover and possibly separating landscape features. Chavez (1992) showed that the NIR waveband contains greater within-scene variation than the red green or blue wavebands. Since NDVI incorporates NIR maximum variability is ensured.

2. The study area and image data

The area studied is part of Fort A. P. Hill in northeastern Virginia. It is located on the gently undulating terrain of the Atlantic Coastal Plain of the United States of America. The site was selected because of its complex topography which gives rise, in part, to the diversity in land cover in a small geographic area. The study area has been intensely dissected by many small ephemeral drainage channels that help to recharge the many ponds and wetlands, but the average relief is only about 15 m. Some of these ponds are evident as blue areas in the pixel map of NDVI from the SPOT image, Figure 1. Drainage is to two main river basins: the Rappahannock and the James. Hence there is a significant watershed crossing the Fort in an W-E direction. The area has mixed land use, the most extensive of which are the hardwood, pine and mixed

forests. In addition there is maintained grassland, shrub, and man-made features such as buildings and roads.

2.1. The images

The image obtained from the SPOT satellite has three wavebands, green (G), red (R) and near infrared (NIR). The normalized difference vegetation index was calculated from the red and NIR wavebands using the usual equation. The part of the SPOT image analysed had 178 rows and 151 columns, giving a total of 26 878 pixels. It covered an area of 3.6 km \times 3.0 km. The 20-m pixel size of the SPOT image was the largest spatial resolution examined in this analysis. The 1 m \times 1 m pixel image obtained from CAMIS sensors has four wavebands, blue (B), green (G), red (R) and NIR. As for SPOT the NDVI was calculated. There were some gaps in the cover of this image because it was formed from a photo-mosaic, comprising 8 499 498 pixels, Figure 2. Both images covered more or less the same area. To explore fully the range of spatial structures that might be present at different scales, the 1-m data was sub-sampled to provide information at an increasingly large separation. At the same time this reduced the amount of data for analysis substantially. Another way of achieving this would have been to average the digital information over the relevant block of pixels. This would have changed the support of the original data and would have reduced the variance present. Since our aim was to examine the extent of redundancy in the data we did not modify the original data by increasing the pixel size. The effect of this is something that should be explored in the future.

Figure 2 shows the effect of combining several separate 1-m images to cover the study area; the colour intensity is not uniform. Since this could affect the variogram analysis we limited the sub-sampling to a maximum separation of 1 pixel in every 15 along each row and column (or 1 pixel in a block of 225). This ensured that the comparisons between pixels did not extend over distances much larger than 1000 m (about a third of the extent of the area).

The first sub-sample retained one pixel in every two along each row and column. This gave a 2-m separation between the centroids of neighbouring pixels. This achieved a 75 % reduction in the data. This process was repeated to give a 3-m separation between pixels (89 % reduction in data), a 6-m separation (97.22 % reduction in data), pixels 10-m apart (99 % reduction in data), and pixels 15-m apart (99.6 % reduction in data). After the last reduction there were 37 553 pixels in the data, which was still more than the number of SPOT pixels.

3 Methodology

Spatial properties vary from place to place and this can occur at more than one scale simultaneously. As a result the spatial structures can vary at scales that differ by several orders of magnitude, from a few metres to hundreds of kilometres. This is known as nested variation. Such variation in spatial properties, including that in spectral imagery, can be described using the theory and methods of *geostatistics* (Oliver *et al.*, 2001). The *variogram* is the central tool of this methodology; it provides an unbiased description of the scale and pattern of spatial variation. It does so by measuring the degree of spatial correlation between sampling points, based on

the notion that the property is more likely to be similar at nearby locations than at distant ones (Webster and Oliver, 2001). The variogram is defined by:

$$\gamma(\mathbf{h}) = \frac{1}{2} E \left[\{Z(\mathbf{x}) - Z(\mathbf{x} + \mathbf{h})\}^2 \right] \quad (1)$$

where $Z(\mathbf{x})$ and $Z(\mathbf{x} + \mathbf{h})$ are the values of Z , the property of interest, at any two places \mathbf{x} and $\mathbf{x} + \mathbf{h}$ separated by \mathbf{h} , which is a vector in both distance and direction, known as the *lag*. The symbol E denotes the expectation. The semivariance, γ , at a given separation is half the expected squared difference between values at that separation. It summarises the way in which the variance of a property changes as the distance and direction separating any two points varies.

We used variography to explore the spatial information in the SPOT and 1-m image data. The standard computing formula for estimating the semivariance at a given lag, \mathbf{h} is:

$$\hat{\gamma}(\mathbf{h}) = \frac{1}{2M(\mathbf{h})} \sum_{i=1}^{M(\mathbf{h})} \{z(\mathbf{x}_i) - z(\mathbf{x}_i + \mathbf{h})\}^2 \quad (2)$$

where $\hat{\gamma}(\mathbf{h})$ is the estimate of $\gamma(\mathbf{h})$, $z(\mathbf{x}_i)$ and $z(\mathbf{x}_i + \mathbf{h})$ are the observed values of Z (the digital numbers in this case) at \mathbf{x}_i and $\mathbf{x}_i + \mathbf{h}$ respectively, and $M(\mathbf{h})$ is the number of paired comparisons at that lag. By changing \mathbf{h} an ordered set of values is obtained, and this is the sample or experimental variogram.

Mathematical functions or models were fitted to the experimental variogram by weighted least squares approximation using GenStat (Payne, 2000). The parameters of the variogram model describe the structure of the spatial variation and the scale(s) of variation present.

4. Analysis and results

Experimental variograms were computed from the digital numbers of the three wavebands of the SPOT image and for the normalized difference vegetation index (NDVI). Since the results for all are similar we describe those for NDVI only. Variograms were computed along the rows and columns of the SPOT image, and these were then averaged to give the overall variogram. They were computed to a maximum lag of 100 pixels (2000 m) for SPOT imagery and 1000 pixels (1000 m) for CAMIS imagery.

Figure 3a shows the average experimental variogram for NDVI from the SPOT image computed to a lag of 100. It is evident that after a lag of about 40 pixels the experimental semivariances become erratic and after a lag of 80 pixels they start to

decrease. Since both of these features can have an adverse effect on modelling the variogram we fitted models to maximum lags of 40 and 80 pixels. A range of authorized mathematical functions was tried; this range is somewhat limited because they must be conditional negative semi-definite (see Webster and Oliver, 2001). The best fitting models to the experimental variograms, in the least squares sense, were nested exponential and spherical functions, which describe more than one spatial scale. Double exponential and spherical functions fitted all experimental variograms, except for that for the 1-m lag, which was fitted best by a triple spherical function. The equation for the double spherical function is:

$$\begin{aligned}\gamma(h) &= c_0 + c_1 \left\{ \frac{3h}{2a_1} - \frac{1}{2} \left(\frac{h}{a_1} \right)^3 \right\} + c_2 \left\{ \frac{3h}{2a_2} - \frac{1}{2} \left(\frac{h}{a_2} \right)^3 \right\} & \text{for } h \leq a_1 \\ \gamma(h) &= c_0 + c_1 + c_2 \left\{ \frac{3h}{2a_2} - \frac{1}{2} \left(\frac{h}{a_2} \right)^3 \right\} & \text{for } h \leq a_2 \\ \gamma(h) &= c_0 + c_1 + c_2 & \text{for } h > a_2\end{aligned}\quad (3)$$

where c_0 is the nugget variance, c_1 is the autocorrelated variance or sill and a_1 is the correlation range or range of spatial dependence of the first spatial structure, and c_2 is the autocorrelated variance and a_2 is the range of the second spatial structure.

The triple spherical function is given by:

$$\begin{aligned}\gamma(h) &= c_0 + c_1 \left\{ \frac{3h}{2a_1} - \frac{1}{2} \left(\frac{h}{a_1} \right)^3 \right\} + c_2 \left\{ \frac{3h}{2a_2} - \frac{1}{2} \left(\frac{h}{a_2} \right)^3 \right\} + c_3 \left\{ \frac{3h}{2a_3} - \frac{1}{2} \left(\frac{h}{a_3} \right)^3 \right\} & \text{for } h \leq a_1 \\ \gamma(h) &= c_0 + c_1 + c_2 \left\{ \frac{3h}{2a_2} - \frac{1}{2} \left(\frac{h}{a_2} \right)^3 \right\} + c_3 \left\{ \frac{3h}{2a_3} - \frac{1}{2} \left(\frac{h}{a_3} \right)^3 \right\} & \text{for } h \leq a_2 \\ \gamma(h) &= c_0 + c_1 + c_2 + c_3 \left\{ \frac{3h}{2a_3} - \frac{1}{2} \left(\frac{h}{a_3} \right)^3 \right\} & \text{for } h \leq a_3 \\ \gamma(h) &= c_0 + c_1 + c_2 + c_3 & \text{for } h > a_3\end{aligned}\quad (4)$$

where c_3 is autocorrelated variance and a_3 is the range of the third spatial structure.

The nested exponential function is given by:

$$\gamma(h) = c_0 + c_1 \{1 - \exp(-h/r_1)\} + c_2 \{1 - \exp(-h/r_2)\} \quad (5)$$

where r_1 and r_2 are the distance parameters of the short-range and long-range spatial components, respectively. The exponential model reaches its sill asymptotically and therefore does not have a definite range of spatial dependence; a working range can be obtained as $a = 3r$.

In the first instance we fitted double spherical and exponential functions to the average experimental variogram computed to a maximum lag of 80 pixels. The best fitting model was the nested exponential one, which has an asymptotic sill as shown in Figures 3b: the symbols are the experimental values and the solid line is the fitted model. The double spherical model is not such a good fit as shown in Figure 3f and by the residual mean square (RMS) in Table 2. The parameters of the fitted models are given in Table 2.

Fitting models to variograms is one of the most controversial aspects of geostatistics; there are no hard and fast rules and no consensus on whether to fit by eye or statistically. We prefer the latter because it provides a means of objective comparison between different models. From experience we know that model fitting is affected by any erratic behaviour in the experimental values. Figures 3a and b show that after a lag of about 40 pixels the variograms fluctuate about their sills.

On closer inspection of the variogram computed to a lag 80 pixels it seemed more sensible to model the experimental variogram to a maximum lag of 40 pixels to achieve a better fit. Table 1 gives the best fitting model to the rows, columns and the average variograms to lag 40 pixels, Figure 3 c, d, and e, respectively. A double spherical provided the best fit in all cases because these variograms flatten to a distinct sill. Table 2 gives the model parameters; particular attention should be paid to the short- and long-range spatial structures. The variogram of the columns suggests that both spatial components have shorter ranges in an E-W direction than those for the rows in the N-S direction. Thus the variation is anisotropic. However, Figure 1 of the NDVI values does not suggest that this is pronounced. Four spatial scales of variation emerge from these variograms: about 130 m, 340 m, 450 m, and 640 m.

We analysed all of the wavebands of the 1-m imagery, but we give the results for NDVI only. We also computed variograms of the rows, columns and average, but we present the results of the average variograms only. The observed differences between those of the rows and columns were similar to those for the SPOT data. We computed the variogram from the 1-m data to a maximum lag of 1000 m, but fitted the model to 800 m, Figure 4a. The double functions fitted to the SPOT data did not provide such a good fit and triple functions were also fitted. The triple spherical model provided the best fit, Figure 4a shows the experimental variogram and best fitting model, and Table 2 gives the model parameters. The double exponential model provided the best fit to all of the variograms of the subsets.

The triple spherical variogram model fitted to the pixels separated by 1-m has a short-range component that matches that of the variograms from the first five sub-samples reasonably (see Table 3). The middle-range component matches that of the short-range component identified in the SPOT image, and the longest range matches that of the longest range fitted to both the SPOT data and to the 1 in 15 sub-sample. The variograms of the sub-samples are remarkably consistent except for the largest pixel spacing of the 1 in 15 sub-sample (1 pixel in a block of 225), Figure 4g. The scale of spatial dependence of the short-range component for the 2-m, 3-m, 4-m, 6-m and 10-m, Figure 4b, c, d, e and f separations is about 33 m, and that for the long-range one is between 310 m and 346 m. There is no equivalent of this short-range component in

the SPOT data because it is close to the size of the pixels. For the longer-range component this is close to the short-range parameter of the average variogram computed to the longer maximum lag (80 pixels), Table 2. For the largest separation between pixels of 1 in 15 the long- and short-range components are similar to those of the average variogram for the shorter maximum lag (40 pixels) for the SPOT data and to the largest range fitted to the 1-m data.

6. Discussion and Conclusions

For these particular data one outstanding conclusion from the results is that for the 1-metre CAMIS imagery there is little to be gained in terms of detecting spatial structures of environmental interest with pixels less than 10-m apart. Therefore, the original 1-m data could be compressed by 1:100 in 2-D space, reducing the data by ~~an~~ 99 % without affecting the variogram results. This suggests that substantial compression of huge 1-metre imagery data sets is possible without losing significant spatial information. On the other hand if information about man-made features or individual trees is of interest then this will not be so, but for imagery that is to be used for monitoring the landscape and other environmental tasks, this degree of data compression would be feasible.

The results of the 1-m data analysis are remarkably consistent in terms of the spatial scales that they identify, and the longer ones match with scales of variation identified from the SPOT data. Nevertheless, the analysis of the 1-m imagery identifies a scale of spatial variation that is not evident from the SPOT data of the same region (Fort A.P. Hill, Virginia, USA). This scale of variation of about 30-m appears because of the increased resolution of the CAMIS imagery. It can be seen on the imagery, Figure 2, and appears as 'pock marks'. It seems likely that this is a shadowing effect from the trees. The scales of variation identified in the sub-sample of 1 pixel in every 15 rows and every 15 columns are similar to those identified from the SPOT data when the maximum lag to which the variogram was calculated is 40 pixels. This finding is significant as researchers attempt to move seamlessly from one scale of spatial resolution to another to satisfy the needs in multi-purpose landscape characterization.

For the SPOT data modelling the variogram was more difficult because of fluctuations in the experimental semivariances once the sill had been reached. Several permutations of modelling these variograms were tried and the results differed more or less (see Figure 3b and f). The approach to modelling can vary according to what the model is to be used for. A principal reason for modelling the variogram is to provide the spatial information needed for geostatistical prediction, kriging. In this case the fit of the variogram close to the origin is the most important because the first few lags only are generally used in local estimation. For exploring the spatial scales of variation present the overall fit of the model to different maximum lags becomes important and that is the approach that we have adopted here.

A geostatistical comparison between information at different pixel separations provides an opportunity for deciding what level of data compression would be acceptable in an objective way. This could be investigated further by examining the quality of predictions from different methods of data restoration such as kriging and wavelet analysis using a cross validation procedure (Oliver, *et al.*, 2000).

7. Acknowledgement

This work has been funded by the United States Army, contract number N68171-97-C-9029.

8. References

- ABARCA-HERNANDEZ, F. and CHICA-OLMO, M., 1999, Evaluation of geostatistical measures of radiometric spatial variability for lithologic discrimination in Landsat TM images. *Photogrammetric Engineering and Remote Sensing*, **65**, 705-711.
- APLIN, ATKINSON and CURRAN, 1997. Fine spatial resolution satellite sensors for the next decade. *International Journal of Remote Sensing*, **18**, 3873-3881.
- BAKER, J., and SUN, X., 1999, A Hyperspectral/Multispectral Imaging System and its Image Georeference, *Proceedings of the Fourth International Airborne Remote Sensing Conference and Exhibition/21st Canadian Symposium on Remote Sensing*, Ottawa, Ontario, Canada, Vol II, pp877-884.
- CARDER, K. L., REINERSMAN, P., STEWARD, R. G., CHEN, R. F., MULLER-KARGER, F., DAVIS, C. O., and HAMILTON, M., 1993, AVIRIS calibration and application in coastal oceanic environments. *Remote Sensing of the Environment*, **44**, 205-216.
- CHAVEZ, P.S., 1992, Comparison of spatial variability in visible and near-infrared spectral images, *Photogrammetric Engineering and Remote Sensing*, **58**, 957-964.
- COLLINS, J.B. and WOODCOCK, C.E., 1999, Geostatistical estimation of resolution-dependent variance in remotely sensed images. *Photogrammetric Engineering and Remote Sensing*, **65**, 41-50.
- ERICKSON, B. J., VORST, J. J. and JOHANNSEN, C. J., 1999, Using hyperspectral analysis to quantify weather-induced crop damage. In *Precision Agriculture '99, Part I*, SCI, edited by J. V. Stafford (Sheffield: Sheffield Academic Press), pp. 81-89.
- OLIVER, M. A., WEBSTER, R. and SLOCUM, K., 2000, Filtering SPOT imagery by kriging analysis. *International Journal of Remote Sensing*, **21**, 735-752.
- Rossi, R.E., Dugan, J.L., and Beck, L.R., "Kriging in the shadows: geostatistical interpolation for remote sensing", *Remote Sensing of the Environment*, Volume 49, pp. 32-40, 1994.
- PAYNE, R. W. (editor) 2000. *The Guide to GenStat: Part 2 Statistics*. VSN International, Oxford.
- WEBSTER, R. and OLIVER, M. A., 2001. *Geostatistics for Environmental Scientists* (Chichester: J. Wiley & Sons).

Figure Captions

Figure 1. Pixel map of NDVI from a SPOT image for part of Fort A. P. Hill, Virginia, USA.

Figure 2. Pixel map of 1-m CAMIS imagery for part of Fort A. P. Hill, Virginia, USA.

Figure 3. Experimental variograms (symbols) and fitted models (solid lines) of NDVI from the SPOT data: a) average of rows and columns computed to 100 lags (2000 m), b) average of rows and columns computed to 80 lags fitted by an exponential function (1600 m), c) rows computed to 40 lags (800 m), d) columns computed to 40 lags (800 m), e) average computed to 40 lags (800 m), f) average of rows and columns computed to 80 lags fitted by a spherical function (1600 m).

Figure 4. Experimental variograms (symbols) and fitted models (solid lines) of NDVI from the CAMIS data: a) 1-m, b) 2-m, c) 3-m, d) 4-m, e) 6-m, f) 10-m and g) 15-m separation between pixels.

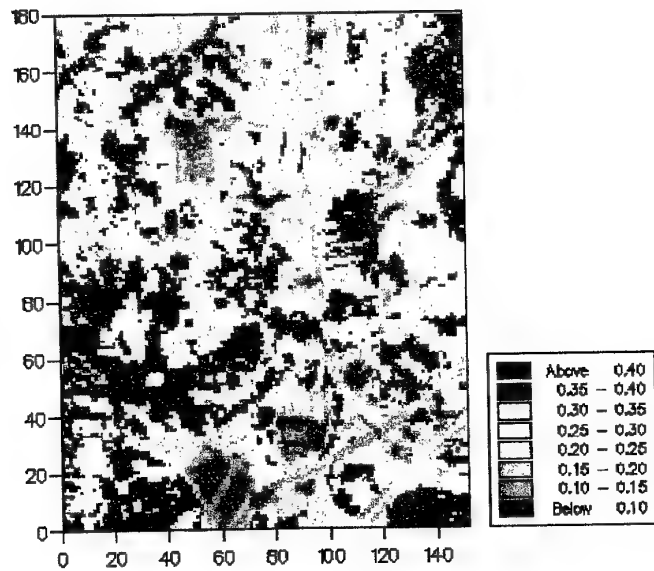


Figure 1



Figure 2

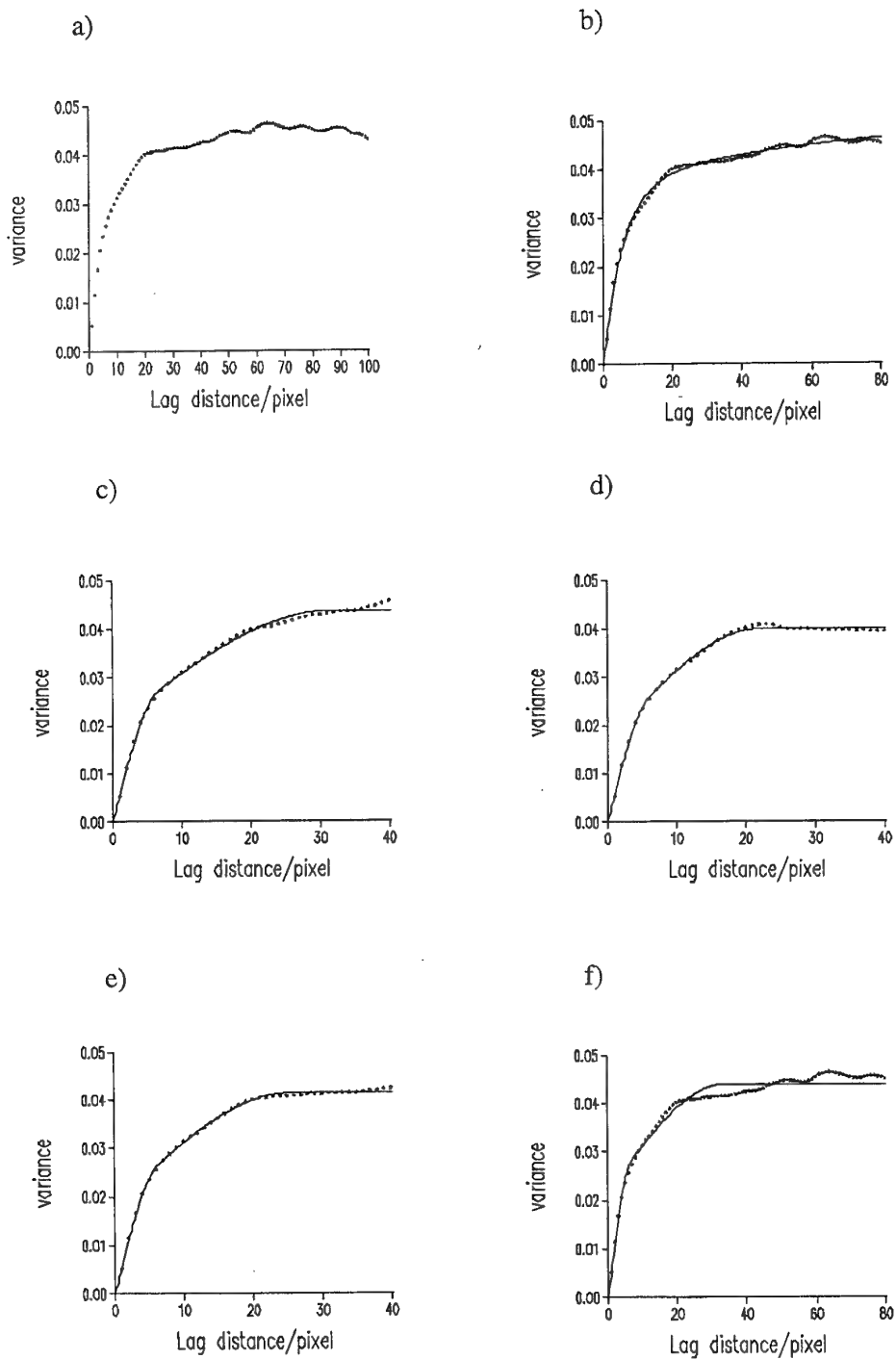


Figure 3

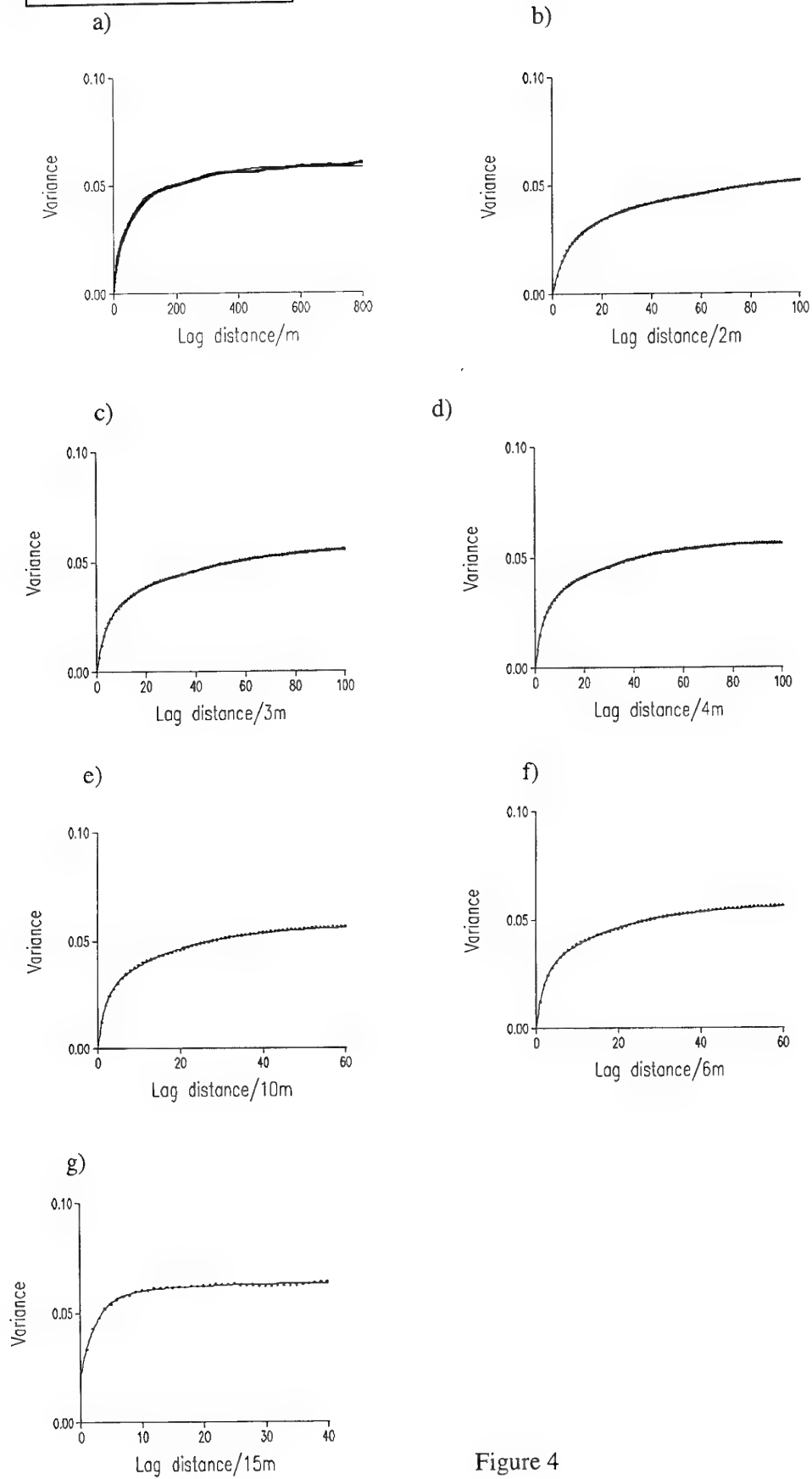


Table 1. Some current sensor systems with their spatial resolution and number of bands

Sensor System	Spatial Resolution	# wavebands
Computerized Airborne Multispectral Imaging System	1-m or less	4
Space Imaging-IKONOS	4-m MSI; 1-m Pan	4, 1
SPOT	20-m MSI; 10-m Pan	3, 1
Landsat Thematic Mapper	30-m	7
HYDICE	0.8 to 4-m	210
Airborne Visible/Infrared Imaging Spectrometer	20-m	224
Advanced Very High Resolution Radiometer	1.1-km	5

Table 2. Model parameters for variograms from the SPOT Imagery

Variogram	Model	RMS	c_0	c_1	c_2	$a_1(m)$	$a_2(m)$
Rows 40	Double exponential	27.61	0	0.0341	0.0560	322.5	10602
Columns 40	Double exponential	No suitable fit achieved for this model					
Average 40	Double exponential	63.21	0	0.0360	0.0080	344.0	1400.4
Average 80	Double spherical	52.39	0	0.0214	0.0225	139.2	674.8

Table 3. Model parameters for the average variograms of different pixel separations for the 1-m imagery

Data set	Model type	Variance				Range		
		c_0	c_1	c_2	c_3	a_1/m	a_2/m	a_3/m
1 metre data	Triple spherical	0	0.01728	0.02560	0.01557	23.42	147.7	620.8
1 in 2 pixels	Double exponential	0	0.0245	0.0318		30.08	317.1	
1 in 3 pixels	Double exponential	0	0.0255	0.0325		33.79	346.2	
1 in 4 pixels	Double exponential	0	0.0250	0.0323		33.74	343.3	
1 in 6 pixels	Double exponential	0	0.0245	0.0325		31.82	320.2	
1 in 10 pixels	Double exponential	0	0.0243	0.0326		31.50	310.2	
1 in 15 pixels	Double exponential	0.0215	0.0354	0.0068		109.1	626.4	

APPENDIX III

Paper submitted to International Journal of mathematical Geology – please do not quote from this or use the information therein.

Haar wavelets and the generalization of the variogram

E. H. Bosch¹, M. A. Oliver² and R. Webster³

The experimental variogram computed in the usual way by the method of moments and the Haar wavelet transform are similar in that they filter data and yield informative summaries that may be interpreted. The variogram filters out the mean; wavelets can filter variation at several spatial scales and thereby provide a richer repertoire for analysis and demand no assumptions other than that of finite variance. This paper compares the two functions, identifying that part of the Haar wavelet transform that gives it its advantages, and suggests how the variogram might be elaborated with additional filter coefficients to reveal features of the data that are not evident in its usual form.

Two examples in which soil data recorded at regular intervals on transects are analysed illustrate the extended form of the variogram. The apparent periodicity of gilgais in Australia seems to be accentuated as filter coefficients are added, but otherwise provides no new insight. Adding filter coefficients in the analysis of the topsoil across the Jurassic scarplands of England changed the upper bound of the variogram; it then resembled the within-class variogram computed by the method of moments. To elucidate these results we simulated several series of data to represent data with no stepped transitions, data with stepped transitions, data with long-range linear trend, and data with local trend. The results suggest that the wavelet variogram can filter out the effects of transitions from one class to another, as across boundaries, and long-range trend, but not local trend.

KEY WORDS: filtering, Haar wavelet, variogram, wavelet analysis.

¹ USACE-ERDC-TEC, 7701 Telegraph Road, Alexandria, VA 22315-3864, USA

² Department of Soil Science, The University of Reading, P O Box 233, Reading RG6 6DW, UK

³ Rothamsted Experimental Station, Harpenden, Hertfordshire AL5 2JQ, UK.

INTRODUCTION

Computing and modelling the variogram have become common in geostatistics, mainly because it, or its equivalent covariance function, is a prerequisite for local estimation by kriging. It has merit in its own right, however, for describing spatial variation. The variogram of a set of data, usually termed an experimental or sample variogram to distinguish it from any underlying function, summarizes the general nature of spatial dependence and its extent and also the magnitude of the variation. Such a summary may then be interpreted (cautiously) in terms of physical process – see, for example, Webster and Cuanalo (1975). When bounded models, such as the circular and spherical functions, fit an experimental variogram well we may interpret them as representing transition structures; they suggest patchy distribution of values in which the patches have extents approximately equal to the ranges of the models. We can take this a step further and look for boundaries between patches at this scale, as did Webster (1973, 1978) and Oliver and Webster (1987). We know that in computing the variogram we lose any information about the mean; the variogram filters it out.

In the last few years, wavelets have started to find application in the earth sciences (e.g. Lark and Webster, 1999, 2001; Oliver *et al.*, 2000). These also filter data and enable structures to be revealed at various scales by multi-resolution analysis. Wavelets have some similarities with the windowed Fourier functions, but the wavelet transform can characterize low frequency and high frequency resolutions simultaneously. Wavelets operate locally, and the analysis starts with the choice of a mother wavelet $w(x)$, for which x is spatial position, that can be dilated or shrunk.

As it happens, one form of wavelet, the wavelet of Haar (1910), was published at about the same time that Student (in Mercer and Hall, 1911) realised that the variation in yield between adjacent trial plots at Rothamsted Experimental Station was derived from two sources: an autocorrelated component (structured) and a random component (locally erratic). This idea predates the variogram of geostatistics by several decades, but it was a definite precursor to it. In the same way, the Haar wavelet (Figure 1) was described long before recently developed wavelet analysis (Daubechies, 1988). The Haar wavelet transform is remarkably similar to the experimental variogram. Wavelets can filter out not only zero and first-order moments, but also higher-order moments. They can also separate variation into components from several spatial scales, by what is known as multi-resolution analysis. They provide a much richer repertoire for spatial analysis than the simple variogram because they are not constrained by the assumption that the underlying variable is random.

The purpose of this paper is to show the similarity between the original Haar wavelet transform and the variogram of a set of data and then to suggest an extension of the latter for more general description.

THE WAVELET

In wavelet analysis a signal (information) is represented in terms of a set of functions, which we denote $w_{su}(x)$, where s signifies scale and u the translation space. These are basis functions or kernels; they are a set of linearly independent functions that can be

used to produce all admissible functions $f(x)$ (Strang and Nguyen, 1996). Furthermore, they are constructed from the single mother wavelet $w(x)$ by scaling it (by 2^s) and translating it (by u):

$$w_{su}(x) = \frac{1}{2^{s/2}} w\left(\frac{x}{2^s} - u\right) \quad (1)$$

Combining the basis functions with the wavelet function gives

$$f(x) = \sum_s \sum_u b_{su} w_{su}(x), \quad (2)$$

where b_{su} is the coefficient of the basis function $w_{su}(x)$ at scale s , translated by u , and the magnitude of which provides a measure of the significance of $w_{su}(x)$.

By varying s and u we can analyse a signal at several resolutions in a multi-resolution analysis of the wavelet transform. The wavelet function $w(x)$ is constructed from a scaling function $\phi(x)$ which can be specified by a discrete low-pass filter l_n . Similarly, the wavelet function $w(x)$ can be specified by a discrete high-pass filter h_n . The low-pass filter smooths the signal, while the high-pass filter retains the detail in the signal. Daubechies (1992) and Mallat (1998) describe the procedures fully.

THE EXPERIMENTAL VARIOGRAM

We start with the familiar formula for computing the variogram based on the method of moments. For n data $z(i)$, $i = 1, 2, \dots, n$, spaced at regular intervals along a line, Figure 1a, the semivariance is

where t , an integer, is the lag separating the data points $z(i)$ and $z(i + t)$. By

$$\begin{aligned} \hat{\gamma}(t) &= \frac{1}{2(n-t)} \sum_{i=1}^{n-t} \{z(i) - z(i+t)\}^2, \\ &= \frac{1}{n-t} \sum_{i=1}^{n-t} \left\{ \frac{z(i) - z(i+t)}{\sqrt{2}} \right\}^2, \end{aligned} \quad (3)$$

incrementing t we obtain the ordered set, the experimental variogram.

To see the relation between it and the Haar wavelet transform we develop the semivariance in terms of matrices. Starting with $t=1$, for which the comparisons are shown in Figure 2a, we define a matrix \mathbf{B}_1 with $n - 1$ rows and n columns:

$$\mathbf{B}_1 = \frac{1}{\sqrt{2}} \begin{bmatrix} 1 & -1 & 0 & 0 & 0 & . & . & . & 0 \\ 0 & 1 & -1 & 0 & 0 & . & . & . & 0 \\ . & . & . & . & . & . & . & . & . \\ . & . & . & . & . & . & . & . & . \\ . & . & . & . & . & . & . & . & . \\ 0 & 0 & 0 & . & . & . & 0 & 1 & -1 \end{bmatrix} \quad (4)$$

Multiplying \mathbf{B}_1 by the data vector $\mathbf{z} = [z(1) \ z(2) \ \dots \ z(n)]^T$ we obtain

$$\mathbf{B}_1 \mathbf{z} = \frac{1}{\sqrt{2}} \begin{bmatrix} 1 & -1 & 0 & 0 & 0 & . & . & . & 0 \\ 0 & 1 & -1 & 0 & 0 & . & . & . & 0 \\ . & . & . & . & . & . & . & . & . \\ . & . & . & . & . & . & . & . & . \\ . & . & . & . & . & . & . & . & . \\ 0 & 0 & 0 & . & . & . & 0 & 1 & -1 \end{bmatrix} \begin{bmatrix} z(1) \\ z(2) \\ . \\ . \\ . \\ z(n) \end{bmatrix} = \frac{1}{\sqrt{2}} \begin{bmatrix} z(1) - z(2) \\ z(2) - z(3) \\ . \\ . \\ . \\ z(n-1) - z(n) \end{bmatrix}. \quad (5)$$

The j th component of $\mathbf{B}_1 \mathbf{z}$ is $\{z(j) - z(j+1)\}/\sqrt{2}$. So to obtain $\hat{\gamma}(1)$ we simply square the elements of $\mathbf{B}_1 \mathbf{z}$, sum them, and divide by $n-1$:

$$\hat{\gamma}(1) = \frac{1}{n-1} (\mathbf{B}_1 \mathbf{z})^T (\mathbf{B}_1 \mathbf{z}) = \frac{1}{n-1} \mathbf{z}^T \mathbf{B}_1^T \mathbf{B}_1 \mathbf{z}. \quad (6)$$

We have thereby computed the square of the Euclidean norm of the vector $\mathbf{B}_1 \mathbf{z}$ and scaled it by dividing it by $n-1$. The square of the Euclidean norm of a vector \mathbf{z} , of length n , refers to the following: $\mathbf{z}^T \mathbf{z} = \sum_{i=1}^n (z_i)^2$, which is the same as the sum of the square of the components of \mathbf{z} . In other words, Equation (6) expresses $\hat{\gamma}(1)$ as a quadratic form – see also Cressie (1993), page 73.

Now, to compute $\hat{\gamma}(2)$ we define a matrix \mathbf{B}_2 :

$$\mathbf{B}_2 = \frac{1}{\sqrt{2}} \begin{bmatrix} 1 & 0 & -1 & 0 & 0 & . & . & . & 0 \\ 0 & 1 & 0 & -1 & 0 & . & . & . & 0 \\ . & . & . & . & . & . & . & . & . \\ . & . & . & . & . & . & . & . & . \\ . & . & . & . & . & . & . & . & . \\ 0 & 0 & 0 & . & . & . & 1 & 0 & -1 \end{bmatrix}. \quad (7)$$

Matrix \mathbf{B}_2 has $n - 2$ rows and n columns. Multiplying it by the data vector \mathbf{z} we obtain

$$\mathbf{B}_2 \mathbf{z} = \frac{1}{\sqrt{2}} \begin{bmatrix} 1 & 0 & -1 & 0 & 0 & \dots & 0 \\ 0 & 1 & 0 & -1 & 0 & \dots & 0 \\ \vdots & \vdots & \vdots & \vdots & \vdots & \ddots & \vdots \\ 0 & 0 & 0 & \dots & 1 & 0 & -1 \end{bmatrix} \begin{bmatrix} z(1) \\ z(2) \\ \vdots \\ z(n) \end{bmatrix} = \frac{1}{\sqrt{2}} \begin{bmatrix} z(1) - z(3) \\ z(2) - z(4) \\ \vdots \\ z(n-2) - z(n) \end{bmatrix}. \quad (8)$$

As for $\hat{\gamma}(1)$ we compute $\hat{\gamma}(2)$ by

$$\hat{\gamma}(2) = \frac{1}{n-2} (\mathbf{B}_2 \mathbf{z})^T (\mathbf{B}_2 \mathbf{z}) = \frac{1}{n-2} \mathbf{z}^T \mathbf{B}_2^T \mathbf{B}_2 \mathbf{z}. \quad (9)$$

In general we can define a matrix \mathbf{B}_k with $n - k$ rows and n columns in which the non-zero values 1 and -1 are placed in the first and $(k + 1)$ th elements of the first row, in the second and $(k + 2)$ th elements of the second row, and so on. On multiplying through we obtain the general expression for the semivariance equivalent to Equation (3) as

$$\hat{\gamma}(k) = \frac{1}{n-k} (\mathbf{B}_k \mathbf{z})^T (\mathbf{B}_k \mathbf{z}) = \frac{1}{n-k} \mathbf{z}^T \mathbf{B}_k^T \mathbf{B}_k \mathbf{z}. \quad (10)$$

THE HAAR WAVELET TRANSFORM

Let us now look at the original Haar wavelet transform. The Haar wavelet transform splits the sequence of data, usually termed the signal in the literature on wavelets, into two sets of components corresponding to the basis coefficients of two orthogonal subspaces. One component contains the information pertaining to the local averages of the signal, the smooth or low-frequency components, while the other contains information on local fluctuations in the signal, the detail or high-frequency components. The Haar wavelet function has the form of a local square wave, shown in Figure 2.

We proceed as follows. We suppose that the signal \mathbf{z} has n values measured at equal intervals, as before, but with the constraint that n is a power of 2, say $n=2^m$. For reasons that will become clear below we shall designate it $\mathbf{z}_1 \equiv \mathbf{z}$. We define two matrices. One, which we denote \mathbf{L}_1 containing 1s and 0s, is for the low-frequency component and appears in Equation (11). The matrix \mathbf{L}_1 is associated with the scaling function $\phi(x)$ described above. The other, denoted \mathbf{H}_1 for the high-frequency component and containing 1s, -1 s and 0s, occupies an analogous position in Equation (12). The matrix \mathbf{H}_1 is associated with wavelet function $w(z)$ described above. Both are of dimensions $n/2$ rows by n columns. We multiply the matrices, scaled by $1/\sqrt{2}$, by the data vector \mathbf{z}_1 to give

$$\mathbf{z}_2 = \mathbf{L}_1 \mathbf{z}_1 = \frac{1}{\sqrt{2}} \begin{bmatrix} 1 & 1 & 0 & 0 & 0 & 0 & . & . & . & 0 \\ 0 & 0 & 1 & 1 & 0 & 0 & . & . & . & 0 \\ 0 & 0 & 0 & 0 & 1 & 1 & . & . & . & 0 \\ . & . & . & . & . & . & . & . & . & . \\ . & . & . & . & . & . & . & . & . & . \\ . & . & . & . & . & . & . & . & . & . \\ 0 & 0 & 0 & . & . & . & 0 & 1 & 1 & . \end{bmatrix} \begin{bmatrix} z_1(1) \\ z_1(2) \\ z_1(3) \\ . \\ . \\ . \\ z_1(n) \end{bmatrix} = \frac{1}{\sqrt{2}} \begin{bmatrix} z_1(1) + z_1(2) \\ z_1(3) + z_1(4) \\ z_1(5) + z_1(6) \\ . \\ . \\ . \\ z_1(n-1) + z_1(n) \end{bmatrix} \quad (11)$$

and

$$\mathbf{d}_2 = \mathbf{H}_1 \mathbf{z}_1 = \frac{1}{\sqrt{2}} \begin{bmatrix} 1 & -1 & 0 & 0 & 0 & 0 & . & . & . & 0 \\ 0 & 0 & 1 & -1 & 0 & 0 & . & . & . & 0 \\ 0 & 0 & 0 & 0 & 1 & -1 & . & . & . & 0 \\ . & . & . & . & . & . & . & . & . & . \\ . & . & . & . & . & . & . & . & . & . \\ . & . & . & . & . & . & . & . & . & . \\ 0 & 0 & 0 & . & . & . & 0 & 1 & -1 & . \end{bmatrix} \begin{bmatrix} z_1(1) \\ z_1(2) \\ z_1(3) \\ . \\ . \\ . \\ z_1(n) \end{bmatrix} = \frac{1}{\sqrt{2}} \begin{bmatrix} z_1(1) - z_1(2) \\ z_1(3) - z_1(4) \\ z_1(5) - z_1(6) \\ . \\ . \\ . \\ z_1(n-1) - z_1(n) \end{bmatrix} \quad (12)$$

We thereby obtain a vector \mathbf{z}_2 containing the sums of neighbouring values (divided by $\sqrt{2}$) and a vector \mathbf{d}_2 of their differences (also divided by $\sqrt{2}$). The elements of the first provide us with a measure of the smoothness of the signal, whilst those of the second tell us about the detail, variation or change in \mathbf{z}_1 . Note that \mathbf{z}_2 and \mathbf{d}_2 consist of half the number of components of \mathbf{z}_1 , which is due to the number of rows of \mathbf{L}_1 and \mathbf{H}_1 respectively.

From the definition of \mathbf{L}_1 and \mathbf{H}_1 it is evident that the rows of \mathbf{L}_1 are orthogonal to one another, as are the rows of \mathbf{H}_1 . The rows of \mathbf{H}_1 are also orthogonal to those of \mathbf{L}_1 . This is true for all orthogonal wavelets. Furthermore, the rows of \mathbf{L}_1 and \mathbf{H}_1 , respectively, form an orthonormal set of basis vectors. From $\mathbf{z}_2 = \mathbf{L}_1 \mathbf{z}_1$ and $\mathbf{d}_2 = \mathbf{H}_1 \mathbf{z}_1$ (the coefficients of the corresponding basis vectors) we can compute the inverse wavelet transform to obtain \mathbf{z}_1 from the following

$$\mathbf{L}_1^T \mathbf{L}_1 \mathbf{z}_1 + \mathbf{H}_1^T \mathbf{H}_1 \mathbf{z}_1 = (\mathbf{L}_1^T \mathbf{L}_1 + \mathbf{H}_1^T \mathbf{H}_1) \mathbf{z}_1 = \mathbf{I} \mathbf{z}_1 = \mathbf{z}_1, \quad (13)$$

where \mathbf{I} is the identity matrix.

We can now take the analysis a step further by splitting \mathbf{z}_2 in a similar way. We define two matrices \mathbf{L}_2 and \mathbf{H}_2 (scaled by $1/\sqrt{2}$) having the same structure as \mathbf{H}_1 and \mathbf{L}_1 , but with $n/4$ rows by $n/2$ columns each instead of $n/2$ rows by n columns, and we multiply them by \mathbf{z}_2 to give the vectors $\mathbf{z}_3 = \mathbf{L}_2 \mathbf{z}_2$ and $\mathbf{d}_3 = \mathbf{H}_2 \mathbf{z}_2$, respectively. As in Equation (13), we can obtain \mathbf{z}_2 from \mathbf{z}_3 and \mathbf{d}_3 . We can repeat the procedure until we exhaust the data. At each step we split the smooth component of the signal from the previous step into orthogonal smooth and detail components. Finally we obtain two sets of vectors, \mathbf{z}_j and \mathbf{d}_j , $j=2, 3, \dots, m+1$, where $n=2^m$. This series of transformations will provide us with a means of analysing the signal at different resolution levels. Furthermore, synthesizing \mathbf{z}_j and \mathbf{d}_j for levels $j=2, 3, \dots, m+1$ to obtain \mathbf{z}_1 provides for a multiresolution analysis; see Walker (1999), page 14.

COMPARISON

The matrices \mathbf{B}_k (of the successive differences, Equation (5)) and \mathbf{H}_j (of the alternate differences, Equation (12)) show the similarities between the variogram and the Haar wavelet transform. However, there is not a one-to-one correspondence between them; we cannot equate the variogram at any particular lag with any high-frequency component of the wavelet transform. This is because in computing \mathbf{d}_j at any particular j we have lost the detail in the original signal at each of the previous $j-1$ steps, and in each of those steps we have halved the number of rows in the matrices.

Nevertheless, by expressing the variogram in terms of the matrices \mathbf{B}_k in Equation (10) we see that $\hat{\gamma}(k)$ does contain terms corresponding to the norm of the high-frequency components $\mathbf{H}_j \mathbf{z}_j$ of the Haar wavelet transform.

Consider first the semivariance $\hat{\gamma}(1)$ at lag $t=1$ and the detail $\mathbf{d}_2 = \mathbf{H}_1 \mathbf{z}_1$ of the wavelet transform. Notice how matrix \mathbf{H}_1 is related to matrix \mathbf{B}_1 used to form the $\hat{\gamma}(1)$ — it consists of the odd-numbered rows of \mathbf{B}_1 only. So let us define a matrix \mathbf{A}_1 such that $\mathbf{A}_1 \equiv \text{Odd rows}(\mathbf{B}_1)$. Then for the case $t=1$

$$\frac{(\mathbf{z}_1 \mathbf{H}_1^T \mathbf{H}_1 \mathbf{z}_1)}{n-1} = \frac{(\mathbf{z}_1 \mathbf{A}_1^T \mathbf{A}_1 \mathbf{z}_1)}{n-1} = \frac{1}{n-1} \sum_{i=1}^{n/2} \left(\frac{z(2i-1) - z(2i)}{\sqrt{2}} \right)^2. \quad (14)$$

Following from the above we find that the semivariance at lag $t=1$ consists of two terms:

$$\begin{aligned}\hat{\gamma}(1) &= \frac{1}{n-1} \sum_{i=1}^{n-1} \left(\frac{z(i) - z(i+1)}{\sqrt{2}} \right)^2 \\ &= \underbrace{\frac{1}{n-1} \sum_{i=1}^{n/2} \left(\frac{z(2i-1) - z(2i)}{\sqrt{2}} \right)^2}_{\text{Odd rows of } \mathbf{B}_1} + \underbrace{\frac{1}{n-1} \sum_{i=1}^{n/2-1} \left(\frac{z(2i) - z(2i+1)}{\sqrt{2}} \right)^2}_{\text{Even rows of } \mathbf{B}_1}\end{aligned}$$

and by Equation (14),

$$= \frac{1}{n-1} (\mathbf{z}_1^T \mathbf{H}_1^T \mathbf{H}_1 \mathbf{z}_1) + \frac{1}{n-1} \sum_{i=1}^{n/2-1} \left(\frac{z(2i) - z(2i+1)}{\sqrt{2}} \right)^2. \quad (15)$$

In words, $\hat{\gamma}(1)$ contains the norm of the detail component of the wavelet transform at level 1 scaled by $1/(n-1)$. When $t=2$ the corresponding $\hat{\gamma}(2)$ contains some components of the norm of the next level of detail, namely $\mathbf{d}_3 = \mathbf{H}_2 \mathbf{z}_2$ of the Haar wavelet transform. However, the norm of $\mathbf{H}_2 \mathbf{z}_2$ contains terms that are not in $\hat{\gamma}(2)$. The same is true for other values of t and different levels of detail, the \mathbf{d}_i of the wavelet transform.

What is striking about the matrices \mathbf{B}_k and \mathbf{H}_i is that both consist of rows the elements of which are only 0, 1 and -1 . In the Haar wavelet transform, the non-zero scaling (smoothing) coefficients are given by $l_1 = l_2 = 1/\sqrt{2}$, whereas the non-zero detail (difference) filter coefficients are $h_1 = 1/\sqrt{2}$ and $h_2 = -1/\sqrt{2}$. All the other coefficients are zero: $l_i = h_i = 0$, for all $i > 2$. The wavelet transform is obtained by shifting by 2 the rows of the matrices \mathbf{L}_i and \mathbf{H}_i . The variogram, however, is obtained by shifting by 1 its rows and by increasing the lag between the non-zero elements of each its rows, Figure 1b. From this we can see that the rows of \mathbf{B}_k (a running difference), which are associated with a two-point variance, are related to filtering data with the Haar wavelet filter coefficients $1/\sqrt{2}$ and $-1/\sqrt{2}$. In general, the variance of n data $z(i)$, $i = 1, 2, \dots, n$, can be computed by a circulant matrix the rows of which are shifts of the following elements: $(n-1)/n, -1/n, \dots, -1/n$. Since the mean of \mathbf{z} is given by

$$\mu = \{z(1) + z(2) + \dots + z(n)\}/n, \text{ and the variance is given by } \sigma^2 = \frac{1}{n-1} \sum_{i=1}^n \{z(i) - \mu\}^2. \text{ We}$$

can express the variance as $(\mathbf{u}^T \mathbf{u})/(n-1)$ which is the same as $(\mathbf{P}_v \mathbf{z})^T (\mathbf{P}_v \mathbf{z})/(n-1)$, where

$$\mathbf{u} = \begin{bmatrix} z(1) - \mu \\ z(2) - \mu \\ . \\ . \\ z(n) - \mu \end{bmatrix} = \begin{bmatrix} \{(n-1)z(1) - z(2) - \dots - z(n)\}/n \\ \{-z(1) + (n-1)z(2) - z(3) - \dots - z(n)\}/n \\ . \\ . \\ \{-z(1) - z(2) - \dots - z(n-1) + (n-1)z(n)\}/n \end{bmatrix} \quad (16)$$

and

$$\mathbf{P}_v = \frac{1}{n} \begin{bmatrix} (n-1) & -1 & -1 & \dots & -1 \\ -1 & (n-1) & -1 & \dots & -1 \\ . & . & . & . & . \\ . & . & . & . & . \\ -1 & -1 & \dots & -1 & (n-1) \end{bmatrix}.$$

It is not difficult to show that $(\mathbf{P}_v)^2 = \mathbf{P}_v$ and $(\mathbf{P}_v)^T = (\mathbf{P}_v)$. In other words, \mathbf{P}_v is a projection and is symmetric. From this relation we can rewrite the variance of \mathbf{z} as follows:

$$\begin{aligned} \sigma^2 &= \frac{(\mathbf{P}_v \mathbf{z})^T (\mathbf{P}_v \mathbf{z})}{n-1} = \frac{(\mathbf{z}^T \mathbf{P}_v^T \mathbf{P}_v \mathbf{z})}{n-1} = \frac{(\mathbf{z}^T (\mathbf{P}_v \mathbf{P}_v) \mathbf{z})}{n-1} = \frac{(\mathbf{z}^T (\mathbf{P}_v)^2 \mathbf{z})}{n-1} \\ &= \frac{(\mathbf{z}^T (\mathbf{P}_v \mathbf{z}))}{n-1}. \end{aligned} \quad (17)$$

This means that the variance of \mathbf{z} can be expressed in terms of a projection matrix thus providing a very simple and elegant way of computing such a measure. Therefore, we can see from Equation (17) that an n -point variance can be couched in terms of shifting the filter coefficients $(n-1)/n, -1/n, \dots, -1/n$.

CONDITIONS FOR WAVELET TRANSFORMS

One of the conditions that must be satisfied for the wavelet transform is that

$$\sum_{i=1}^k h_i = 0,$$

where k (finite) corresponds to the number of filter coefficients.

Clearly, from the paragraph above, this holds for the Haar wavelet, for $h_1 = -h_2$ and all the other coefficients are zero. The same coefficients are also present in the formula for the variogram but in a different order because of the lag parameter t in the variogram. Nevertheless, despite their differences, both formulae provide measures of detail or variation in a signal at several scales.

EXTENTION

We have seen above that there are just two non-zero filter elements in \mathbf{H}_t and \mathbf{L}_t . Nevertheless, wavelet transform filters can contain more elements. So, by analogy, why do we not introduce more terms into the variogram? We start with

$$\hat{\gamma}(t) = \frac{1}{n-t} \sum_{i=1}^{n-t} \{h_1 z(i) + h_2 z(i+t)\}^2, \quad (18)$$

where $h_1 = 1/\sqrt{2}$ and $h_2 = -1/\sqrt{2}$, and we add a third and fourth terms to give

$$\hat{\gamma}(t) = \frac{1}{n-2t} \sum_{i=1}^{n-2t} \{h_1 z(i) + h_2 z(i+t) + h_3 z(i+2t)\}^2, \quad (19)$$

and

$$\hat{\gamma}(t) = \frac{1}{n-3t} \sum_{i=1}^{n-3t} \{h_1 z(i) + h_2 z(i+t) + h_3 z(i+2t) + h_4 z(i+3t)\}^2, \quad (20)$$

on the condition that at least we have $\sum_{i=1}^k h_i = 0$. Note that in Equation (16), the filter coefficients $(n-1)/n, -1/n, \dots, -1/n$ also sum to 0 (the filter has one vanishing moment). Equation (16) shows that if $\sigma^2=0$ then $\mathbf{z}=0$ or $\mathbf{z}=\mathbf{c}$ (constant).

Furthermore, in general, the h_1 and h_2 in Equation (19) are not the same as those of either Equation (18) or Equation (20). Similarly, the h_1, h_2 and h_3 of Equation (20) are not related to those of Equation (19), and so on. Increasing the number of filter coefficients h_i allows for such coefficients to satisfy other conditions. We shall elaborate on these conditions below.

Remember also that the wavelet transform is local. And so we should expect the detail filter coefficients to smooth out the long-range (low-frequency) features in the signal while retaining the high-frequency ones.

Incorporating these coefficients into the formula for the variogram may be beneficial in that it embodies more information than just the differences between pairs of points. The matrices for three non-zero coefficients become

$$\mathbf{B}_1 = \begin{bmatrix} h_1 & h_2 & h_3 & 0 & 0 & . & . & . & 0 \\ 0 & h_1 & h_2 & h_3 & 0 & . & . & . & 0 \\ . & . & . & . & . & . & . & . & . \\ . & . & . & . & . & . & . & . & . \\ . & . & . & . & . & . & . & . & . \\ 0 & 0 & 0 & . & . & . & h_1 & h_2 & h_3 \end{bmatrix} \quad (21)$$

so that

$$\gamma(1) = \frac{1}{n-2} \mathbf{z}^T \mathbf{B}_1^T \mathbf{B}_1 \mathbf{z},$$

and

$$\mathbf{B}_2 = \begin{bmatrix} h_1 & 0 & h_2 & 0 & h_3 & . & . & . & 0 \\ 0 & h_1 & 0 & h_2 & 0 & h_3 & . & . & 0 \\ . & . & . & . & . & . & . & . & . \\ . & . & . & . & . & . & . & . & . \\ . & . & . & . & . & . & . & . & . \\ 0 & 0 & 0 & . & h_1 & 0 & h_2 & 0 & h_3 \end{bmatrix} \quad (22)$$

and

$$\gamma(2) = \frac{1}{n-4} \mathbf{z}^T \mathbf{B}_2^T \mathbf{B}_2 \mathbf{z},$$

In general with three non-zero coefficients we shall have

$$\gamma(k) = \frac{1}{n-2k} \mathbf{z}^T \mathbf{B}_k^T \mathbf{B}_k \mathbf{z}.$$

This is more restrictive than for the usual variogram because we have only $n - 2k$ terms in the sum instead of $n - k$, and so we run out of data more readily. Alternatively, we may see it as demanding more data. The situation will be accentuated if we want more than three filter coefficients.

VANISHING MOMENTS

To see how to elaborate the variogram as suggested above we need to understand the concept of vanishing moments. We explain the concept via the y -transform of the filter coefficients, setting $y = \exp(i\omega)$, where $i = \sqrt{-1}$, and ω is the frequency variable, and forcing the transform to have η zeros at $\omega = 0$, i.e. $y = 1$. (The quantity η is the number of vanishing moments, and 2η is the number of filter coefficients). This allows the filter to cancel out the signal's low-frequency content. We shall see below that cancelling the low frequencies is related to cancelling polynomials of order up to $2\eta - 1$. The y -transform of the filter is given by

$$p_{2\eta}(y) = \sum_{k=0}^{2\eta-1} h_k y^{-k}$$

or equivalently

$$p_{2\eta}(\omega) = \sum_{k=0}^{2\eta-1} h_k \exp(-i\omega k). \quad (23)$$

(Note that $p_{2\eta}(y)$ is not a polynomial in y since the exponents of y are negative). For computational convenience the filter coefficients are given by $h_0, h_1, \dots, h_{2\eta-1}$. Forcing the polynomial equation to have η zeros at $\omega = 0$ means that

$$p_{2\eta}(\omega) = \sum_{k=0}^{2\eta-1} h_k \exp(-i\omega k) = \omega^\eta r(\omega), \quad (24)$$

where $r(\omega)$ is a polynomial in terms of ω . Note that for $p_{2\eta}(\omega)$ to have η zeros at $\omega = 0$ also means that its first $\eta - 1$ derivatives are 0 when $\omega = 0$. That is,

$$\frac{d^m p_{2\eta}(\omega)}{d\omega^m} = \sum_{k=0}^{2\eta-1} h_k (-ik)^m \exp(-i\omega k) = 0, \quad (25)$$

for $0 \leq m \leq \eta - 1$. Factoring $(-i)^m$ from the right hand side of Equation (25) and letting $\omega = 0$ we obtain the vanishing moment conditions for values of m where $0 \leq m \leq \eta - 1$:

$$\sum_{k=0}^{2\eta-1} h_k k^m = 0, \text{ which is the same as} \quad (26)$$

$$h_0 1 + h_1 1^0 + h_2 2^0 + \dots + h_{2\eta-1} (2\eta-1)^0 = 0, \text{ when } m = 0$$

$$h_0 0^1 + h_1 1^1 + h_2 2^1 + \dots + h_{2\eta-1} (2\eta-1)^1 = 0, \text{ when } m = 1$$

...

The fact $h_0 0^{\eta-1} + h_1 1^{\eta-1} + h_2 2^{\eta-1} + \dots + h_{2\eta-1} (2\eta-1)^{\eta-1} = 0, \text{ when } m = \eta - 1.$

that Equation (26) is zero means that increasing the number of vanishing moments in the filter will also reduce to zero sections of length 2η of polynomial curves of degree $0 \leq m \leq \eta - 1$, when the filter coefficients are convolved with such polynomials. That is, not only will the filter coefficients h_i reduce to zero the powers of $0, 1, 2, \dots, 2\eta-1$, but the powers of $(0+r), (1+r), (2+r), \dots, (2\eta-1+r)$, where r is any fixed real number, are also reduced to zero. It is important to note that Equation (26) is not a polynomial function of k , since k is just an index in the range of $0 \leq k \leq 2\eta-1$.

Interesting properties are obtained when the filter coefficients h_i , with η vanishing moments, are applied to a polynomial of degree $m \geq \eta$. This operation acts on the polynomial like a derivative of order $m-\eta$, producing a polynomial of degree $m-\eta$. For example, consider the following polynomial $s(y)$

$$\begin{aligned} s(y) &= \sum_{k=0}^{2\eta-1} h_k (k+y)^m, \\ &= \sum_{k=0}^{2\eta-1} h_k \sum_{i=0}^m \binom{m}{i} y^i k^{m-i} \end{aligned} \quad (27)$$

where $m \geq \eta$, h_k are the usual filter coefficients with exactly η vanishing moments and $(k+y)^m$ is a polynomial in y of degree m . Equation (27) can be rewritten as

$$\begin{aligned} s(y) &= \sum_{k=0}^{2\eta-1} h_k \sum_{i=0}^m \binom{m}{i} y^i k^{m-i} \\ &= \sum_{i=0}^m \binom{m}{i} y^i \sum_{k=0}^{2\eta-1} h_k k^{m-i} = \sum_{i=0}^m \binom{m}{i} y^i c_i, \end{aligned} \quad (28)$$

where $c_i \equiv \sum_{k=0}^{2\eta-1} h_k k^{m-i} = \begin{cases} 0, & m-i \leq \eta-1 \Leftrightarrow i \geq m-\eta+1 \\ \text{non zero real number,} & m-i \geq \eta \Leftrightarrow 0 \leq i \leq m-\eta. \end{cases}$

Clearly, since c_i is nonzero for $0 \leq i \leq m-\eta$, we have that $s(y) = \sum_{i=0}^{m-\eta} \binom{m}{i} c_i y^i$ is a

polynomial in y of degree $m-\eta$. Therefore, the degree of the polynomial $(k+y)^m$ has been reduced to $m-\eta$ from m . This means that as the filter runs over the signal, those portions of the signal consisting of polynomials of order $m < \eta$ will be reduced to zero or sustain a reduction in order if $m \geq \eta$. This is what occurs with the ordinary variogram except that the filter coefficients $1/\sqrt{2}$ and $-1/\sqrt{2}$ cancel out only constant trend (polynomials of order zero). Real data in general do not consist exactly of polynomial functions unless a polynomial (exact or in the least squares sense) is fitted through the data points. Nevertheless, as the filter's number of vanishing moments increases, the wavelet-based variograms may be useful to identify higher-order polynomial global trend in a signal.

APPLICATION

We have shown above the relation between the conventional experimental variogram and the filter provided by the Haar wavelet coefficients. We used the relation to suggest a generalization of the variogram so that it could incorporate other filter coefficients such as (but not limited to) Daubechies's 2η coefficients. Daubechies's wavelet filters are a natural extension of Haar's wavelet filter. For an even number of filter coefficients 2η , the wavelets satisfy η orthogonal conditions as well as η vanishing moments.

We have used Daubechies's high-frequency filter coefficients for $2\eta = 2, 4, 6$, and 8 . (When $2\eta = 2$ we have the Haar filter.) Table 1 lists their values. Since the wavelet transform is the convolution of a signal with a wavelet filter followed by sub-sampling, the operation requires the filter (or the signal) to be reversed. The values in Table 1 are listed in reverse order (relative to the wavelet transform) to show the order in which the coefficients have been applied to Equations (18), (29) and (30). We emphasize that if we choose a different order for the wavelet coefficients we shall obtain different results. Nevertheless, note that in Equation (3) for the ordinary variogram we have $\{h_1z(i) + h_2(i+t)\}^2 = \{h_2z(i) + h_1z(i+t)\}^2$. This indicates that the order is not important since there are only two filter coefficients that differ only by their sign and the whole quantity is squared.

We now apply the ideas to soil data from two transects, both of which have been re-analysed recently by Lark and Webster (1999) using wavelets.

Caragabal transect

Caragabal is on the Bland Plain of Eastern Australia. The topography is flat, but the Plain is pocked by gilgai, that is by small depressions typically from a 10 to 40 cm deep, 2 – 3 m across, and 20 to 40 m apart and which occur in a seemingly regular pattern. The soil is dominantly clay but with a sandier surface horizon of variable thickness, alkaline and locally saline, especially in the gilgais themselves.

The soil was sampled by Webster (1977) using a 7.5-cm diameter corer at 365 points at 4-m intervals along a transect. We used the records of the soil's electrical conductivity, a measure of its salinity, at 30 – 40 cm for our application. Table 2 summarizes the data. The measured values are strongly skewed, and we have transformed them to their common logarithms for our analysis. Table 2 summarizes their statistics, and Figure 3 shows the (erratic) trace of the data as the solid line.

Variograms were computed with the usual formula, Equations (3) and (18), and then with its wavelet-based extension

$$\hat{\gamma}(t) = \frac{1}{n-3t} \sum_{i=1}^{n-3t} \{h_1 z(i) + h_2 z(i+t) + h_3 z(i+2t) + h_4 z(i+3t)\}^2 \quad (29)$$

and

$$\hat{\gamma}(t) = \frac{1}{n-5t} \sum_{i=1}^{n-5t} \{h_1 z(i) + h_2 z(i+t) + h_3 z(i+2t) + h_4 z(i+3t) + h_5 z(i+4t) + h_6 z(i+5t)\}^2, \quad (30)$$

corresponding to Daubechies's high-frequency filter coefficients 4 and 6, respectively. Figure 4 shows the result. The three variograms are remarkably similar to one another, though we see that as the number of filter coefficients increases so does the amplitude of the periodic component. See Table 1 for a list of several of Daubechies's wavelets. This is a consequence of the wavelet's sensitivity to the variation in the data. Wavelets in general eliminate smooth variation such as trend functions that can be represented by low-order polynomials, but not the local fluctuation. However, the variation introduced in Equations (29) and (30) by the additional terms $z(i+kt)$ and the filter coefficients is minimum.

Sandford transect

Sandford-St-Martin lies on the Jurassic scarplands in Central England. The soil there has formed by the weathering of the gently dipping limestone, sandstone, siltstone, and shale of the Jurassic era, and in Recent alluvium. Webster and Cuanalo (1975) surveyed a transect 3.2-km long across the outcrops by digging pits at 10-m intervals and recording the soil to 1 m depth. For present purposes we have analysed the clay content at two depths, topsoil (centred at 8 cm) and subsoil (centred at 65 cm), in the profile. Their statistics are summarized in Table 3, and Figure 5a and b shows the data for the topsoil and subsoil, respectively, plotted against position on the transect. As for Caragabal, the solid lines join the observed values and show much point-to-point variation. The bold dashed lines show the step changes in the mean at the boundaries between the geological formations.

Again, as for Caragabal, we computed variograms with the usual formula and then with its extension containing the wavelet-based coefficients. Figures 6 and 7 display the results for the topsoil and subsoil, respectively. The variogram of the clay in the topsoil (Figure 6a) seems clearly bounded. Webster and Oliver (1990) modelled it successfully with spherical and pentaspherical functions, with a sill variance of about $200 (\%)^2$ and a range of about 250 m. The wavelet-based variograms with Daubechies's high-frequency filter coefficients 4 and 6, however, increase more gradually and have smaller maxima $\sim 125 (\%)^2$, which they reach at shorter lags (150 m for Daubechies's 4 and about 100 m for Daubechies's 6, Figure 6a). All appear to approach the same value on the ordinate.

To explore possible causes for the difference between the usual variogram and the wavelet based variograms we examined the influence of the marked boundaries along the transect. We removed their effect by computing the residuals from the geological segment means and computed the variograms on these residuals. The result is the pooled within-segment variogram, Figure 6b. The three variograms are very similar to one another. The usual variogram of the residuals now has a much smaller maximum

of $100(\%)^2$ which it reaches at 75 m. This is the same for the wavelet-based variograms. It seems that the latter remove the effect of the boundaries (see Figure 6a) — Webster and Cuanalo (1975) identified 14. Geostatisticians might regard these local step functions as deterministic features to be removed before computing variograms on the residuals. It appears that the wavelet variogram filters out such trends where they occur.

The variogram of the subsoil clay content was fitted best by a pentaspherical model. It increases to a sill of about $700(\%)^2$ at 260 m (the range), Figure 7a. The variogram from Daubechies's 4 high-frequency filter coefficients is similar, Figure 7a. That for Daubechies's 6 rises more steeply to a slightly larger maximum at about the same lag distance as above, Figure 7a. The variograms computed from the residuals of the segment means, Figure 7b, are similar to one another.

To try to explain the reasons for the difference between the wavelet-based variograms of the top- and sub-soil we did an analysis of variance to determine the proportion of the total variance accounted for by geology. The results of the analysis of variance are given in Table 4. The proportion of the topsoil variance explained by geology is 36.8% and that for the subsoil is 39%. This difference is not sufficient to explain why the wavelet-based variograms filter out the effects of the boundaries for the topsoil, but not the subsoil. A possible explanation for this is the large difference between the mean for the first part of the transect, positions 1 to 158, and that of the second part, positions 159 to 321.

Simulated transects

To attempt to understand the results of the above analyses we simulated a one-dimensional sequence of values in three ways using LU decomposition (see Goovaerts, 1997, for a description of the method). We used a spherical variogram function with zero nugget and a sill variance of 1 for each simulation. The spherical function is widely encountered in the earth sciences and provided the best fit to the experimental variograms for the Sandford data. The first simulation was of a single process based on this variogram with a range of 45 units, Figure 8a (fine line). To emulate the effect of boundaries, such as those along the Sandford transect, the second simulation incorporated a stepped function superimposed on it with a variance of 0.75, Figure 8b. The lengths of the segments were drawn at random from an exponential process with a mean of 0.035. Burgess and Webster (1984) discovered that such lengths in the real world are well fitted by exponential distributions. Although we simulated the steps by random processes, we often know from prior information in the field where to expect them, as on the Sandford transect. They can be thought as a form of regional trend because they result in predictable changes in the mean.

Regional trend also results from a gradual change in values with autocorrelated random fluctuation superimposed. An example of this is the top of the sub upper chalk surface described by Moffat *et al.* (1986). The third simulation was based on the same variogram function as the first, but with a linear trend of 0.02 superimposed, Figure 8c.

Local trend or drift is also a feature of the real world, where smooth predictable change in a property occurs over short distances. The electrical resistivity measured at Beckesbourne by Webster and Burgess (1980) is one such example. Solifluction and soil creep on hillslopes are also likely to give rise to local drift. To simulate this effect the first simulation was smoothed by an 11-point moving average, Figure 8a.

Simulation with a single random process

The sequence of simulated values in Figure 8a shows them fluctuating about a mean value. The usual variogram and the wavelet-based variograms with Daubechies's high-frequency filter coefficients 4 and 6 were computed for these data. Figure 9 shows the result; they reach a similar upper bound, but the wavelet ones fluctuate more on reaching their maximum.

Simulation with a stepped function superimposed with a random process

Figure 8b shows the simulation with stepped functions of random extent (the dashed line) with an average extent of 45 units and variance of 0.893, superimposed on a random process generated by a spherical variogram with zero nugget, sill of 0.25 and a range of 15 units. The latter is the average extent of the within-segment variation. There were nine boundaries or step changes and so the sequence no longer fluctuates about the mean; there are sections where the average value is small and others where it is larger.

The usual variogram for this simulation reaches an upper bound at about 40 units, which is close to the average spacing between the boundaries of 45 units, Figure 10a. There is a kink in this variogram at around 15 units which signals the nested structure simulated. The wavelet-based variogram with Daubechies's high-frequency filter coefficients 4 reaches a smaller maximum at about 20 units of distance and then decreases, as does that for Daubechies's 6 which fluctuates more about the upper bound. These results suggest, as for the topsoil clay content of the Sandford transect, that the wavelet variograms filter out the effects of the long-range transitions in the variation. This is confirmed by the variograms computed on the residuals from the class means for this simulation, Figure 10b. The three variograms are similar to each other – they reach an upper bound of about 0.25 which is reached at about 15 units. This reflects closely the short-range function used for simulation.

Simulation of a random process with a linear trend superimposed

The sequence of values in Figure 8c shows the smooth regional progression in values from left to right with random fluctuation superimposed on this. Variograms were computed as above for this simulation. There is a clear difference between the usual variogram and the wavelet-based ones, Figure 11. The former is unbounded, it is the kind of variogram we should expect where the data contain a marked linear trend. The

wavelet-based variograms, Figure 11, describe more closely the spherical function used to simulate the random process. This result also suggests that the wavelet variograms filter out the effects of regional trend in the data as well as those of transition features.

Simulation of a smooth process

Figure 8a shows the 11-point moving average of the underlying random process generated from a spherical model with zero nugget, a sill of 1 and a range of 45 units (thick solid line). The local smoothness or continuity in these values is evident in the concave slope near to the origin of the usual variogram, Figure 12. In geostatistics such data should be analysed using a structural analysis (Olea, 1975) to remove the local trend. The effect of the latter appears to be amplified in the wavelet-based variograms; their concave slopes near to the origin are more pronounced, Figure 12. Thus it seems that wavelet-based variograms do not provide a solution to local drift, and this should continue to be dealt with geostatistically.

DISCUSSION AND CONCLUSION

We show above the mathematical similarity of the method-of-moments variogram and those derived from the high frequency wavelet coefficients, Daubchies's 4 and 6. The experimental variogram computed in the usual way is sensitive to local and regional trends in the data. Their presence is usually evident in the shape of the variogram and is a sign that the stationarity assumptions on which much of the standard geostatistical technique is based will not hold. As a consequence the residuals from the regional (arising from gradual and stepped changes) and local trend should be determined and used for further analyses. The wavelet-based variograms appear to filter out regional trends that can result from smooth or stepped changes in the regional mean. This would avoid the need to examine the data for trend first. The effects of local trend or drift, which are less common in most earth science data, appear to be amplified by the wavelet-based variograms, however.

This is a preliminary comparison of the wavelet-based variograms with Matheron's estimator, and we urge caution in assuming that these results are general. More sequences of data need to be analysed to generalize our observations.

Finally we should add that our circumspection is augmented by the large differences in simulations from the same function, but with different seeds. The inconsistencies concern us, yet many researchers continue to place great faith in simulation. We had some difficulty in obtaining sequences with experimental variograms like those with which they had been simulated.

ACKNOWLEDGEMENT

This work has been supported by the United States Army as part of contract N68171-01-M-5808.

REFERENCES

- Burgess, T. M. and Webster, R., 1984, Optimal sampling strategies for mapping soil types. I. Distribution of boundary spacings. *Journal of Soil Science*, v. 35, p. 641–654.
- Cressie, N. A. C., 1993, *Statistics for Spatial Data*, revised edition. John Wiley and Sons, New York.
- Daubechies, I., 1988, Orthonormal bases of compactly supported wavelets. *Communications on Pure and Applied Mathematics*, v. 41, p. 909–996.
- Daubechies, I., 1992, *Ten Lectures on Wavelets*. Society for Industrial and Applied Mathematics (SIAM), Philadelphia.
- Haar, A., 1910, Zur Theorie der orthogonalen Funktionensysteme. *Mathematische Annalen*, v. 69, p. 331–371.
- Lark, R. M. and Webster, R., 1999, The analysis and elucidation of soil variation using wavelets. *European Journal of Soil Science*, v. 50, p. 185–206.
- Lark, R. M. and Webster, R., 2001, Changes in variance and correlation of soil properties with scale and location: analysis using an adapted maximal discrete wavelet transform. *European Journal of Soil Science*, v. 52, p. 547–562.
- Mallat, S., 1998, *A Wavelet Tour of Signal Processing*, second edition. Academic Press, San Diego.
- Moffat, A. J., Catt, J. A., Webster, R. and Brown, E. H., 1986, A re-examination of the evidence for a Plio-Pleistocene marine transgression on the Chiltern Hills. I. Structures and surfaces. *Earth Surface Processes and Landforms*, v. 11, p. 95–106.
- Nguyen, T. and Strang, G., 1996, *Wavelets and Filter banks*. Wellesley–Cambridge Press, Wellesley, Massachusetts.
- Olea, R. A., 1975, *Optimum Mapping Techniques Using Regionalized Variable Theory*. Series on Spatial Analysis, No 2, Kansas Geological Survey, Lawrence.
- Oliver, M. A., Bosch, E. H. and Slocum, K., 2000, *Wavelets and Kriging for Filtering and Data Reconstruction*. *Geostatistics 2000*, Volume 2, Cape Town, South Africa, pp. 571–580.
- Oliver, M. A. and Webster, R., 1987, The elucidation of soil pattern in the Wyre Forest of the West Midlands, England. II. Spatial distribution. *Journal of Soil Science*, v. 38, p. 293–307.
- Walker, J. S., 1999, *A Primer on Wavelets and their Scientific Applications*. Chapman & Hall/CRC, Boca Raton, Florida.
- Webster, R., 1973, Automatic soil boundary location from transect data. *Journal of the International Association of Mathematical Geology*, v. 5, p. 27–37.
- Webster, R., 1977, Spectral analysis of gilgai soil. *Australian Journal of Soil Research*, v. 15, p. 191–204.
- Webster, R., 1978, Optimally partitioning soil transects. *Journal of Soil Science*, v. 29, p. 388–402.

- Webster, R. and Cuanalo de la C., H. E., 1975, Soil transect correlograms of north Oxfordshire and their interpretation. *Journal of Soil Science*, v. 26, p. 176–194.
- Webster, R. and Burgess, T. M., 1980, Optimum interpolation and isarithmic mapping of soil properties. III. Changing drift and universal kriging. *Journal of Soil Science*, v. 31, p. 505–524.
- Webster, R. and Oliver, M. A., 1990, *Statistical Methods in Soil and Land Resource Survey*. Oxford University Press, Oxford.

Table 1. High-frequency Haar and Daubechies filter coefficients (in reverse order) for $\eta=1, 2, 3$, and 4, i.e. $2\eta=2$ (Haar), 4, 6, and 8.

2η	h_1	h_2	h_3	h_4	h_5	h_6	h_7	h_8
2	-0.7071	0.7071	0	0	0	0	0	0
4	0.1294	0.2241	-0.8365	0.4830	0	0	0	0
6	-0.0352	-0.0854	0.1350	0.4599	-0.8069	0.3327	0	0
8	0.0106	0.0329	-0.0308	-0.1870	0.0280	0.6309	-0.7148	0.2304

Table 2. Summary statistics of the soil's electrical conductivity at 30–40 cm at Caragabal from 365 data

	Electrical conductivity	
	mS cm ⁻¹	Log ₁₀ (mS cm ⁻¹)
Minimum	0.06	-1.214
Maximum	5.10	0.707
Mean	0.985	-0.230
Median	0.54	-0.267
Variance	0.959	0.192
Standard deviation	0.975	0.428
Skewness	1.64	0.100

Table 3. Summary statistics of the clay content as percentage by weight in the topsoil (5–10 cm) and subsoil (62–67 cm) at Sandford from 321 sampling points.

	Topsoil	Subsoil
Minimum	5.0	0
Maximum	80.0	90.0
Mean	25.6	39.1
Median	20.0	36.0

DRAFT

Variance	255.5	936.8
Standard deviation	16.0	30.6
Skewness	1.24	0.16

Table 4. The results of an analysis of variance for the top- and sub-soil clay content along the Sandford transect.

Source of variation	Topsoil clay content (%)			
	Degrees of freedom	Sum of squares	Mean square	Component of variance
Variation due to geology	14	53013.4	3786.7	176.1
Residual variance	306	28744.5	93.9	93.9
Total variance	320	81757.8	255.5	255.5
Subsoil clay content (%)				
Variation due to geology	14	187905.8	13421.8	622.7
Residual variance	306	111874.6	365.6	365.6
Total variance	320	299780.4	936.8	936.8

FIGURE CAPTIONS

- Figure 1** (a) Comparisons made in computing the variogram, (b) Comparisons for the Haar wavelet, and (c) Points embraced when computing the wavelet-based variograms with four Daubechies's coefficients.
- Figure 2.** The Haar wavelet.
- Figure 3.** Trace of the electrical conductivity (mS cm^{-1}) transformed to common logarithms at Caragabal, with the solid line joining the data.
- Figure 4** Variograms of the electrical conductivity. The usual variogram is shown by \bullet , the wavelet-based variogram with Daubechies's 4 coefficients by \times , and with Daubechies's 6 coefficients by \square .
- Figure 5** Sandford transect; (a) clay content in topsoil and (b) subsoil, with data shown by the solid lines and the geologic boundaries by the dashed bold lines.
- Figure 6** Variograms of the clay content in the topsoil at Sandford: (a) for the raw data, and (b) for the residuals from the means of the geologic classes. The usual variogram is shown by \bullet , the wavelet-based variogram with Daubechies's 4 coefficients by \times , and with Daubechies's 6 coefficients by \square .
- Figure 7** Variograms of the clay content in the subsoil at Sandford: (a) for the raw data, and (b) for the residuals from the means of the geologic classes. The usual variogram is shown by \bullet , the wavelet-based variogram with Daubechies's 4 coefficients by \times , and with Daubechies's 6 coefficients by \square .
- Figure 8** Plots of the simulated data using LU decomposition: (a) by a spherical function with zero nugget, unit sill and a range of 45 units (thin line), superimposed by a 35-point moving average shown by the thicker line, (b) by a spherical function with zero nugget, unit sill, range of 15 units and a random stepped process with an average extent of 45 units, shown as the heavier dashed line, and (c) by a spherical function with zero nugget, unit sill and a range of 45 units with a linear trend of 0.02 added.
- Figure 9** Variograms of the values simulated by a spherical function with zero nugget, unit sill and a range of 45 units. The usual variogram is shown by \bullet , the wavelet-based variogram with Daubechies's 4 coefficients by \times , and with Daubechies's 6 coefficients by \square .
- Figure 10** Variograms of the values simulated by a spherical function with zero nugget, unit sill, a range of 15 units, and a step function with an average extent of 45 units: (a) for the raw data, and (b) on the residuals from the means of the classes created by the step function. The usual variogram is shown by \bullet , the wavelet-based variogram with Daubechies's 4 coefficients by \times , and with Daubechies's 6 coefficients by \square .
- Figure 11** Variograms of the values simulated by a spherical function with zero nugget, unit sill and a range of 45 units smoothed by a 35-point moving average. The usual variogram is shown by \bullet , the wavelet-based variogram with Daubechies's 4 coefficients by \times , and with Daubechies's 6 coefficients by \square .
- Figure 12** Variograms of the values simulated by a spherical function with zero nugget, unit sill and a range of 45 units with an added linear trend of 0.02. The usual variogram is shown by \bullet , the wavelet-based variogram with Daubechies's 4 coefficients by \times , and with Daubechies's 6 coefficients by \square .

DRAFT

a)



b)



c)

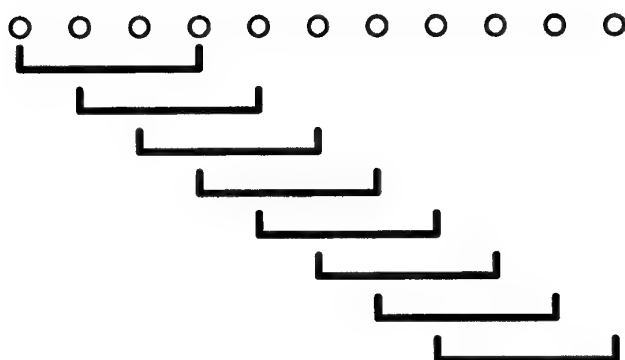


Fig 1

DRAFT

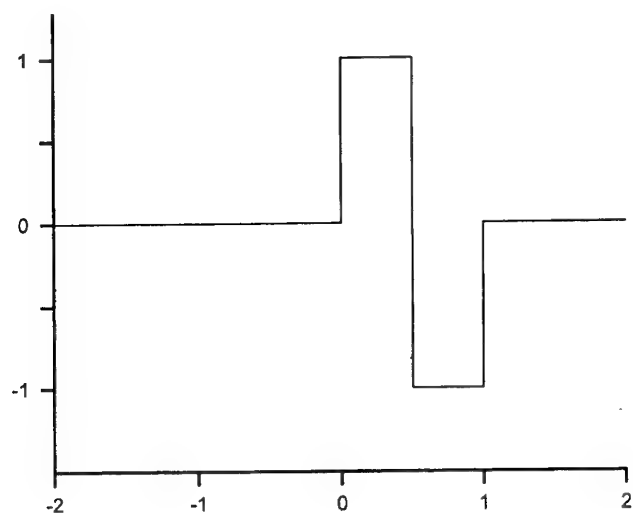


Fig 2

DRAFT

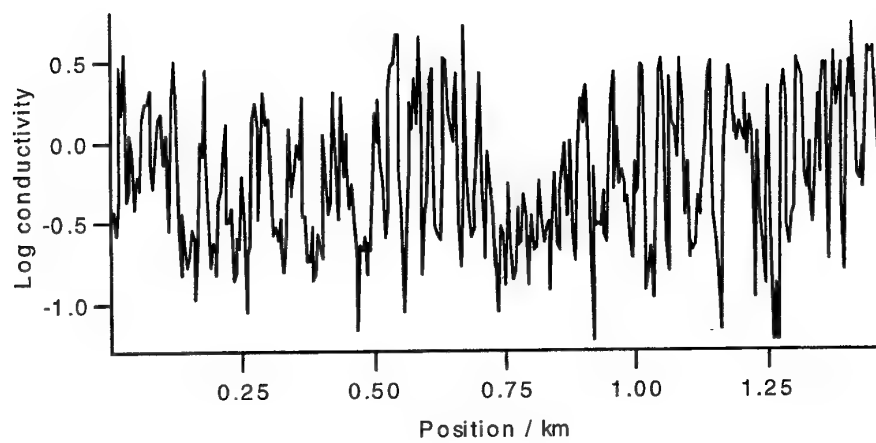


Fig 3

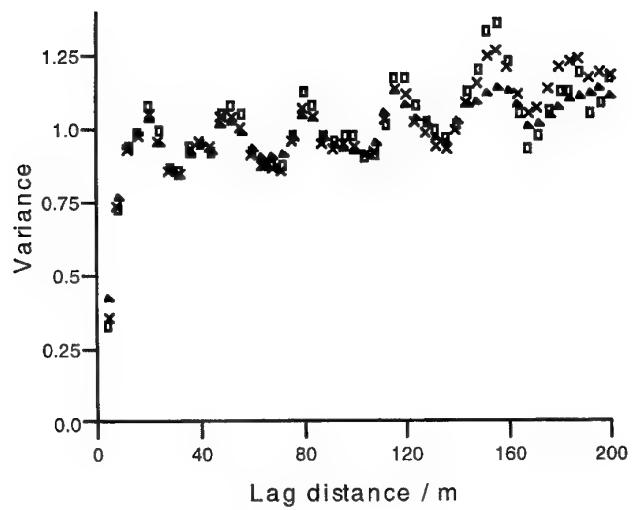
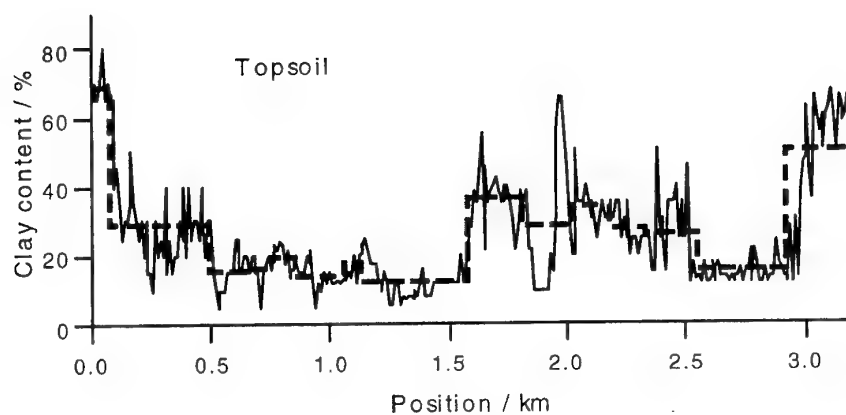


Fig 4

DRAFT

a)



b)

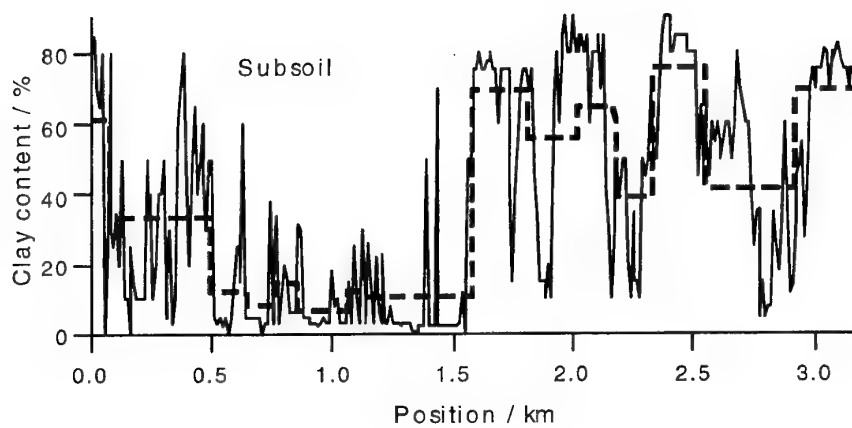
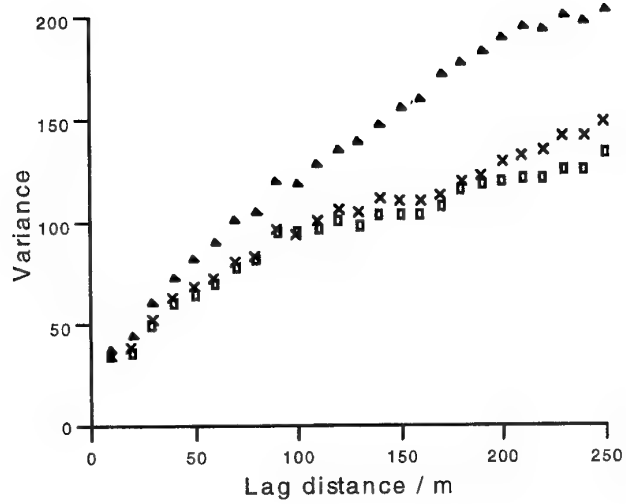


Fig 5

DRAFT

a)



b)

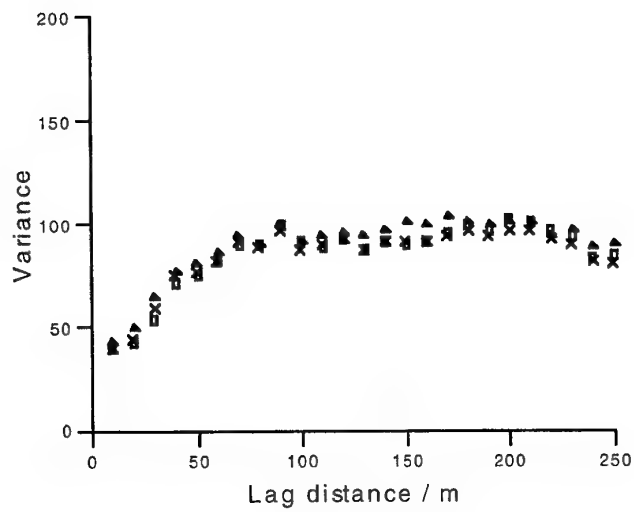
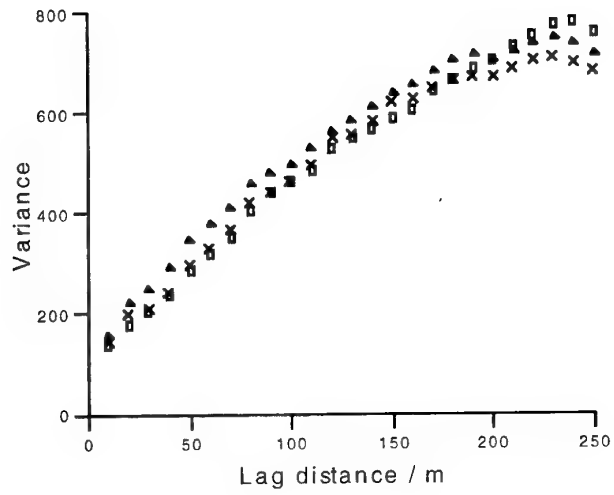


Fig 6

a)



b)

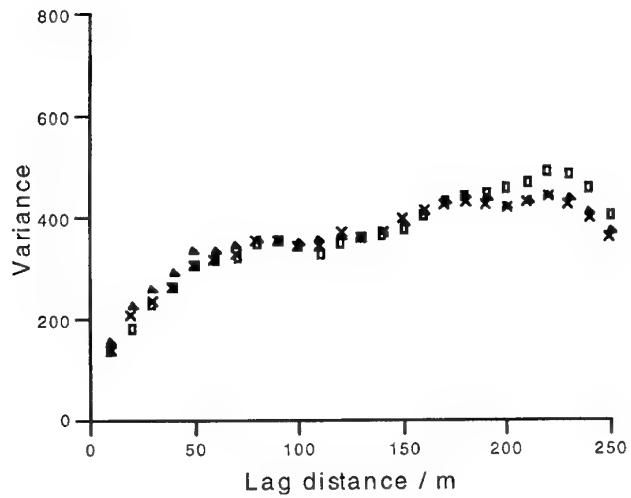
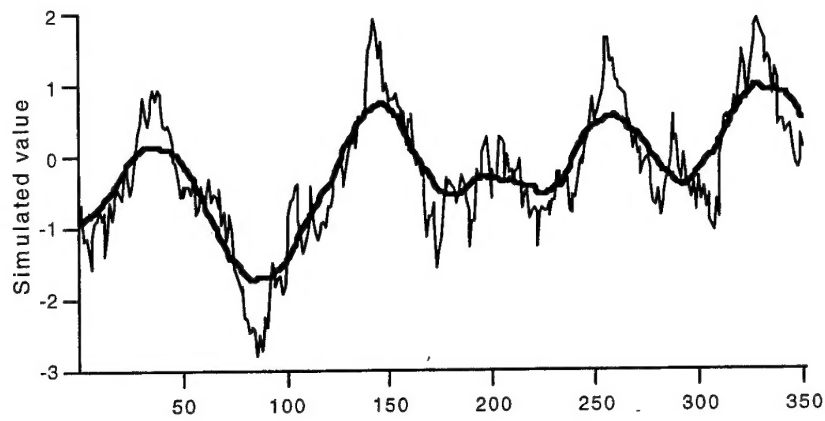
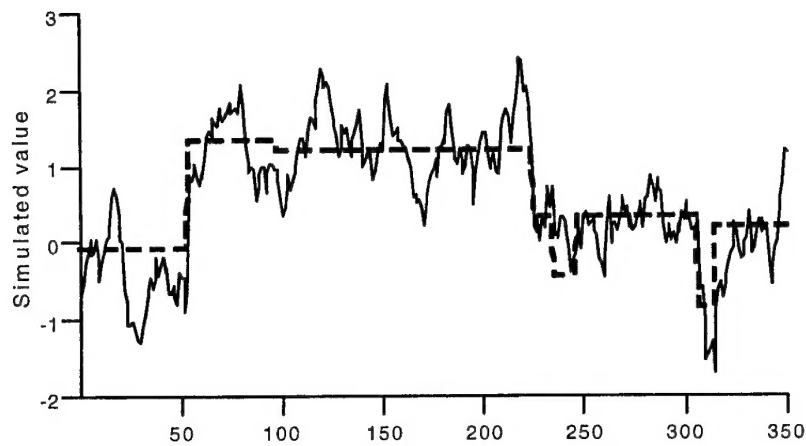


Fig 7

a)



b)



c)



Fig 8

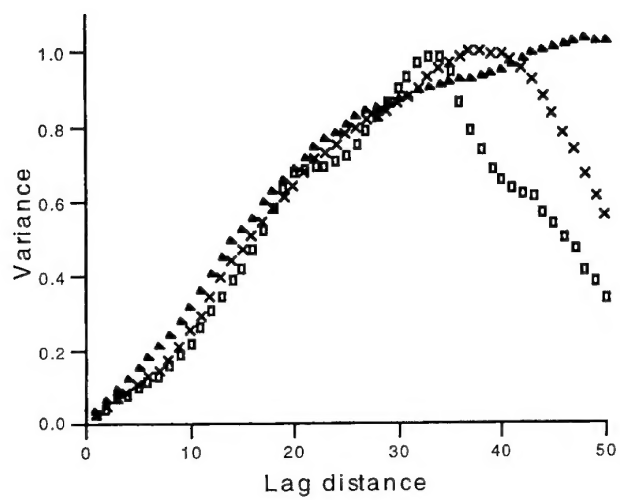
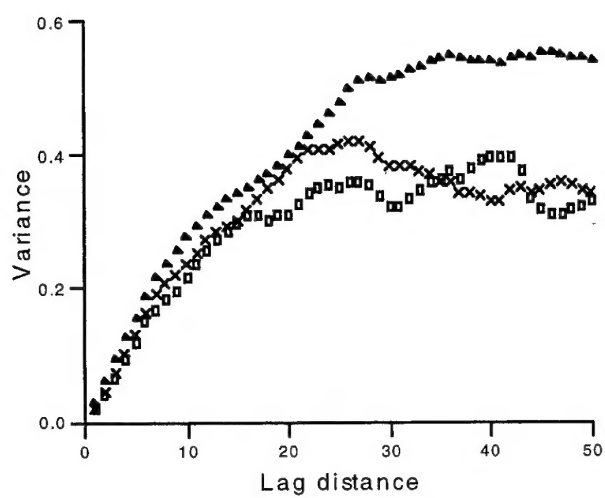


Fig 9

a)



b)

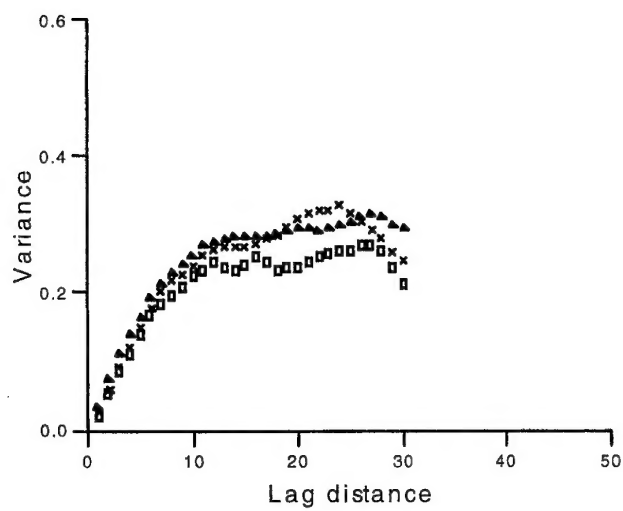


Fig 10

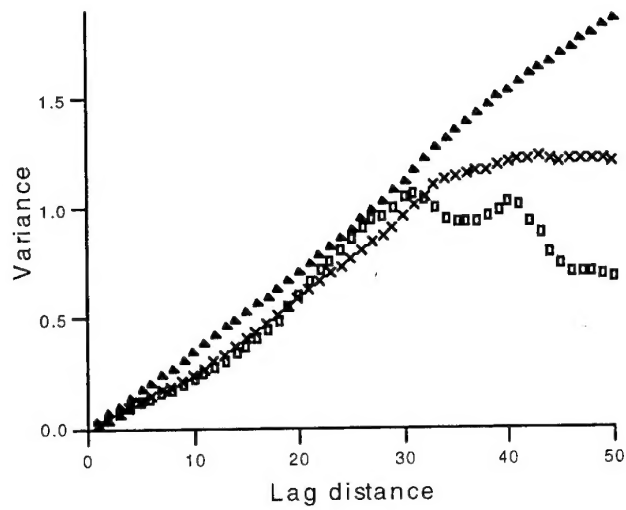


Fig 11

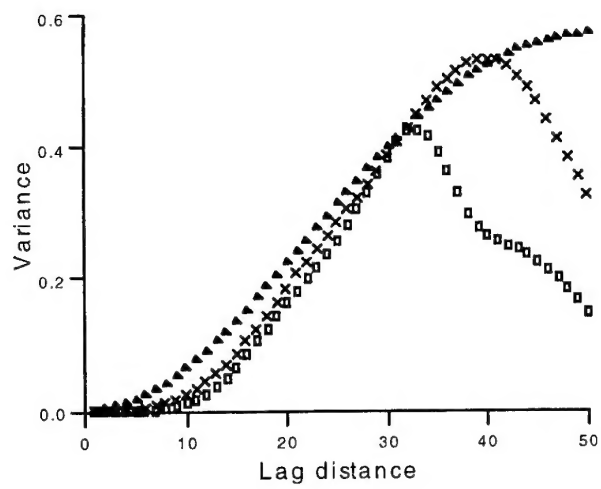


Fig 12